TRACER-AQ Analysis in Houston

FINAL REPORT

Grant Number: 582-18-81339
Proposal for Grant Activities No. 582-22-31913-020
Tracking No. 2022-39

Prepared for the Texas Commission on Environmental Quality (TCEQ)

Principal Investigators:
James Flynn, University of Houston
Yuxuan Wang, University of Houston
Rebecca Sheesley, Baylor University
Sascha Usenko, Baylor University
Paul Walter, St. Edward's University
Mark Estes, St. Edward's University

May 31, 2023

Table of Content

Executive Summary

The Department of Energy's TRacking Aerosol Convection ExpeRiment (TRACER)was designed to study how fine particles interacted with convective clouds and the associated impacts on precipitation and occurred in 2021-2022 in the Houston area, with the primary measurement location at the La Porte airport. To leverage the large contingent of instruments and scientists that would be deployed the TCEQ and NASA partnered to support the TRACER-Air Quality (TRACER-AQ) study which deployed scientists and equipment from the University of Houston, Baylor University, and St. Edward's University, as well as the Department of Energy and NASA, to build an intensive research effort that has been carried out during the August and September 2021. Key findings from the analysis of these efforts are included below.

- Only one of the ozone episodes during TRACER-AQ 2021, 24–27 September 2021, followed the post-frontal ozone episode pattern observed in previous studies. The other events appear to have arisen due to waning influence from the Bermuda High, which resulted in weak surface pressure gradients and thus stagnant conditions (3.5.1).
- Long-range transport analysis showed air masses during ozone pollution episodes were transported from the central/northern US. In addition, local recirculation of air masses and pollutant accumulation across Houston contributed to the ozone exceedances (3.1.3.4).
- Stagnation/re-circulation of air parcels over the Houston region is a key factor leading to pollution accumulation and elevated levels of ozone (and other pollutants) (3.1.1).
- Isoprene contributed a significant fraction of the total OH reactivity at the San Jacinto Battleground site (3.1.3.3).
- High O_3 at coastal locations was often associated with afternoon winds coming from Galveston Bay or the Gulf of Mexico (3.3.3.5).
- The CAMx model showed elevated ozone production rates across the Houston metropolitan area, with hotspots mainly over Houston city and industrial districts of the Houston Ship Channel (HSC) (3.2.3).
- Transported VOC-rich air masses from northerly flows brought ozone precursors to the region, causing a transition in the ozone formation tendency from VOC-limited to NO_x-limited conditions. However, the city of Houston and HSC remained in a VOC-limited regime due to local NO_x emissions that preponderated the impact of transported VOCs (3.2.3).
- Two periods of biomass burning were detected, September 7-11 and 21-26. Elevated ozone levels occurred on days following the identification of enhanced biomass burning influence the night before (3.4.1).

1 INTRODUCTION

The Houston-Galveston-Brazoria ozone non-attainment area is one of the most intensively studied polluted regions in the world. Large-scale field campaigns designed to study pollutant emissions, ambient concentrations, formation, accumulation, and transport were carried out in 1993, 2000, 2006, 2009, and 2013. In addition, the TCEQ and its predecessor agencies have funded dozens of studies independent of the field campaigns. Consequently, our understanding of many of the atmospheric processes leading to pollution events in Houston is greatly improved. Despite these efforts to gain a scientific understanding of ozone events in Houston, some gaps remain. One of these gaps is a clear understanding of the subtle meteorological dynamics over the waters of Galveston and Trinity Bays and the Gulf of Mexico and how those dynamics interact with the complex emissions of the nearby industrial areas. Making measurements over water is a difficult challenge; only the TexAQS 2006 study has been able to successfully carry out useful over-water studies due to the presence of the Research Vessel *Ronald H. Brown* during that field campaign (e.g., Osthoff et al. 2008; Tucker et al. 2010; Sommariva et al. 2011; Williams et al. 2009). Recently, however, successful and interesting scientific studies have been done in Chesapeake Bay, Long Island Sound, and Lake Michigan, and the techniques and analyses that were successful for those studies indicate the time was right for a sophisticated study of air pollution over Houston's nearby bays. The TRacking Aerosol Convection ExpeRiment-Air Quality (TRACER-AQ) study has marshaled the resources of the TCEQ, the University of Houston, Baylor University, and St. Edward's University, as well as the Department of Energy and NASA, to build an intensive research effort that has been carried out during the summer of 2021 and will continue into 2022.

Previous field campaigns determined that the highest ozone concentrations observed in the Houston area were, without exception, linked to the industrial emission sources in and near the Ship Channel (Ryerson et al. 2003; Daum et al. 2003; 2004; Berkowitz, Spicer, and Doskey 2005; Parrish et al. 2009). The petrochemical emission sources in Chambers, Galveston, and Brazoria Counties were also implicated in creating high ozone concentrations, though usually not in Houston (de Gouw et al. 2009; Wert et al. 2003).

2 METHODS

2.1 Measurement platforms and observational data

Comprehensive measurements in the Houston-Galveston-Brazoria region, a joint effort from DOE, NASA, and TCEQ, were made during the September 2021 TRACER-AQ intensive operating period (**Figure 2.1.1**) and included ground-based and aircraft-based ozone lidars, Pandora and AERONET, mobile laboratories and boat-based measurements, and ozonesondes.

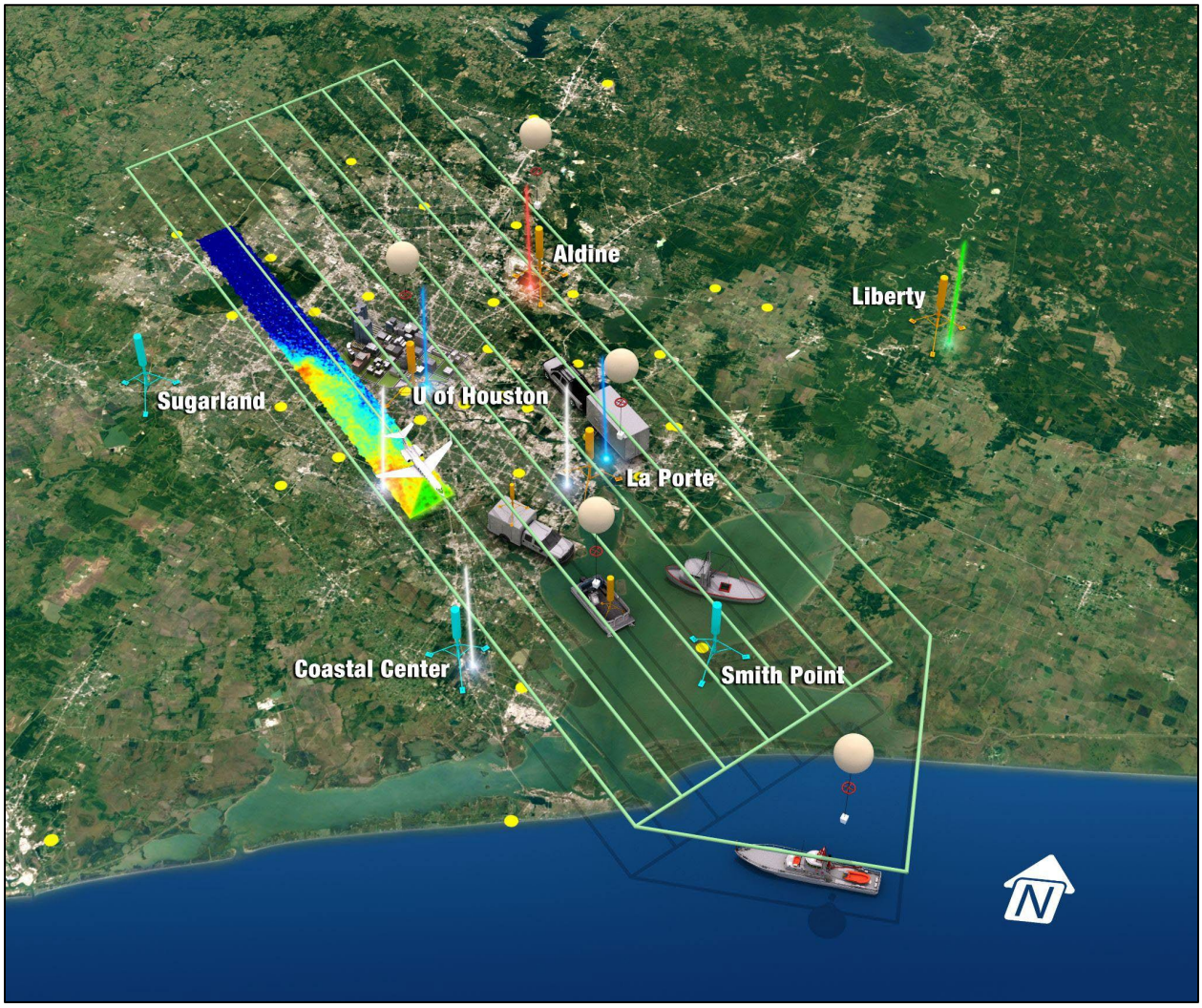

Figure 2.1.1: *A diagram overviewing the measurements taken during the September 2021 intensive operating period of the TRACER-AQ campaign. Image credit: Tim Marvel/NASA LaRC*

Mostly air quality data used in this data analysis project are from the measurement platforms and instrumentation listed in **Table 2.1**. In brief, the University of Houston owned Mobile Air Quality Lab (MAQL1) measured a suite of VOCs, trace gases, and meteorological variables a suite of VOCs, trace gases, and meteorological variables alternated between stationary, mainly at the La Porte site, and mobile measurements which were made across the Houston-Galveston-

Brazoria (HGB) region. The Baylor University owned Mobile Air Quality Lab (MAQL2) was deployed at the San Jacinto Battleground Historic Site and measured a suite of VOCs and trace gases. In addition, three boats were outfitted with instrumentation to obtain the ozone, oxidant, ad meteorological parameters offshore, which includes the commercial ocean-going marine vessel (the Red Eagle boat) operated out of Galveston, TX offshore in the Gulf of Mexico, a commercial shrimper (the shrimp boat) operated on the east side of Galveston Bay out of Smith Point, TX, and a UH-owned pontoon boat (the Pontoon boat) operated in the Galveston Bay. Furthermore, a total of 96 ozonesonde launches from June to October were included in this analysis project.

In addition these measurement platforms, air quality and meteorological data from TCEQ monitoring stations with nearly complete observational records back to 2000 were also used. Data from past field campaigns including Texas Air Quality Study (TexAQS) 2000, TexAQS 2006, SHARP 2009, and DISCOVER-AQ 2013 are also used.

Table 2.1: *Platforms and instrumentation deployed during the TCEQ TRACER-AQ1 project*

Platform	Instrument	Measurements
MAQL1	Peak Performer 1 Reducing Compound Photometer	Isoprene
MAQL1	liquid-phase reaction and fluorescence light technique	Formaldehyde
MAQL1	Rapid Alkene Detector	Highly reactive VOCs (lumped ethene, propene, butadiene, and isoprene)
MAQL1	AROMA VOC analyzer	Rapid scan mode for bulk compound classes (e.g. aromatics, dienes, and chlorinated compound classes). Speciated mode for benzene, toluene, ethylbenzene, xylene, styrene, and isoprene
MAQL1	Pandora Spectrometer	Columnar values of NO2, O3, and formaldehyde
MAQL1	Trace gas analyzers	NO, NOx/NO2, NOy, O3, SO2, and CO
MAQL1	Other parameters	jNO2, temperature, RH, pressure, wind speed, wind direction, and GPS
MAQL2	Proton Transfer Reaction Mass Spectrometer with a Selective Reagent Ionization (PTR-SRI-MS)	Formaldehyde, acetonitrile , acetaldehyde, acetone, isoprene, methyl vinyl ketone plus methacrolein, benzene, toluene, styrene, C2-alkylbenzenes, C3-alkylbenzenes, C4-alkylbenzenes, monoterpenes, propene, ethylene, and 1,3- butadiene
MAQL2	Tricolor Absorption Photometer	Aerosol absorption
MAQL2	Tricolor nephelometer	Aerosol scattering

Platform	Instrument	Measurements
MAQL2	Trace gas analyzers	NO, NO_X/NO_2, NO_Y, O_3, SO_2, and CO
MAQL2	Other parameters	jNO2, temperature, RH, pressure, wind speed, wind direction, and GPS
The Red Eagle	2B Technology Model 205 dual-beam ozone analyzer	O_3
The Red Eagle	Weather station	Temperature, relative humidity, pressure, and wind speed and direction
The Red Eagle	Ozonesonde launch	Vertical profiles of O_3, temperature, and RH; GPS location, and GPS-derived wind speed and direction
The shrimp boat	2B Technology Model 205 dual-beam ozone analyzer	O_3
The shrimp boat	Weather station	Temperature, relative humidity, pressure, and wind speed and direction
The shrimp boat	Vaisala CL-51 ceilometer	Boundary layer height
UH Pontoon Boat	2B Technology Model 205 dual-beam ozone analyzer and NO2 photocell	O_3 and NO_2
UH Pontoon Boat	Pandora spectrometer	Columnar values of NO_2, O_3, and formaldehyde
UH Pontoon Boat	Vaisala CL-51 ceilometer	Boundary layer height
UH Pontoon Boat	Ozonesonde launch	Vertical profiles of O_3, temperature, and RH; GPS location, and GPS-derived wind speed and direction

2.2 Airmass Trajectory and Transport Modeling

The Weather Research and Forecasting (WRF) model was employed to simulate meteorological fields for three domains over the contiguous United States (d01: 12km × 12km), Southeast Texas (d02: 4km × 4km), and the Houston-Galveston-Brazoria region (d03: 1.33km × 1.33km). Using the WRF-generated meteorological fields, 3-dimensional backward trajectory analysis was performed using the Hybrid Single-Particle Lagrangian Integrated Trajectory (HYSPLIT) model and FLEXible PARTicle (FLEXPART) dispersion model to track the pathway and dispersion of air masses transporting pollutants to the Houston area during the TRACER-AQ campaign. The HYSPLIT model was used to derive regional-scale transport patterns using coarse resolution (12 km) meteorological fields, while the FLEXPART model was employed to simulate local-scale (4 km) plume dispersion (backward in time).

2.3 Multi-scale photochemical modeling

The Comprehensive Air quality Model with extensions (CAMx) was employed using the WRF-simulated meteorology to model 3-dimensional chemical fields over the study domains. The CAMx outputs include 3-D distributions of ozone and its precursors (i.e., NO_X and speciated VOCs) along with ozone production rates by different chemical pathways and have been evaluated against TRACER-AQ observations. A semi-Lagrangian framework was defined by coupling FLEXPART dispersed plumes with CAMx-generated chemical fields in which the levels of different pollutants and ozone production rates from CAMx were sampled along the path of air parcels derived from the FLEXPART model.

2.4 NASA Langley Research Center (LaRC) zero-dimensional model

Ozone (O_3) formation and destruction rates and OH reactivity of VOCs are calculated by the NASA LaRC zero-dimensional model (Crawford et al., 1999; Olson et al., 2006). A comparison of several model mechanisms including LaRC based on the Texas-II Radical and Aerosol Measurement Project (TRAMP) campaign can be found in Chen et al. (2010). The model is run in time-dependent mode assuming diurnal steady state with standard constraints and formaldehyde as of its latest application in the San Antonio Field Studies in 2017 (SAFS 2017) (Guo et al., 2021). Among the model inputs, trace gases, meteorological parameters, photolysis rate of NO_2, and designated VOCs are from real-time measurements, while a subset of VOCs required but unmeasured by the PTR-MS are adapted from TCEQ CAMS site at Lynchburg Ferry. More details on the ozone formation rate ($F(O_3)$), ozone destruction rate ($D(O_3)$), the OH reactivity of VOCs, and the NO_X-VOC sensitivity derived from the LaRC model are provided in their corresponding sections.

3 ANALYSIS TOPICS

3.1 High Ozone Event Investigations

3.1.1 Summary and Key Findings

- During the observational periods from June 4 to October 8, a total eight high ozone episodes where ozone concentrations exceeded the maximum daily 8-hour average were observed.
- The ozone exceedance days on June 14–19, 2021 had near stagnant winds that led to overnight residual layer ozone contributing to the next day's boundary layer ozone.
- The exceedance day on July 26, 2021 had a land-bay breeze circulation similar to what is described in Banta et al. (2005). Ozone that was aloft in the morning over Galveston Bay likely was able to mix into the afternoon boundary layer.
- On September 9, coastal sites that exceeded the ozone standard had contributions from the transport of high ozone concentrations offshore of Galveston in the Gulf of Mexico. Inland sites that exceeded likely had contributions from the downward transport and mixing of elevated residual layer ozone at the surface.
- The ozone episode during September 23–26, 2021 occurred in post-frontal conditions. Subsidence led to a deep dry layer of air above the boundary layer. On September 24, there was a layer of enhanced ozone near ~2.5 km throughout the HGB region.
- Backward trajectory analyses showed the two September post-frontal ozone episodes have different transport patterns on a local scale, although both were affected by synoptic scale circulations.
- Stagnation/re-circulation of air parcels over the Houston region is a key factor leading to pollution accumulation and elevated levels of ozone (and other pollutants).
- Average O_3 values observed from the three marine vessels 'offshore ozone' was higher than the averaged 'onshore' values, derived from averaging (25) stationary TCEQ sites, in all months of the campaign. Likely due in part to the lack of titration occurring overnight and in the early morning from urban/industrial emissions at the boat platforms.
- High O_3 (>70 ppbv) values recorded at the near shore monitor of Seabrook (C45) show they are associated with wind directions related to Galveston Bay as the upwind source region.
- Maximum Daily 8-hour Average (MDA8) O_3 was higher onshore vs offshore during all but one high O_3 event, which was in the wake of Hurricane Nicholas and was a uniquely coastal event.
- Peak 1-hour average O_3 values were higher onshore during all high O_3 episodes, with the exception of September 17th when the daily peak 1-hr ozone concentration was recorded over Galveston Bay by the UH Pontoon boat.

- The median of the hourly-averaged F(O3) was 28.3 ± 17.5 ppbv h−1 for 6:00 to 19:00 CST for high ozone days, approximately 10% higher than that of the non-exceedance days (25.7 ± 16.2 ppbv h−1). The same elevated ozone formation period between 9:00 and 15:00 CST were observed for both high ozone days and non-exceedance days. Two F(O3) peaks between 9:00-10:00 CST (49.9 ppbv h−1) and 12:00-13:00 CST (46.6 ppbv h−1) were observed during high ozone days. For non-exceedance days, the first peak (46.6 ppbv h−1) was also observed between 9:00-10:00 CST, but the second peak (44.4 ppbv h−1) was delayed to 13:00-14:00 CST.
- The total OH reactivity of VOCs increased by 17%, from 4.1 ± 0.6 s−1 in non-exceedance days to 4.8 ± 0.8 s−1 in high ozone days. But the fractional contributions of individual VOC groups were similar. In both cases, isoprene (2.4 ± 0.9 s−1 and 51% in high ozone days; 1.9 0.6 s−1 and 45% in non-exceedance days) was the dominant species followed by lumped alkenes (0.7 ± 0.3 s−1 and 15%; 0.6 ± 0.1 s−1 and 15%), while the fractional contributions of all the rest of the VOC reactivities were below 10%.

3.1.2 Methodology

Ozone profiles for this project were measured using the electrochemical concentration cell (ECC) type ozonesonde instrument (Komhyr 1972; Komhyr 1986). All ozonesondes use 0.5% KI solution recommended by the Jülich Ozone Sonde Intercomparison Experiment (JOSIE), which found biases <5%, a precision of 3–5%, and an accuracy of 5–10% below 30 km (Smit et al. 2007; Thompson et al. 2019). The ozonesonde ECC cathode and anode solutions were prepared and provided by Brian Johnson (NOAA). Patrick Cullis (NOAA) maintains a website (https://www.patrickcullis.com/ozonesonde-instructions.html) that describes the ozonesonde conditioning and calibration procedures.

The campaign employed the InterMet iMet-4RSB radiosonde, which collects pressure, temperature, humidity, GPS location, and GPS-derived wind speed and direction. The radiosondes are connected to the ozonesondes and transmit data (~one data packet per second) that can be received by an antenna at the surface.

Our default balloon size is the 600-gram balloons that carry our payloads to 27–30 km before bursting. We used 350-gram balloons that carried our payloads to altitudes of 22–24 km before bursting in instances when a lower burst altitude had a more favorable expected landing site based on the balloon trajectory. On some occasions we used a type of 350-gram balloon that reached approximately 18 km prior to burst, which was again to accommodate a more favorable landing location.

Ozonesonde data is processed by Skysonde software. The data is then converted to the ICARTT format, which consists of a text file with a header followed by columns of data in comma separated values (csv) format, found on the NASA TRACER-AQ data archive (https://www-air.larc.nasa.gov/cgi-bin/ArcView/traceraq.2021?SONDE=1). In most cases,

the data on the archive has been reprocessed to correct for a pressure offset of the radiosonde measurement (Stauffer et al., 2014).

For analysis purposes, it is common to determine the planetary boundary layer height (PBLH) from the ozonesonde profiles. PBLH is determined by examining gradients in relative humidity (RH), O_3, temperature, and potential temperature (θ) and is identified as the height at which most (if not all of) these variables show a sharp change in their vertical gradients. Typically, for an afternoon potential temperature profile, just above the surface $\partial\theta/\partial z < 0$, the air is unstable (due to surface heating). After the initial negative gradient near the surface, the potential temperature is approximately constant ($\partial\theta/\partial z = 0$) to the top of the boundary layer near 3.9 km AMSL on this day. A near-zero gradient in potential temperature is common. The atmosphere is generally stable above the boundary layer, as indicated by the positive potential temperature gradient ($\partial\theta/\partial z > 0$). The larger a positive potential temperature gradient is, the stronger the atmosphere's stability at that altitude. The potential temperature will reach the same value that it is at the surface at the top of the PBL (Haman, Lefer, and Morris 2012). In some cases, there are multiple possible layers present, and there is uncertainty in the estimated PBLH based on which layer is chosen.

- High O_3 events identified by an exceedance of MDA8 O_3 at a stationary monitor or boat platform during the operational period.
- Averaged O_3 mixing ratios from 25 TCEQ sites considered ‘onshore’ as well as the three instrumented boats, considered ‘offshore’, for each month of the campaign. Data for July and October, when the boats did not operate for the entire month, TCEQ data was matched with time periods the boats were collecting data.
- Wind direction data was plotted against O_3 mixing ratios for the boats and TCEQ sites near Galveston Bay and the Gulf of Mexico and colored using the time of day for each month.
- Diurnal values of boundary layers observed by the pair of operating CL-51 ceilometers were analyzed for the two boats while co-sampling during July and August.
- From LaRC modeling, O_3 formation rate ($F(O_3)$) is calculated from three main NO_2 generating pathways in the LaRC model output: HO_2+NO, RO_2+NO, and CH3O2+NO (where CH3O2 is specifically the methyl peroxy radical, which is not included in the RO_2 parameter), as subsequent NO_2 photolysis and the association of O(3P) with O_2 are sufficiently fast and non-rate-limiting. O_3 destruction rate ($D(O_3)$) is calculated from a combination of five main OH production reaction (O(1D)+H_2O), HO_X-driven O_3-depleting chain reactions (HO_2+O_3, OH+O_3) under lower-NO_X conditions, the termination of both NO_X and HO_X in forming HNO_3 (NO_2+OH) under higher-NO_X conditions, and the reactions of O_3 with specific VOCs (O_3+NMHC),

particularly those with carbon-carbon double bonds. Net $P(O_3)$ is calculated as the difference between $F(O_3)$ and $D(O_3)$.

- The relative importance of a specific VOC (or lumped VOC) with respect to the formation of secondary O_3 is determined by its atmospheric abundance and how quickly it reacts with OH. The reactivity of a VOC species (VOCR) is defined as the product of its concentration and reaction rate constant (k) with OH and is also calculated from the LaRC model output.

3.1.3 Results

Table 3.1 shows a calendar of ozone levels during the measurement period in 2021 from June to October. A total of eight high ozone events where ozone concentrations exceeded the maximum daily 8-hour average were observed. These events lasted from one to six days.

Table 3.1: *A summary of the 96 ozonesondes in 2021. The color code of the ozone air quality index (AQI) is shown for each day. For days where ozone concentrations exceeded the maximum daily 8-hour average (orange or red), the number of monitors in the Houston-Galveston-Brazoria (HGB) region in exceedance of the ozone standard (MDA8 [O_3] > 70 ppbv) and MDA8 ozone value of the highest monitor is shown.*

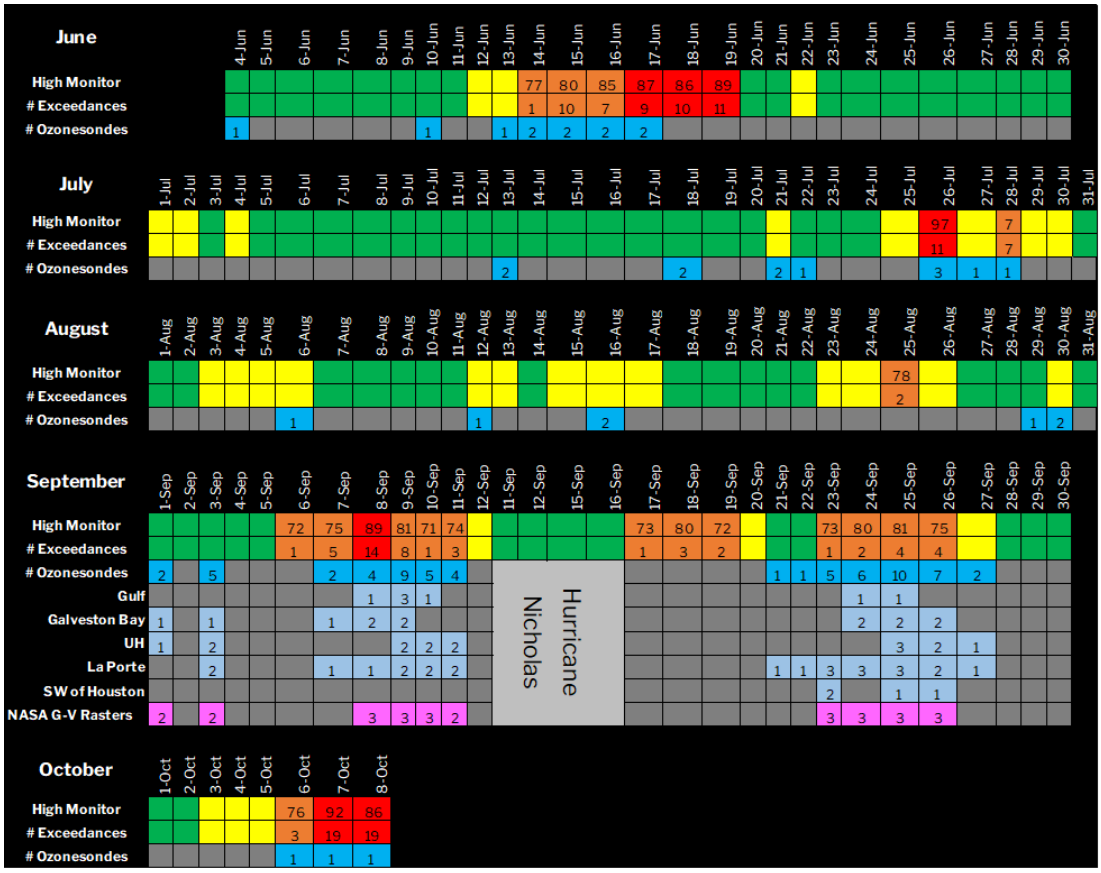

3.1.3.1 Synoptic Setup for High Ozone Episodes

Geopotential height at 850mb is a good indicator of where high- and low-pressure centers are located synoptically as this height does not see the diurnal variation seen at the surface. Plots of geopotential heights during six of the identified high O_3 episodes (July 26, August 25, September 6–11, September 17–19, September 23–26, and October 6–8) are shown in **Figure 3.1.1** and display the synoptic setup for high ozone episodes identified during the observational period. Data for these plots was generated using the North American Regional Reanalysis (NARR) dataset. **Figure 3.1.1 a** and **b** show the synoptic setup for the first two high ozone episodes (July 26 and August 25), during these periods the Bermuda high pressure retreated eastward allowing for light synoptic forcing over the HGB region. This setup allows the local land-bay breeze circulation to be the dominant forcing and promotes recirculation of an aged air mass between Galveston Bay and the inland areas of central and southeast Houston.

Figure 3.1.1 c, **e** and f show the synoptic setup for the September 6–11 and September 23–26 as well as the October 6–8 episodes, these high O3 events were all driven by the passage of cold frontal boundaries changing the cleaner marine air mass generally over the HGB region to a continental air mass. These time periods display stronger pressure gradients across the United States with low pressure to the N/NE and high pressure to the south and west. This setup puts Houston in a northerly continental flow that veers to easterly flow after the frontal passage.

Figure 3.1.1 d shows the setup for a unique high ozone episode, from September17–19 that was not well forecast occurring after the passing of tropical system Nicholas. The synoptic setup for this exceedance was light northerly veering to easterly winds in the wake of tropical system Nicholas cutting off the synoptic forcing to the east and creating an environment of smaller pressure gradients across the eastern United States.

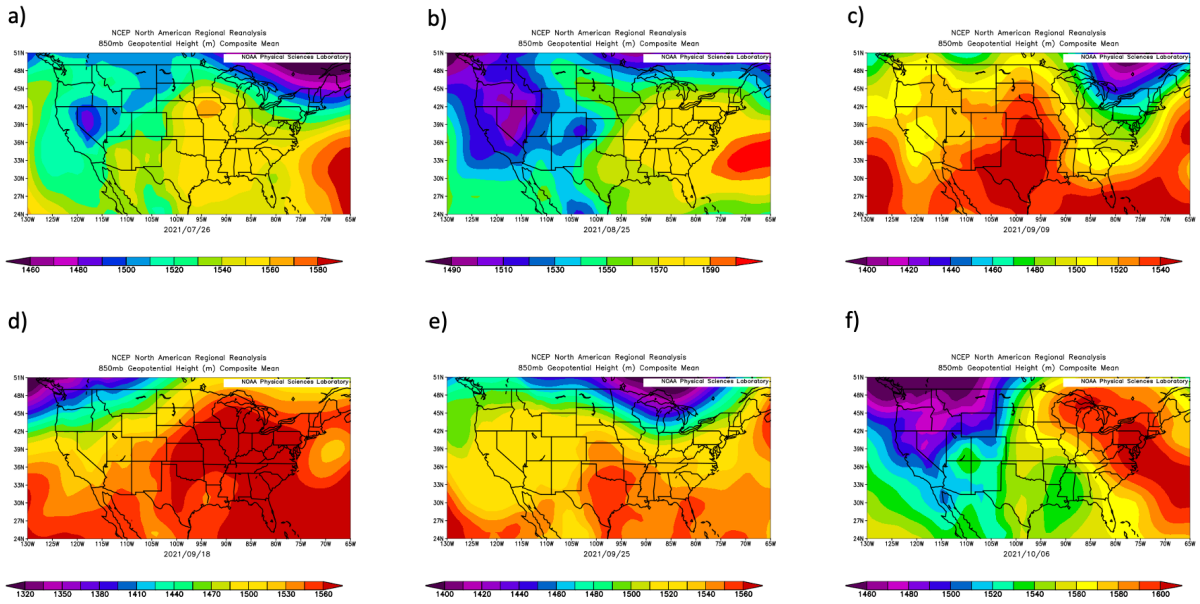

Figure 3.1.1 *Geopotential height at 850 mb during six high-ozone episodes observed during the TRACER-AQ 1 campaign on a) July 26, b) August 25, c) September 9, d) September 18, e) September 25, and f) October 6 plotted from North American Regional Reanalysis (NARR) data. S Warmer colors show areas of higher pressure while the cooler colors show regions of lower pressure.*

3.1.3.2 Select High Ozone Episodes

3.1.3.2.1 Episode June 14-19

An ozone episode with six consecutive ozone exceedance days during 14–19 June 2021 was characterized by light winds where each day was designated an ozone action day for Houston. On 14–17 June, ozonesondes were launched twice a day, one at dawn and the other in the afternoon, and those profiles are shown in **Figure 3.1.2**. The early morning ozonesonde launches provide profiles of the residual layer that may mix into that day's boundary layer. As observed by the light blue curve of the ozone concentration for the morning ozonesonde flights (focusing below the black horizontal line, which is the estimated afternoon boundary layer height), the ozone in the residual layer was elevated on 15–17 June.

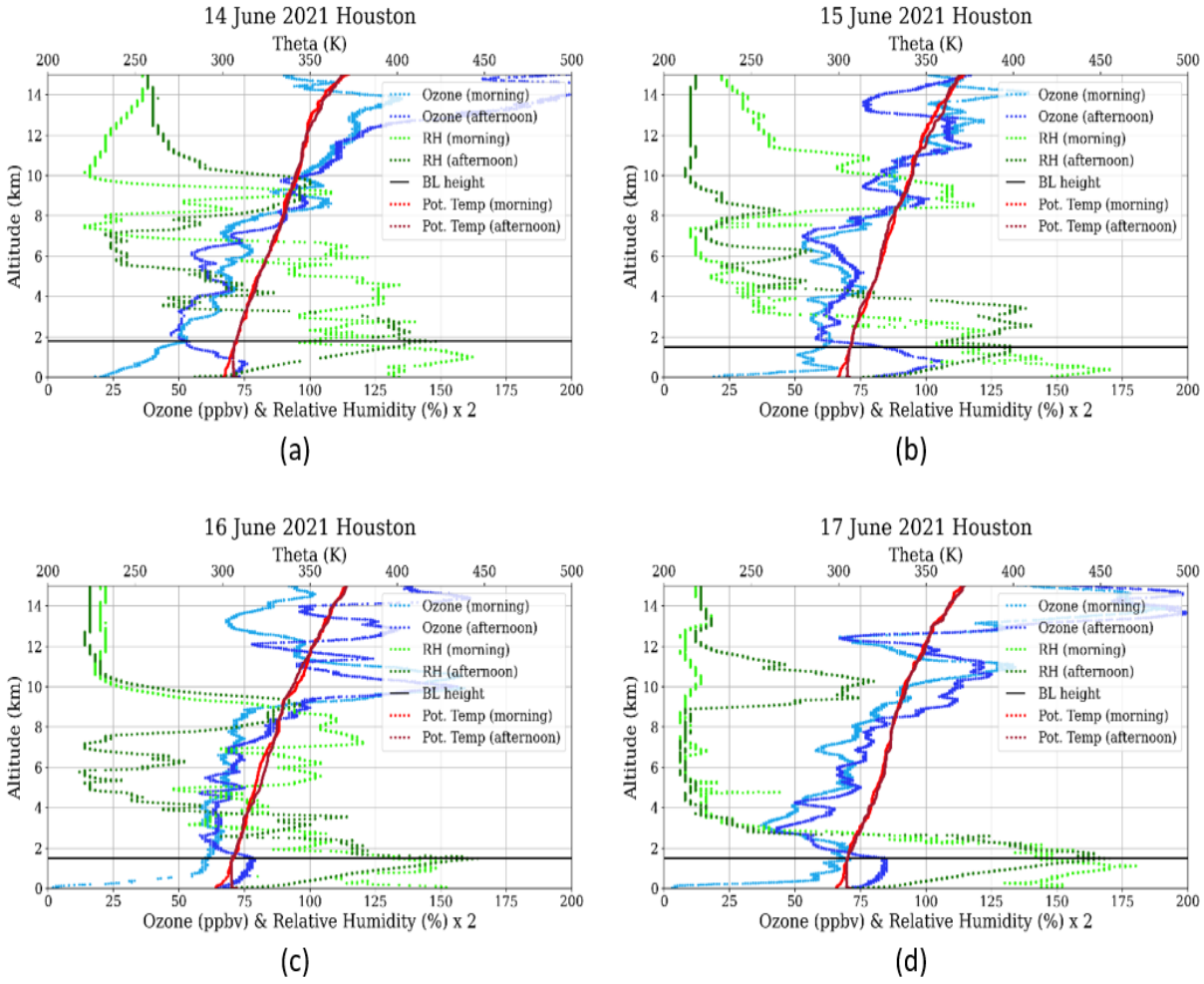

Figure 3.1.2: *Dawn (light blue) and afternoon (dark blue) ozone profiles from the University of Houston on (a) 14 June 2021, (b) 15 June 2021, (c) 16 June 2021, and (d) 17 June 2021.*

3.1.3.2.2 Episode 26 July

26 July 2021 was forecasted to be a high ozone day and was designated an 'Ozone Action Day' by TCEQ. The UH pontoon boat operated in Galveston Bay from morning to late afternoon on the west side of Galveston Bay. The C35 Deer Park #2 monitor ultimately observed the highest MDA8 O_3 concentration of 97 ppbv. **Figure 3.1.3** shows a map of the HGB area with noted TCEQ monitors near Galveston Bay and ozonesonde launch sites from 26 July.

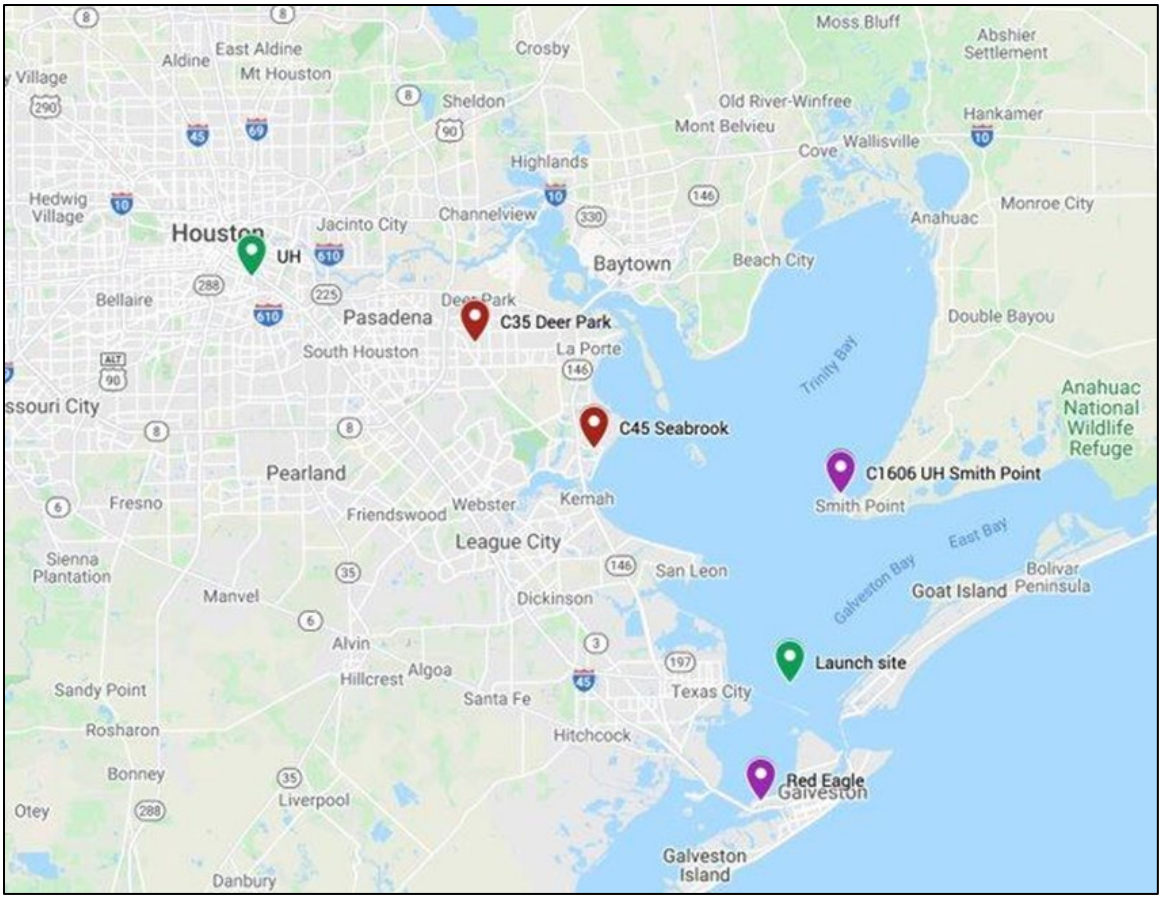

Figure 3.1.3: *Map of Houston and Galveston Bay reflecting measurements taken on 26 July 2021. An ozonesonde was released in the morning from Galveston Bay (green pin) and a late afternoon ozonesonde was released from the University of Houston main campus (green pin). The locations of the C35 Deer Park #2 and C45 Seabrook monitors are shown (red pins).*

The UH pontoon boat deployed from Kemah, TX, and initially headed south towards the Texas City Dike for an ozonesonde launch in the SW area of Galveston Bay. A morning ozonesonde was released from the UH pontoon boat in Galveston Bay near the Texas City Dike (29.383° N, 94.831° W). The morning sounding (8:37 CST) on 26 July, shown in **Figure 3.1.4**, had missing data during the ascent from 0.57–1.13 km AMSL. The profile shows a marine layer height of 0.31 km AMSL, and an ozone enhancement of 66 ppbv above the surface at 1.13 km AMSL that would have the potential to mix down to the surface as the depth of the boundary layer grew throughout the day. Within an hour of the release of the ozonesonde the ozone concentrations began to rapidly rise at the C1606 Smith Point monitor (and where the Shrimp Boat was located on this day).

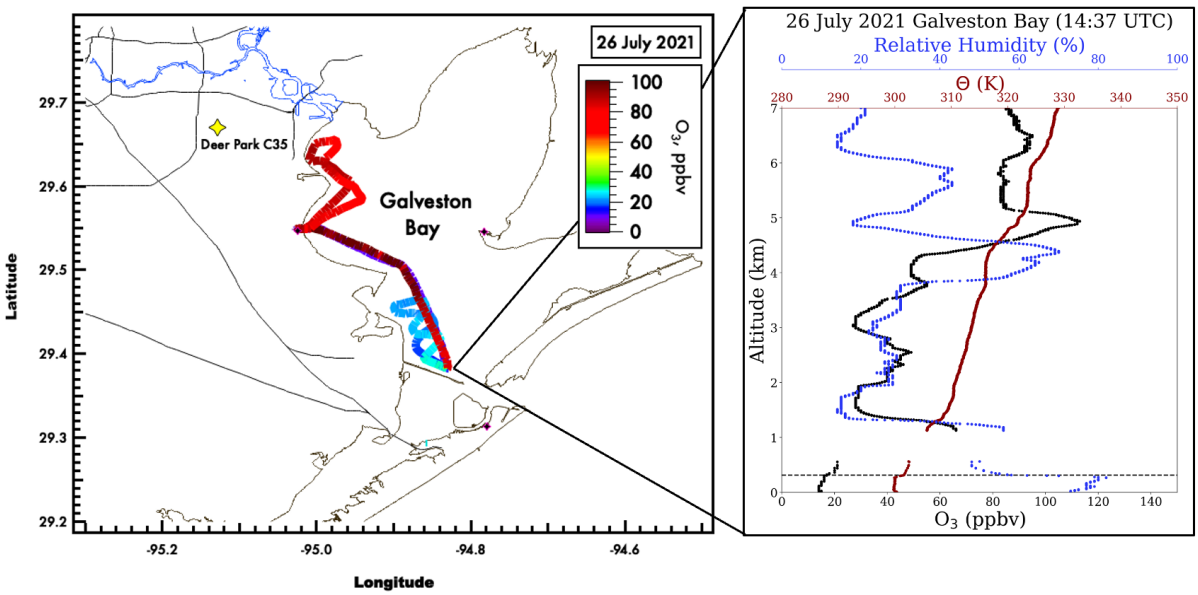

Figure 3.1.4: *Spatial plot of the UH pontoon with associated ozone mixing ratio and ozonesonde vertical profile from morning overwater launch on 26 July 2021.*

Figure 3.1.5.c shows the wind run for the C35 Deer Park #2 on 26 July and **Figure 3.1.5.d** shows the wind run for the C45 Seabrook monitor. Each wind run starts from the 00 CST hour, located at (0, 0) on the graph, and concludes on the 23 CST hour. The wind runs show wind vectors for each hour with distances in km. The color of the hourly wind vectors is based on the hourly ozone concentration, ranging from 0 ppbv (dark purple) to 130 ppbv (dark red). The large black arrow represents the vector sum.

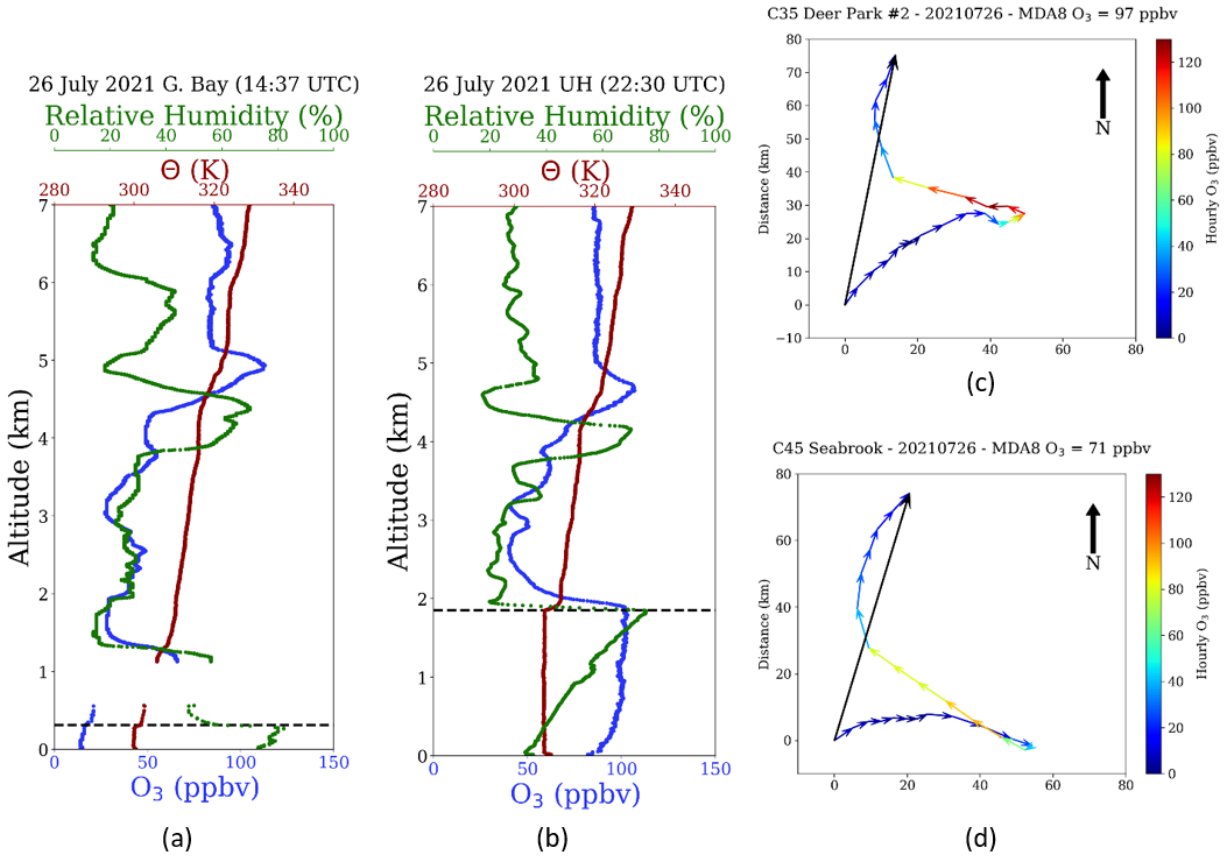

Figure 3.1.5: *Ozonesonde profiles and wind runs for 26 July 2021. (a) Morning ozonesonde profile from Galveston Bay. (b) Late afternoon ozonesonde profile from the University of Houston main campus. (c) Hourly wind vectors (colored by hourly ozone concentration) and 24-hour wind run at the C35 Deer Park #2 monitor. (d) Hourly wind vectors (colored by hourly ozone concentration) and 24-hour wind run at the C45 Seabrook monitor.*

Wind runs from different locations can show how much the wind pattern varies through the urban area for a given day. Quite often, ozone exceedance days exhibit distinctive wind run patterns (e.g., Li et al., 2020). **Figure 3.1.5.c** and **Figure 3.1.5.d** show a land breeze in the late morning changing to a bay breeze in the afternoon coinciding with elevated ozone concentrations, consistent with Banta el al. (2005).

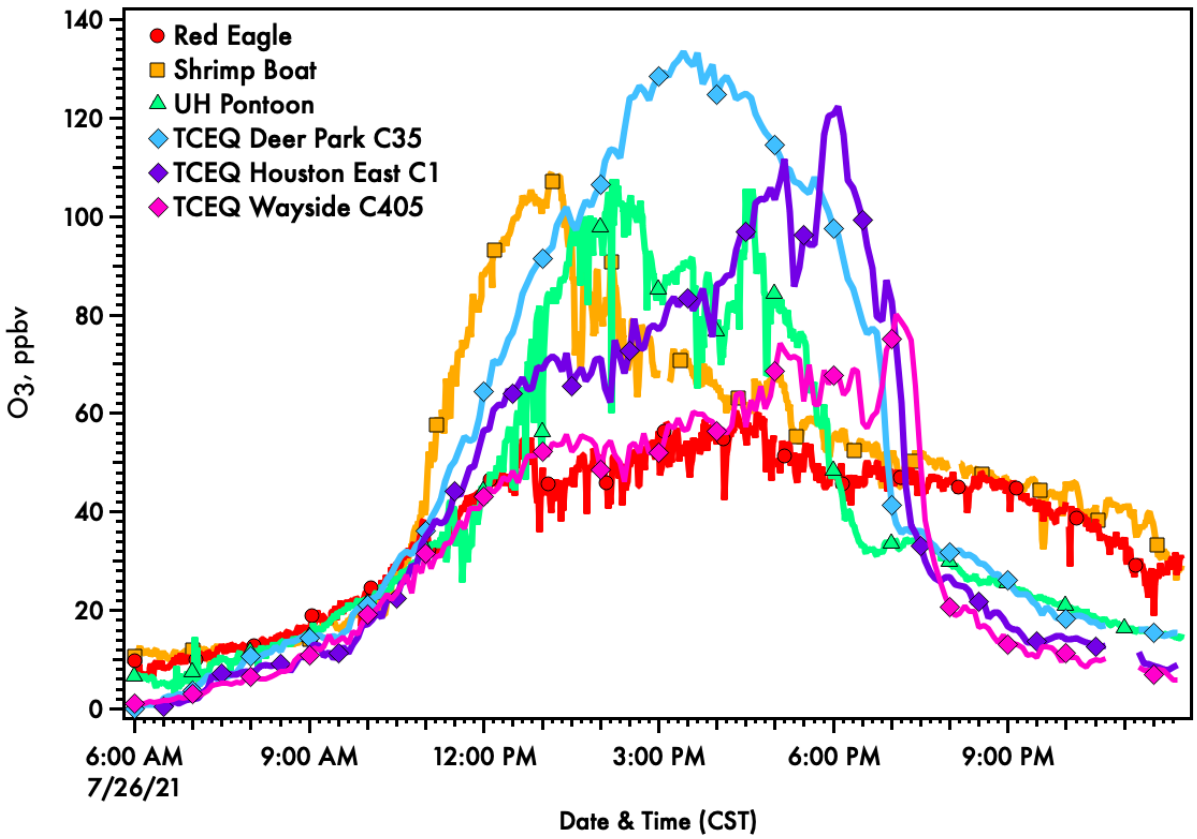

Figure 3.1.6: *Time-series of ozone from the three boat platforms as well as selected TCEQ monitoring sites. Colored from red to purple going southeast (coastal) to northwest (inland).*

July 26, 2021 was a day in which over-water observations verified the conceptual model described by Banta et al. 2005 observed during the TexAQS 2000 field campaign. This high ozone day in the HGB region resulted from the recirculation of a polluted air mass over the water of Galveston Bay and then returning the aged airmass with the rotating winds due to the development of a bay breeze. The July 26, 2021 ozone plume can be seen in the peaks in the time series in **Figure 3.1.6**, which are color-coded red to purple from SE to NW respectively. Ozone concentrations initially rapidly increased at the shrimp boat stationed in Smith Point, TX (along with the C1606 monitor). Increasing ozone levels were then observed on the UH pontoon boat as it transited northward toward Kemah to refuel. With the winds rotating to be out of the southeast, the UH pontoon boat later observed ozone above 100 ppbv, after redeploying in the W/NW portion of Galveston Bay. Once on land, the ozone plume had the highest recorded value at the Deer Park (C35) monitor, followed by smaller ozone peaks at subsequent monitors further inland. Noteworthy, is the consistently low values recorded at the Red Eagle platform, which was docked in Galveston, TX all day. These observations show the ozone plume did include the over water area of Galveston Bay, but did not extend further south into Galveston, TX or offshore.

3.1.3.2.3 Episode September 6-11

September 9, 2021 was amid six continuous MDA8 ozone exceedance days (6–11 September) in the HGB region. Air quality forecasts using photochemical models predicted high ozone offshore of Galveston Island in the Gulf of Mexico and Galveston Bay (**Figure 3.1.7**). Due to the air quality concerns, 9 September was an intensive operational day, which included nine ozonesonde (**Figure 3.1.7**) releases in the HGB region in coordination with overpasses of the NASA G-V aircraft.

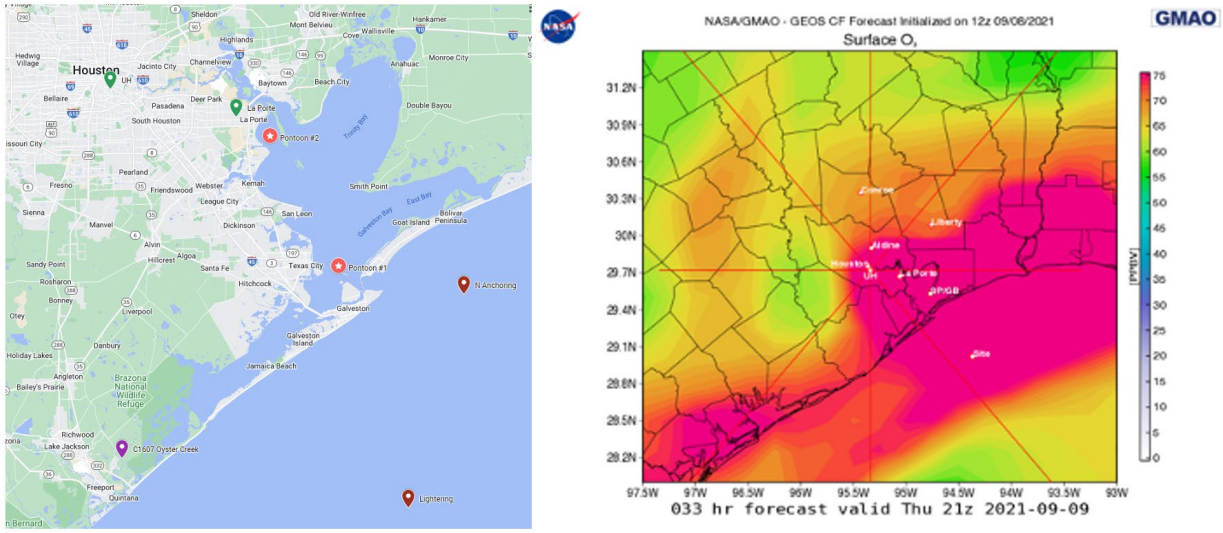

Figure 3.1.7: *(Left) The map shows the locations where nine ozonesondes were released on 9 September 2021: two each from the University of Houston and La Porte (green pins), two from the UH Pontoon Boat in Galveston Bay (salmon circles with stars), and three from the Gulf of Mexico (red pins, two from the N Anchoring location and one from the Lightering area). The purple pin shows the location of the C1607 Oyster Creek monitor. (Right) NASA GMAO forecast model output for 21z on 9 September 2021.*

The Red Eagle was chartered on 9 September to assess the levels of ozone encountered in the Gulf of Mexico while deploying to the Galveston Anchorage and Lightering areas, approximately 16 and 42 km offshore, respectively. The Red Eagle, while offshore in the Galveston ship lightering area of the Gulf of Mexico, approximately 42 km offshore, observed 1-minute surface ozone concentrations as high as 110 ppbv (**Figure 3.1.8**). Shortly after, while still in the lightering area, an ozonesonde (**Figure 3.1.8**) was launched from the deck of the Red Eagle and observed > 100 ppbv of ozone well-mixed within a shallow (370 m) marine boundary layer (black dashed line).

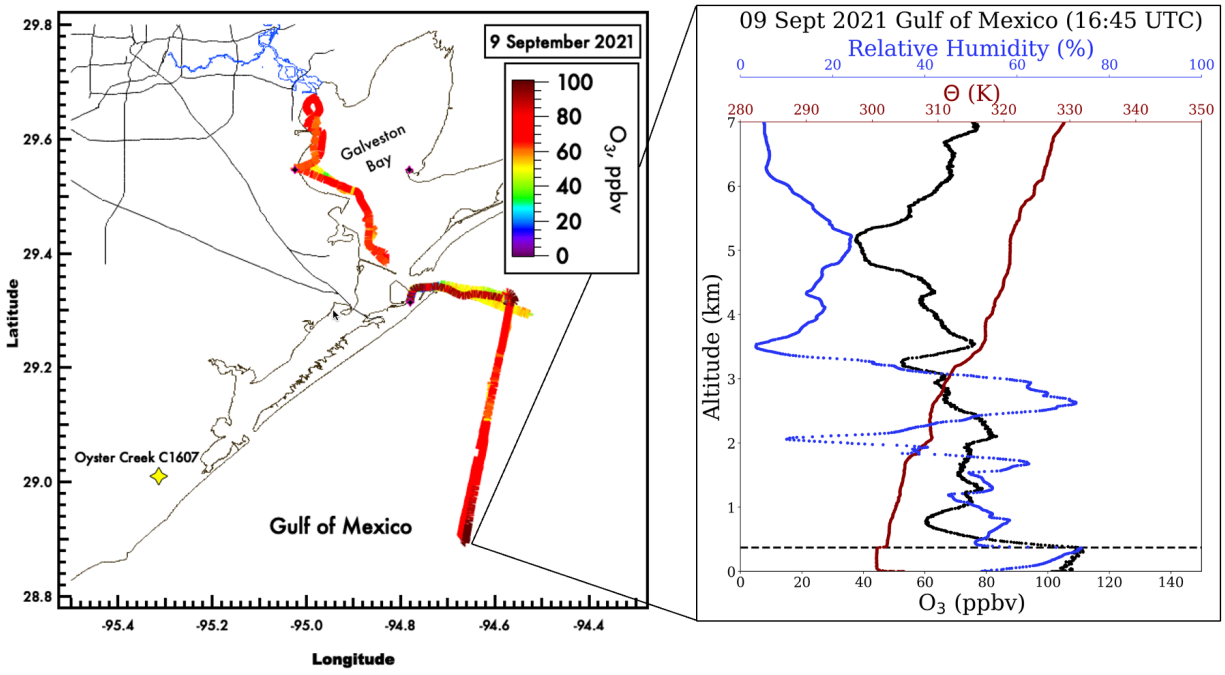

Figure 3.1.8: *(Left) A spatial plot of the UH pontoon and Red Eagle Boats with associated 1-minute averaged ozone values on 9 September 2021. (Right) Vertical profile from an ozonesonde launched off the deck of the Red Eagle in the Galveston lightering area, the black dashed line denotes the boundary layer height.*

The C1607 Oyster Creek monitor had the highest MDA8 O3 (81 ppbv) in the HGB area. The 24-hour wind run for that monitor is shown in **Figure 3.1.9**. In the morning, the winds were out of the northwest before becoming easterly in the afternoon. That wind pattern is consistent with ozone and its precursors being transported from the Houston area to the Gulf in the morning. The Lightering area in the Gulf of Mexico is east of the C1607 Oyster Creek monitor (**Figure 3.1.7**). The afternoon wind speeds were high enough that it is unlikely that the higher ozone concentrations observed by the C1607 monitor were produced locally but were instead transported from nearby in the Gulf of Mexico.

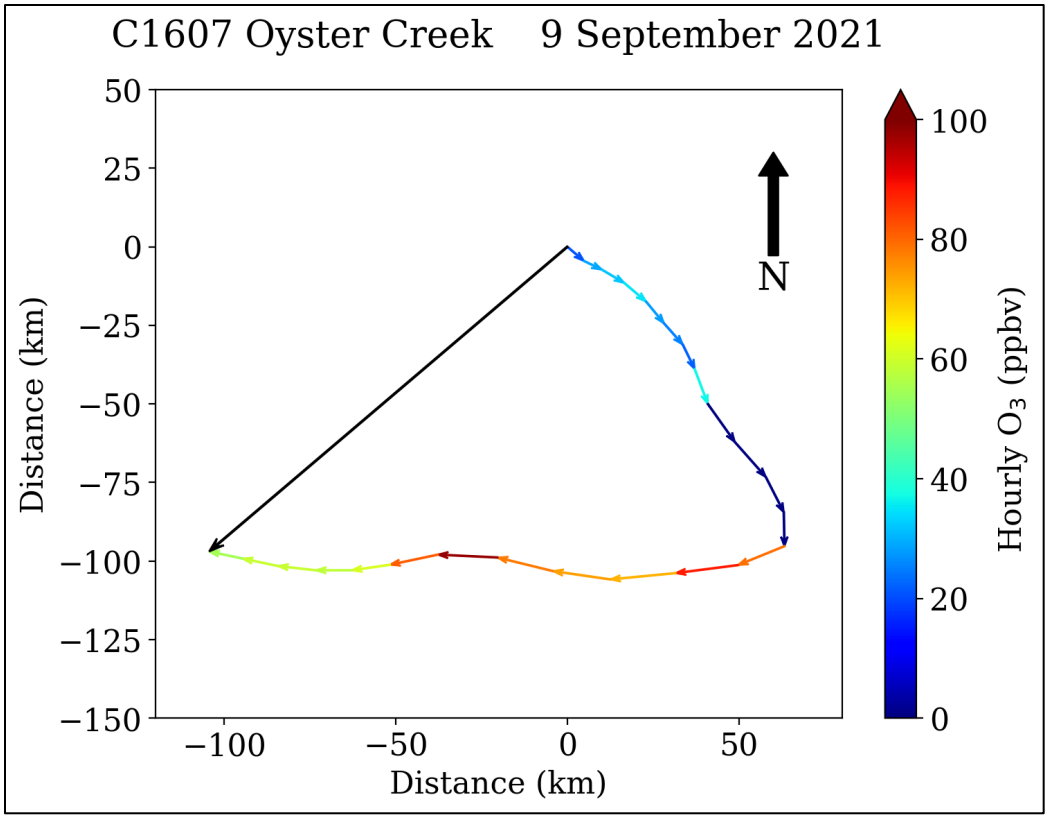

Figure 3.1.9: *24-Hour wind run from stationary monitor Oyster Creek (C1607) which saw the highest MDA8 O3 on 9 September 2021.*

It may be that the mechanism that led to the high ozone observed at coastal sites, such as C1607 Oyster Creek (MDA8 O3 81 ppbv), C1016 Lake Jackson (79 ppbv), C1034 Galveston (71 ppbv), and C620 Texas City (75 ppbv), had differences from the high ozone observed further inland at and nearer to Houston, such as C84 Manvel Croix (79 ppbv), C558 Tom Bass (72 ppbv), C53 Houston Bayland Park (72 ppbv), C409 Croquet (71 ppbv). The coastal sites C1607, C1016, C1034, and C620 all likely had contributions from the high ozone concentrations offshore of Galveston in the Gulf that were transported to the sites upon the afternoon transition to easterly winds. The inland sites likely had influences from subsidence resulting in the transporting of residual layer ozone to the surface. Ozone lidar data from La Porte in **Figure 3.1.10** shows elevated levels of ozone in the overnight residual layer transported down to the surface.

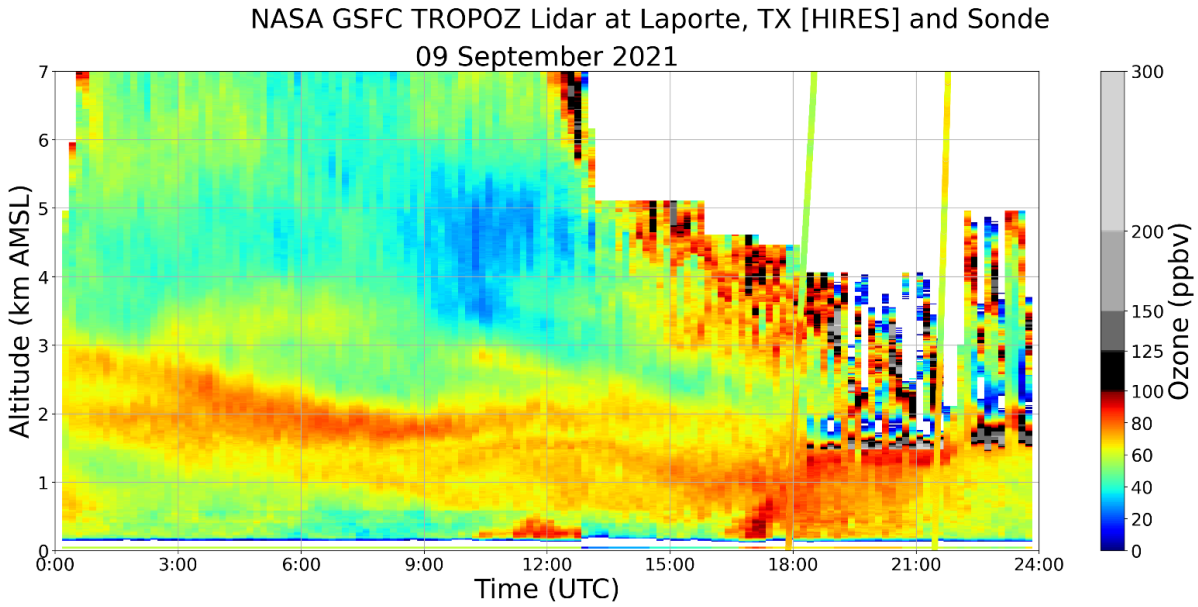

Figure 3.1.10: *NASA Goddard Space Flight Center (GSFC) tropospheric ozone (TROPOZ) differential absorption lidar data for September 9, 2021 from La Porte, TX. Overlaid are two ozone profiles from ozonesondes released from La Porte at 17:53 UTC and 21:27 UTC. Data courtesy of John Sullivan (NASA).*

Figure 3.1.11 shows two ozonesonde profiles from La Porte. The first ozonesonde was released in the early afternoon at 17:53 UTC (12:53 CDT) and the second was released later in the afternoon at 21:27 UTC (16:27 CDT). In the early afternoon profile, there is an ozone enhancement at an altitude of ~3 km that was also observed by the High Spectral Resolution Lidar-2 (HSRL2) Differential Absorption Lidar (DIAL) aboard the G-V. Later in the afternoon, convection developed that allowed for some of the higher ozone concentrations observed aloft to mix down to the surface. In the late afternoon ozonesonde profile, the convection is observed from the choppiness of the potential temperature profile (dark red) and the relative humidity profile (green) just above the top of the boundary layer (black dashed line). This convection led to ozone being fairly well mixed up to an altitude near 3 km.

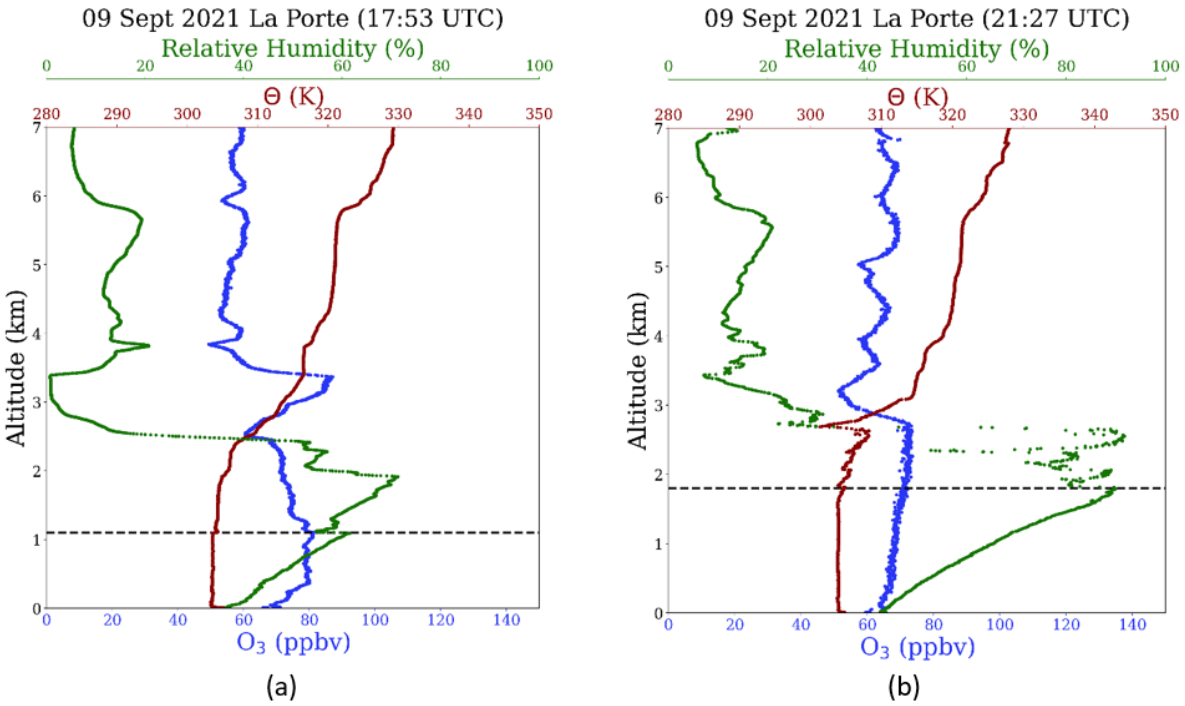

Figure 3.1.11: *Ozonesonde profiles from the early afternoon (17:53 UTC) and late afternoon (21:27 UTC) from La Porte.*

The UH pontoon boat was sampling over the western half of Galveston Bay simultaneously with the Red Eagle in the Gulf. The UH pontoon boat observed moderately high values (> 60 ppbv) over large areas of the western half of Galveston Bay during the mission, showing a relatively homogeneous spatial distribution of ozone over water from approximately 10:00–16:30 CDT.

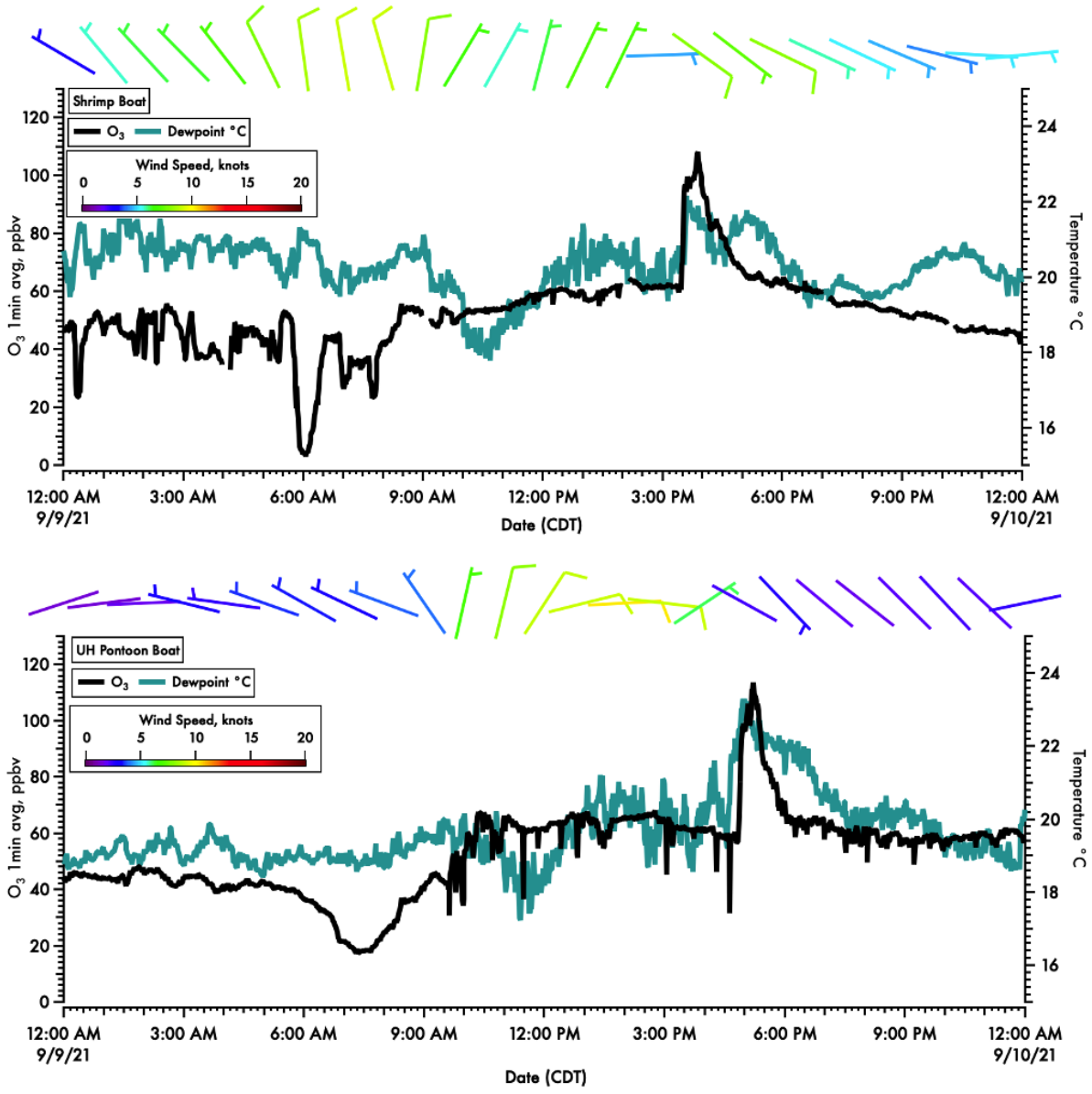

Figure 3.1.12: *Time series of 1-minute averaged ozone, dew point and 1-hour averaged wind barb for the shrimp boat (top panel) and the UH pontoon boat (bottom panel).*

The time series of ozone mixing ratios on 9 September 2021 (**Figure 3.1.12**) show a distinctive feature of a rapid ozone enhancement observed at the UH Pontoon Boat and the shrimp boat. In the late afternoon, there was a rapid and substantial increase in surface ozone of 48 ppbv in 25 minutes at the shrimp boat and 56 ppbv in 23 minutes at the UH Pontoon Boat. This event coincided with a bay breeze feature identified on radar along with wind shifts and an uptick in dew point temperatures, first observed at the Shrimp boat followed by the UH Pontoon Boat (**Figure 3.1.12**).

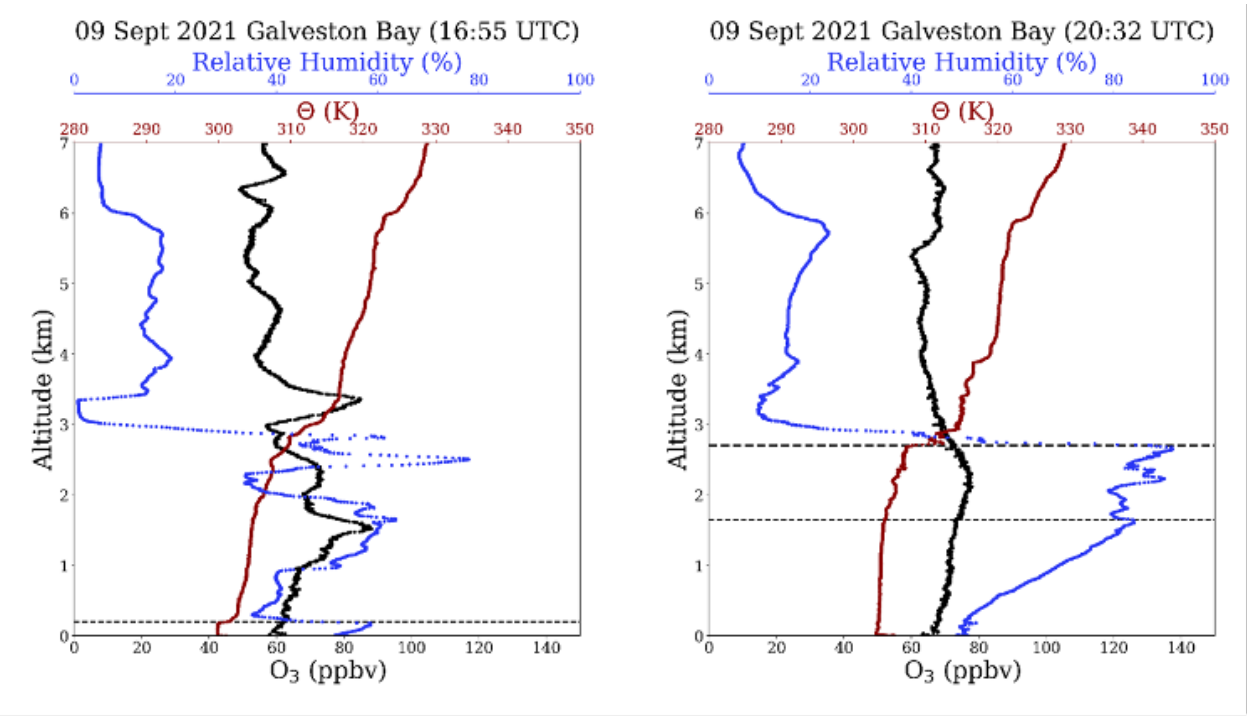

Figure 3.1.13: *Ozonesonde profiles from morning (left) and afternoon (right) launches over Galveston Bay on 9 September 2021. The dashed lines represent boundary layer height locations.*

Two ozonesondes were launched from the UH Pontoon Boat while operating in Galveston Bay (**Figure 3.1.13**). The profiles show considerable growth of the marine boundary layer throughout the day to approximately 1.65 km. However, the surface ozone concentrations remained relatively steady during the sampling route. These vertical profiles, combined with the surface data collected from the UH Pontoon Boat show the rapid ozone enhancement observed in the afternoon was likely adverted to the monitor from offshore rather than over Galveston Bay.

3.1.3.2.4 Episode September 17-19

17 September 2021 was not forecast as a high ozone day by air quality models and was designated as a 'moderate' ozone day by the state monitoring agency TCEQ. This day was included in the high ozone episode from 17–19 September 2021 and followed the passage of a tropical system, Hurricane Nicholas. The UH pontoon boat observed high ozone values over the waters of Galveston Bay (**Figure 3.1.14**). In the Gulf, the Red Eagle observed ozone of less than 40 ppbv on the outgoing path at ~12:00 CDT. On the incoming pass back to dock in Galveston, shortly after 17:00 CDT, ozone concentrations had increased to over 70 ppbv.

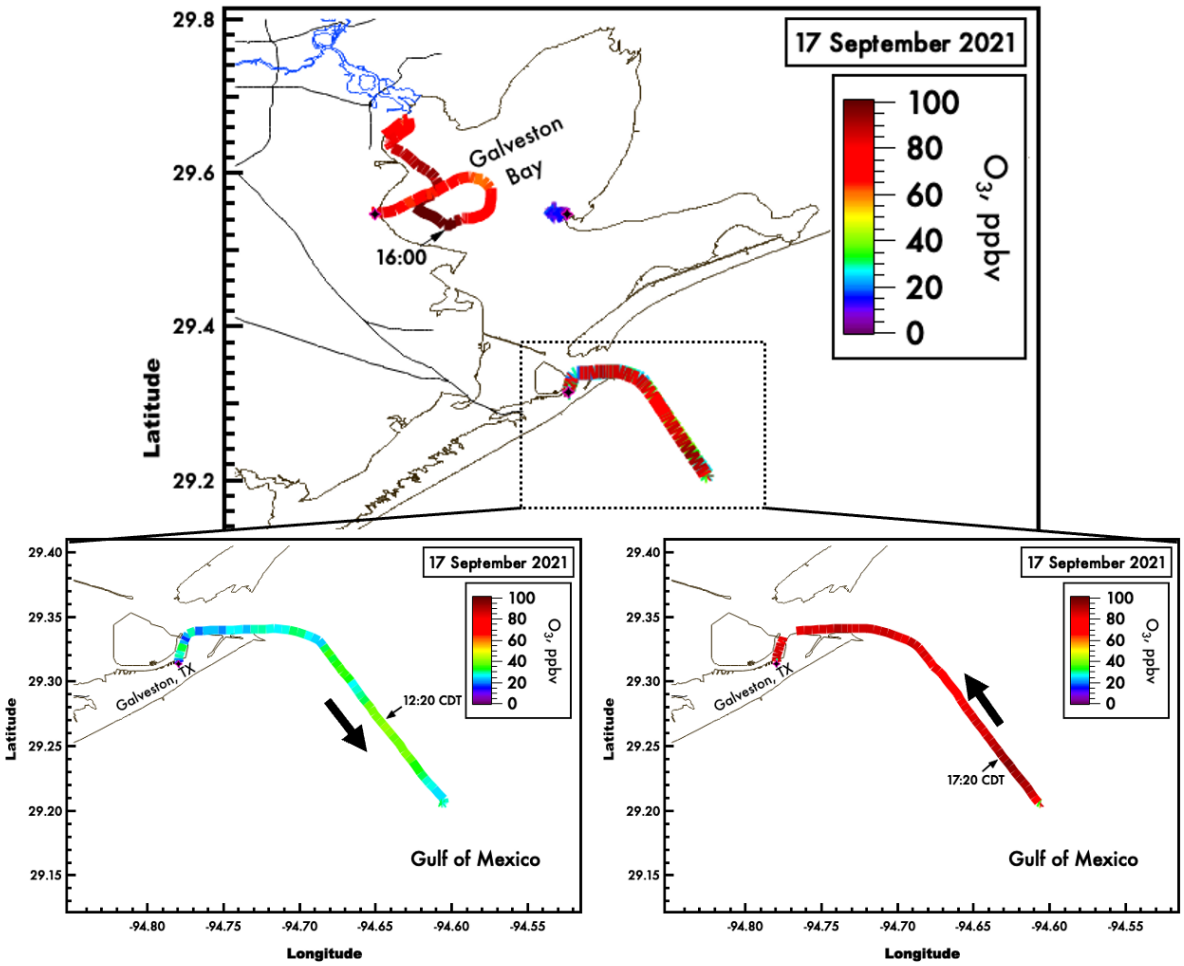

Figure 3.1.14: *A spatial plot of the UH pontoon boat (Galveston Bay) and the Red Eagle (Gulf of Mexico) with associated ozone mixing ratio on 17 September 2021. The inset plots are a zoomed-in view of the Red Eagle path showing the large difference between the outgoing (left) and incoming (right) legs.*

A unique feature of the 17–19 September high ozone episode, which this day was a part of, was that the locations that exceeded the MDA8 ozone standards were all coastal monitors. Additionally, on 17 September the UH pontoon boat observed the highest 1-hr average of ozone in the HGB region, recorded at 92 ppbv while over Galveston Bay, as seen in **Figure 3.1.14**.

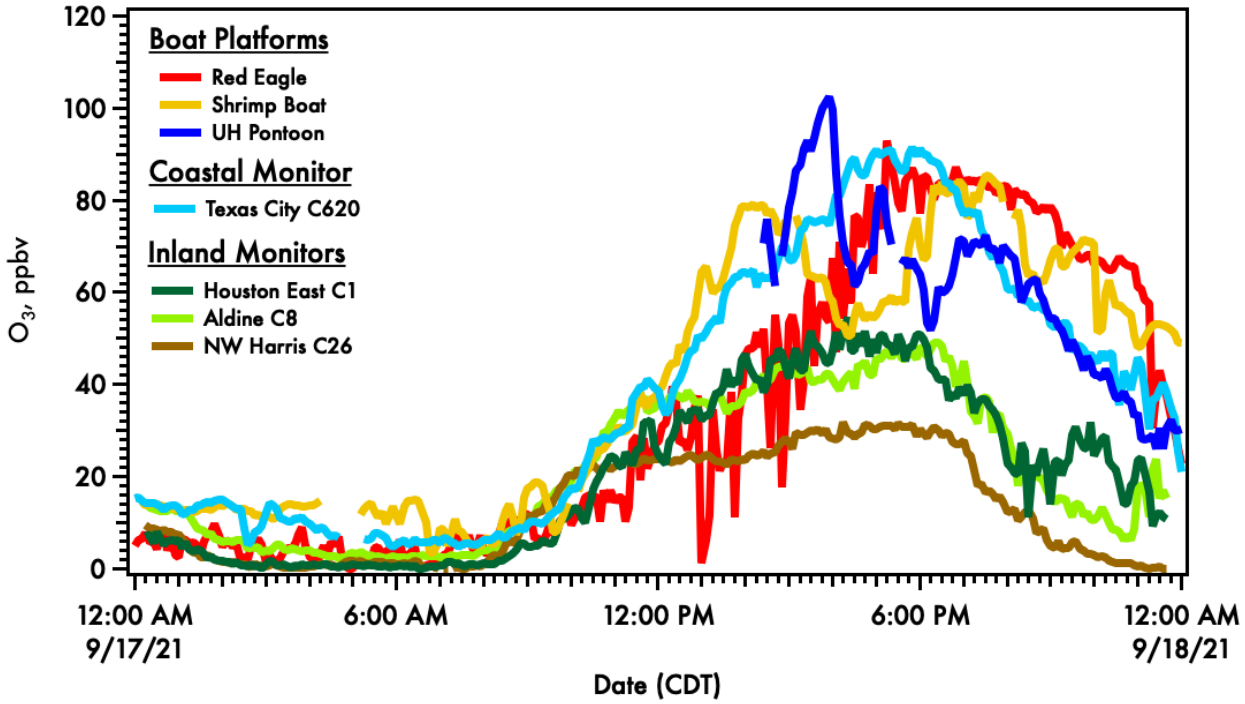

Figure 3.1.15: *Time-series of the three boat platforms and the coastal TCEQ monitor that exceeded the MDA8 standard, as well as three inland TCEQ monitors that recorded low to moderate ozone values.*

Figure 3.1.15 shows seven monitoring locations on 17 September, four near-shore monitors, the three boat platforms, and the TCEQ coastal monitor that exceeded the MDA8 ozone standard. Three inland monitors on the east and north sides of the HGB area are also shown that observed low to moderate ozone values throughout the day.

3.1.3.2.5 Episode September 23-26:

There was a series of four ozone exceedance days during 23–26 September 2021 during post-frontal conditions with veering winds. **Figure 3.1.16** shows the HYSPLIT back trajectories starting from 22 UTC on 23 September 2021, which show continental background influences. The ozonesonde profiles on these days were all characterized by dry air above the boundary layer as a result of subsidence across the region.

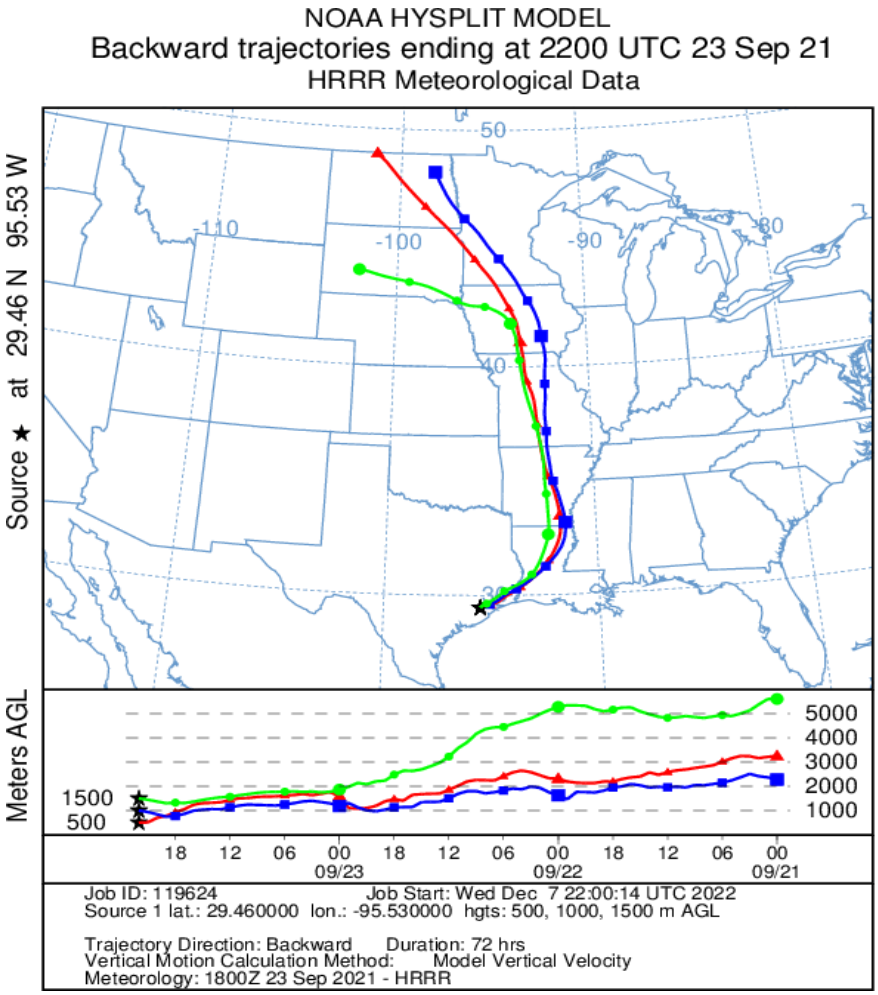

Figure 3.1.16: *72-hour HYSPLIT back trajectory starting from Kitty Hollow Park (29.46°N, 95.53°W) near Houston at 22 UTC on September 23, 2021.*

On 23 September, five ozonesondes were released, three from La Porte (only the last two collected ozone data) and two from Kitty Hollow Park (29.46°N, 95.53°W), southwest of Houston (**Figure 3.1.17**). The only CAMS to exceed the MDA8 ozone standard was C53 Houston Bayland Park (73 ppbv; 29.70°N, 95.50°W) on the SW side of Houston but N of Kitty Hollow Park. The late afternoon easterly winds (**Figure 3.1.16**) led to the highest ozone concentrations being observed southwest of Houston

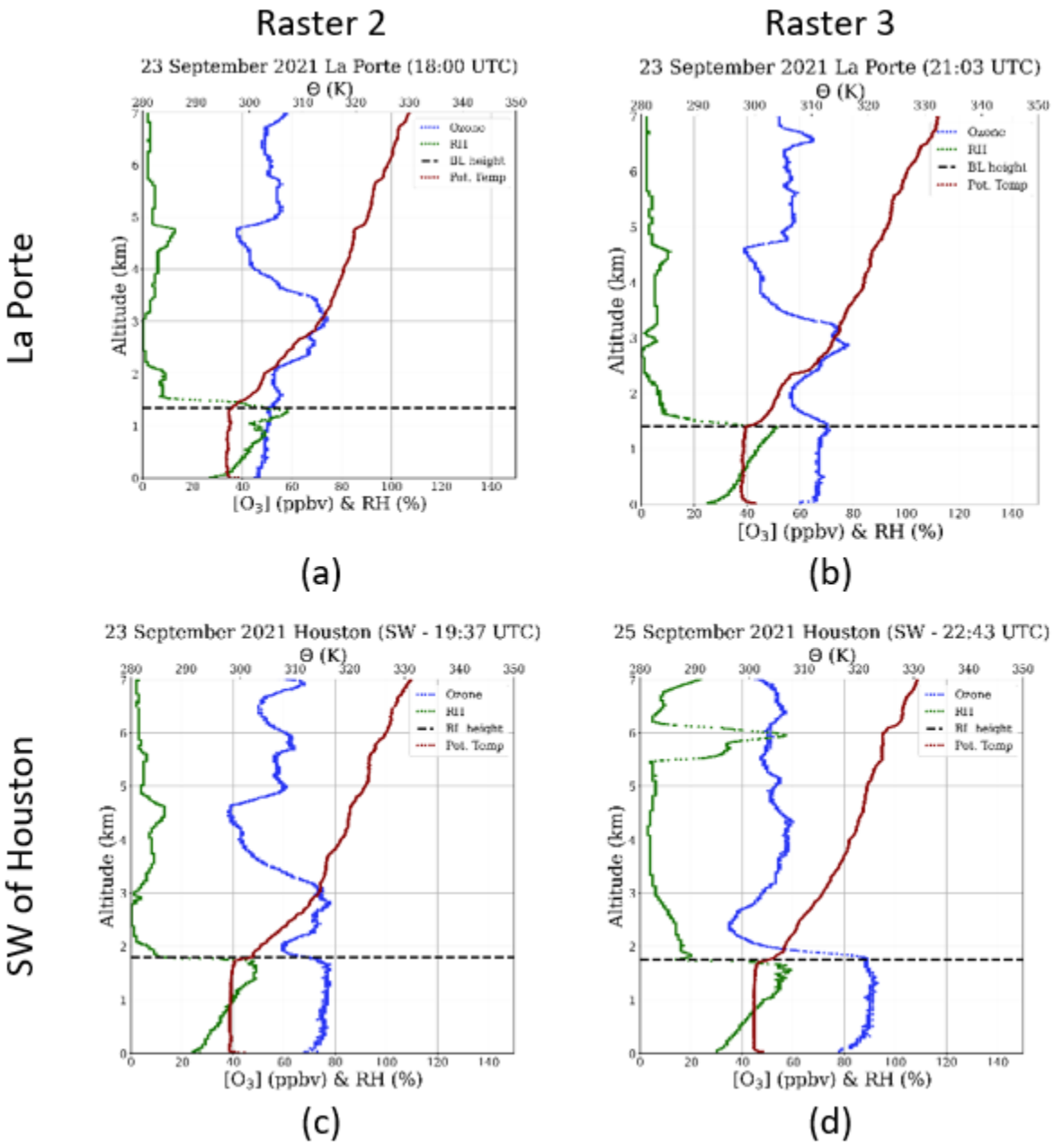

Figure 3.1.17: *Ozonesonde profiles from September 23, 2021. Profiles (a) and (b) were from La Porte coordinated with NASA G-V aircraft overpasses during its second and third raster patterns. Profiles (c) and (d) were from Kitty Hollow Park southwest of Houston.*

Figure 3.1.18 shows the ozonesonde profiles from 24 September. Profiles (a) and (c) were from Galveston Bay and profile (b) was from the S Anchorage area offshore of Galveston in the Gulf of Mexico. Profiles (e–f) are from La Porte. All six profiles show an enhancement in ozone at ~2.5 km. **Figure 3.1.19** shows that layer aloft with enhanced ozone was also observed from the NASA GSFC tropospheric ozone (TROPOZ) differential absorption lidar

(stationed in La Porte) measurements and the measurements from the HSRL2 DIAL aboard the NASA G-V aircraft. The HSRL2 DIAL measurements suggest the thin layer of enhanced ozone was widespread throughout the region.

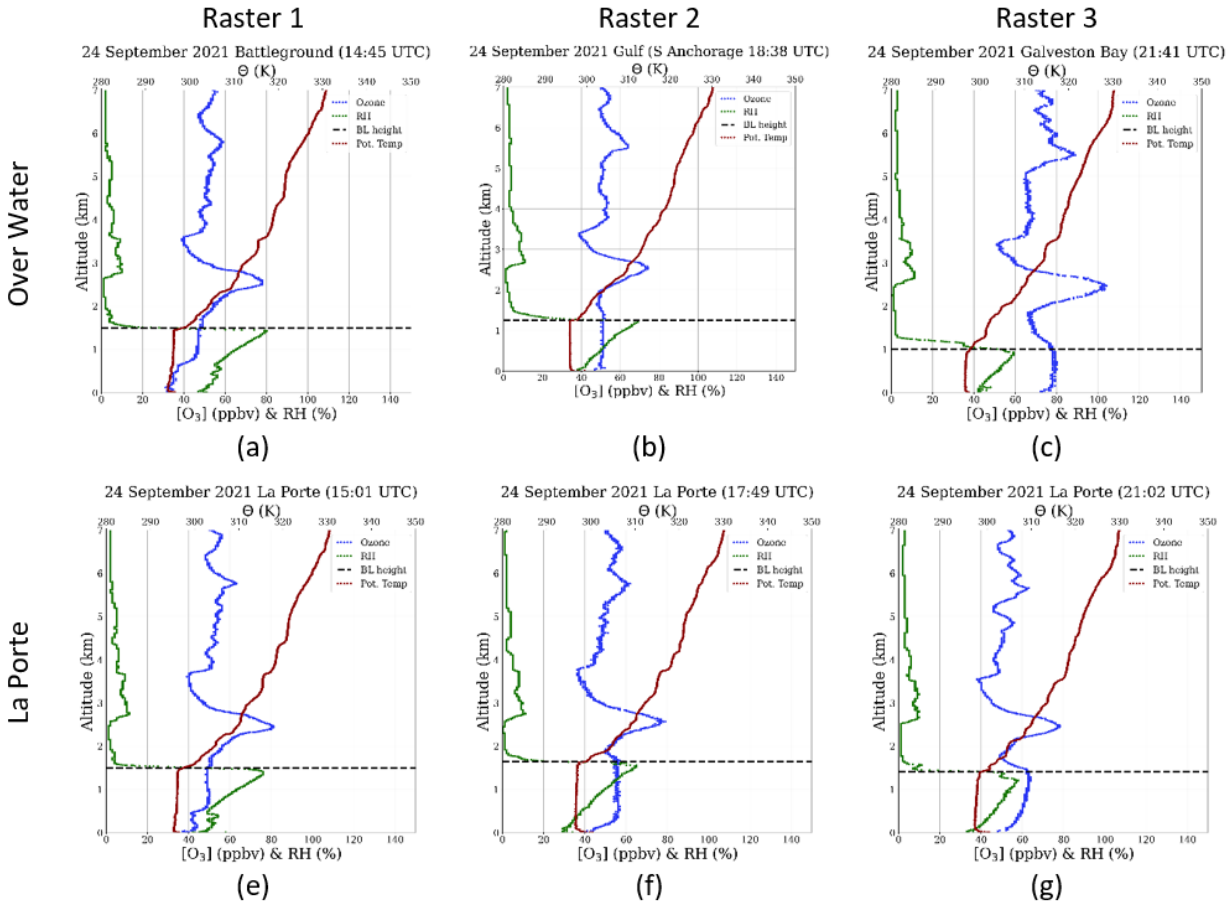

Figure 3.1.18: *Ozonesonde profiles from 24 September 2021 that were coordinated with overpasses of the G-V aircraft (one of three raster patterns). Profiles (a) and (c) were from Galveston Bay and profile (b) was from offshore of Galveston in the Gulf of Mexico at the S Anchoring area. Profiles (e-g) were from La Porte.*

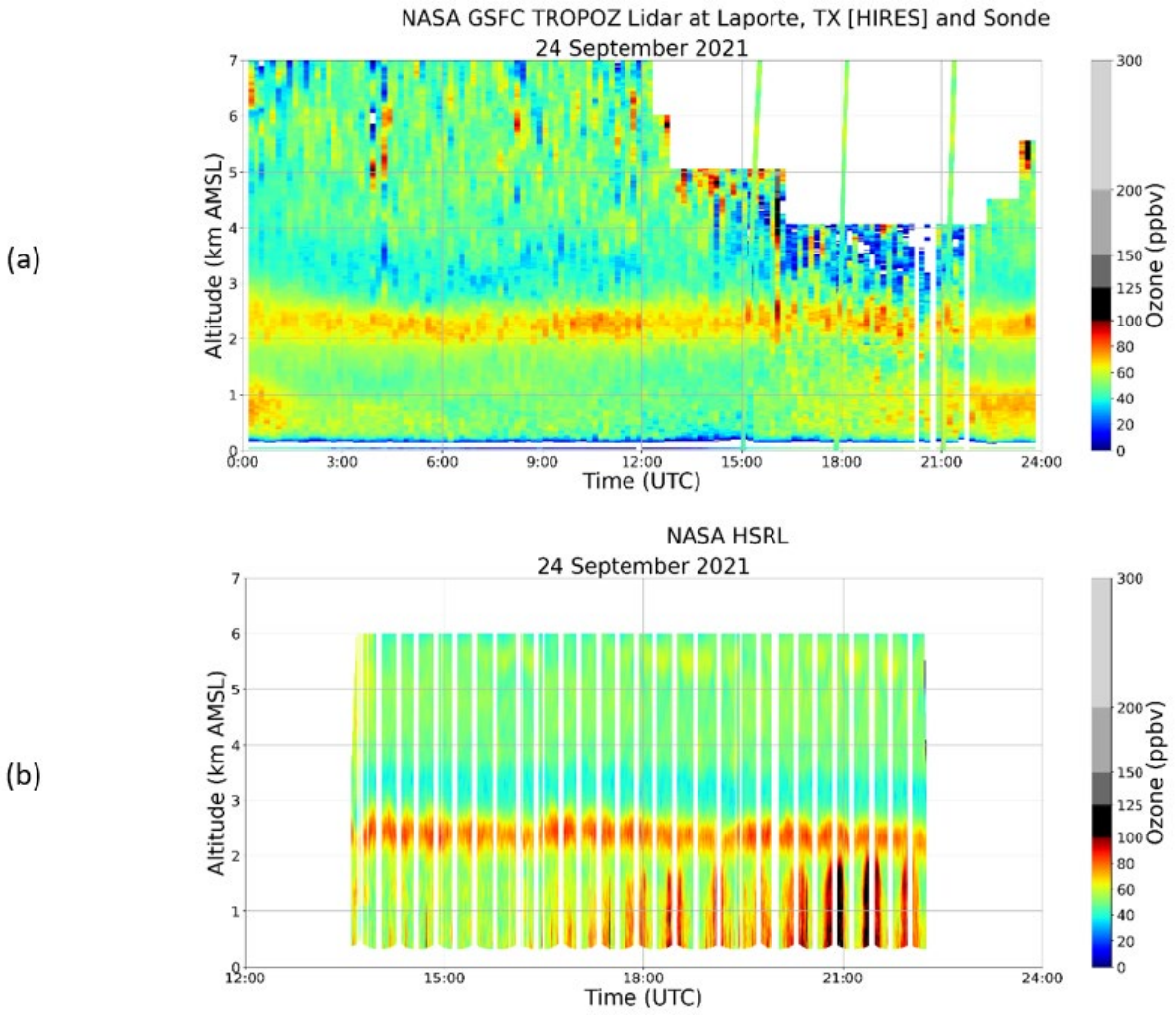

Figure 3.1.19: *For 24 September 2021: (a) NASA GSFC TROPOZ lidar measurements with the ozone profiles from the three ozonesondes released from La Porte overlaid. (b) HSRL2 DIAL ozone measurements from the NASA G-V aircraft. Data courtesy of John Sullivan and John Hair (NASA).*

Four CAMS exceeded the MDA8 ozone standard on 25 September 2021: C558 Tom Bass (81 ppbv), C409 Croquet (76 ppbv), C554 West Houston (74 ppbv) and C84 Manvel Croix (72 ppbv). Ten ozonesonde profiles from 25 September are shown in **Figure 3.1.20**. The enhanced ozone near 2.5 km that was present on 24 September is no longer present by the afternoon of 25 September. The ozonesonde in profile (i) was released in the late afternoon (22:43 UTC) from Rosenberg and had the highest boundary layer ozone concentrations observed in the ozonesonde profiles on that day.

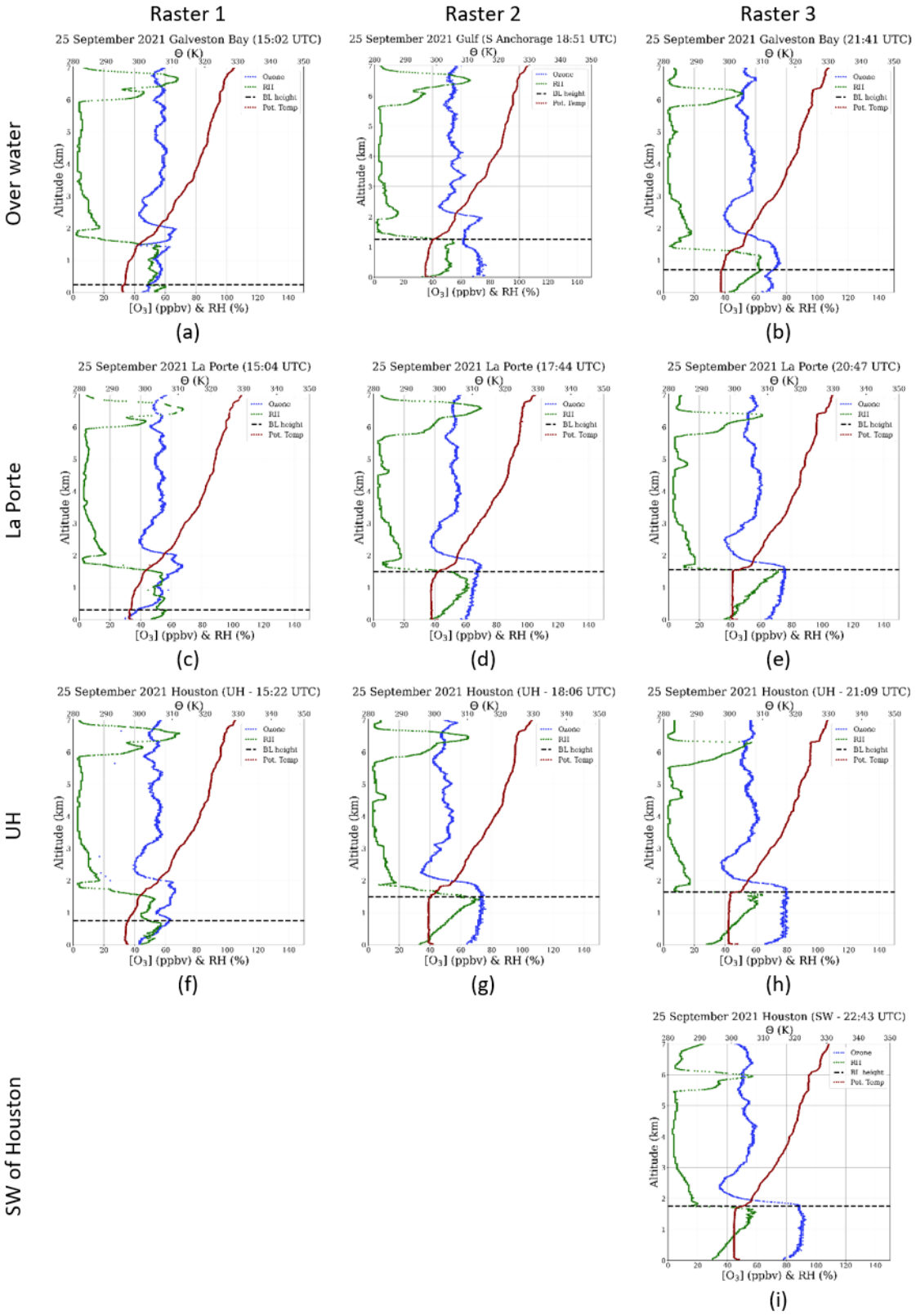

Figure 3.1.20: Ten *ozonesonde profiles from 25 September 2021, which were released in coordination with overpasses (one of three separate raster patterns) of the NASA G-V aircraft.*

Figure 3.1.21 shows the seven ozonesonde profiles from 26 September 2021, an ozone exceedance day in which the NASA G-V aircraft completed three raster patterns. Profile (d) from La Porte shows the profile of an ozonesonde at dawn (before the G-V began its flight) that there was ~50 ppbv of ozone just aloft of the surface in the residual layer. Profile (a) from Galveston Bay shows a shallow marine layer depth of 0.2 km. As the depth of the marine layer grew over Galveston Bay through the afternoon (profile (b)), the residual layer ozone was able to mix into the boundary layer. The inland potential temperature (dark red) profiles at the University of Houston (e-f) and southwest of Houston (g) show a hard cap atop the afternoon boundary layer. All profiles show dry air aloft above the boundary layer starting at an altitude of ~2 km.

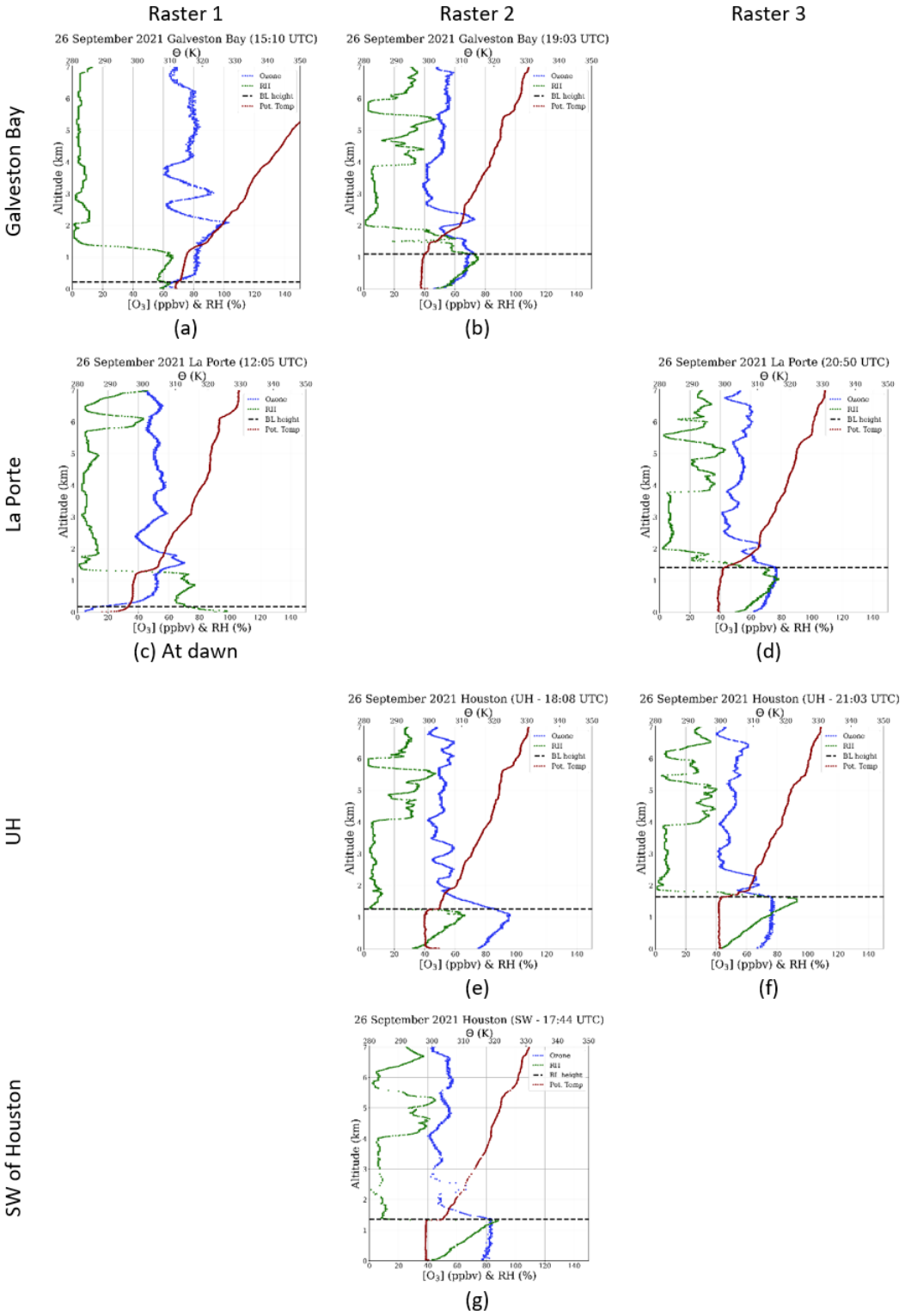

Figure 3.1.21: *Ozonesonde profiles from 26 September 2021. Six of the seven ozonesondes were coordinated with overpasses (one of three separate raster patterns) with the NASA G-V aircraft. Profile (d) from La Porte is of an ozonesonde released at dawn before the aircraft was in flight.*

3.1.3.3 Comparison of ozone chemistry between high ozone days and non-exceedance days in September from LaRC modeling

At Battleground Site during the month of September 2021, the median of the hourly-averaged $F(O_3)$ was 26.6 ± 16.4 ppbv h^{-1} for 6:00 to 19:00 CST with a morning to early afternoon elevated period between 9:00 and 15:00 CST averaged about 40.6 ± 4.2 ppbv h^{-1} (**Figure 3.1.22**, left). Two peaks between 9:00-10:00 CST (46.5 ppbv h^{-1}) and 12:00-13:00 CST (45.0 ppbv h^{-1}) were observed. Among the pathways of ozone formation, RO_2+NO (11.4 ± 7.1 ppbv h^{-1}) and HO_2+NO (11.4 ± 7.1 ppbv h^{-1}, 41%) were the largest contributors (43% each) to $F(O_3)$, followed by CH_3O_2+NO (3.8 ± 2.3 ppbv h^{-1}, 14%). For components of $D(O_3)$ (**Figure 3.1.22**, right), NO_2+OH was the dominant pathway, followed by $O(^1D)$+H_2O, O_3+NMHC and HO_2+O_3. Specifically, NO_2+OH (1.1 ± 0.7 ppbv h^{-1}, 68%) was significant throughout the early morning to late afternoon, while $O(^1D)$+H_2O (0.4 ± 0.4 ppbv h^{-1}, 27%), O_3+NMHC (0.1 ± 0.1 ppbv h^{-1}, 7%) and HO_2+O_3 (0.1 ± 0.1 ppbv h^{-1}, 7%) became noticeable from noon to afternoon. In general, $D(O_3)$ averaged 1.7 ± 1.0 ppbv h^{-1} and was smaller than $F(O_3)$ by an order of magnitude, leading to a potential high rate of net ozone production $P(O_3)$.

The total OH reactivity of VOCs (4.3 ± 0.7 s^{-1}) was dominated by isoprene (2.1 ± 0.8 s^{-1}, 50%) and lumped alkenes (0.7 ± 0.2 s^{-1}, 15%) during the month of September, while the fractional contributions of all the rest of the VOC reactivities were below 10% (**Figure 3.1.23**). Lumped alkanes (0.4 ± 0.2 s^{-1}, 8%), lumped aromatics (0.3 ± 0.1 s^{-1}, 8%), ethene (0.2 ± 0.2 s^{-1}, 6%) and propane (0.1 ± 0.1 s^{-1}, 2%) each contributed to the total OH reactivity of VOCs, while that of formaldehyde, acetone, ethane, and benzene were negligible (<1%). In general, the large contribution (50%) of isoprene reactivity underscores the importance of biogenic VOC, and the anthropogenic emissions (e.g. lumped alkanes, lumped alkenes, lumped aromatics, ethene, propane) added up the other 40%. The low formaldehyde reactivity indicates minimal secondary VOC impact at the Battleground Site, which is consistent with the location of the site as a source region instead of a downwind receptor.

According to **Table 3.1:** A summary of the 96 ozonesondes in 2021. The color code of the ozone air quality index (AQI) is shown for each day. For days where ozone concentrations exceeded the maximum daily 8-hour average (orange or red), the number of monitors in the Houston-Galveston-Brazoria (HGB) region in exceedance of the ozone standard (MDA8 [O_3] > 70 ppbv) and MDA8 ozone value of the highest monitor is shown. , days where ozone concentrations exceeded the maximum daily 8-hour average (orange or red) in the month of September were 09/06-09/11, 09/17-09/19, 09/23-09/26. By grouping the LaRC modeling results from these high ozone days, we compared the daytime diurnal profiles of $F(O_3)$, $D(O_3)$ and OH reactivity of VOCs with those from non-exceedance days (**Figure 3.1.24**–**Figure 3.1.27**). The median of the hourly-averaged F(O3) was 28.3 ± 17.5 ppbv h−1 for 6:00 to 19:00 CST for high ozone days, approximately 10% higher than that of the non-exceedance days (25.7 ± 16.2 ppbv h^{-1}). The same elevated period between 9:00 and 15:00 CST were observed for both high ozone days and non-exceedance days, yet the $F(O_3)$

averaged about 43.7 ± 4.3 ppbv h^{-1} for high ozone days, also approximately 10% higher than that of the non-exceedance days (39.6 ± 5.0 ppbv h^{-1}). Two $F(O_3)$ peaks between 9:00-10:00 CST (49.9 ppbv h^{-1}) and 12:00-13:00 CST (46.6 ppbv h^{-1}) were observed during high ozone days. For non-exceedance days, the first peak (46.6 ppbv h^{-1}) was also observed between 9:00-10:00 CST, but the second peak (44.4 ppbv h^{-1}) was delayed to 13:00-14:00 CST.

The difference in the fractional contributions of different ozone formation pathways between high ozone days and non-exceedance days was minimal. In both cases, RO_2+NO (42% for high ozone days and 43% for non-exceedance days, respectively) and HO_2+NO (43% and 42%) were the largest contributors to $F(O_3)$, followed by CH_3O_2+NO (14% and 14%). For components of $D(O_3)$, the fractional contribution of NO_2+OH increased from 56% in high ozone days to 80% in non-exceedance days, while those of HO_2+O_3 and O_3+OH reduced. In general, $D(O_3)$ averaged 1.9 ± 1.1 ppbv h^{-1} in high ozone days and 1.5 ± 1.0 ppbv h^{-1} in non-exceedance days. Both were smaller than their corresponding $F(O_3)$ by an order of magnitude and led to considerable net ozone production $P(O_3)$.

The total OH reactivity of VOCs increased by 17%, from 4.1 ± 0.6 s^{-1} in non-exceedance days to 4.8 ± 0.8 s^{-1} in high ozone days. But the fractional contributions of individual VOC groups were similar. In both cases, isoprene (2.4 ± 0.9 s^{-1} and 51% in high ozone days; 1.9 0.6 s^{-1} and 45% in non-exceedance days) was the dominant species followed by lumped alkenes (0.7 ± 0.3 s^{-1} and 15%; 0.6 ± 0.1 s^{-1} and 15%), while the fractional contributions of all the rest of the VOC reactivities were below 10% (**Figure 3.1.26**–**Figure 3.1.27**).

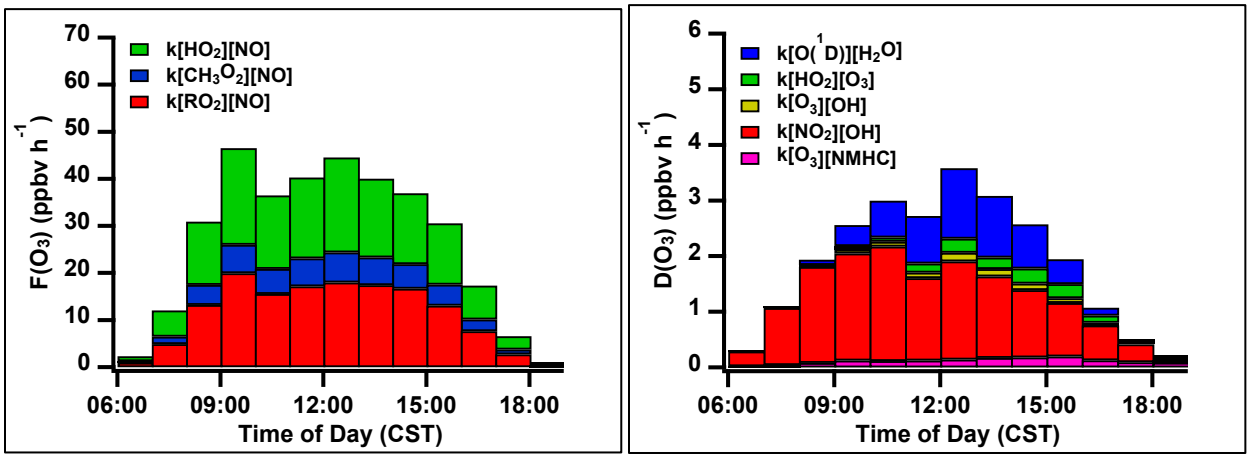

Figure 3.1.22: *Median of the hourly-averaged daytime profiles of $F(O_3)$ (left) and $D(O_3)$ (right) estimated at Battleground Site using the LaRC model for the month of September 2021.*

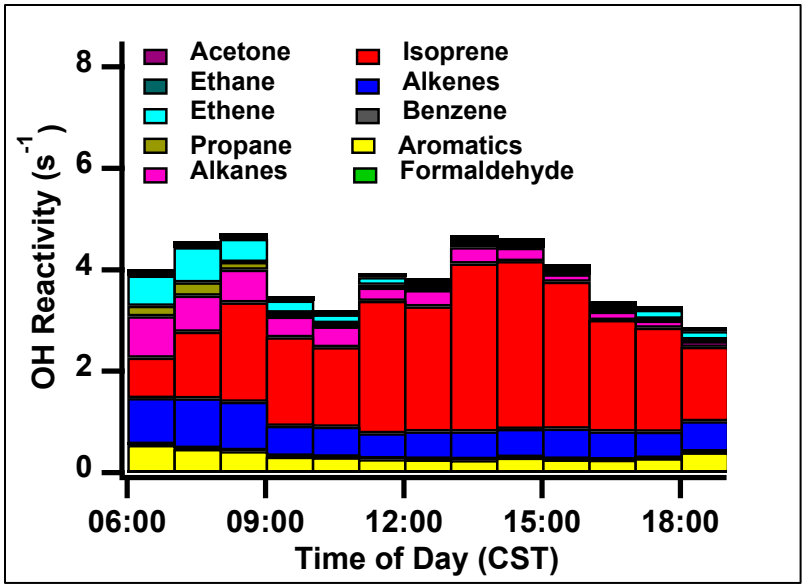

Figure 3.1.23: *The OH reactivity of VOCs estimated at Battleground Site using the LaRC model for the month of September 2021.*

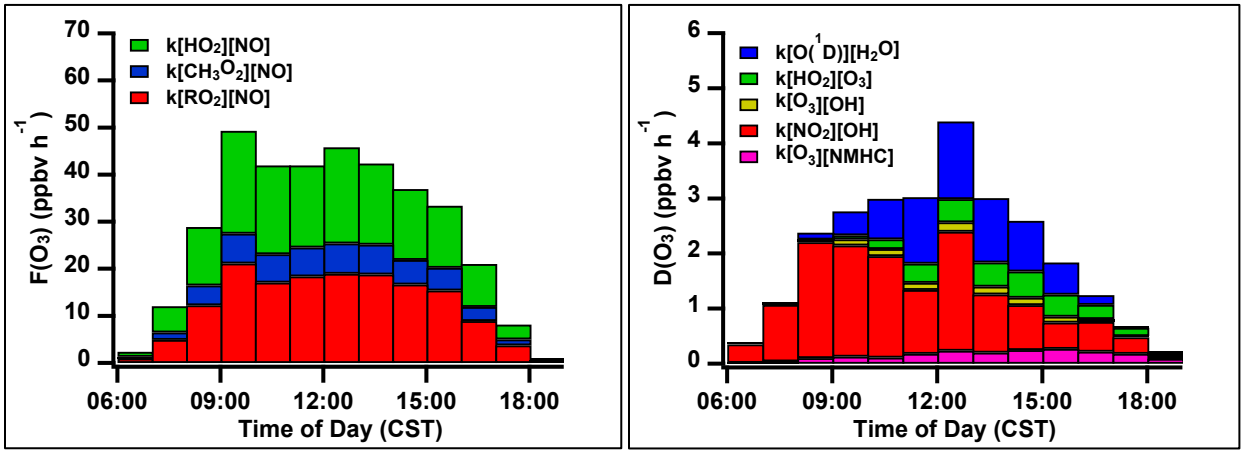

Figure 3.1.24: *Median of the hourly-averaged daytime profiles of $F(O_3)$ (left) and $D(O_3)$ (right) estimated at Battleground Site using the LaRC model for the high ozone days in September 2021.*

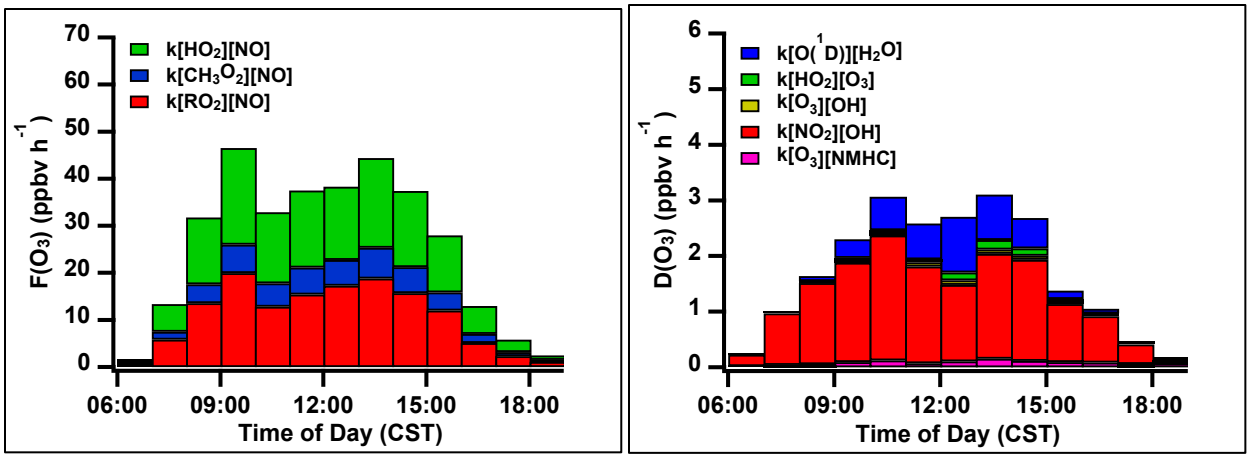

Figure 3.1.25: *Median of the hourly-averaged daytime profiles of $F(O_3)$ (left) and $D(O_3)$ (right) estimated at Battleground Site using the LaRC model for the non-exceedance days in September 2021.*

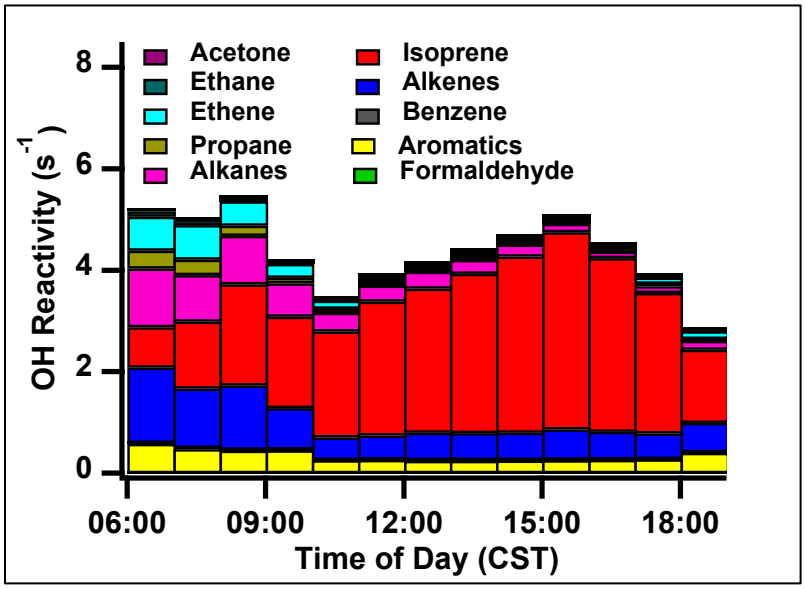

Figure 3.1.26: *The OH reactivity of VOCs estimated at Battleground Site using the LaRC model for the high ozone days in September 2021.*

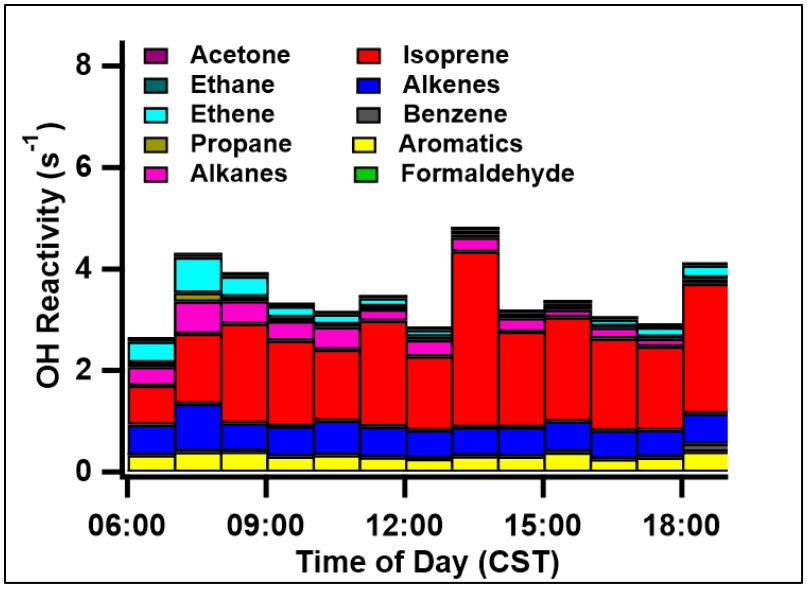

Figure 3.1.27: The OH reactivity of VOCs estimated at Battleground Site using the LaRC model for the non-exceedance days in September 2021.

3.1.3.4 Identification of source region and transport pattern of air masses for two high ozone episodes in September

Figure 3.1.28 shows the main transport pathways of air masses arriving in Battleground at 2000 m and 200 m altitudes during September 2021. The pathways were derived by applying the HYSPLIT cluster algorithm to all the back trajectories generated in hourly intervals at each location. The back trajectories with receptor at 2000 m distinctly indicated the sources to have origin in (1) northern US, (2) south of the Gulf of Mexico, (3) east of the Gulf of Mexico, and (4) central US. The transported air parcels were dominantly from central US (38%) and south of the Gulf of Mexico (34%), followed by northern US (19%) and east of the Gulf of Mexico (9%). The back trajectories with receptor at 200 m were similar to that of 2000 m except for two additional clusters (cluster 5 and cluster 6). Cluster 5 represents the air parcels originating from the Gulf of Mexico, similar to cluster 2, but the source location is closer to the coastline than cluster 2. Air parcels from this cluster have remained closer to the investigated area for the duration of analysis (i.e., 72 hours). Cluster 6 is similar to cluster 4, both originating from central US, but with slight differences in their directions. The trajectory analysis revealed the ozone episodes were predominantly associated with the transport of pollutants from central and northern US (clusters 1,4, and 6), while the source region of air masses during the non-episode days were mainly from the Gulf of Mexico (clusters 2,3, and 5).

(a)

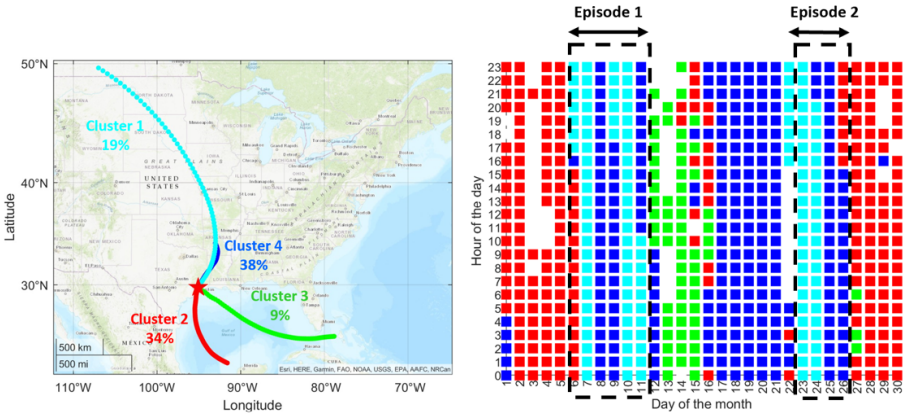

(b)

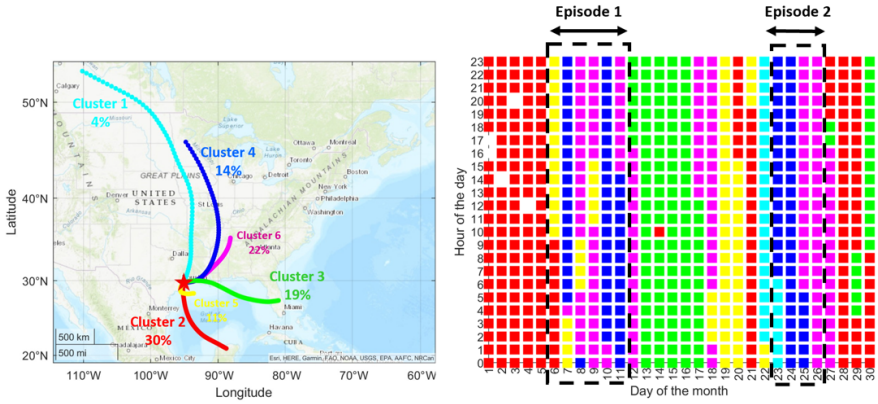

Figure 3.1.28: *Long-range transport pathway of air masses to the Houston region for receptors at (a) 2000 m and (b) 200 m AGL. The left column refers to the HYSPLIT-derived trajectory clusters and the right column shows the hourly transport pathways with respect to the attributed cluster for September 2021.*

Figure 3.1.29 represents the local-scale HYSPLIT-resolved backward trajectory pathways (at both 200 m and 2000 m altitudes) for receptor at Battleground during 6–11 September and 23–26 September ozone episodes. Regarding the receptor at 2000 m AGL, trajectory pathways showed northerly air masses on 6–7 September which then gradually deflected toward eastern regions until 11 September. When the receptor was located at 200 m AGL, the source region of air masses was from the north during 7–9 September and it switched to east within 10–11 September. In addition, recirculation of air masses was seen during 8–9 September at the near-surface level in Battleground, while the air masses were mostly from the east during 7 September and 10–11 September. The backward trajectory analyses for 23–26 September showed that air masses arriving at Battleground (both at 200 m and 2000 m AGL) were from northeast Houston on 23 September while they gradually deflected toward eastern Texas and finally the Gulf of Mexico on 26 September. Unlike the 6–11 September

episode, recirculation was not observed in the local transport pathway of air masses during 23–26 September episode.

Figure 3.1.30 summarizes the outputs of the FLEXPART-WRF model when the receptor was at Battleground location. As already shown in HYSPLIT, the transport pattern of pollutants rotated clockwise from the Gulf of Mexico toward northern regions starting from 6 September. This observation is in agreement with FLEXPART-WRF model for 6 September where air masses have been transported from western areas to the Houston region during noon (12 p.m.–3 p.m.). Starting from 7 September, the transport pathways have further deflected toward the north and northeast directions. Finally, the transport pathway of air masses changed toward eastern Texas during 10–11 September. The vertical profile of back trajectories showed that the plume experienced subsidence from higher altitudes (> 2000 m) during 6–7 September and 10–11 September, suggesting the transport of ozone from the free troposphere to the near-surface level. During the 23–26 September episode, the source region of air masses was northern Texas on 23 September, and it switched toward eastern regions from 24–26 September. Unlike the 6–11 September episode, the source region of air masses remained at altitudes < 2000 m for the duration of analysis, precluding the potential impact of ozone from higher altitudes on the surface-level ozone during the 23–26 September episode.

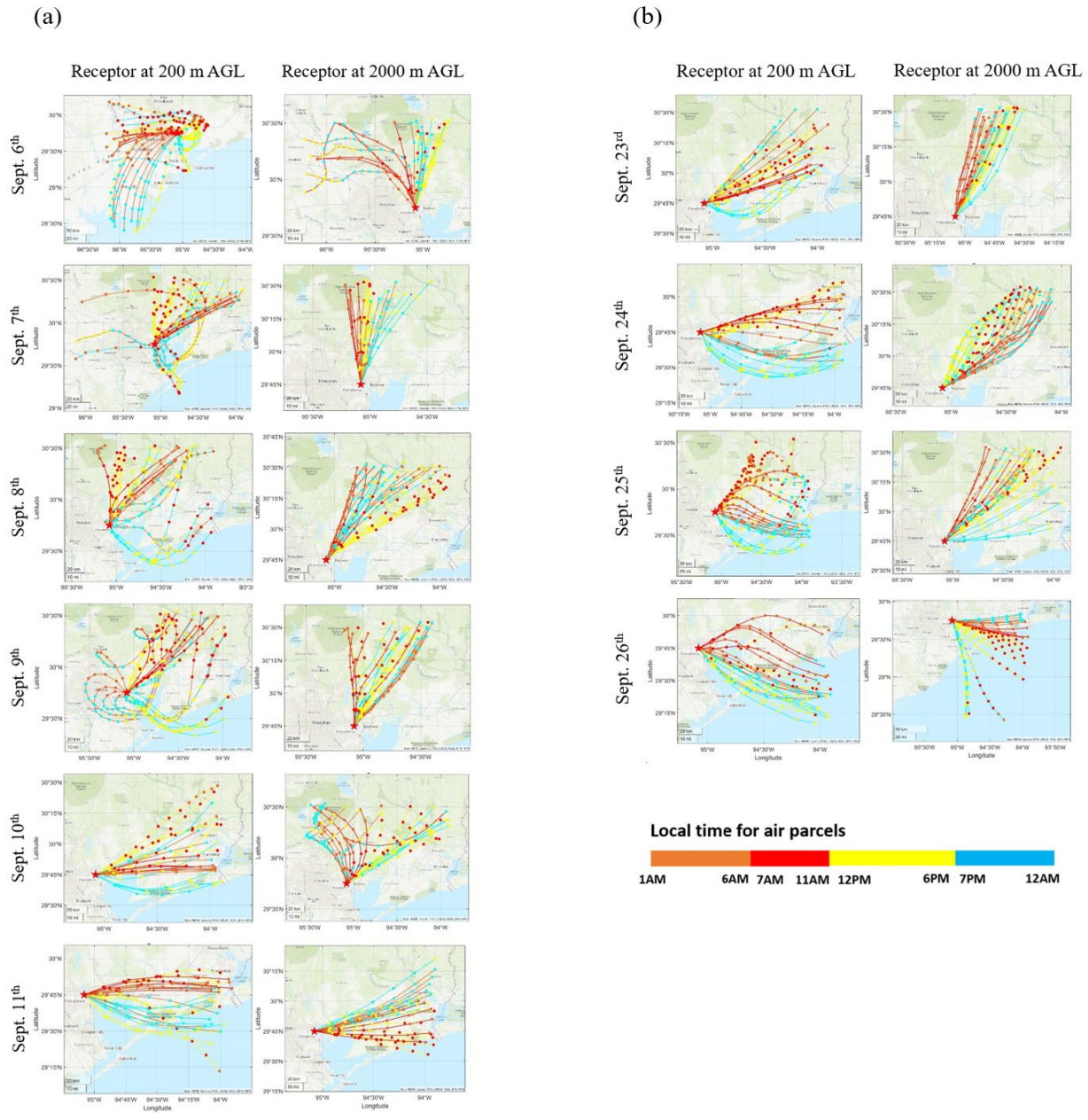

Figure 3.1.29: *Results of backward trajectory analyses with receptor at Battleground. Multiple back trajectories were run (starting at 200 m and 2000 m AGL) from the receptor on an hourly basis (CST) during (a) 6-11 September, and (b) 23-26 September. The trajectory lines are color-coded by the trajectories' initiation time (CST) at the receptor. The filled circles on the trajectory lines use the same color code as the trajectory lines, with their colors indicating the time (CST) of the trajectory's locations.*

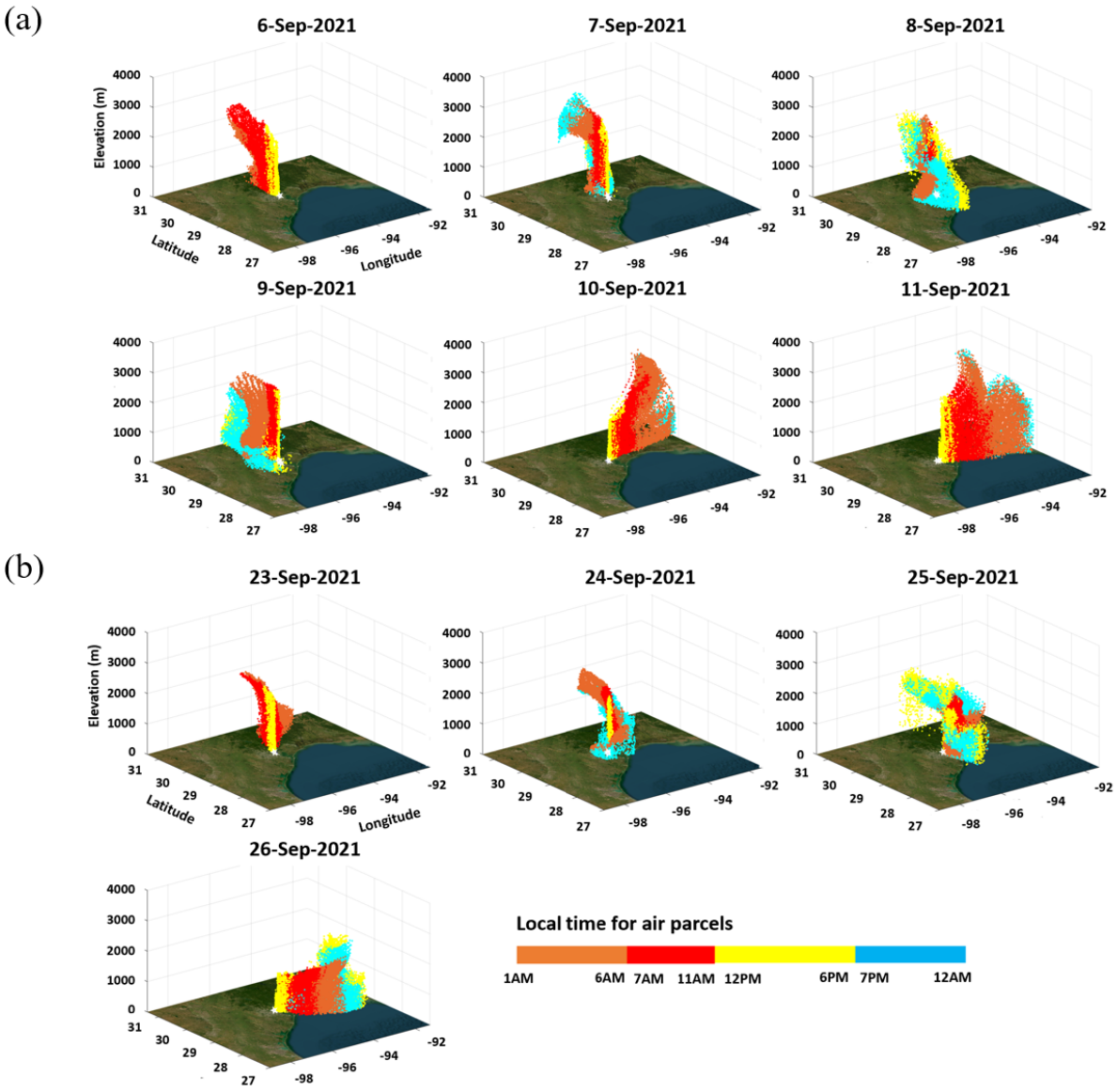

Figure 3.1.30: *Results of FLEXPART-WRF backward trajectory analysis with receptor at 15 m AGL during (a) 6-11 September episode and (b) 23-26 September. The colored dots indicate the time (CST) of air masses along the trajectory pathway.*

3.1.3.5 Afternoon ozonesondes from the Gulf:

Figure 3.1.31 shows the PBLH and peak PBL O_3 in for the six ozonesondes from offshore of Galveston in the Gulf of Mexico during September 2021 that were in the afternoon. The highest ozone in the Gulf was observed on 9 September, a day in which the PBLH for both afternoon ozonesondes was 0.37 km, substantially lower than what was observed on lower days. The surface winds were calm on 9 September and ozone and its precursors were transported from the Houston area overnight and during the morning. The lower boundary

layer height led to there being a relatively smaller volume to mix into when photochemical production of ozone was taking place.

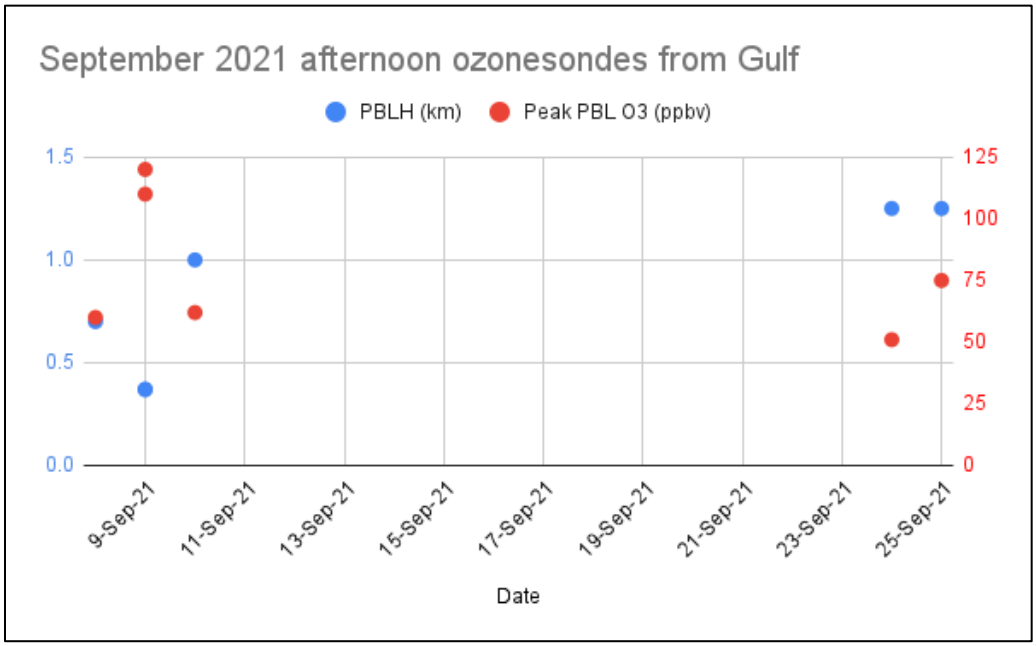

Figure 3.1.31: *The planetary boundary layer heights (PBLH, blue) and associated peak PBL ozone (red) are shown for the six ozonesondes that occurred in the afternoon during September 2021 from the Red Eagle offshore of Galveston in the Gulf of Mexico.*

3.2 VOC or NOx Limited Regimes (Yuxuan, Fangzhou & Eugenia)

3.2.1 Summary and Key Findings

- CAMx ozone production rate (PO3) increased by factors of ~3 and ~2 during Episode 1 and Episode 2, respectively.
- The hotspots of ozone production during the ozone episodes were in the southeast region of the downtown Houston area, extending from the Houston Ship Channel (HSC) to Galveston Bay.
- During the ozone episodes, the suburban regions experienced more NOx sensitivity, while downtown Houston and the HSC remained VOC-sensitive.
- The mean NOx levels across the entire region did not undergo a significant change during pollution episodes (it increased by 10-25% over the city of Houston and the HSC). Our analyses showed that neither NOx nor Peroxyacetyl nitrate (PAN) has not been dominantly transported to the region during the ozone episodes.
- The surface levels of aged/oxygenated VOCs increased by on average ~110% (during Episode 1) and ~40% (in Episode 2) across the entire region. The spatial variation in

VOCs levels along with the results of back trajectory analysis suggested that aged VOCs have been mostly transported to the Houston region (rather than local formation).

- The OH loss rate (and in turn HO2 production rate) experienced 2- and 1.5-fold increases respectively during Episode 1 and Episode 2 due to the elevated levels of VOCs.
- During the stationary measurement period at Battleground Site, 53% of the LaRC modeled period was in VOC-sensitive regime, with an average NO of 9.8 ppbv and $P(O_3)$ of 23.2 ppbv hr^{-1}, while 44% of the period was in a NO_X-sensitive regime, with an average NO of 0.7 ppbv and significantly higher average $P(O_3)$ of 36.6 ppbv hr^{-1}.
- Approximately 4% of the period was in the transitional regime with an average NO of 1.4 ppbv in consistent with the qualitative evaluation of the NO turning over point between 1 and 2 ppbv. The transitional regime has the highest average $P(O_3)$ of 42.3 ppbv hr^{-1}, an 83% increase from the average of the VOC-sensitive regime and a 16% increase from that of the NO_X-sensitive regime.
- The net ozone production rate was 24.8 ± 15.5 ppbv hr^{-1} throughout the daytime and was most active from 9:00 to 15:00 CST when the ozone formation regime was first VOC-sensitive, then shifted to NO_X-sensitive.

3.2.2 Methodology

3.2.2.1 Comprehensive Air Quality Model with Extensions (CAMx) model

We used the Comprehensive Air Quality Model with Extensions (CAMx) model to simulate pollutant concentrations and access the sensitivities of pollutants to various control scenarios. The photochemical simulation is driven by the Weather Research & Forecasting Model (WRF) model.

We retrieved OH loss rate, HO_2 production rate, and the net ozone production rate (PO3) which is calculated by deducting ozone destruction from the total ozone production from the model. We resolved two types of ozone regime indicators, the ratio of production rates of hydrogen peroxide to nitric acid ($P(H_2O_2)/P(HNO_3)$) and the ratio of total radical loss to production (LN/Q). We attributed ozone production rate to VOC and NO_X sensitivity based on a $P(H_2O_2)/P(HNO_3)$ cutting point of 0.35.

3.2.2.2 NASA LaRC modeling

The quantification of O_3-NO_X-VOC sensitivity and O_3 formation regimes (e.g., Kleinman, 1994; Sillman et al., 1995; Kleinman, 2005) was performed (Guo et al., 2021) based on the "LRO_X/LNO_X" metric recommended by Schroeder et al. (2017), in which O_3 formation is thought to be NO_X-sensitive when HO_X radical loss via OH + NO_2 accounts for less than half of total HO_X radical loss. In specific, the radical termination reaction of OH with NO_X to form HNO_3 is referred to as LNO_X, and radical-radical reactions (including RO_2 and RO_2

self-reactions, RO_2 and HO_2 reactions, and RO_2 reactions with a different RO_2) resulting in stable peroxide formation are referred to as LRO_X ($RO_X = RO_2+HO_2$). The ratio of radical termination rate from LRO_X to LNO_X will provide a good indicator of NO_X-sensitive ($LRO_X/LNO_X>\sim0.5$, which corresponds to $Ln/Q < 2/3$, where $Ln = LNO_X$ and $Q = LNO_X + LRO_X$), VOC-sensitive ($LRO_X/LNO_X<\sim0.3$), and transitional ($0.3<LRO_X/LNO_X<0.5$) O_3 formation regimes (Kleinman et al., 2005; Schroeder et al., 2017).

3.2.3 Results

3.2.3.1 Modeling O_3-NO_X-VOC sensitivity during September 2021

The dependence of ozone production on NO_X and VOCs was further assessed by evaluating the ratio of L_N/Q (3.1), where an L_N/Q of 0.5 is defined as the threshold to differentiate VOC sensitivity from NO_X sensitivity. The Houston metropolitan area was found to be primarily in a VOC-limited regime during non-episode days, but it moved towards more NO_X sensitivity during ozone episodes, with the VOC-limited regions restricted to downtown Houston and the HSC. Analysis of 24-hour mean L_N/Q also revealed a transition in ozone production tendency from VOC-limited to NO_X-limited during episodes, except for downtown Houston and the HSC. This transition may be due to the variations in atmospheric levels of ozone precursors across the Houston area.

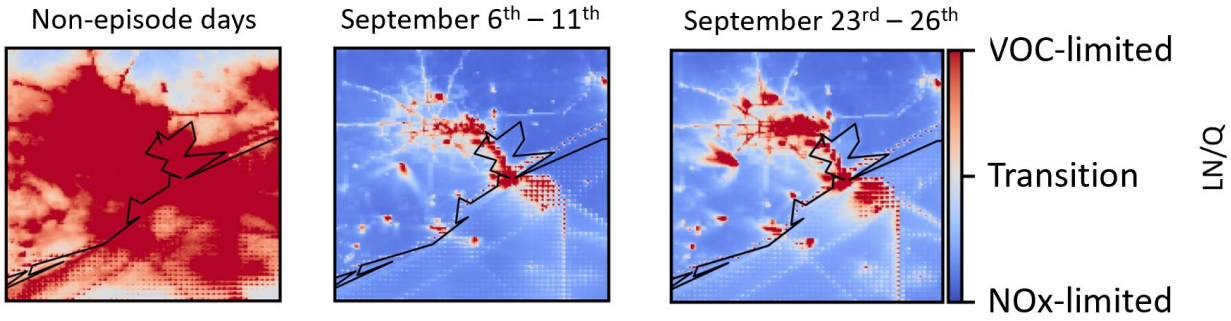

Figure 3.2.1: *Ozone production sensitivity based on CAMx-resolved L_N/Q during 12 p.m.–3 p.m. in non-episode and episode days.*

Figure 3.2.2 illustrates the levels of NO_X and peroxyacetyl nitrate (PAN) from 12 p.m. to 3 p.m. across the Houston area. During ozone episodes, the levels of NO_X in the afternoon decreased by approximately 40%, as shown in **Figure 3.2.2**(a). However, our analysis showed the 24-hour NO_X levels increased by approximately 10% and 25% during the September 6–11 and September 23–26 episodes, respectively, across the Houston area and the HSC. The decrease in NO_X levels during the afternoon across the study domain can be attributed to the photochemical removal of NO_X when ozone production peaks. On the other hand, the enhanced 24-hour NO_X levels during ozone episodes are partly associated with stagnation and accumulation of pollutants, especially in local emission hotspots such as major highways in Houston and the HSC. Additionally, NO_X may have been transported to the region by means of PAN, a well-known tropospheric reservoir of NO_X that can travel

over long distances. **Figure 3.2.2** (b) depicts the spatial distribution of PAN across the study area in the afternoon. The hotspots of PAN were found within Houston, and the levels of this pollutant decreased away from urban areas. Hence, the elevated levels of PAN in Houston during ozone episodes were mostly due to the local formation of PAN, suggesting that NO_X had not been transported to the region by means of PAN. Consequently, the increased daily levels of NO_X during ozone episodes are related to meteorological conditions that trap locally emitted NO_X and lead to the accumulation of pollutants near the source regions. Therefore, variations in NO_X levels restricted to major highways and industrialized districts cannot solely explain the observed transition to NO_X-limited conditions over the rest of the Houston metropolitan area, which suggests the potential impact of elevated VOCs on changing the ozone formation tendency.

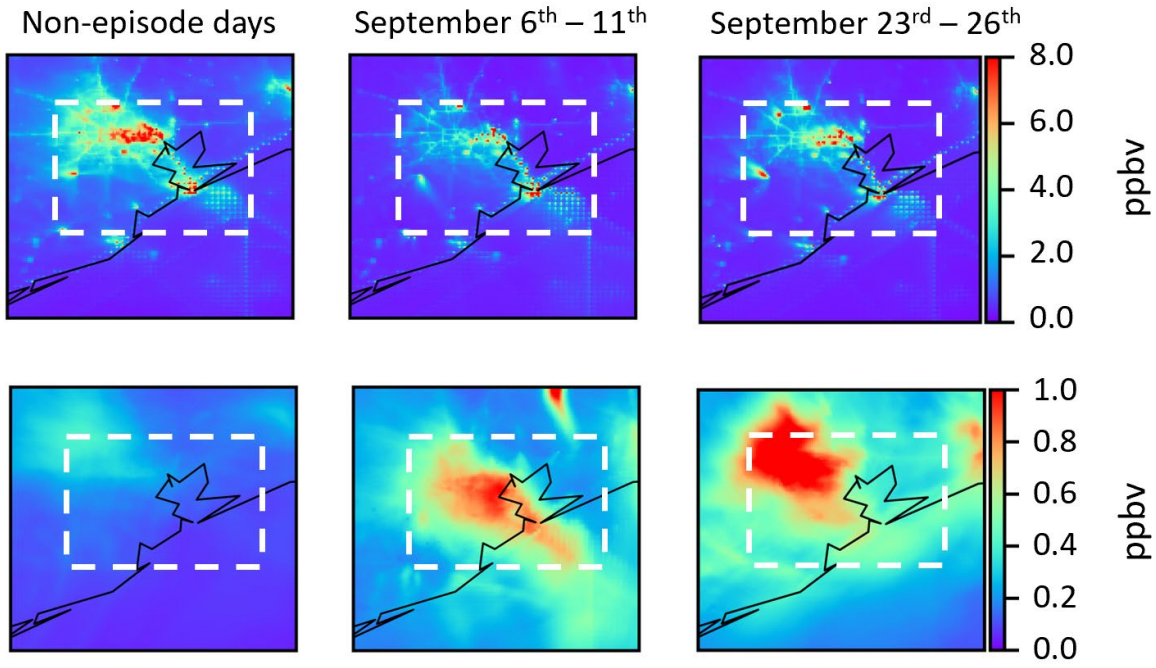

Figure 3.2.2: *Spatial variations in levels of (a) NOx, and (b) PAN during non-episode and episode days. All the parameters were averaged during 12 p.m.–3 p.m. local time. The corresponding mean±SD values for each parameter across d03 and the white dashed domain (i.e., Southeast Houston, HSC, and Galveston Bay) are summarized in Table 3.1.*

The surface concentrations of VOCs belonging to different functional groups were modeled during both non-episode and episode days, as shown in **Figure 3.2.3**. The formation of proxy radicals, such as HO_2, which later take part in ozone formation, is caused by the reaction of VOCs with OH radicals. The levels of olefins and aromatics were similar during both non-episode and episode days, whereas paraffins increased by approximately 120% (September 6–11 episode) and 45% (September 23–26 episode) across the investigated domain. During these ozone episodes, the concentrations of biogenic VOCs (consisting of isoprene and monoterpenes) decreased by approximately 40% and 60%, respectively, reflecting enhanced

oxidation of BVOCs during ozone episodes. The aldehydes (formaldehyde, acetaldehyde, propionaldehyde, and higher aldehydes) increased significantly by approximately 95% during September 6–11 episode (and 30% in September 23–26 episode), while the levels of ketones (acetone and compounds with a ketone carbon bond) increased by a factor of 2.5 and 1.5 in Episodes 1 and 2, respectively. The 24-hour mean levels of these functional groups during non-episode and episode days showed similar results.

Olefins and aromatics have short lifetimes and cannot be efficiently transported across long distances. Similarly, BVOCs are too short-lived to survive transport. Paraffins, on the other hand, have low reactivity and long lifetimes and can be transported over long distances, representing aged emissions. Aldehydes act as temporary reservoirs, releasing HO_X free radicals, and participate in catalytic cycles producing ozone. Oxygenated VOCs such as acetone can also be present in aged air masses. Functional groups with longer lifetimes, such as paraffin and aged VOCs, were the main drivers of enhanced VOCs during ozone episodes, indicating the transport of long-lived species to the Houston region. Although the Houston area experienced high levels of VOCs during ozone episodes, NO_X levels remained almost constant away from major emission sources, resulting in excessive ambient VOCs concentrations and NO_X-limited conditions. Elevated levels of NO_X over industrial districts, particularly near the HSC, counterbalanced the effects of transported VOCs, resulting in VOC-limited areas.

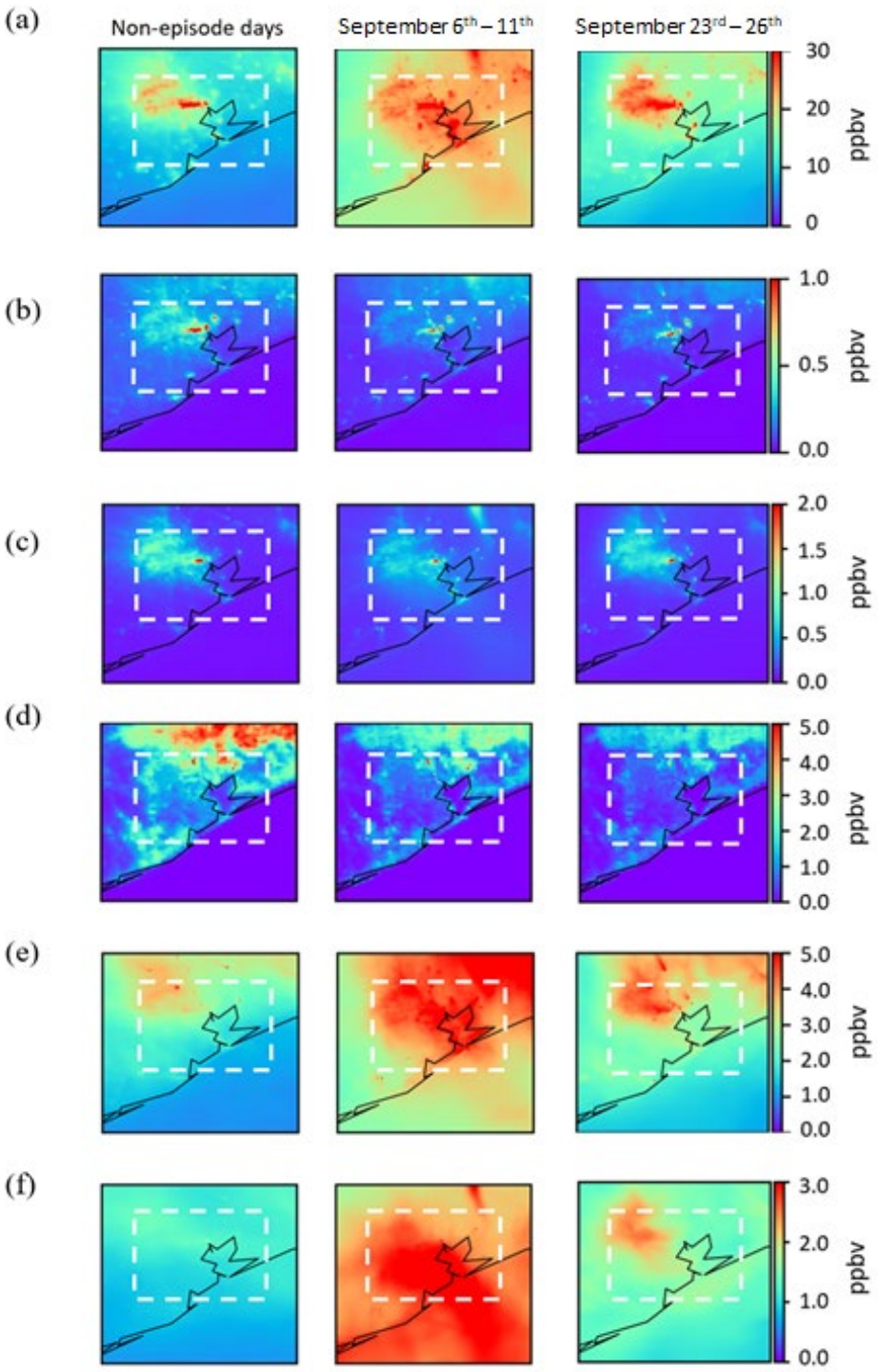

Figure 3.2.3: *CAMx-simulated surface levels of (a) paraffins, (b) olefins, (c) aromatics, (d) biogenic VOCs, (e) aldehydes, and (f) ketones during 12 p.m.–3 p.m. within non-episode and episode days. The corresponding mean±SD values for each parameter across d03 and the white dashed domain (i.e., Southeast Houston, HSC, and Galveston Bay) are summarized in* ***Table 3.2****.*

Table 3.2: *Summary of the mean values for levels of NOx, PAN, and VOCs over the Southeast Houston, HSC, and Galveston Bay regions (shown in bold – corresponding to the white rectangle in* ***Figure 3.2.2****, and* ***Figure 3.2.3****).*

Parameter (unit)	Non-episode days	September 6th – 11th	September 23rd – 26th
NO_x (ppbv)	1.24±1.93	0.74±1.22	0.75±1.16
	2.45±3.23	**1.48±2.50**	**1.56±2.17**
PAN (ppbv)	0.14±0.19	0.36±0.32	0.43±0.29
	0.17±0.19	**0.53±0.43**	**0.61±0.35**
		VOCs	
Paraffins (ppbv)	9.44±7.34	20.49±8.82	13.52±5.93
	12.50±8.49	**24.46±10.06**	**17.72±6.83**
Olefins (ppbv)	0.13±0.21	0.09±0.12	0.07±0.09
	0.21±0.28	**0.15±0.14**	**0.11±0.12**
Aromatics (ppbv)	0.17±0.29	0.24±0.21	0.17±0.18
	0.31±0.43	**0.38±0.26**	**0.29±0.25**
Biogenic VOCs (ppbv)	1.11±2.40	0.64±0.85	0.46±0.60
	1.35±1.83	**0.82±0.75**	**0.55±0.48**
Aldehydes (ppbv)	1.95±1.36	3.78±1.80	2.55±0.99
	2.29±1.33	**4.53±1.69**	**0.39±0.51**
Ketones (ppbv)	0.98±0.76	2.57±1.12	1.50±0.72
	1.12±0.78	**2.77±1.29**	**0.72±0.80**

Finally, the time series of folded FLEXPART-CAMx plume averaged for daily releases during ozone episodes is displayed in **Figure 3.2.4**. The graph shows that ozone levels in the plume increased from approximately 47.3 ppbv on September 5 to 57.0±4.6 ppbv during September 6–11, before dropping to ~32 ppbv on September 13, indicating increased levels of ozone in the transported plume during the September 6–11 episode. On September 8th, the levels of ozone peaked at an average level of around 62 ppbv along the plume, which was likely due to the recirculation of air masses over the Houston area and ozone hotspots. We found that ozone formation during transport in September 6–11 episode was mainly NO_X-limited (0.84±0.34 ppb/hr) compared to being VOC-limited (0.18±0.13 ppb/hr), as the contribution of VOCs to ozone formation decreased from ~39% on September 4–5 to ~17% during the September 6–11 episode. **Figure 3.2.4**(b) shows that the mean levels of NO_X and PAN slightly increased during September 6–9. The levels of VOCs in the plume increased by 2–4 times during the September 6–11 episode.

During the September 23–26 episode, ozone levels along the plume increased from around 37 ppbv (pre-episode) to 49.9±7.3 ppbv (during September 23–26 episode), as shown in **Figure 3.2.4**. We found that ozone formation during the September 23–26 episode was a combination of VOC-limited (0.68±0.71 ppb/hr) and NO_X-limited (0.57±0.21 ppb/hr) ozone productions, unlike the September 6–11 episode, where it was mainly NO_X-limited. The

analysis of ozone precursors showed that NO_X and PAN increased by a factor of around 2 and 4, respectively, during the September 23–26 episode, compared to pre- and post-episode. The levels of VOCs (except BVOCs) increased on average by a factor of around 2 during this ozone episode. Due to the significant increase in NO_X levels along the plume, the ozone formation tendency showed VOC sensitivity, resulting in VOC-limited ozone production.

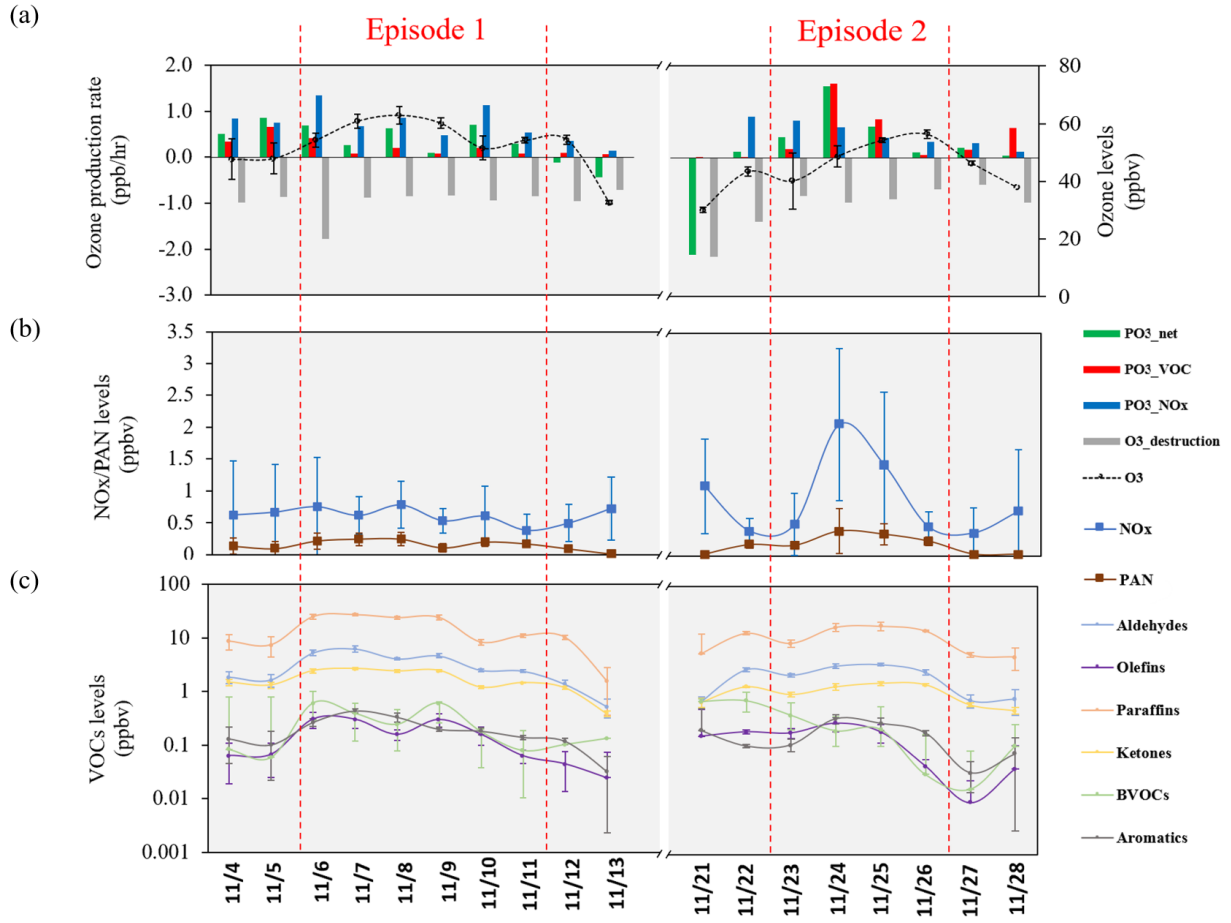

Figure 3.2.4: *Plume evolution based on variations in mean (a) ozone/ozone production, (b) NO_X/PAN, and (c) volatile organic compounds throughout the FLEXPART-modeled plume. Error bars correspond to one standard deviation. The analysis encompasses two days prior to ozone episodes onset (i.e., Sept. 4–5 and Sept. 21–22) and two days after the termination of ozone episodes (i.e., Sept. 12–13 and Sept. 27–28).*

3.2.3.2 LaRC Modeling of Variations in O_3-NO_X-VOC Sensitivity

During the stationary measurement period at Battleground Site, the NO_X or VOC-sensitive ozone formation regimes were estimated from the LaRC model qualitatively by the relationship between the net ozone production rate ($P(O_3)$) and NO (Figure 3.7.3.1) and quantitatively by the LRO_X/LNO_X metric introduced above (Figure 3.7.3.3). In Figure 3.7.3.1, a turning over point of net ozone production rate ($P(O_3)$) was observed at NO

concentration of approximately 1~2 ppbv, indicating a transition from NO_X-sensitive regime (in which the increase of NO leads to an increased O_3 production rate) to VOC-sensitive regime (in which the further increase of NO results in limited O_3 production rate).

Compared to Figure 3.7.3.2, in which $P(O_3)$ generally increased with the total OH reactivity of VOCs and photolytic activity, the highest $P(O_3)$ occurrence did not coincide with the highest total OH reactivity of VOCs. Instead, $P(O_3)$ peaked at a moderately high total OH reactivity of VOCs (~10 s^{-1}) where an intense photolytic activity existed (jNO2 > 0.01 s^{-1}).

Based on the LRO_X/LNO_X ratio (Figure 3.7.3.3), 53% of the LaRC modeled period was in VOC-sensitive regime, with an average NO of 9.8 ppbv and $P(O_3)$ of 23.2 ppbv hr^{-1}, while 44% of the period was in a NO_X-sensitive regime, with an average NO of 0.7 ppbv and significantly higher average $P(O_3)$ of 36.6 ppbv hr^{-1}. Approximately 4% of the period was in the transitional regime with an average NO of 1.4 ppbv in consistent with the qualitative evaluation of the NO turning over point between 1 and 2 ppbv. Despite its limited occurrence, the transitional regime has the highest average $P(O_3)$ of 42.3 ppbv hr^{-1}, an 83% increase from the average of the VOC-sensitive regime and a 16% increase from that of the NO_X-sensitive regime.

The diurnal variation of LRO_X/LNO_X (Figure 3.7.3.3) indicated that $P(O_3)$ was mainly VOC-sensitive in the morning from 6:00 to 10:00 CST throughout the modeled period at the Battleground Site. During the morning period, a peak $P(O_3)$ of 44.3 ppbv hr^{-1} was observed at 9:00 CST. Between 10:00 and 11:00 CST, the O_3 formation regime transitioned from VOC-sensitive to NO_X-sensitive regime. Around noon (12:00 CST), a second peak of $P(O_3)$ of 41.1 ppbv hr^{-1} was observed. Throughout the afternoon, even though there were frequent conditions during which the ozone formation regime fell in the VOC-sensitive regime, the NOX-sensitive regime governed the monthly-long modeled period from an overall perspective. On average, the net ozone production rate was 24.8 ± 15.5 ppbv hr^{-1} throughout the daytime and was most active from 9:00 to 15:00 CST. During the elevated $P(O_3)$ period, the ozone formation regime was first VOC-sensitive, then shifted to NO_X-sensitive. Such a pattern was comparable to the results from DISCOVER-AQ in 2013 (Mazzuca et al., 2016), where a shift from VOC- to NO_X-sensitive regime was observed between 9:00 and 11:00 CST accompanied by the peak in net ozone production.

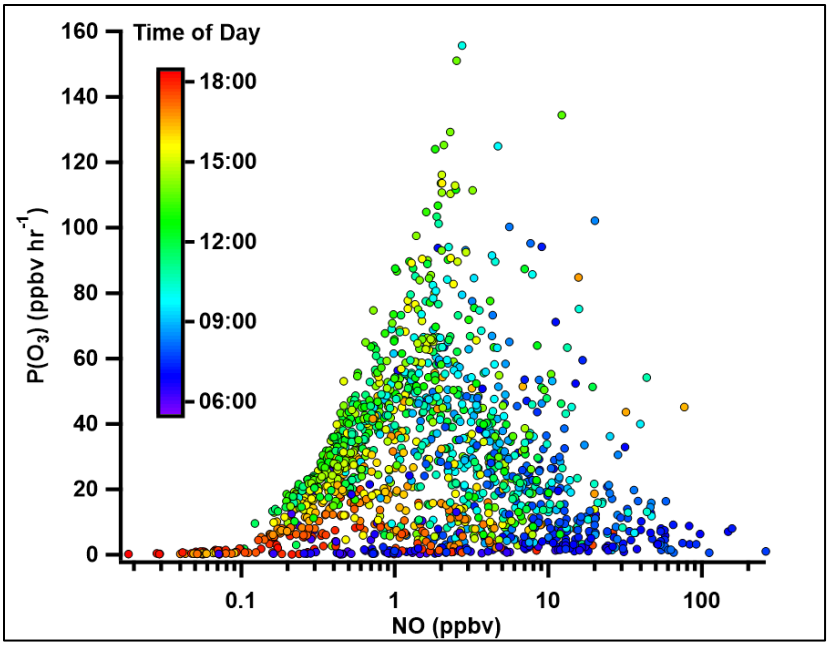

Figure 3.2.5: *Modeled net ozone production rate ($P(O_3)$) versus NO concentration colored by time of day (CST) at Battleground Site.*

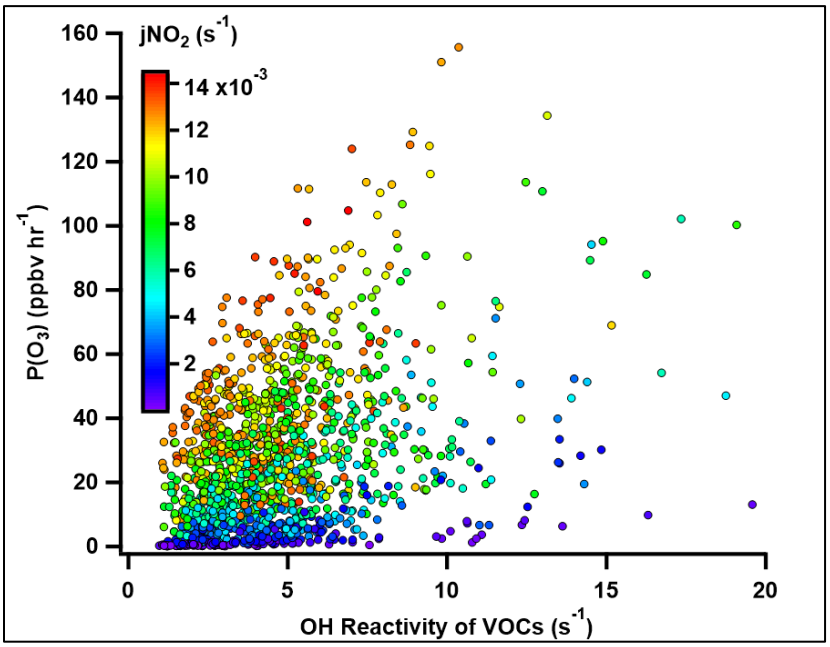

Figure 3.2.6: *Modeled net ozone production rate ($P(O_3)$) versus the total OH reactivity of VOCs colored by the total photolysis rate of NO_2 at Battleground Site.*

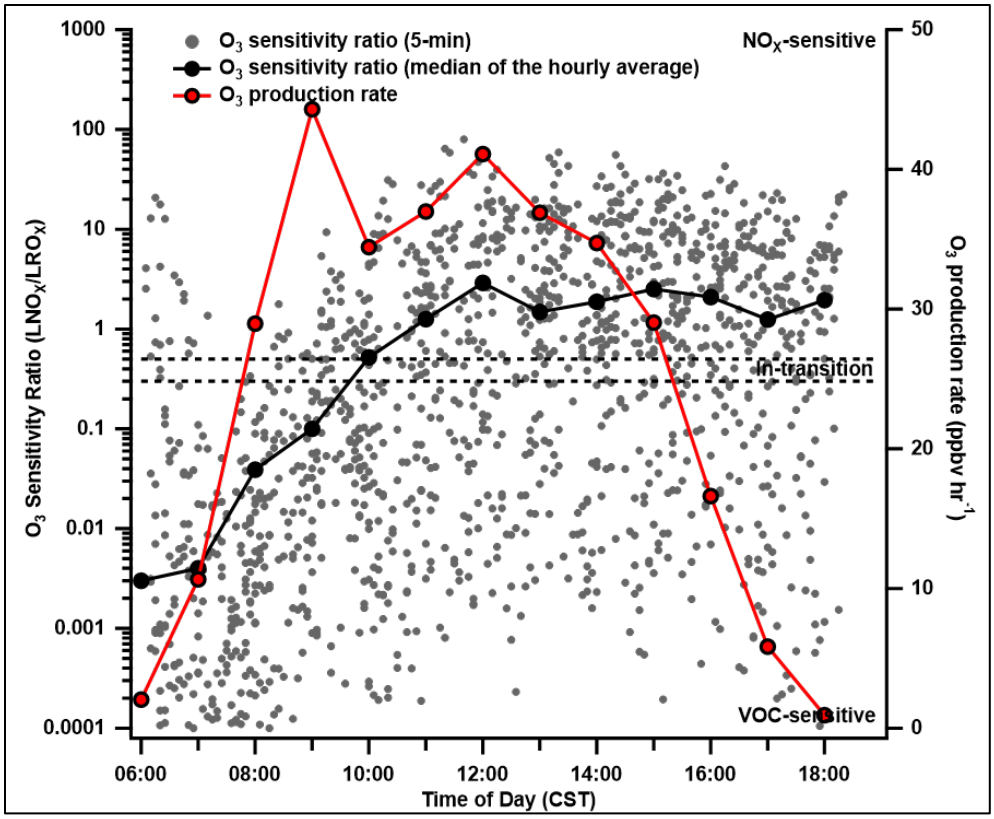

Figure 3.2.7:*The 5-min (grey points) and median of the hourly average (black line with markers) daytime profiles of O_3 sensitivity ratio (LRO_X/LNO_X) on the left axis, and the modeled net ozone production rate ($P(O_3)$, red line with markers) on the right axis. The two horizontal dash lines on the left axis at values of 0.3 and 0.5 indicate the transition regime between NO_X- and VOC-sensitive regimes.*

3.3 Over Water Ozone and Dynamics

3.3.1 Summary and Key Findings

CAMx ozone production rate (PO3) increased by factors of ~3 and ~2 during Episode 1 and Episode 2, respectively.

3.3.2 Methodology

3.3.2.1 Sampling

To address the observational gap in over water air quality monitoring, we developed and installed two automated sampling systems on commercial boats and one enhanced and monitored instrument package on a UH research boat operating in Galveston Bay. One of the commercial boats, the shrimp boat, and the UH pontoon boat operated in Galveston Bay while the second commercial boat, the Red Eagle, primarily operated in the waters offshore of Galveston Island in the Gulf of Mexico. Ozonesondes were also launched from the UH boat within Galveston Bay and on the Red Eagle in the Gulf of Mexico on select occasions.

Instrument Packages

The automated instrument packages consist of a 2B Technology Model 205 dual-beam O_3 analyzer, Global Positioning System (GPS), and a ruggedized industrial computer (PC). The PC was configured to boot and shut down with an external switch or with the application or loss of power which automatically started or stopped the instrumentation and data logging. A compact, all-in-one weather station was installed to measure temperature, relative humidity, pressure, wind speed and direction. An internal digital compass was used with GPS data to correct winds for the motion of the boat. This equipment was installed into a light-colored (yellow) weatherproof enclosure to protect the instrumentation and reduce heat. Additional insulation and a radiant barrier further reduced solar heating. A thermoelectric heat exchanger attached to the enclosure further reduced heat and maintained a stable environment for the instrumentation. Desiccant bags were also used to help control internal relative humidity. This enclosure was secured to the boat exterior on top of the cabin. A Teflon sample line was run from the sample pump in the O_3 monitor to an elevated location on each boat for the sample inlet. A Teflon rain shroud prevented water from entering the 90 mm Teflon particle filter before being sampled. The relatively large area of the filter required less frequent access to the boat and equipment for filter changes.

A valve was used to periodically route the sample through an ozone-destroying charcoal volume to assess the instrument baseline. Instruments were calibrated prior to and after deployment by comparison with O_3 standards directly traceable to the EPA Region 6 standard reference photometer for O_3.

Data was logged internally and then transferred to servers at UH via integrated cellular modems when the boat was within the cellular coverage area. There was excellent cellular coverage over most of the areas where the boats operated in Galveston Bay, with the exception of spotty signal at Smith Point itself. Cell coverage in the Gulf was also typically available as far out as the anchorage locations but not at the lightering area. The data, which included instrument diagnostic information such as instrument temperatures, pressures, and flows, was displayed on the same system used to visualize and edit data from the network of UH monitoring sites. The network connection also allowed investigators to log into the computers on the boat via LogMeIn to evaluate instrument performance and aid in troubleshooting.

Vaisala CL-51 ceilometers were installed on the UH pontoon boat and the shrimp boat. The ceilometers operated and collected data continuously, however the ceilometer on the UH pontoon boat suffered a failure on August 30th. Since the shrimp boat was not going out as frequently as hoped due to poor shrimping conditions, the team removed the ceilometer from the shrimp boat and installed it on the UH pontoon boat. The data, both mobile and stationary, is used to better understand O_3 processes in and around the Galveston and Trinity Bay area.

3.3.2.2 Platforms

Commercially operated vessels around Galveston Bay were considered for platforms to operate air quality instruments on, with two boats being chosen due to operating profiles and willingness to partner for the endeavor. On the east side of Galveston Bay, a shrimper from Smith Point was chosen (**Figure 3.3.1**). As described to the science team, their operating pattern would follow the shrimp in the Bay as they slowly migrated through various portions of eastern Galveston Bay, unlike oyster boats which visit fixed locations. Since the boat docked at Smith Point it would also provide excellent opportunities for comparison with C1606. For the Gulf of Mexico, a charter boat (**Figure 3.3.2**) service was selected as their operations would take them to the various anchoring and lightering areas off Galveston Island frequently, sometimes multiple times per day.

Figure 3.3.1: *Commercial shrimping vessel, independently owned and operating out of Smith Point, TX.*

Figure 3.3.1 shows the shrimp boat with the mobile sampling package installed onto the roof of the pilothouse. A dedicated high output marine alternator and battery was installed for additional power to operate the science equipment while underway. The shrimp boat operator was expected to be on the bay typically four days a week, when shrimping conditions were suitable. Based on pre-campaign discussions, on a typical day he would leave the Smith Point area around dawn and return around 2:00 p.m., depending on the season and catch. The shrimp boat operator based his boat at the basin in the RV park where the UH Smith Point (C1606) monitoring site is located, allowing for routine comparisons with the O_3 monitor just 260 m east of the dock. The early season influence of freshwater in the Bay from local rains decreased the quality of catch during 2021 and resulted in a significantly lower number of outings and spatial coverage by the shrimp boat. COVID related issues also limited his ability to operate for a couple of weeks in August and September.

Figure 3.3.2: *Commercial vessel R/V Red Eagle, operated by Ryan Marine in Galveston, TX.*

The Red Eagle (**Figure 3.3.2**) is a 100’ long crew/utility vessel with two 40 kW 110/208V three-phase power generators. The typical operating profile for the Red Eagle was to depart the Galveston docks to service larger vessels in the Galveston Anchorages and Lightering areas, depending on their clients’ needs. The Red Eagle on occasion conducted operations as far west as Matagorda Bay and north into Galveston Bay and through the ship channel to the port of Houston. The Red Eagle would go up to 50 miles offshore, if needed, and these activities would occur 24-hours a day and in all weather conditions.

Figure 3.3.3: *A pontoon boat owned and operated by the University of Houston, operating out of Kemah, TX.*

Finally, a pontoon boat (**Figure 3.3.3**) owned and operated by the UH Earth and Atmospheric Science Department, was outfitted with an instrument package and was deployed on selected days in July, August, September, and October to sample in situ O_3, O_X ($O_3 + NO_2$ - added September 17th), boundary layer heights and meteorological variables around Galveston Bay. Additionally, twenty-seven ozonesondes were launched from the UH pontoon boat throughout the sampling period to determine the vertical distribution of O_3 and the marine boundary layer height. In combination the three boat platforms sampled Galveston Bay and the offshore waters of the Gulf of Mexico extensively.

3.3.3 Results

3.3.3.1 Over Water Vs. Over Land Ozone

The averaged O_3 mixing ratios from the three observational boat platforms were higher in all months of the campaign than the averaged 'onshore' component (**Table 3.3**), averaged from twenty-five stationary monitoring sites around the HGB area. The months of September and October both showed average ozone values deviating higher towards the offshore boat platforms compared to the onshore stationary measurements. This reflects the wind flow regime change from generally onshore in the months of July and August to frequently offshore in the months of September and October with the beginning of cold front passages. This setup puts the coastal regions downwind of the urban and industrial areas of the HGB region. The standard deviation values are higher onshore throughout all high ozone episodes (**Table 3.3**) illustrating the increased variability in the diurnal cycle at inland locations compared to the coastal sites.

Table 3.3: *Averaged ozone concentrations from twenty-five air quality monitoring stations in the HGB region constituting the 'onshore' components. The three boat platforms were averaged to form the 'offshore' component.*

Month	Onshore	Offshore
July	23.6 ± 17.5	26.7 ± 14.6
August	22.5 ± 15.2	26.3 ± 12.7
September	26.6 ± 18.6	34.1 ± 17.9
October	25.8 ± 17.3	33.9 ± 14.2

High O_3 events were identified as any day with a maximum daily 8-hr average (MDA8) that exceeded the National Ambient Air Quality Standard (NAAQS) of 70 ppbv from either a stationary monitor or boat platform. Twenty-five Texas Commission on Environmental Quality (TCEQ) stationary monitors around the Houston-Galveston-Brazoria (HGB) region were averaged during the episodes for the 'onshore' component and the three operational boats were

averaged for the 'offshore' component. The total average O_3 was higher offshore compared to onshore reflecting less titration overnight/early morning at the offshore locations compared to the largely urban/industrial HGB region that comprised the onshore locations. Higher peak 1-hr ozone values were recorded for the onshore locations during all ozone episodes. A larger difference in the peak 1-hr values were observed for episodes 1 and 2, which were bay/sea breeze driven recirculation events compared with episodes 3–6 which were driven synoptically from cold front and tropical system passage. Higher peak MDA8 O_3 values were observed during all but episode 4, which was a uniquely coastal case in the wake of a tropical system, hurricane Nicholas. Given the larger amount of precursor emissions onshore higher MDA8 O_3 is expected to be higher inland. During episode 4 the monitors that observed higher values were those closer to the coast as well.

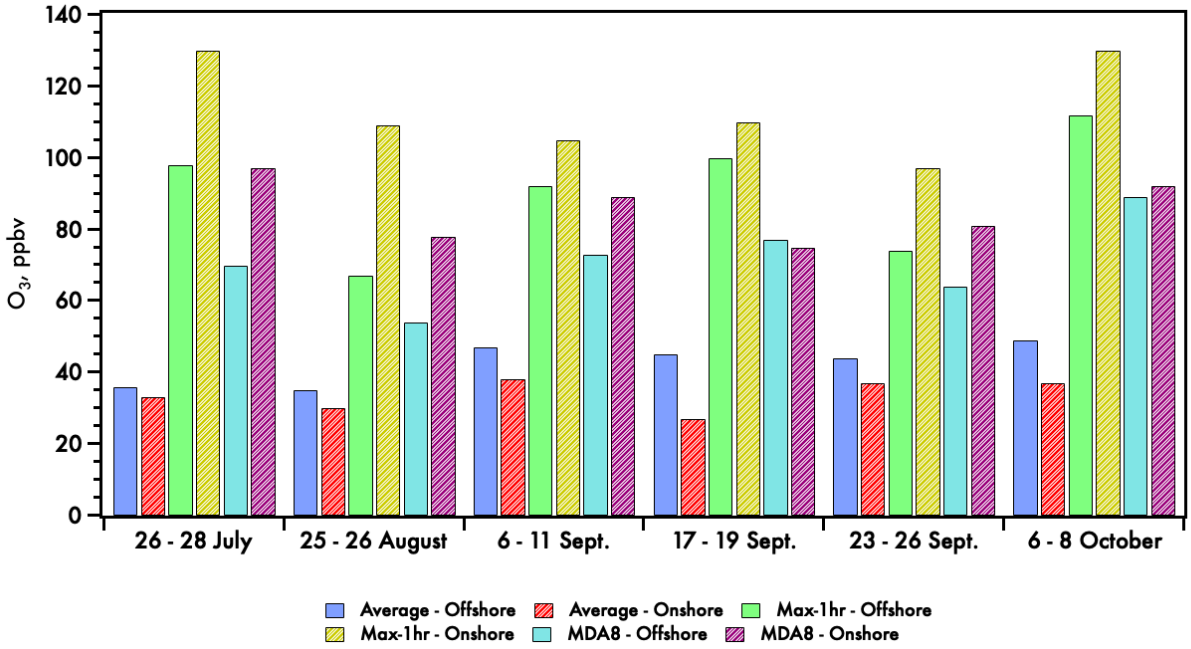

Figure 3.3.4: *Box plot of the six identified high O_3 episodes in chronological order.*

The monthly diurnal profiles of O_3 mixing ratios from the three operating boat platforms and ten stationary TCEQ air quality monitoring stations around the HGB region show a distinct separation between the boat platforms and land-based monitors during the early morning hours, before sunrise, and in the evenings, after sunset (**Figure 3.3.4**). This separation is especially prevalent in the months of September and October when O_3 was highest on average. Interestingly, the UH pontoon boat, docked in the water near the western edge of Galveston Bay, showed a diurnal profile that split between the other boat platforms and land-based monitors during the early morning hours. This underscores the steep gradients that occur at the land-water interface. Multiple factors are likely contributing to the observed difference between inland and

boat monitors including titration of ozone overnight from local NO_X emissions as well as differences in the nocturnal boundary layer at the different locations.

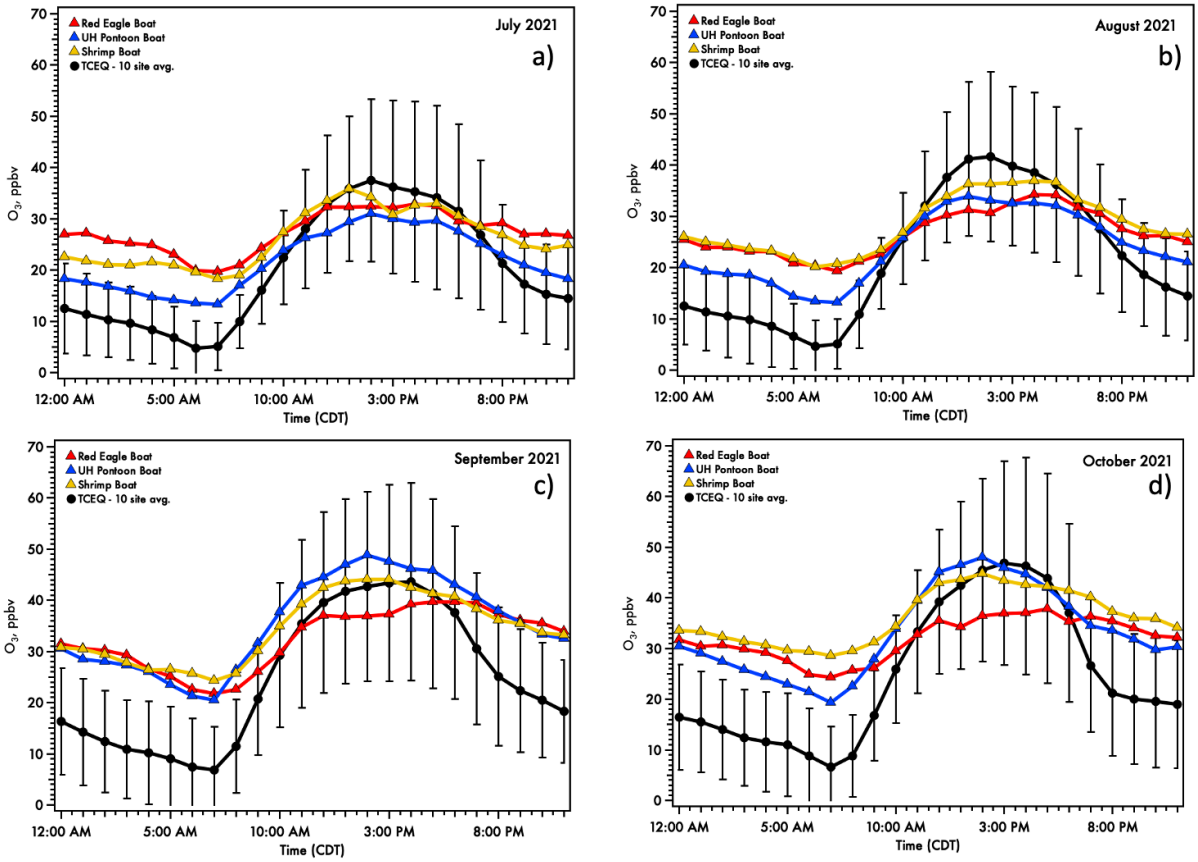

Table 3.4: *Diurnal ozone profiles of the three boat platforms and the average of ten stationary air quality monitoring stations around the HGB region, the error bars for the stationary diurnal profile represent the average of the standard deviations.*

3.3.3.2 Monthly Over Water Spatial Distribution of Ozone

Due to fuel limitations, personnel constraints, and dependence on water conditions for sampling in certain parts of Galveston Bay a sampling bias towards areas closer to the marina and times generally through 08:00–16:00 CDT is seen in the data over Galveston Bay. An element of chance was also involved with the commercial instrument packages as our instruments were passive passengers and subject to the times and locations of the vessels' needs.

High O_3 episodes were observed over water during all four months of the campaign, driven by multiple mechanisms and source regions, including locally produced ozone during recirculation events as well as enhanced ozone from long-range transport after frontal passages. During July and August high O_3 was observed less often over the water and tended to be more isolated to Galveston Bay compared with September and October. September saw

the largest areas of high O_3 over the waters of both Galveston Bay and the Gulf of Mexico, an observation of over 100 ppbv O_3 was recorded over 26 miles offshore on September 9th, 2021 (during episode 3). Climatologically September begins the transition into fall with frontal boundaries beginning to make it to the HGB region driven by changes in upper-air patterns. These periods often drive high O_3 episodes 1–3 days after passage (Lei 2018).

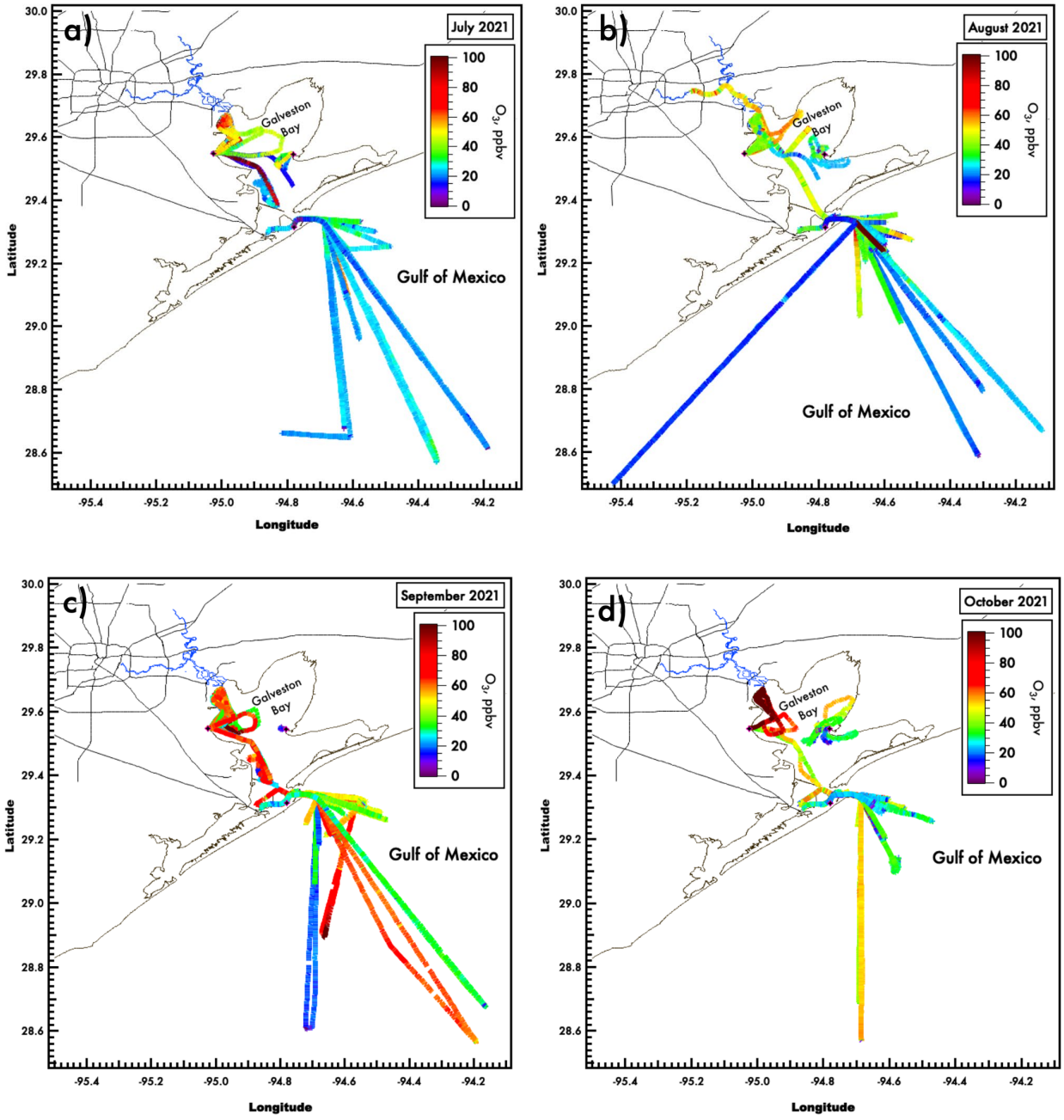

Figure 3.3.5: *Monthly spatial plots of the three instrumented boats with the associated 1-minute averaged O_3 mixing ratios.*

3.3.3.3 Monthly Boat Wind Roses

Wind rose plots (**Figure 3.3.6**) at the three boats show the distribution of wind speed and direction during the four months of the campaign. Winds at the UH pontoon boat were weaker than the other boats in all months of the campaign. Often weak winds at the UH pontoon boat had a W/SW component, which is the direction of land from the dock, showing the weak land breeze that often develops due to the temperature gradient between the land-water interface in the absence of strong synoptic forcing. Winds during September and October tended to be stronger, compared with July and August, and with increased easterly and northerly components at all boats with the start of frontal passages.

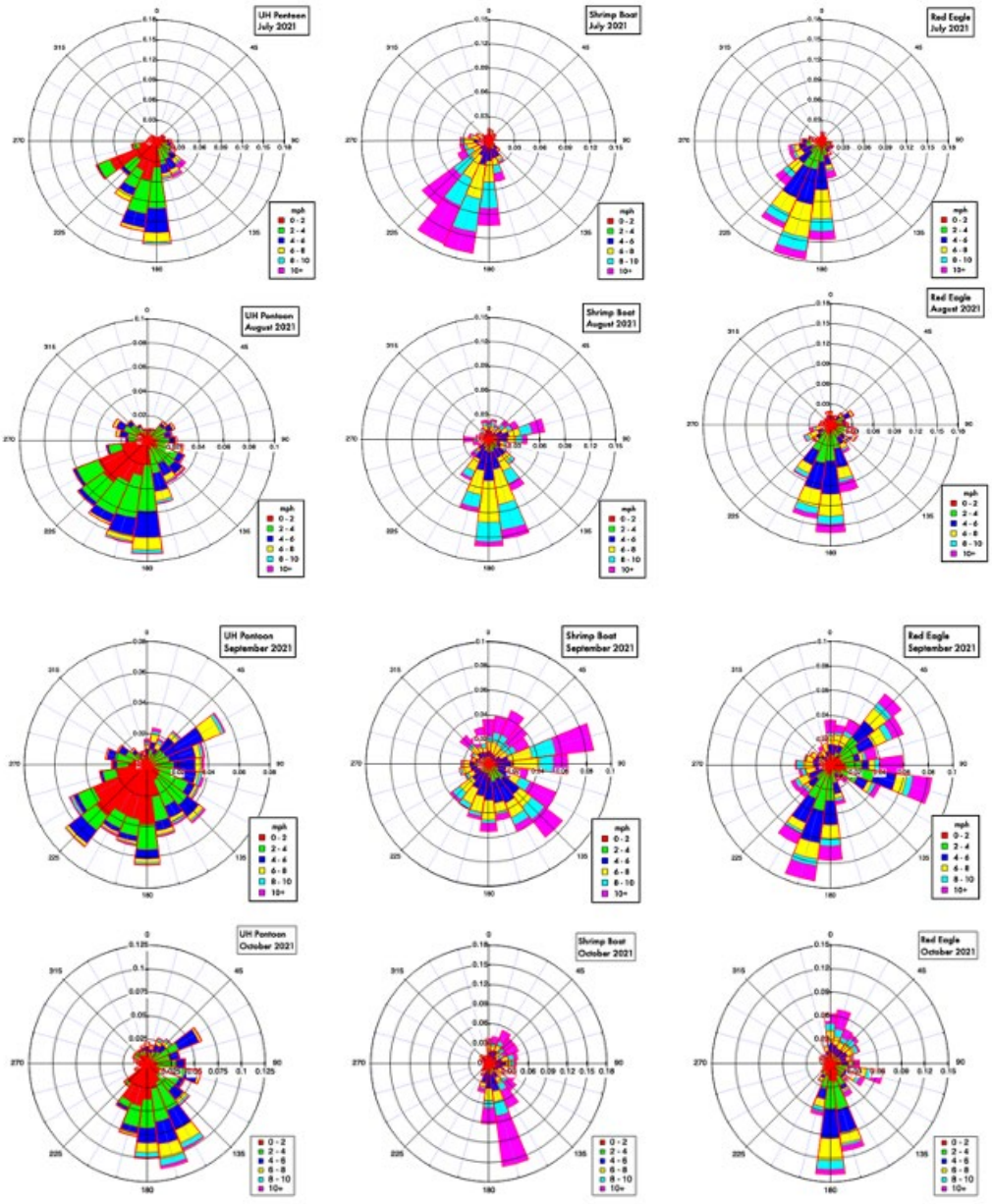

Figure 3.3.6: *Wind rose plots for all boat platforms during the four months of the campaign.*

3.3.3.4 High Ozone Over Water

Six high ozone episodes were identified during the operational period using the exceedance criteria for the NAAQS MDA8 ozone greater than 70 ppbv at either a boat platform or continuous ambient monitor in the HGB region. The prevailing wind conditions, peak 1-hr and maximum daily 8-hr ozone are shown in **Table 3.5** for the identified high ozone episodes.

Table 3.5: *Peak 1-hr and Maximum Daily 8-hr ozone average for the boat platforms constituting the 'offshore,' and twenty-five continuous stationary air quality monitoring stations around the HGB region constituting the 'onshore' category.*

High O_3 Episodes	**Peak 1-hr O_3 (ppbv)**		**MDA8 [O_3] (ppbv)**		**Wind Conditions**
(2021)	**Onshore**	**Offshore**	**Onshore**	**Offshore**	
07/26 - 07/28	130	98	97	70	Light N veering to ESE in the afternoon
08/25-08/26	109	67	78	54	Light N veering to ESE in the afternoon
09/06 - 09/11	105	92	89	73	Northerly veering to easterly in the afternoon
09/17 - 09/19	110	100	75	77	Light NW becoming Southerly at the coast
09/23 - 09/26	97	74	81	64	Northerly veering to easterly in the afternoon
10/06 - 10/09	130	112	92	89	Northerly veering to easterly in the afternoon

Ozone exceeding 70 ppbv, directly contributing to MDA8 ozone exceedances, was observed over the water on 5 of 6 high ozone episodes identified during the campaign; the 25–26 August episode had lower (moderate) values over Galveston Bay. During four of the six episodes, ozone above 70 ppbv was observed over Galveston Bay as well as the offshore waters of the Gulf of Mexico. The two episodes that did not see high ozone over the Gulf of Mexico, The 26–28 July and 25–26 August episodes, had limited operations and only included one offshore trip. Furthermore, while docked in Galveston, TX, the Red Eagle, and the stationary monitor Galveston C1034 did not record any MDA8 or 1-hr ozone exceedances during these episodes. This finding suggests that high ozone episodes driven by light synoptic forcing and bay breeze recirculation can produce high ozone over the waters of Galveston Bay but do not seem to extend into the offshore waters of the Gulf of Mexico.

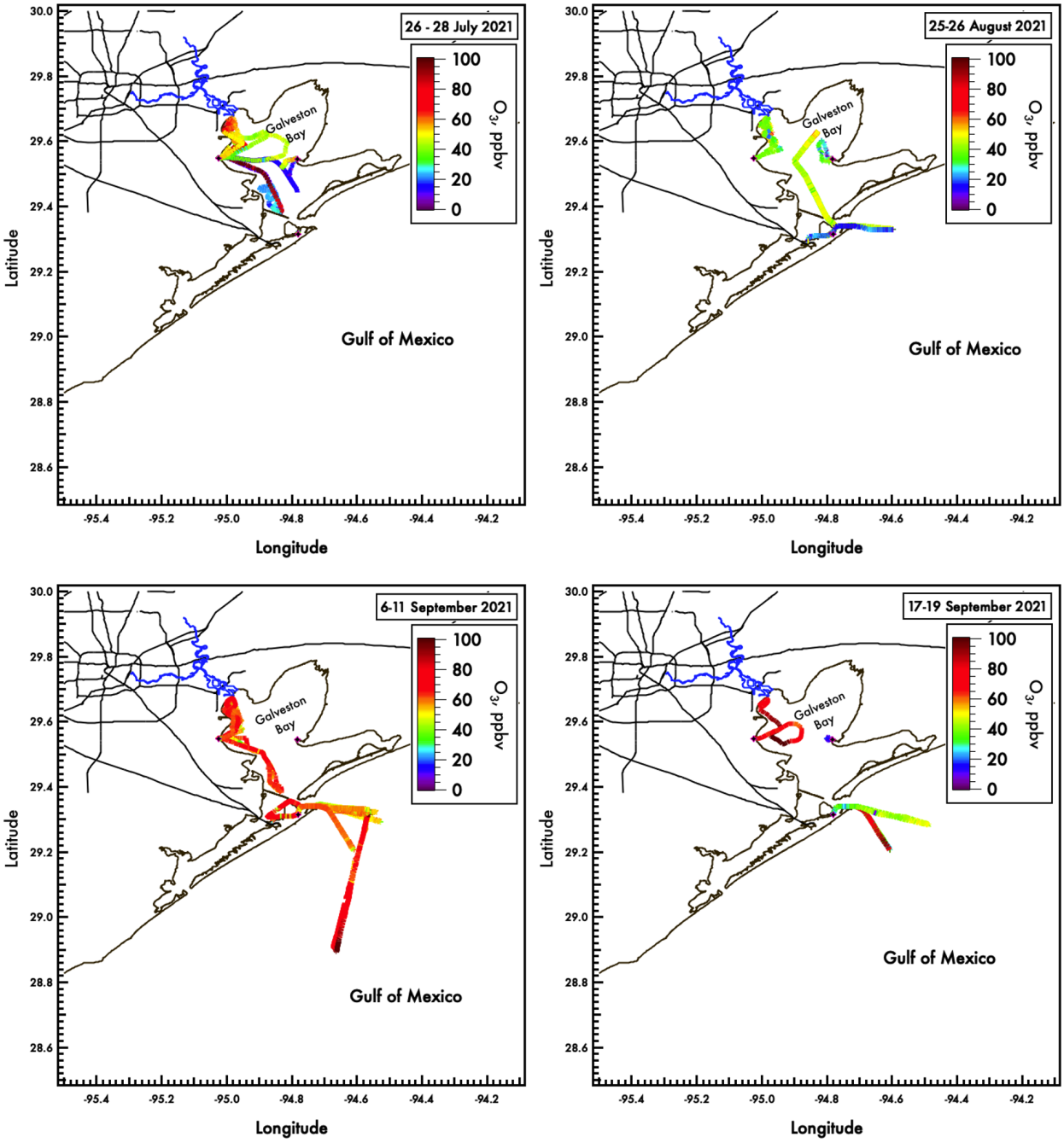
26 - 28 July 2021
25-26 August 2021
6-11 September 2021
17-19 September 2021
Galveston Bay
Gulf of Mexico
Latitude
Longitude
O3, ppbv
100
80
60
40
20
0
30.0
29.8
29.6
29.4
29.2
29.0
28.8
28.6
-95.4
-95.2
-95.0
-94.8
-94.6
-94.4
-94.2

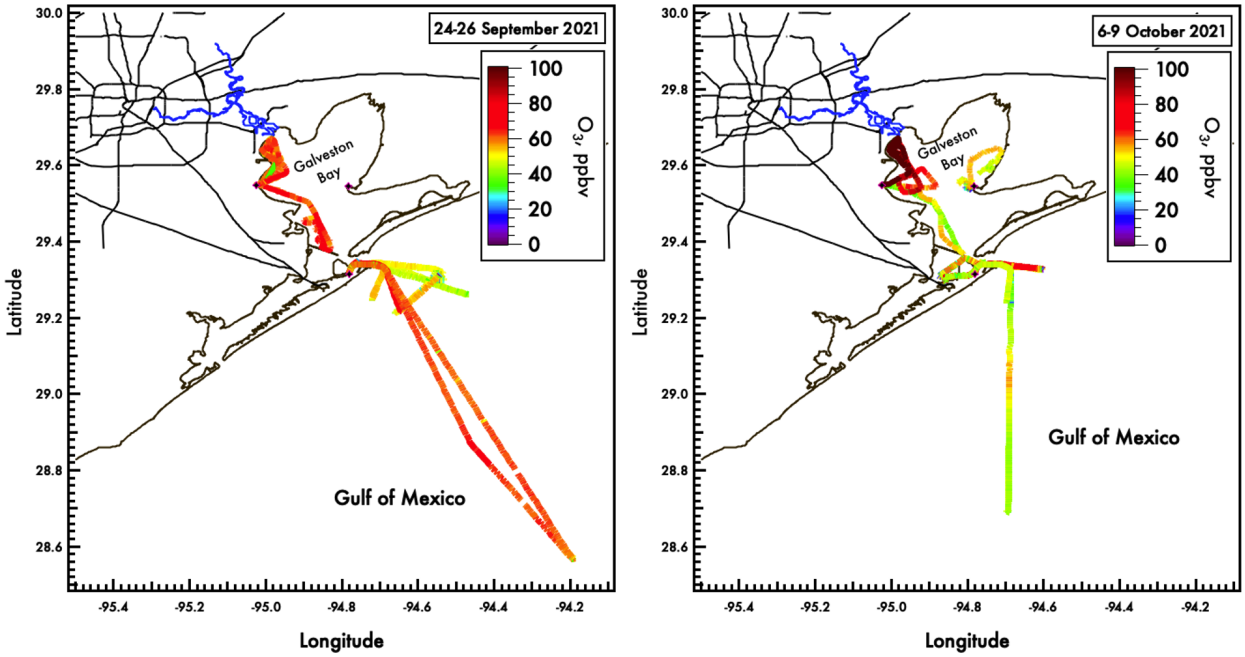

Figure 3.3.7: *Spatial plots of all mobile sampling with the associated ozone mixing ratios from the three boats during noted high ozone events.*

High ozone episodes in September and October 2021 observed high ozone over the Gulf of Mexico and Galveston Bay driven by synoptic scale forcing of frontal and tropical system passages (**Figure 3.3.7**). The 17–19 September 2021 episode was a unique case where light winds on the lee side of the tropical system, Hurricane Nicholas, produced a high ozone episode that air quality models did not forecast. This event may have been driven by light northerly winds resulting from cutting off the westward extension of the high-pressure center of the Bermuda High. This high ozone episode was also a localized coastal event, with all monitoring stations that exceeded the MDA8 ozone standard being < 10 km from Galveston Bay or the Gulf of Mexico.

3.3.3.5 >70 ppbv Ozone and Wind Direction

Near-shore monitoring locations have often recorded the daily maximum ozone concentrations exceeding the regulatory standard of MDA8 ozone > 70 ppbv with a flow reversal associated with mesoscale circulations (i.e., Gulf and Bay breezes) driven by differential heating of the land and water (Banta et al., 2005, Stauffer et al. 2012, Sullivan et al. 2019). During the 2021 field campaign, this pattern was maintained, and the highest 5-minute averaged ozone concentrations at all three boats while docked at the shoreline were from the over water direction.

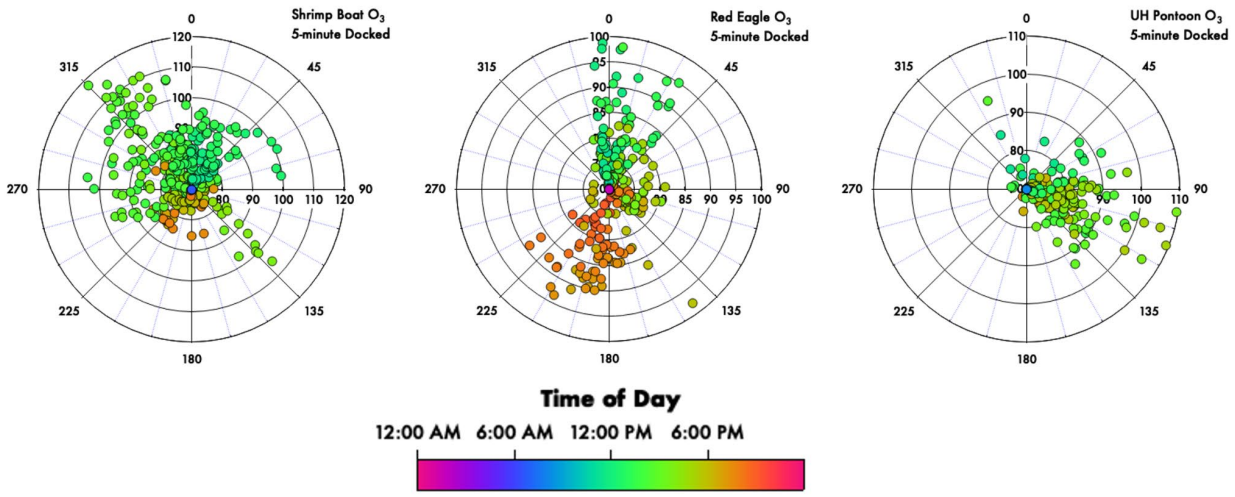

Figure 3.3.8: *Wind direction polar plots of the shrimp boat (left), Red Eagle (middle) and UH Pontoon Boat (right) with associated time of day. The origin of the plots is at 70 ppbv with increasing radius values going outwards for July–October 2021.*

Periods of ozone exceeding 70 ppbv observed at the UH Pontoon Boat generally had an easterly wind component, with most observations coming from the E/SE directions and tended to occur in the early-midafternoon period (**Figure 3.3.8**). The UH Pontoon Boat dock location on the shoreline of West Galveston Bay points towards the bay as the upwind direction for these observations and the timing is coincident with a typical bay breeze flow reversal from offshore to onshore winds. The shrimp boat, docked at Smith Point on the east side of Galveston Bay, recorded the majority of greater than 70 ppbv ozone observations coming from the NW direction, observations that point back towards the HGB region which would have been transported over Galveston Bay. The Red Eagle, docked on the North side of Galveston Island, observed a distinct bimodal distribution of greater than 70 ppbv ozone in the 5-minute docked data. High ozone values detected at the Red Eagle came from the N/NE and S/SW, these directions line up with Galveston Bay and the Gulf of Mexico as areas the air masses traveled over and interacted with respectively. The high ozone advected from the direction of the Gulf of Mexico in the late afternoon and early evening was associated with a late-developing Gulf Breeze.

3.4 Biomass Burning Influence on High Ozone Days

3.4.1 Summary and Key Findings

We identified several days in September with biomass burning (BB) influence using the same methodology as the TCEQ BC2 network (Black and Brown Carbon).

- September 7–11:
  - When temporally compared with peak ozone, the September 7–11 time period of frequent biomass burning influence overlaps with an extended time period of elevated ozone (September 7–11). **Figure 3.4.1** highlights ozone concentrations and BB influence identified both by the measurements at Battleground for TRACER-AQ as well as synoptic measurements from the BC2 network for the same time period (Aldine and Galveston). AAE above the brown carbon threshold at Aldine, Galveston and Battleground adds confirmation to a Houston-scale event, and not a local site event.
  - The NOAA smoke and HYSPLIT back trajectories indicate that the region had smoke cover during September 7–11 and back trajectories travel through smoke-impacted regions.
- September 21–26:
  - This period of increasing ozone across Houston also had high AAE/BB influence at both Battleground and Aldine (**Figure 3.4.2**).
  - The NOAA HMS smoke and HYSPLIT back trajectory analysis (**Figure 3.4.7**), indicate that there was not consistent smoke overhead in Houston, but air masses did travel through smoke- and fire-impacted regions before arriving at Aldine and Battleground.
- Further investigation is needed to understand the mechanism of impacts for BB influence on ozone chemistry in the Houston area. For both the September 10–11 and September 22–26, the aerosol identification of BB occurred the night before an elevated ozone event.
- Additional investigation is needed for September 3–6 (see results) as there is potentially overlapping Saharan dust and BB events just prior to the peak ozone day on September 6 (***Figure 3.4.3***). The AAE has sustained enhancement, which is often is often indicative of Saharan dust and the back trajectories indicate periods of intersection with fire and smoke in Louisiana.

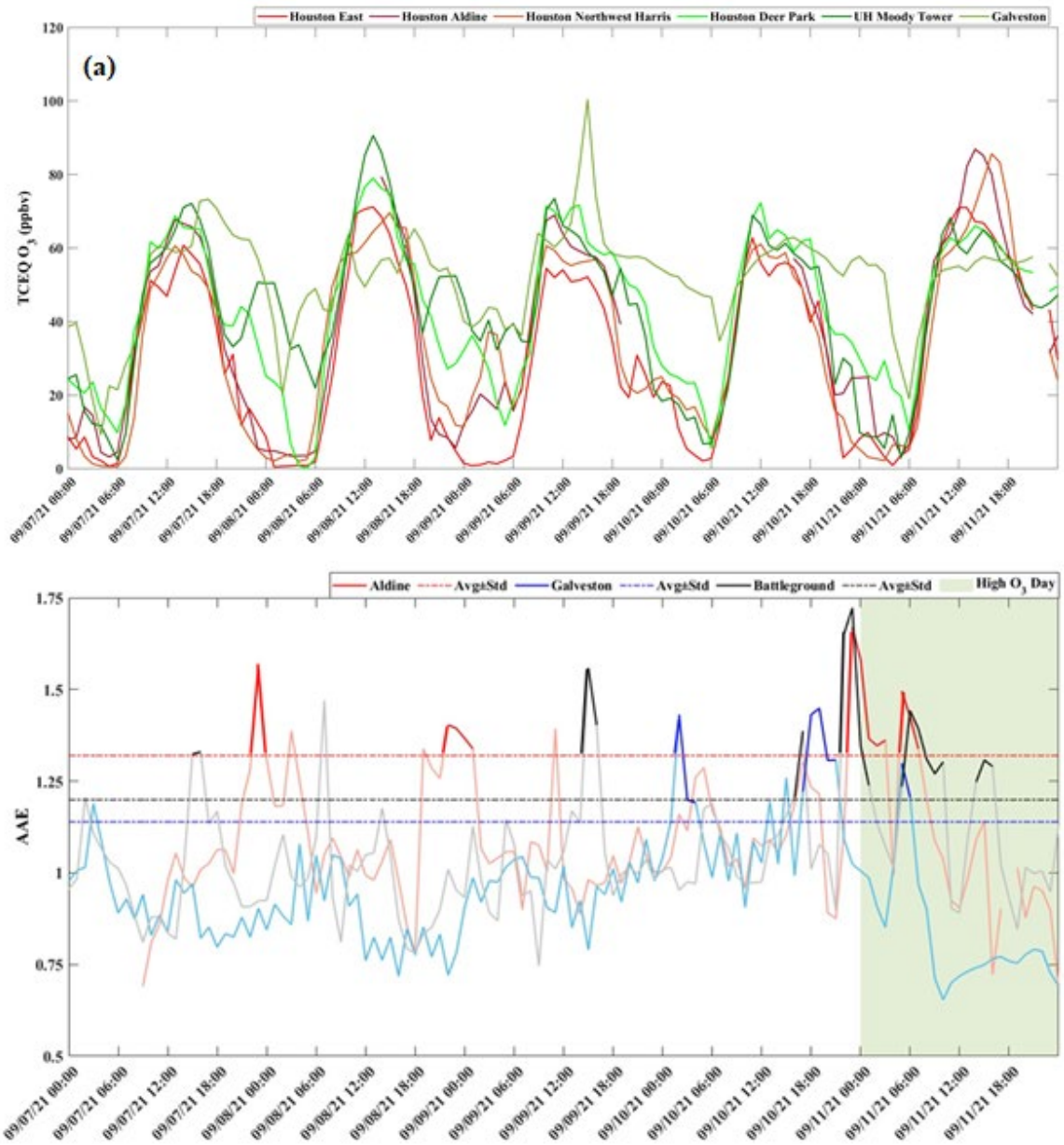

Figure 3.4.1: *Time series of (a) O3 concentrations reported by TCEQ sites in Houston; (b) AAE observed at Battleground during TAQ1 and at BC2-sites in Houston from September 7 to September 11. The highlighted area in green indicates a high O3 day reported by TCEQ monitor at Aldine. Bold lines for the AAE indicate times when that site was above the threshold for BB identification.*

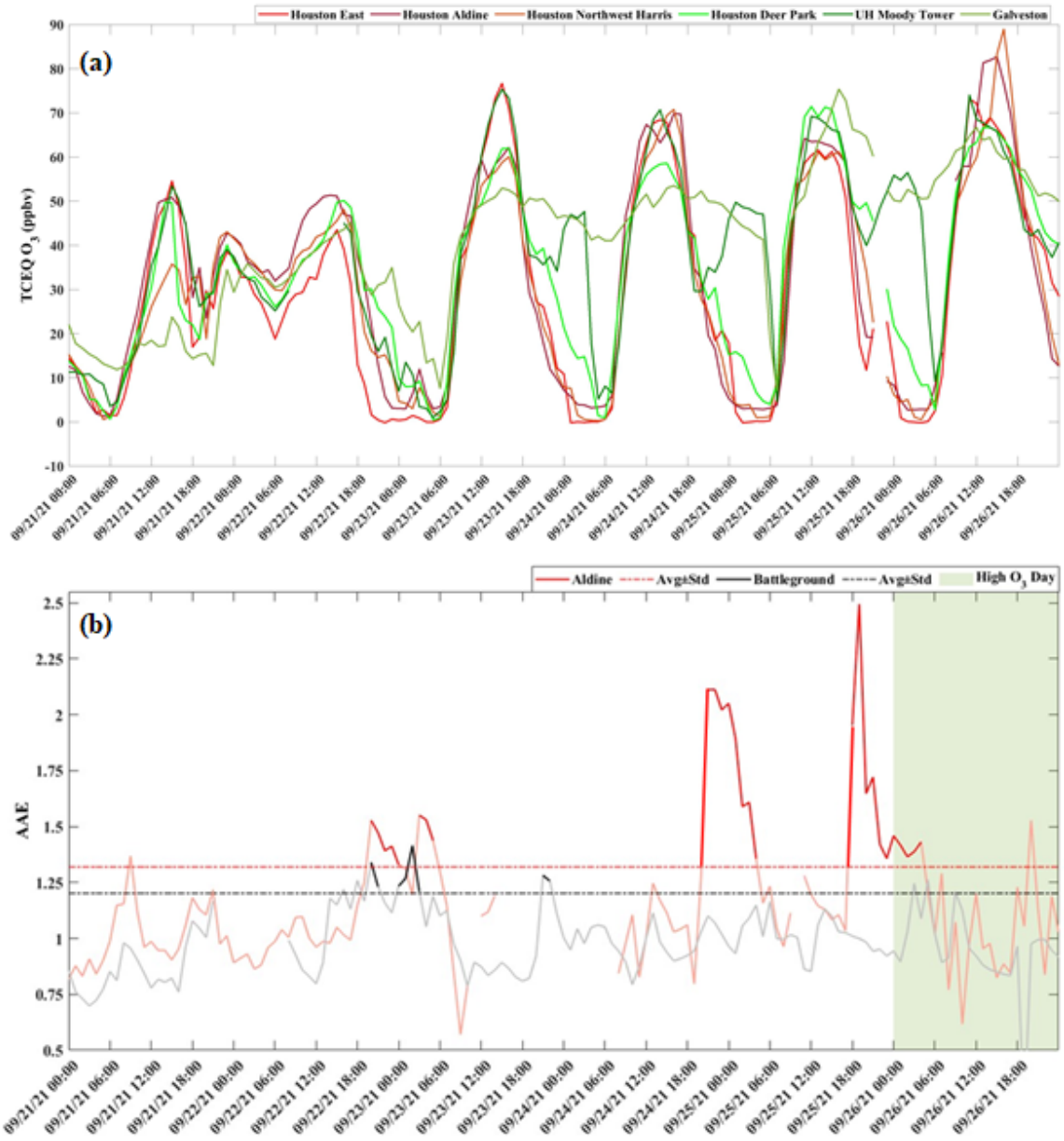

Figure 3.4.2: *Time series of (a) O_3 concentrations reported by TCEQ sites in Houston; (b) AAE observed at Aldine and Battleground during TAQ1 from September 21 to September 26. The highlighted area in green indicates a high O_3 day reported by TCEQ monitor at Aldine.*

3.4.2 Methodology

To assess the potential influence of biomass burning during September of the TRACER-AQ campaign, we employed the same methodology as in the BC2 network. This utilizes real-time aerosol optical measurements, calculation of Angstrom exponents (absorption and scattering; AAE and SAE, respectively), preliminary assessment of smoke cover using NOAA HMS fire and smoke products (https://www.ospo.noaa.gov/Products/land/hms.html#maps), and back trajectory analysis.

3.4.3 Results

A table of identified BB days is included below. Each set of days is then followed by graphs comparing BB influence by AAE with ozone across Houston, and then maps of NOAA smoke and fire products with back trajectories. Each event period is discussed briefly in the caption.

Start	Stop	Average AAE	AAE Threshold	Average SAE	SAE Threshold	GAL event?	LIB event?	HMS overhead	BT through smoke	Filter sample
9/8/2021 19:25	9/9/2021 1:30	1.34	1.32	1.78	1	Y	N/a	Y	Y	Y
9/10/2021 22:35	9/11/2021 2:20	1.48	1.32	1.86	1	Y	N/a	Y	Y	Y
9/17/2021 20:10	9/18/2021 0:30	1.49	1.32	1.58	1	N/a	N/a	Y	Y	N
9/18/2021 21:00	9/19/2021 2:40	1.37	1.32	1.58	1	N/a	N/a	Y	Y	N
9/22/2021 19:25	9/23/2021 6:20	1.41	1.32	1.67	1	N/a	N/a	N	N	N
9/24/2021 20:50	9/25/2021 4:35	1.7	1.32	1.79	1	N/a	N/a	N	Y	N
9/25/2021 18:10	9/26/2021 4:55	1.47	1.32	1.95	1	N/a	N/a	N	Y	N
9/10/2021 01:40	9/10/2021 04:50	1.27	1.18	1.72	1	Y	N/a	Y	Y	Y
9/10/2021 16:55	9/10/2021 22:55	1.47	1.18	1.75	1	Y	N/a	Y	Y	Y
9/4/2021 13:00	9/5/2021 1:00	1.44	1.2	N/a	1	N/a	N/a	N	Y	N
9/5/2021 18:00	9/5/2021 21:00	1.23	1.2	0.59	1	N/a	N/a	N	Y	N
9/10/2021 16:00	9/11/2021 2:00	1.43	1.2	2.13	1	N/a	N/a	Y	Y	N
9/11/2021 5:00	9/11/2021 11:00	1.33	1.2	1.93	1	N/a	N/a	Y	Y	N
9/11/2021 14:00	9/11/2021 17:00	1.28	1.2	2.07	1	N/a	N/a	Y	Y	N
9/12/2021 1:00	9/12/2021 4:00	1.33	1.2	2.16	1	N/a	N/a	Y	Y	N
9/13/2021 13:00	9/14/2021 5:00	1.65	1.2	0.48	1	N/a	N/a	N	Y	N
9/18/2021 17:00	9/18/2021 22:00	1.33	1.2	1.92	1	N/a	N/a	Y	Y	N
9/22/2021 16:00	9/22/2021 22:00	1.26	1.2	2.19	1	N/a	N/a	N	N	N
9/23/2021 0:00	9/23/2021 4:00	1.28	1.2	2.12	1	N/a	N/a	N	Y	N

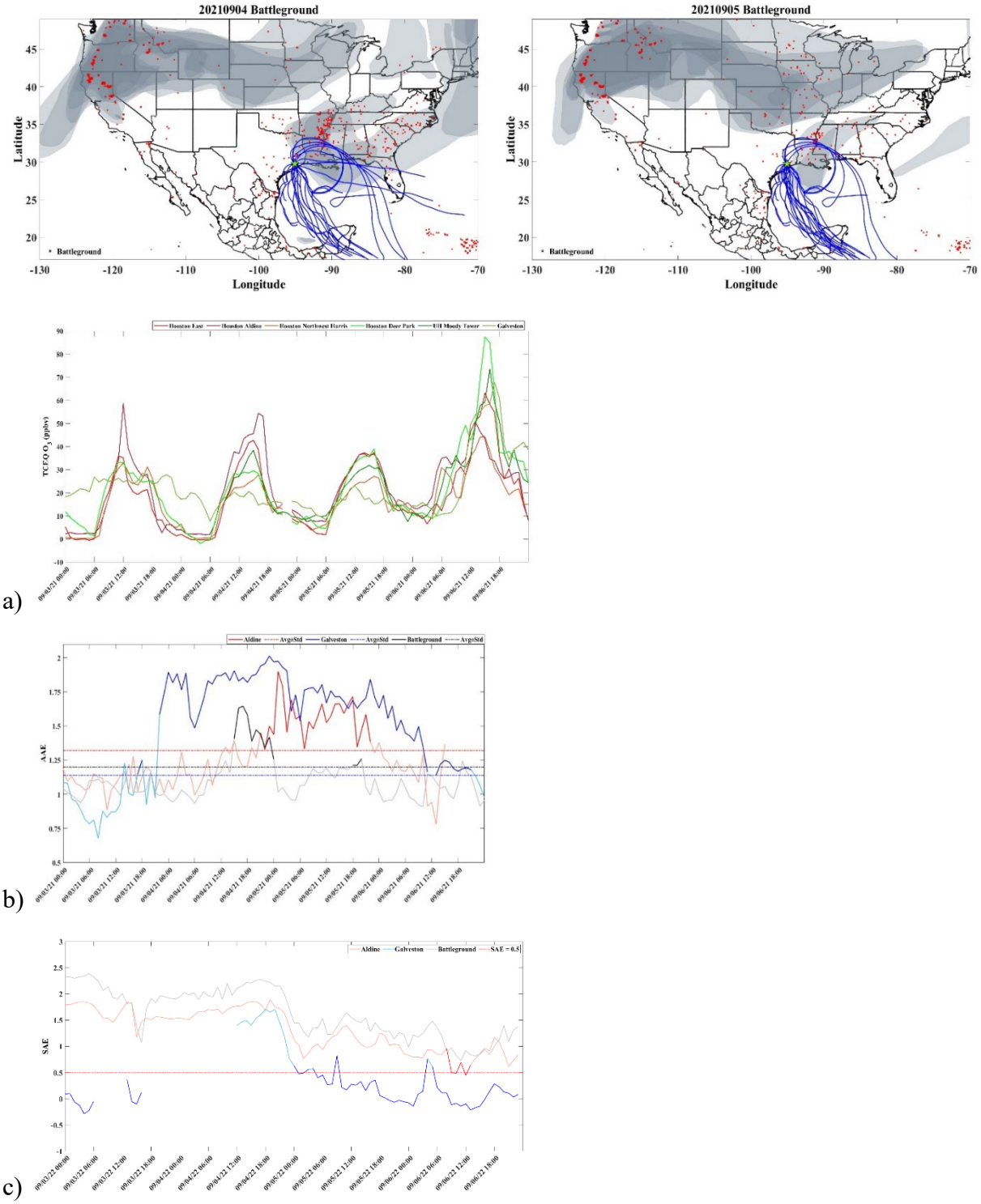

Figure 3.4.3: *Back trajectories, HMS smoke cover and open fire spots for September 4-5 at Battleground. Time series of (a) O_3 concentrations reported by TCEQ sites in Houston (Houston East, Aldine, Houston Northeast, Deer Park, UH Moody Tower, and Galveston); (b) AAE observed at Battleground during TAQ1 and at BC2-sites in Houston (Aldine, Galveston and Battleground). There was a long Saharan dust period of influence in this time period, but the HMS and back trajectory indicates potential overlapping smoke influence at the same time. The Scattering Angstrom Exponent (SAE), an indicator of relative size,*

is included in panel (c); a dust event is evident at Galveston only for Sept 5-6 (tan box). Although there is missing data, the higher SAE and high AAE overnight on Sept 4 likely indicates BB. This is confirmed by back trajectories on September 4 which also indicate air mass transport over fire and smoke regions in Louisiana. The elevated AAE at Aldine and Battleground includes no low SAE, so these periods are only impacted by BB at those two sites. Particularly since there is an ozone event on 9/6, this time period needs additional evaluation.

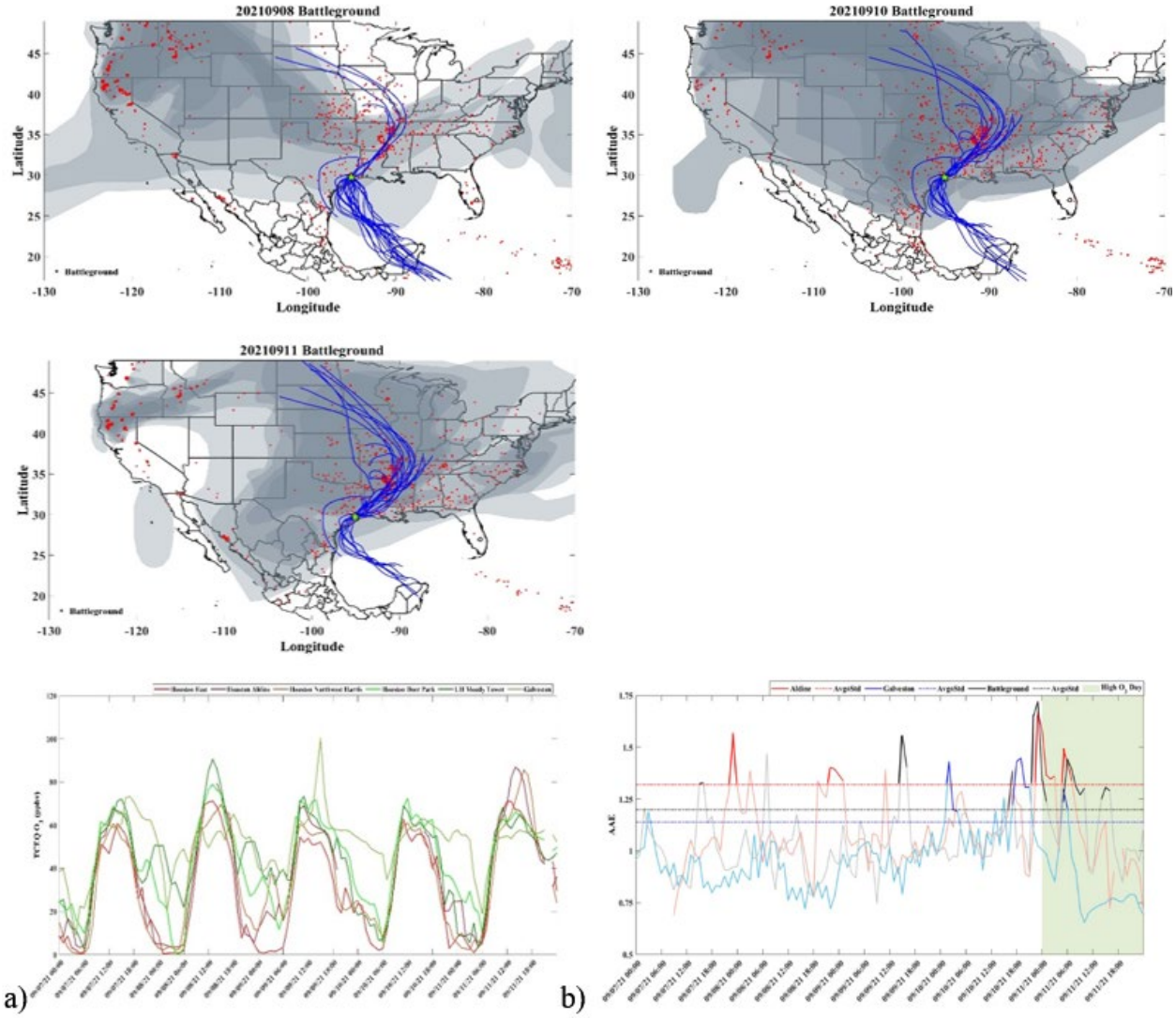

***Figure 3.4.4: Back** trajectories, HMS smoke cover and open fire spots for September 7-11 at Battleground. Ozone (Houston East, Aldine, Houston Northeast, Deer Park, UH Moody Tower, and Galveston) and AAE (Aldine, Galveston and Battleground) for select Houston sites (a and b, respectively). There was constant smoke cover in the HMS and the AAE had frequent exceedances of threshold for BB identification in this time period.*

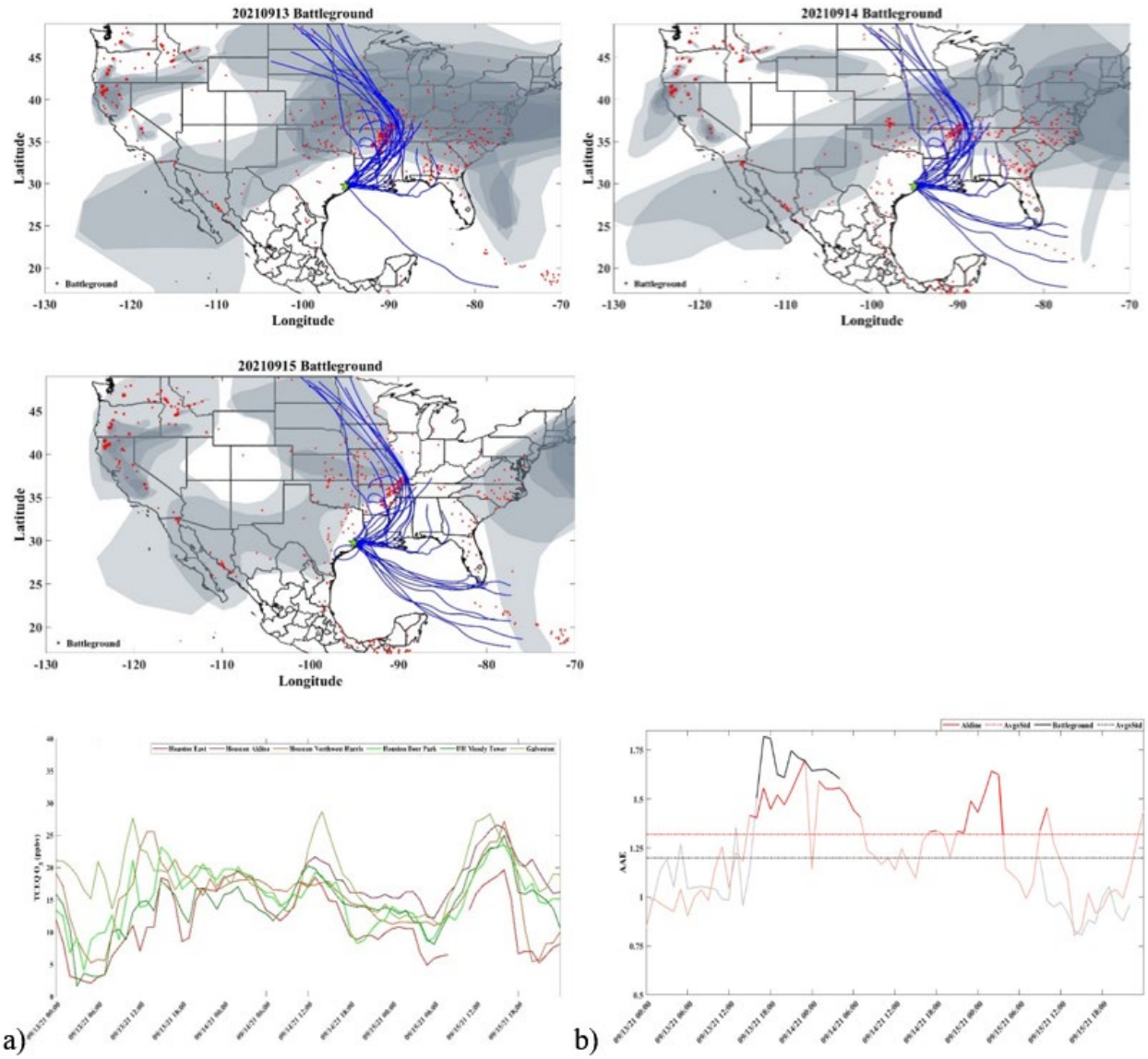

Figure 3.4.5: *Back trajectories, HMS smoke cover and open fire spots for September 13 – 15 at Battleground. Time series of* ***(a)*** *O_3 concentrations reported by TCEQ sites in Houston (Houston East, Aldine, Houston Northeast, Deer Park, UH Moody Tower, and Galveston);* ***(b)*** *AAE observed at Battleground during TAQ1 and at BC2-sites in Houston (Aldine, Galveston and Battleground). There was influence of BB at Aldine and Battleground during this period, but the ozone was not elevated.*

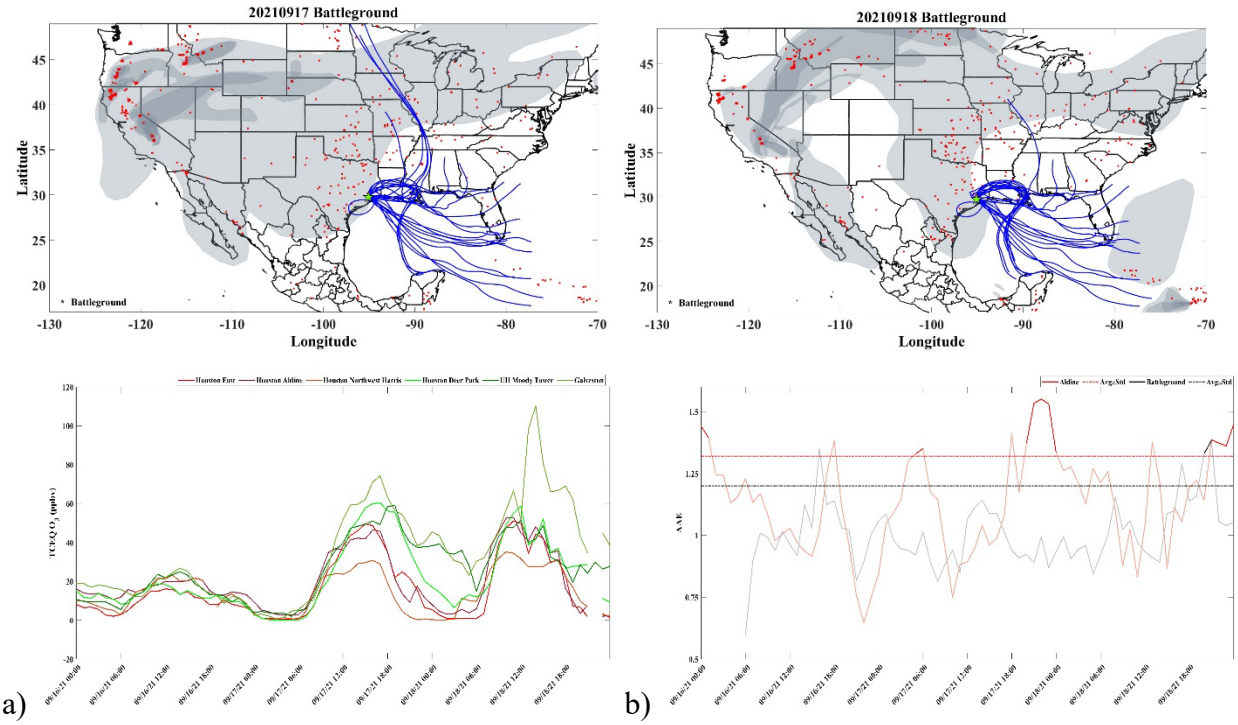

Figure 3.4.6: *Back trajectories, HMS smoke cover and open fire spots for September 17-18 at Battleground. Time series of (a) O3 concentrations reported by TCEQ sites in Houston (Houston East, Aldine, Houston Northeast, Deer Park, UH Moody Tower, and Galveston); (b) AAE observed at Battleground during TAQ1 and at BC2-sites in Houston (Aldine, Galveston and Battleground). There was evidence of BB at Aldine intermittently during this period and the ozone was elevated across Houston, particularly in Galveston.*

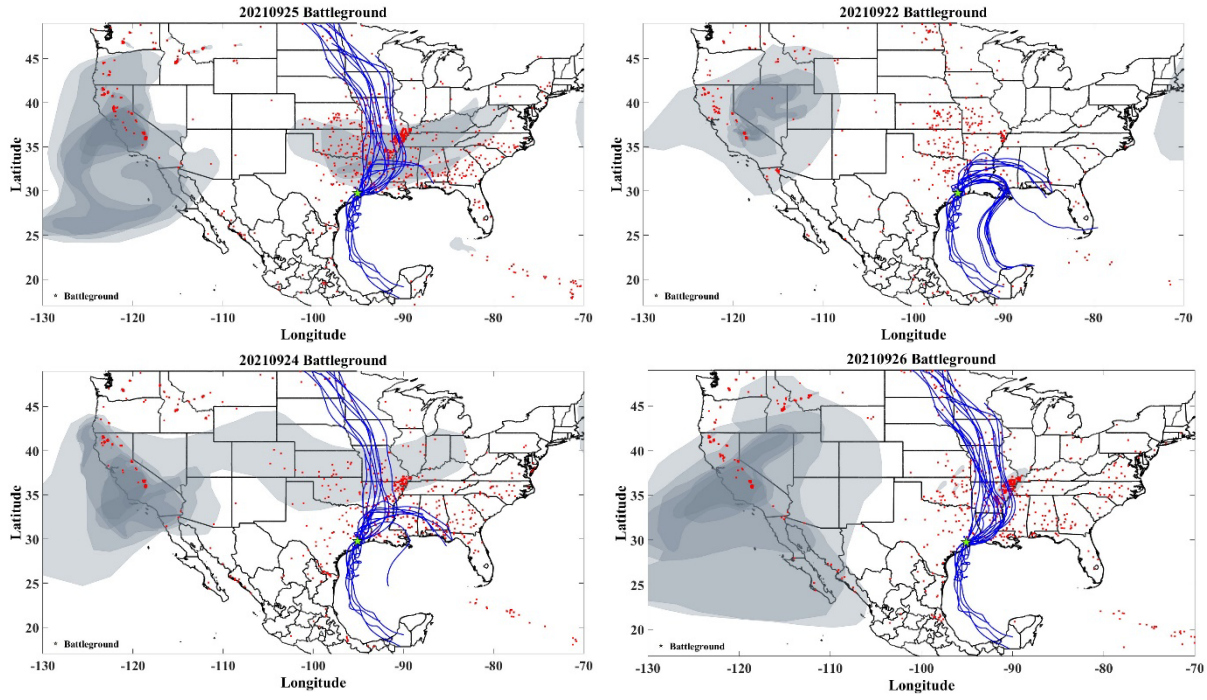

a)

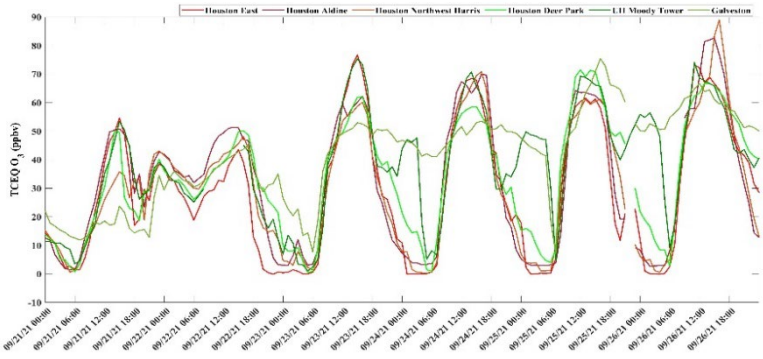

b)

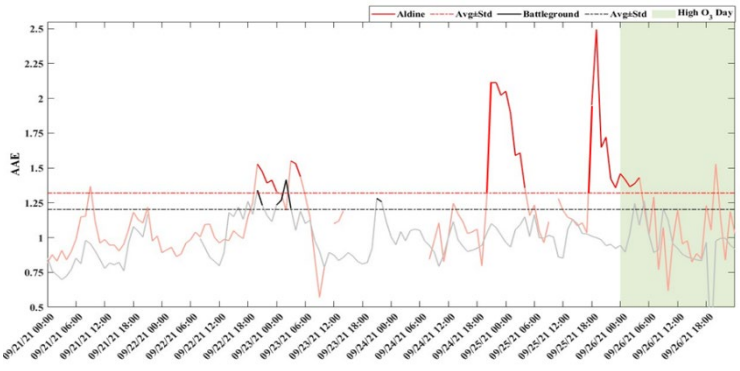

Figure 3.4.7: *Back trajectories, HMS smoke cover and open fire spots for September 22-26 at Battleground. Time series of* ***(a)*** *O_3 concentrations reported by TCEQ sites in Houston (Houston East, Aldine, Houston Northeast, Deer Park, UH Moody Tower, and Galveston);* ***(b)*** *AAE observed at Battleground during TAQ1 and at BC^2-sites in Houston (Aldine, Galveston and Battleground). There was evidence of BB at both Aldine and Battleground during this time period and extended elevated ozone across Houston. Back trajectories show that air masses crossed through smoke plumes, but there was not consistent smoke above the sites.*

3.5 Historical analyses of Houston air quality conditions, and comparisons to TRACER-AQ 2021 (Mark)

3.5.1 Summary and Key Findings

- The TRACER-AQ study had several ozone episodes during June-September 2021, but their frequency and intensity were not anomalous. Based upon wind run data, wind conditions were more conducive to ozone formation than 2000 or 2013, but about the same as 2006. Even though the winds were similar in 2006 and 2021, the intensity of high ozone episodes in 2006 was much greater than in 2021. The field study with the least ozone-conducive conditions, based upon wind run, was TexAQS 2000, but it had the most intense and frequent high ozone days. Its intensity can be attributed to the lack of ozone precursor controls in HGB, and the higher background ozone.
- Only one of the ozone episodes during TRACER-AQ 2021, 24–27 September 2021, followed the post-frontal ozone episode pattern observed in previous studies. The other events appear to have arisen due to waning influence from the Bermuda High, which resulted in weak surface pressure gradients and thus stagnant conditions.
- VOC observations indicate that concentrations of most HRVOCs have dropped substantially since 2004, but after 2010 the concentrations have remained steady aside from small interannual variations. Most sites and VOCs also observed a drop in 2020, followed by a rise in 2021; this pattern can be attributed to the pandemic and its consequences.
- At Milby Park, 1,3-butadiene concentrations have remained high at the 95th percentile level for the entire measurement period. Lynchburg Ferry has observed high ethene and propene at the 95th percentile level in recent years, though there were improvements early in the data record. Other sites have shown a steady decline. Auto-GCs in the eastern part of the Ship Channel have shown unusual patterns in isoprene concentrations that suggest an anthropogenic source of isoprene is present. All other sites have exhibited isoprene behavior consistent with biogenic emissions. Aromatic compounds with high reactivity such as xylenes do not appear to be increasing with time, nor do they show spiky behavior consistent with large emission events.
- The TRACER-AQ field campaign did not measure most of the radicals or radical precursors needed to make a direct, quantitative comparison to previous field campaigns. However, the photochemical grid modeling carried out by Wang et al. provided a way to compare some of the chemical characteristics of the high ozone days. To facilitate the comparison to the TexAQS 2006 period, the results from a TCEQ high resolution photochemical grid modeling exercise were accessed. The comparison among these episodes suggests slower ozone production in 2021 than in 2006, but similar spatial patterns of VOC- and NOx-sensitivity. The comparison of 2021 episodes to 2013 data indicates similar temporal patterns of VOC- and NOx-sensitivity.

3.5.2 Methodology

For previous field campaigns, there has usually been an effort by the TCEQ or others to examine how the weather and trace gas concentrations during days of the field campaign compare to the historical record. The results of a field campaign are more broadly applicable to the overall air quality situation in a city if they were gathered during typical conditions instead of unusual or extreme conditions. The following analyses are intended to determine the conditions in the Houston-Galveston-Brazoria area, and whether these conditions were reasonably representative of the conditions usually experienced during the summer months. The conditions, or the state of the urban atmosphere, have been evaluated in these analyses using trace gas data collected by the TCEQ and its partners in the HGB area, particulate matter data, and meteorological data.

Another question that can be answered with such a historical analysis is whether the concentrations of pollutants or their precursors have changed substantially over the analysis period.

The historical field campaigns examined are Texas Air Quality Study (TexAQS) 2000, TexAQS 2006, SHARP 2009, DISCOVER-AQ 2013, and TRACER-AQ 2021. SHARP 2009 took place during the spring months, which makes this study less representative of the late summer months of the TRACER-AQ study; hence the SHARP 2009 field campaign results are not always included.

3.5.2.1 Monitoring stations

For ozone monitoring, data from stations with nearly complete observational records back to 2000 were used. **Table 2.1** shows which stations are included in ozone and wind analyses.

Table 3.6: *Monitoring sites used in ozone and wind analyses in the HGB area. These sites have been in operation continuously since 2000, with only occasional interruptions.*

Site name	TCEQ ID number	Notes
Houston Aldine	C8	
Northwest Harris County	C26	
Galveston Galveston 99th Street	C34 C1034	Moved to different site at the same airport
Deer Park	C35	
Bayland Park	C53	
Conroe Conroe Relocated	C65 C78	Moved to different site in same town

Site name	TCEQ ID number	Notes
Clinton	C403	
North Wayside	C405	Ozone data but no wind data until 2021
Monroe	C406	Ozone data but no wind data
Lang	C408	Ozone data but no wind data
Croquet	C409	
Westhollow	C410	

3.5.2.2 Auto-GC data

For auto-GCs, all valid data were included in the trend analyses. During TexAQS 2000, there were few auto-GCs in operation in the HGB area. Clinton and Deer Park had permanently installed auto-GCs, but the Deer Park monitor was not functioning during part of the TexAQS 2000 study. A third monitor was installed at Bayland Park for part of the summer of 2000, but it was moved to Aldine for the later part of the summer. In 2003 and 2004, the number of auto-GCs vastly increased, with instruments operating at Channelview, Danciger, Mustang Bayou, Lake Jackson, Texas City 34th Street, Milby Park, Wallisville, HRM3, Lynchburg Ferry, and Cesar Chavez High School added to the network, in addition to the monitors at Deer Park and Clinton.

For auto-GC analyses, a data capture rate of at least 70% was required before the data for a chemical species would be included in the analysis. Consequently, several sites that did not meet the criterion were excluded during certain years. Data capture rates suffered most during hurricane years, i.e., in 2008 during Hurricane Ike, and in 2017 during Hurricane Harvey. Likewise, some sites are inherently more vulnerable due to their low elevation or exposure to bodies of water; these sites, especially Lynchburg Ferry, have lower data capture rates than other sites.

Auto-GC target species. Although the TCEQ data download webpages list many target compounds, not all these compounds are quantified and reported. When the auto-GCs began operating in Houston, more compounds were targeted for routine quantification. But as data collection proceeded over months and years, it became obvious that some targeted compounds could not be consistently quantified, for a variety of reasons. These reasons included co-elution of auto-GC peaks, unusually shaped peaks that defied the ability of the automated quantification algorithm to measure, peaks with variable elution times or that swapped positions with other peaks, or compounds that consistently registered undetectable concentrations. Consequently, these compounds were removed from the target list, though not from the databases. For this analysis, all alkene compounds listed in the database were evaluated to determine whether enough data were available for trend analysis. The analysis

found that the following compounds had practically no usable data: isobutene, 3-methyl-1-butene, cyclopentene, 2-methyl-2-butene, 4-methyl-1-pentene, 2-methyl-1-pentene, 1-hexene, t-2-hexene, and c-2-hexene. In addition, a few alkene compounds were no longer quantified after 2004: t-2-pentene, 1-pentene, c-2-pentene. Other compounds that did not have usable data include the following compounds that could be considered high reactivity or important in other ways: all ethyl toluenes, alpha- and beta-pinene. After this examination of the databases, the following compounds were used to calculate trends up to 2021: ethene, propene, 1-butene, t-2-butene, 1,3-butadiene, isoprene, 1,2,3-trimethylbenzene, 1,2,4-trimethylbenzene, 1,3,5-trimethylbenzene, para- and meta-xylene, ortho-xylene. Since c-2-butene is tightly correlated with t-2-butene, it was not analyzed.

3.5.2.3 Wind data from TCEQ sites.

Data from 10 monitoring sites (Table 1) were used to assess the degree of ventilation and stagnation occurring during each day of the four field campaigns studied. The sites were selected because of their high degree of data capture during the field campaigns back to 2000. Hourly wind speed and direction data were converted to u and v vector data. These data were used to calculate daily wind runs (Allwine and Whiteman, 1994) for each monitoring site. The vector addition of each hour of wind data calculates a theoretical distance traveled by an air parcel exposed to the same conditions as the monitoring site for that day. The resulting wind run distance represents how well the site in question was ventilated during the day. The wind run for all sites were averaged together each day to obtain a daily average wind run value for the HGB area. The Galveston site was excluded from this calculation, because wind conditions at that site were substantially different from all other sites included in this analysis, probably because of its coastal location.

Using the wind run data, we can determine whether the wind conditions in the HGB area during the TRACER-AQ study were substantially different from the conditions observed during other field campaigns. Although other variables are also important in determining pollutant concentrations in the HGB area, the wind run at least allows the pollutant data to be interpreted while accounting for winds.

Because the daily wind run requires adding the hourly wind run data, missing data can alter the daily wind run value. Consequently, monitoring sites with more than 5% missing data during June-September were not included in wind run calculations.

In addition to the wind run, the same wind data can be used to ascertain whether the air has been recirculating at a given site. The recirculation index in Allwine and Whiteman (1994), which has a value between 0 and 1, was calculated for each day for each site. A recirculation index of 0 indicates that the wind run and the overall resultant displacement are equal, and therefore the wind has blown in the same direction all day long. A recirculation index of 1 indicates complete recirculation, such that the wind run begins and ends at the same place,

i.e., the overall resultant displacement is zero. Previous internal analyses at the TCEQ by Breitenbach and Mercado, Lambeth et al., and others have shown that recirculation can be a key factor in creating ozone-conducive conditions in Houston.

3.5.2.4 Ozone data

Daily maximum eight-hour ozone data for each monitoring site were used in the analysis of ozone during the field campaigns. The sites available for these analyses are listed in Table 1. The Galveston and Conroe sites were each moved once between 2000 and 2021, but the data from both sites were merged and treated as a single continuous site. These two sites essentially represent the northern and southern boundaries of the HGB domain.

3.5.3 Results

3.5.3.1 Historical ozone comparison

Trend analyses of ozone are readily available from State Implementation Plan documentation and other TCEQ analyses; those will not be repeated here. Instead, the full frequency distribution of MDA8 ozone concentrations will be examined for four field study periods: June-September 2000, 2006, 2013, and 2021. In 2000, the Texas Air Quality Study (TexAQS) 2000 field campaign was carried out during August and September. In 2006, the follow-up TexAQS 2006 field campaign occurred in Houston to examine how the partial implementation of ozone control strategies affected the ozone. In 2013, a field campaign led by the National Aeronautics and Space Administration (NASA) occurred during September, mostly to validate satellite measurements of air pollutants. The 2013 field study was called DISCOVER-AQ (Deriving Information on Surface Conditions from Column and Vertically Resolved Observations Relevant to Air Quality). Finally, the first phase of the TRACER-AQ (Tracking Aerosol Convection Experiment—Air Quality) field campaign took place in 2021; the analyses presented in this report examine the results of that campaign. The June-September period for each of these field campaigns will be analyzed to compare the conditions during TRACER-AQ to its predecessor studies.

In **Figure 3.5.1** below, the maximum daily eight-hour ozone (MDA8) concentrations at each long-term ozone monitoring site (**Table 3.6**) were calculated, and then the overall maximum ozone was selected for each day. By using a subset of monitoring sites that have been operating since 2000, the varying number and spatial distribution of monitoring sites will not affect the maximum concentration shown. For each year, the data were ranked by magnitude, and the ranked data were plotted for each field study period.

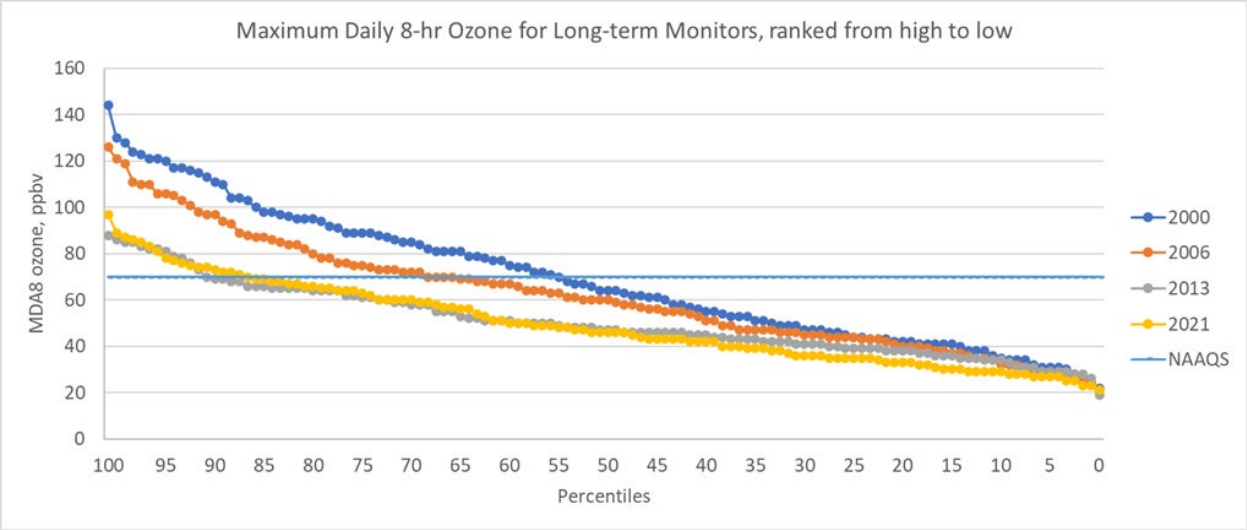

Figure 3.5.1: *Ranked MDA8 concentrations from long-term monitors, for each day from June 1 - September 30 of each year of interest.*

Figure 3.5.1 clearly shows that the highest concentrations were observed during 2000, with the second highest during 2006. For these older periods, the concentrations were much higher above the 35th percentile than for the two newer field campaigns. Concentrations during 2013 and 2021 were very similar to each other through most of the distribution. Note that during 2000, about 45% of the days exceeded the current eight-hour ozone standard of 70 ppbv, but during 2021, only about 15% exceeded.

Background ozone. It is difficult to estimate background ozone. The ideal technique would determine how much of the observed peak ozone in a city has been caused by distant emissions and how much has been caused by local emissions. Answering this question is so important that it is worthwhile to continue to attempt an estimation of background ozone, even if none of the techniques that can be used are ideal. Below are presented the results of a technique described in Berlin et al. (2013). Briefly, this technique examines ozone at monitoring sites at the periphery of a city, then chooses the lowest MDA8 ozone from all these sites as the background. Ideally, the ozone concentrations at this chosen site for that day represent the ozone that would be observed in the location of the city if the city wasn't there. In other words, it represents the ozone concentration that would result if the city's emissions were not contributing. The method may be biased low, because it always chooses the lowest value, so if there are spatial gradients in background concentrations, the method will chose the low end. If the emissions from the city are fully recirculating, the "background" monitor may sample air that contains emissions from the city instead of emissions from outside the city. Finally, coastal sites are sometimes excluded from the analysis because air from the Gulf of Mexico impacts a coastal site but not any other sites in the HGB area, so its low ozone concentration does not represent the background that the rest of the city has been exposed to on that day. An advantage of this technique is that the daily

8-hour concentration should account for the downward mixing of ozone from the residual layer, because it includes a large portion of the day. Techniques that only use an hour or two of surface ozone data, especially in the morning, cannot properly account for that.

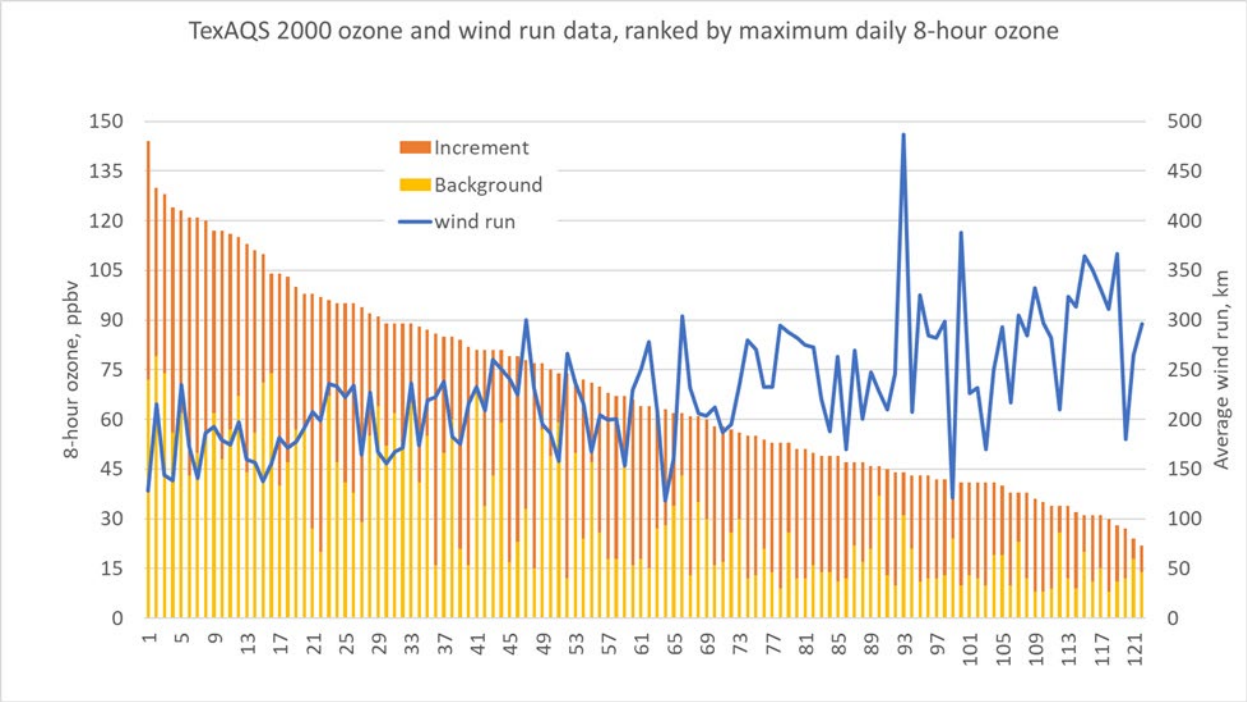

Figure 3.5.2: *Maximum daily ozone, background ozone, incremental ozone, and average wind run for June 1 - September 30, 2000, ranked by long-term site MDA8 ozone.*

Figure 3.5.2 shows data from the TexAQS 2000 study period. The background ozone in yellow bars, the increment between the background ozone and the long-term site MDA8 ozone in orange, and the average wind run, for each day from June 1–September 30 of the year of interest, have all been plotted together. All data have been ranked according to the long-term site MDA8 ozone. The combined height of the background bar plus the increment bar equals the MDA8 ozone as calculated from the long-term sites. **Figure 3.5.2**, **Figure 3.5.3**, and **Figure 3.5.4** show the same data for 2006, 2013, and 2021, respectively.

Note that in all of these figures there is a roughly inverse relationship between MDA8 ozone and wind run, with higher ozone usually observed on days with less local ventilation.

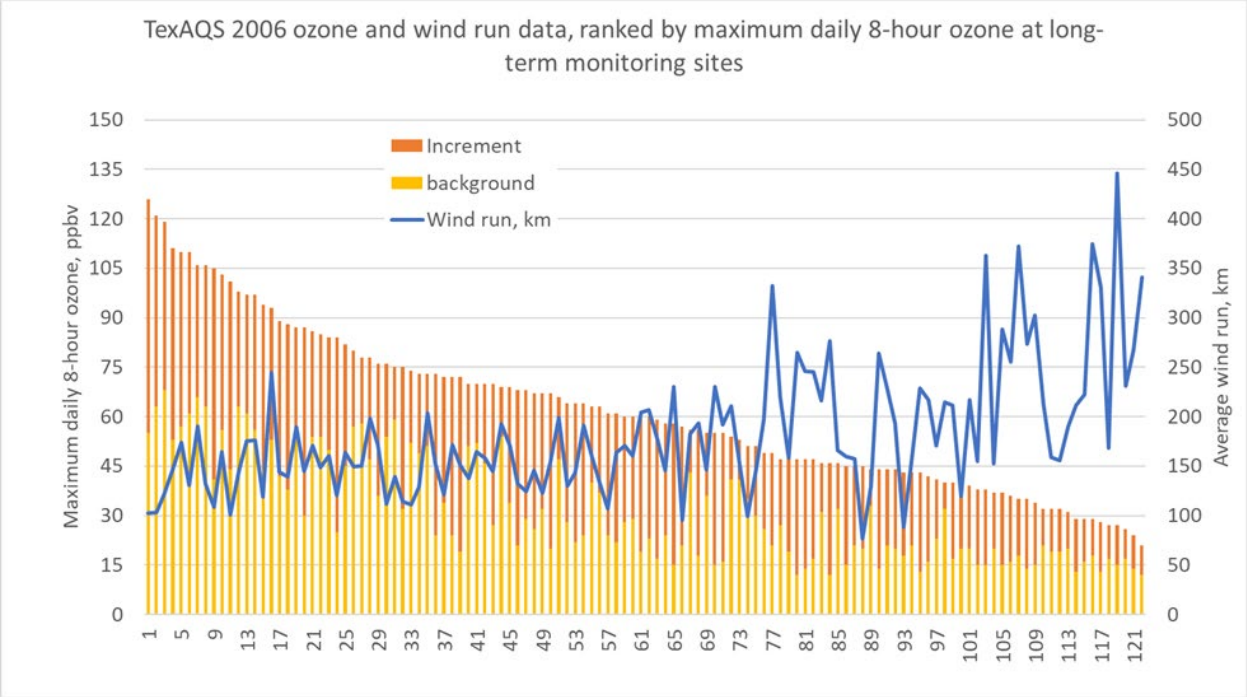

Figure 3.5.3: *Maximum daily ozone, background ozone, incremental ozone, and average wind run for June 1–September 30, 2006, ranked by long-term site MDA8 ozone.*

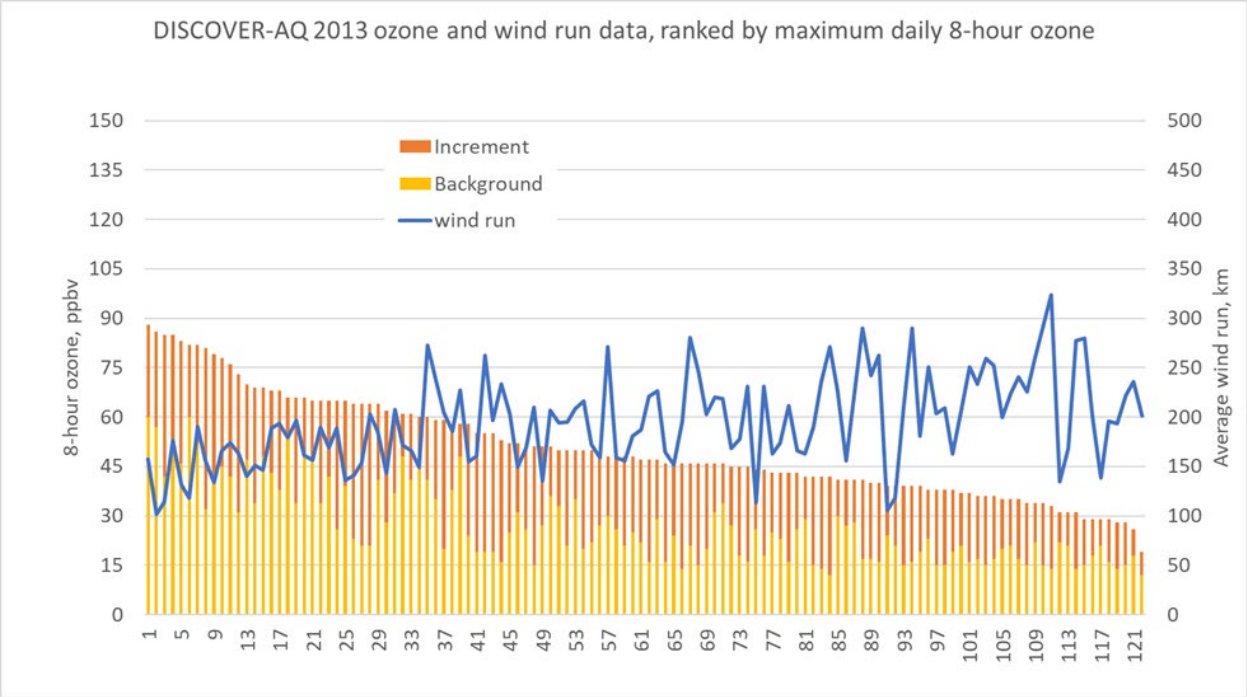

Figure 3.5.4: *Maximum daily ozone, background ozone, incremental ozone, and average wind run for each day from June 1 - September 2013, ranked by MDA8 ozone.*

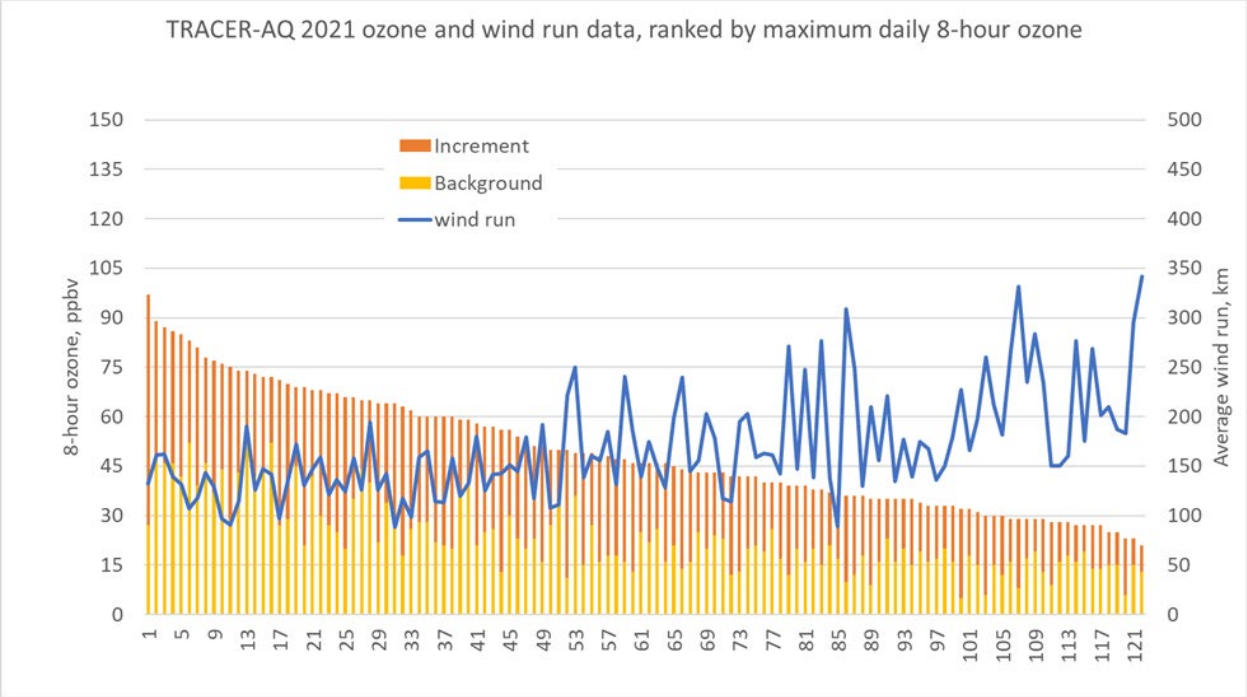

Figure 3.5.5: *Maximum daily ozone, background ozone, incremental ozone, and average wind run for each day from June 1 - September 30, 2021, ranked by MDA8 ozone.*

As expected, MDA8 ozone is highest during 2000 and 2006. The TexAQS 2000 field campaign occurred before major ozone control strategies were implemented in the HGB area. The TexAQS 2006 field campaign took place after some (but not all) of the controls had gone into effect. The DISCOVER-AQ study occurred after the major controls were fully in effect, plus the summer was dominated by southerly flow from the Gulf, and therefore ozone was not especially high during the field campaign. Ozone concentrations during 2021 were of similar magnitude to 2013, even though a larger part of the summer was more conducive to ozone formation.

The TexAQS 2000 study also appears to have observed higher background ozone concentrations than 2013 or 2021. Studies have indicated that background ozone concentrations have been decreasing in the Houston area (Berlin et al. 2013, Cooper et al., Wang et al. 2016, EPA); these data also reflect that decrease.

Maximum ozone appears to be linked to wind run, with the highest concentrations generally associated with wind run values below 150 km, and no high ozone associated with wind runs over 200 km after 2000.

Figure 3.5.6 shows the daily average wind run data for each day for each year, sorted according to daily average wind run. The TexAQS 2000 period had the highest winds, with DISCOVER-AQ 2013 having the second highest, and TexAQS 2006 and TRACER-AQ 2021 having similar wind magnitudes. These data strongly indicate that the high ozone in 2000 was linked to higher emissions, and not to weather conditions that were unusually

conducive to high ozone. Even though the winds were highest during 2000, the concentrations of ozone were also the highest.

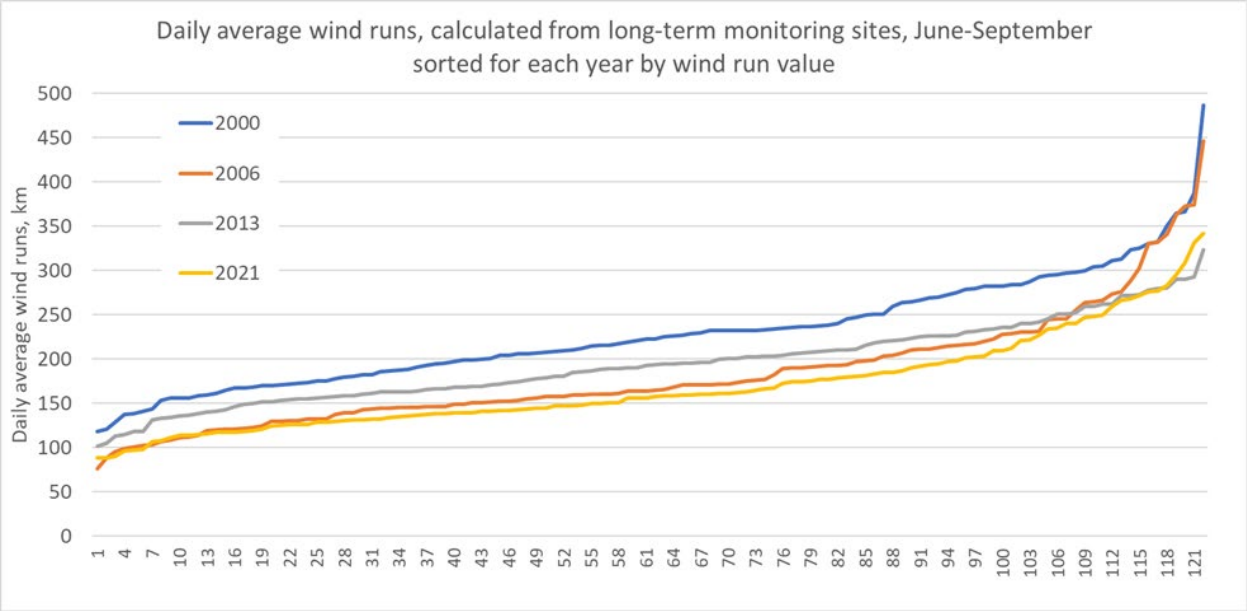

Figure 3.5.6: *Daily average wind runs for each year.*

Given the similarity between the TexAQS 2006 period and the TRACER-AQ 2021 period, as shown in **Figure 3.5.6**, additional analyses were undertaken to test these apparent similarities further. **Figure 3.5.7** shows wind run vs. recirculation index for TexAQS 2006 and TRACER-AQ 2021.

Figure 3.5.7 shows that the wind data from the two years appears to be very similar, with considerable overlap present. By contrast, **Figure 3.5.8** and **Figure 3.5.9** compare 2021 to 2000 and 2013; neither of these two years are as similar to 2021 as 2006. In fact, 2000 shows considerably higher winds than all of the other field campaigns.

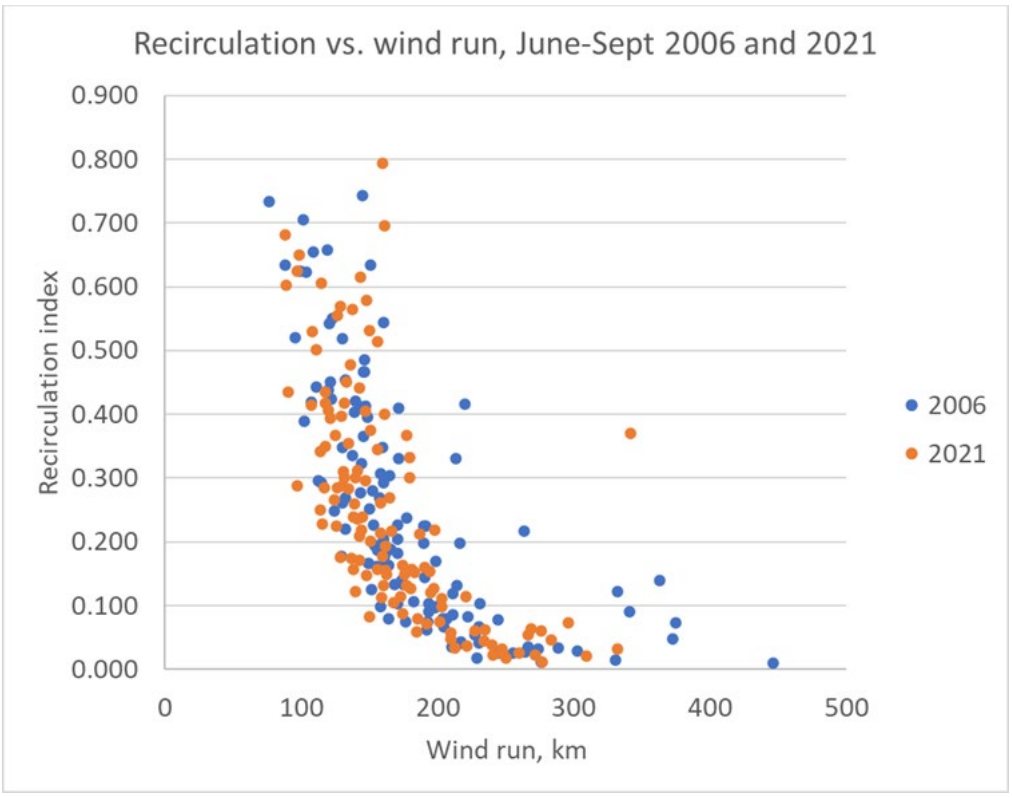

Figure 3.5.7: *Recirculation vs. wind run in 2006 and 2021.*

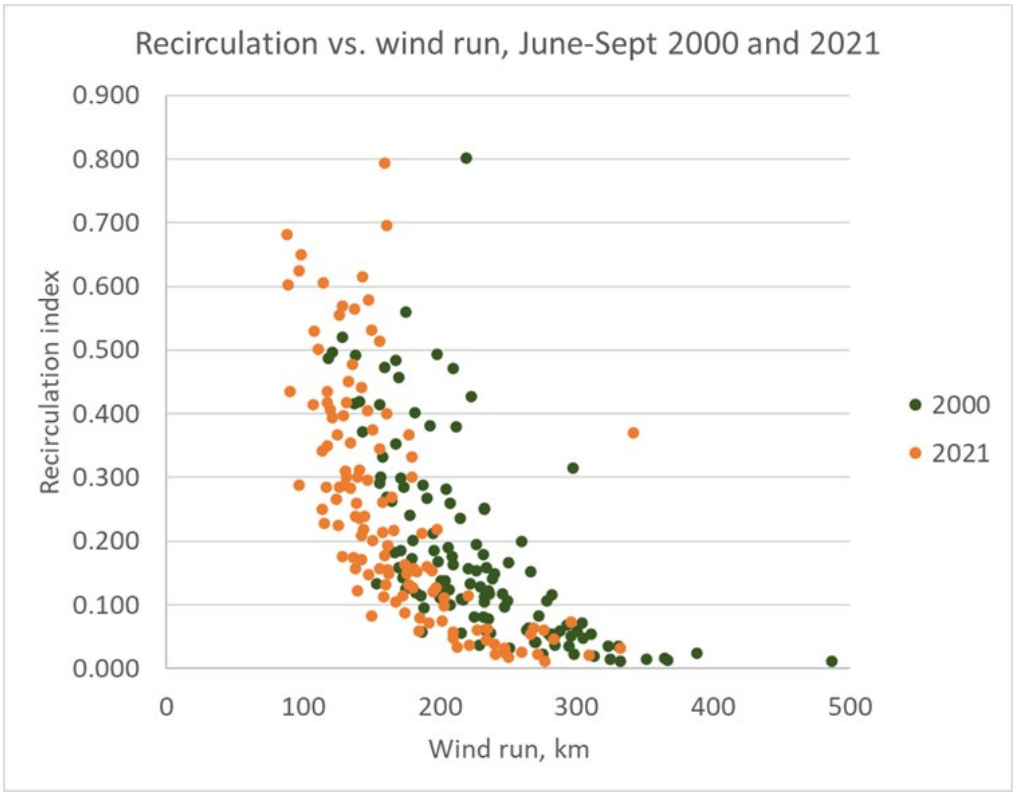

Figure 3.5.8: *Recirculation vs. wind run in 2000 and 2021.*

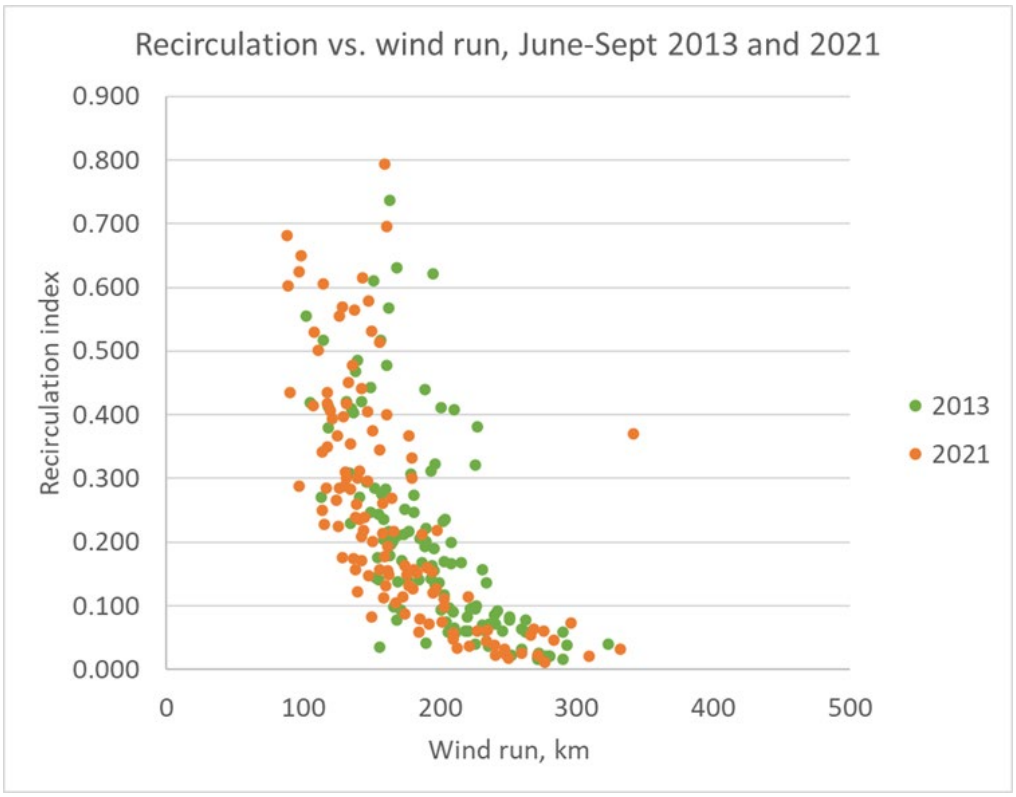

Figure 3.5.9: *Recirculation and wind run in 2013 and 2021.*

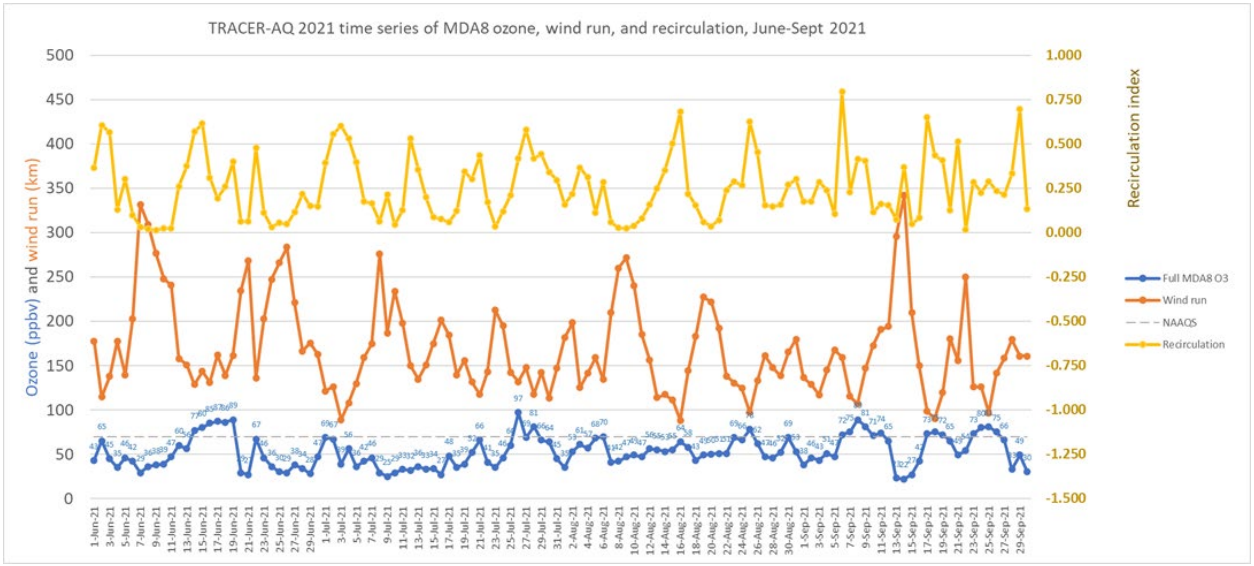

Figure 3.5.10: *Daily comparison of MDA8 ozone from all available sites, wind run, and recirculation index.*

In **Figure 3.5.10**, the relationship between MDA8 ozone and wind conditions is examined in greater detail. Usually, a high recirculation index is linked with lower wind run, and sometimes is linked to higher ozone. The largest wind run days are invariably linked with lower ozone. Whenever high recirculation index and low wind run coincide, the ozone is

almost always elevated, e.g., June 14–15 and 19, July 26 and 28, Aug 16 and 25, September 7–8 and 17–18.

Examination of frontal passages during the period (at https://www.wpc.ncep.noaa.gov/dailywxmap/) indicates that the event on 24–27 September 2021 is the only 2021 event that fits the post-frontal high ozone pattern, as described by Lefer et al. (2010) and Lei et al. (2018). These authors noted that the post-frontal environment offered conditions suitable to local ozone formation (clear skies, subsidence, low synoptic forcing) and higher background ozone (due to flow from the continent instead of the Gulf of Mexico). All other days with high ozone observed very weak surface pressure gradients in HGB, usually due to lack of dominance by the Bermuda High (Wang et al. 2016) or any other synoptic system.

The relationships between wind run, recirculation and high ozone repeat for TexAQS 2006 as well, though they are not always predictive. **Figure 3.5.11** shows the relationships between wind conditions and ozone for June–September 2006. The relationship between wind run and high ozone is stronger than the relationship between recirculation and high ozone. Apparently, recirculation can occur without triggering high ozone (e.g., 11 September 2006), and high ozone can occur without strong recirculation (e.g., 14 September 2006).

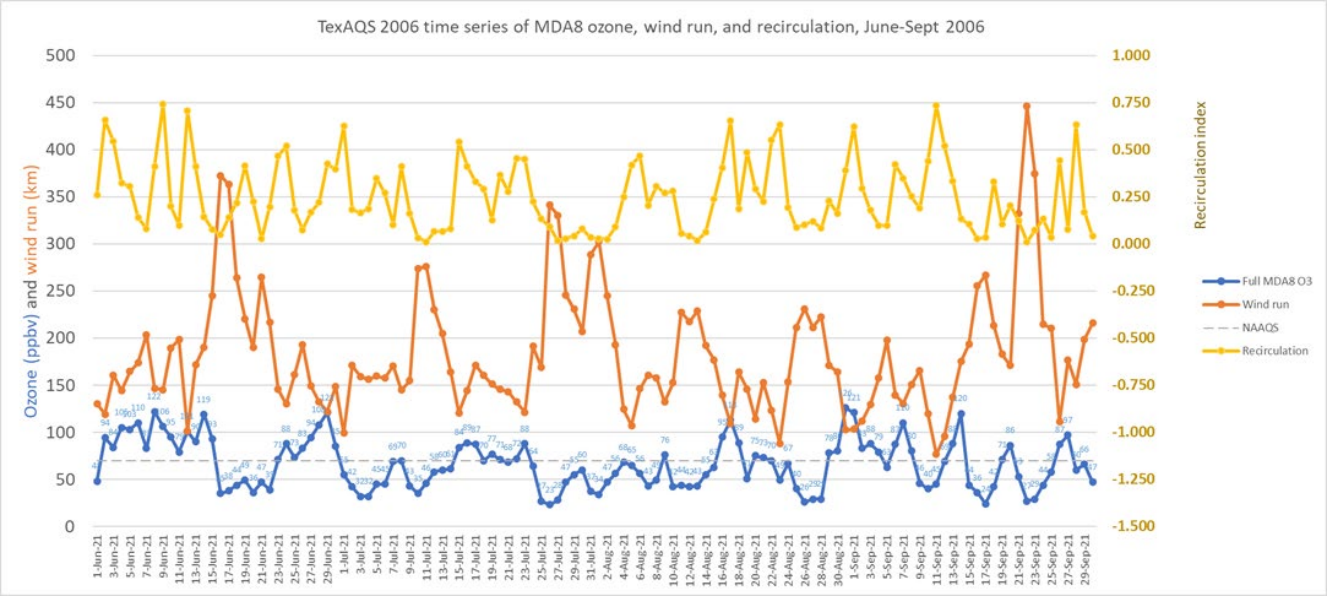

Figure 3.5.11: *Daily comparison of MDA8 ozone from all available sites, wind run, and recirculation index.*

Based upon these analyses, the TRACER-AQ period appears to have been slightly more conducive to ozone than the 2000 and 2013 study periods, but similar in conditions to the TexAQS 2006 study period.

3.5.3.2 Volatile organic compound analyses

The highly reactive volatile organic compounds (HRVOCs) that TCEQ regulates as ozone precursors are ethene, propene, 1-butene, isobutene, c-2-butene, t-2-butene, and 1,3-butadiene. These compounds have been linked to high ozone production (e.g., Ryerson et al. 2003; Daum et al., 2003, 2004; Zhou et al., 2014). The following analyses examine the concentrations of these HRVOCs during 2021, and compares them to observations from previous years.

Table 3.7 shows the automated gas chromatography (auto-GC) sites in HGB, and their abbreviations. Other sites with short data records have not been included in these analyses. Most of the sites listed below have data back to 2004; HRM16, OYCK, CHWT, and GAPK however have been operating for only a few years.

Table 3.7: *Auto-GC abbreviation key*

Site abbreviation	TCEQ ID code	Full name
HRM3	C603	Houston Regional Monitoring 3
LYNF	C1015	Lynchburg Ferry
WALV	C617	Wallisville Road
TX34	C620	Texas City 34th Street
LKJK	C1016	Lake Jackson
CLIN	C403	Clinton
DRPK	C35	Deer Park
MIPK	C169	Milby Park
HCHV	C15	Channelview
HRM7	C607	Houston Regional Monitoring 7
HRM16	C1614	Houston Regional Monitoring 16
OYCK	C1607	Oyster Creek
CHWT	C1036	Channelview Water Tower
GAPK	C1667	Galena Park
CECH	C1020	Cesar Chavez High School

3.5.3.2.1 Ethene

Figure 3.5.12 and **Figure 3.5.13** examine ethene concentrations from HGB auto-GCs between 2004 and 2021. For each chemical species examined, both median and 95th percentile values were calculated. Median values provide the central tendency of the data set without being skewed by unusually large concentrations. The 95th percentile shows some of these high concentrations, which can be associated with emission events due to inefficient flaring or other contingencies (Al-Fadhli et al. 2012; Pavlovic et al. 2012; Webster et al. 2007).

At the beginning of the time series shown in **Figure 3.5.12**, the concentrations are at their highest, especially at the four industrial sites: HRM3, HCHV, LYNF, and CLIN. The median concentrations drop quickly, however, through 2009. After 2010, however, the concentrations do not drop systematically anymore. Although there are year-to-year fluctuations, the concentrations apparently leveled out and created a new baseline after the HRVOC regulations took full effect. Most site experienced a drop in concentrations from 2019 to 2020, and then an increase from 2020 to 2021, back to approximately previous levels. This dip can almost certainly be attributed to the COVID epidemic and its consequences.

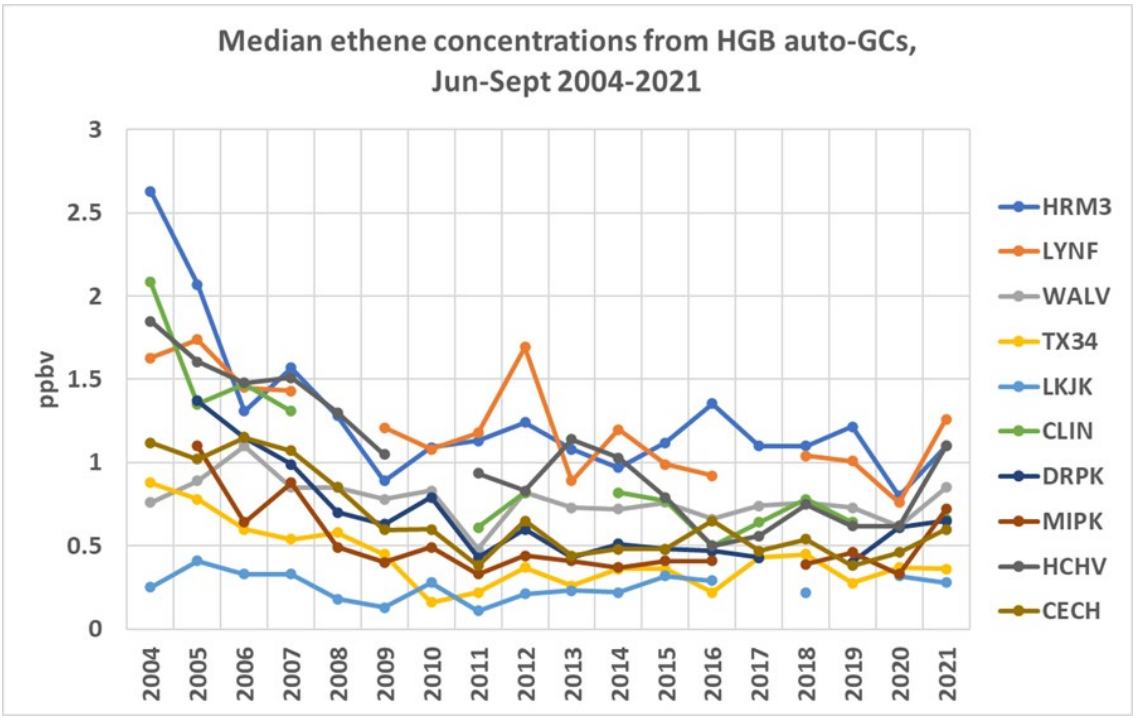

Figure 3.5.12: *Median ethene concentrations observed in HGB during June-September each year from 2004-2021.*

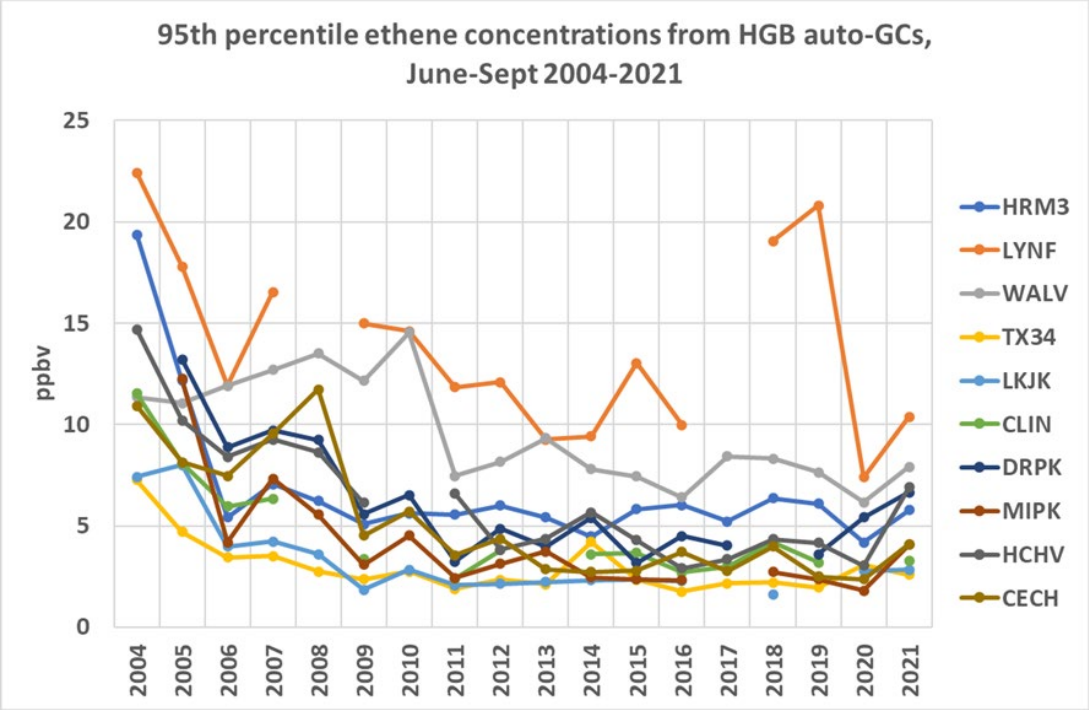

Figure 3.5.13: *95th percentile ethene concentrations observed in HGB during June-September each year from 2004-2021.*

The pattern displayed in **Figure 3.5.12** is somewhat repeated in **Figure 3.5.13**. There are larger differences between two sites (LYNF and WALV) and the other sites, probably because of the proximity of these two sites to ethene emissions. DRPK experienced increases in ethene during 2020 and 2021, in spite of the pandemic. Given this observation, and the extremely high concentrations observed during TRACER-AQ, there may be a new or recently enhanced ethene source in the vicinity of Deer Park or La Porte.

3.5.3.2.2 Propene

Figure 3.5.14 and **Figure 3.5.15** show the trends in propene concentrations in HGB for the past 18 years. Although the propene median concentrations have similar trends overall to the ethene trends, there are a few differences. First, LYNF propene concentrations are considerably higher than other sites almost every year. HCHV concentrations spiked in 2018, but returned to previous levels afterwards. HRM3 concentrations are very high between 2004 and 2010, but drop off to levels matching most of the other sites in later years. For the 95th percentiles, LYNF, WALV, and DRPK are notably higher than other sites, with LYNF continuing to exceed 10 ppbv, nearly twice the concentration of other sites. DRPK is missing a considerable amount of data in 2018 and 2019, which required removing data from the analysis due to poor data capture.

Most sites do not appear to have high propene concentrations, but LYNF and DRPK still have 95th percentile concentrations that have not systematically decreased appreciably since

about 2011. WALV 95th percentile concentrations have been decreasing systematically and continuously since 2004.

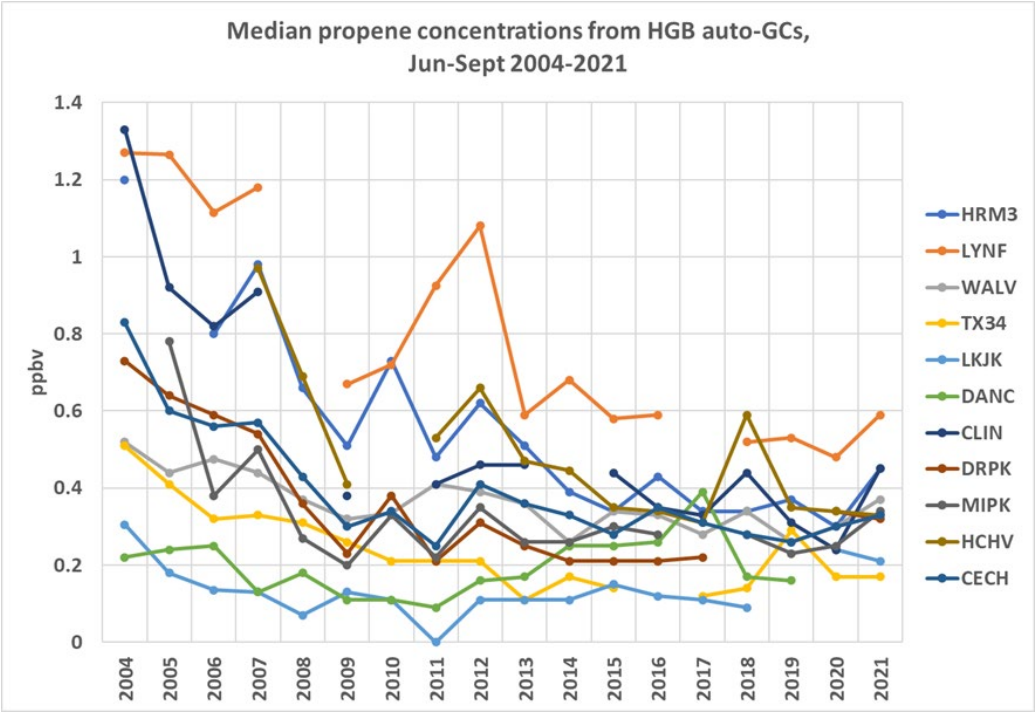

Figure 3.5.14: *Median propene concentrations observed in HGB from June-September each year from 2004-2021.*

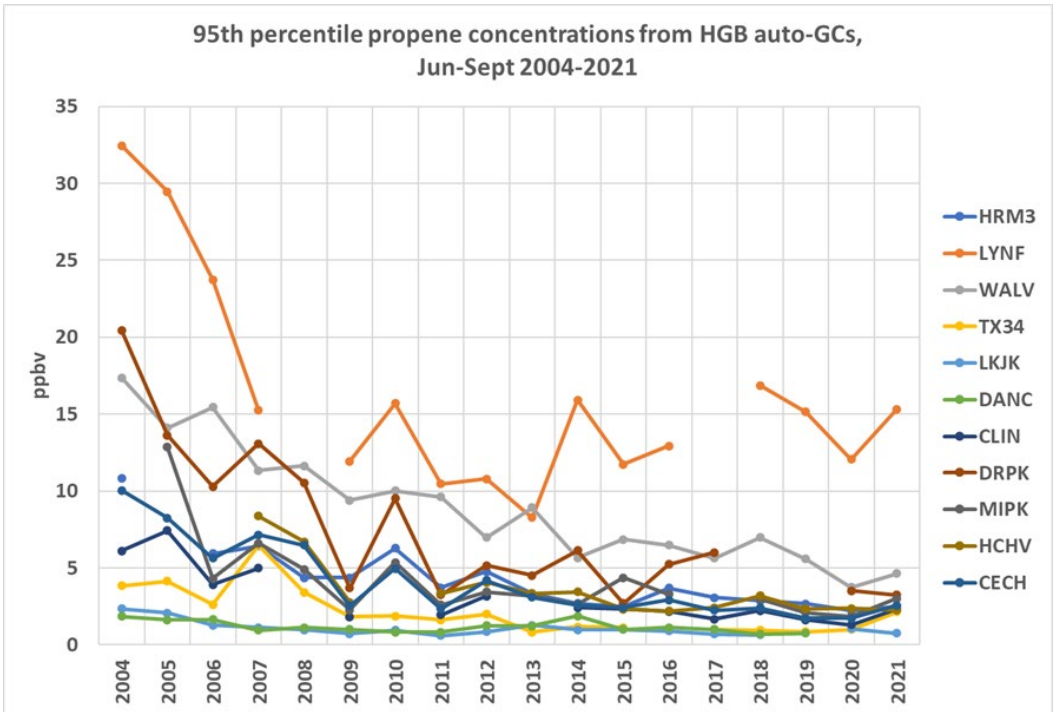

Figure 3.5.15: *95th percentile concentrations observed in HGB from June-September each year from 2004-2021.*

3.5.3.2.3 1,3-butadiene

Concentrations of 1,3-butadiene are usually considerably lower than either ethene or propene. **Figure 3.6.16** and **Figure 3.6.17** show median and 95th percentile trends for the HGB area. The 95th percentile chart has a logarithmic concentration scale because the data have such a huge variation in magnitude. In Figure 16, most sites show a systematic decline in 1,3-butadiene concentrations from 2004 to 2010, and then essentially a steady state from 2010 to 2021. Milby Park, however, shows huge interannual variations in median values. The MIPK site is located near known sources of 1,3-butadiene, but these data suggest that the concentrations experienced at this site have not diminished appreciably during the data record. The median concentration in 2021 was only exceeded in 2005 and 2007.

The 95th percentile trend chart in **Figure 3.5.16** clearly shows how different MIPK concentrations are compared to the other sites. No downward trend is present in these data. Most sites group together with moderate concentrations (LYNF, WALV, CLIN, DRPK, HCHV, and CECH). These sites show a gradual downward trend from 2004 to 2021. A third group (LKJK, TX34, and DANC) have concentrations far below those of the other sites.

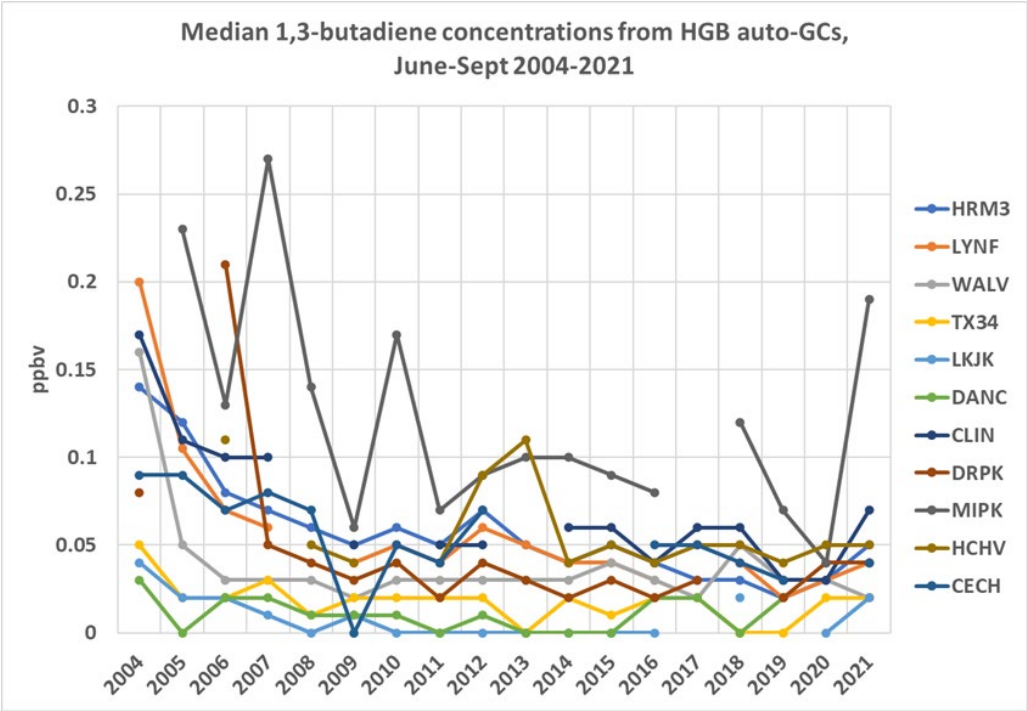

Figure 3.5.16: *Median 1,3-butadiene concentrations in HGB from June-September during 2004-2021.*

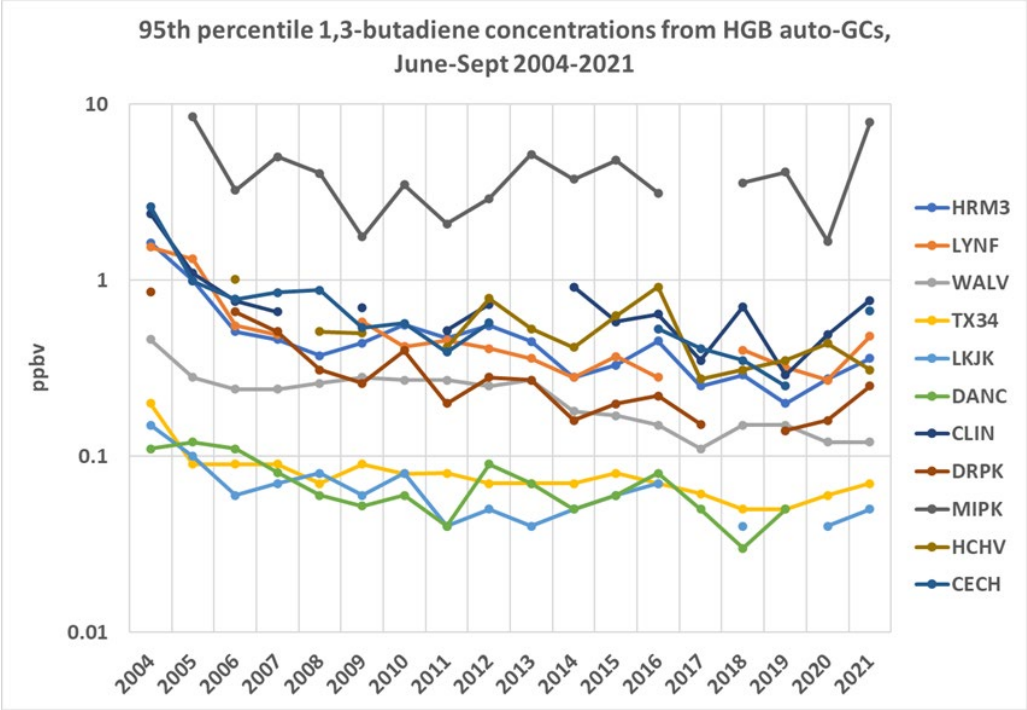

Figure 3.5.17: *95th percentile 1,3-butadiene concentrations in HGB in June-September during 2004-2021.*

3.5.3.2.4 1-butene

Concentrations of 1-butene (and the other butenes) are considerably lower than those of the other HRVOCs. It is possible that the auto-GCs often cannot adequately quantify the concentrations of these compounds. Figure 18 shows the 95th percentile concentrations of 1-butene.

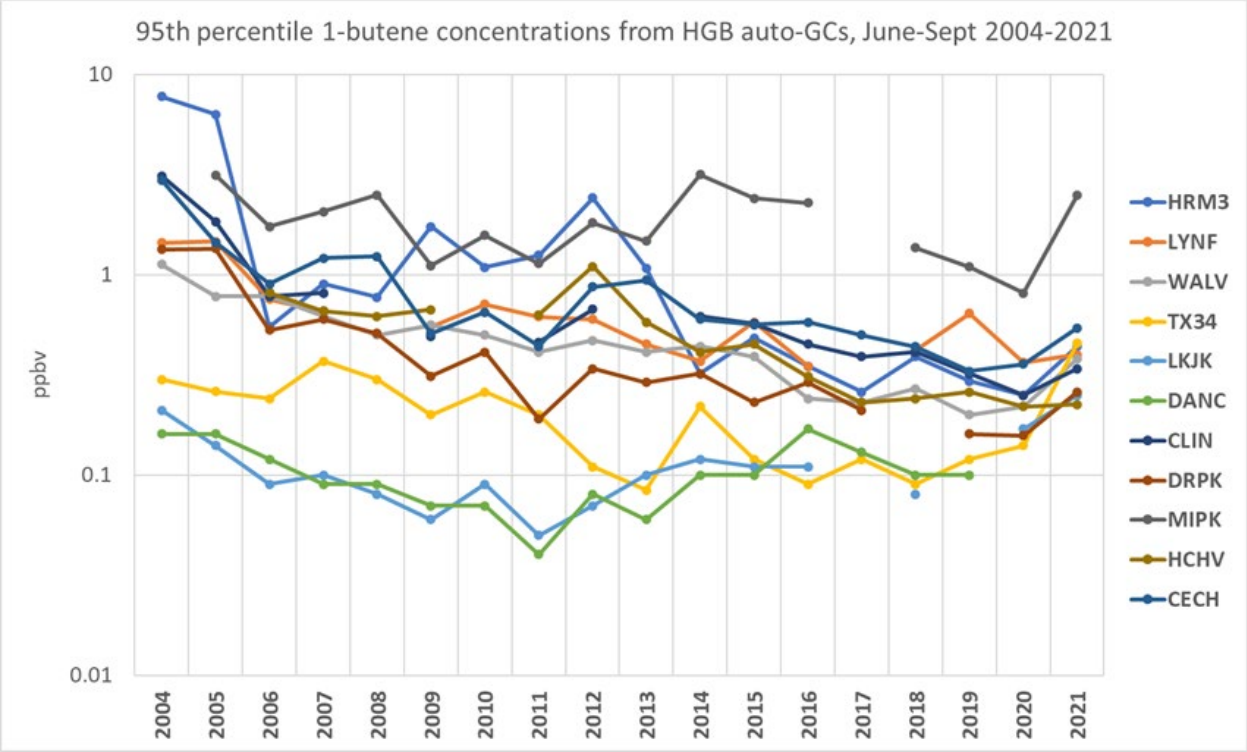

Figure 18: 95th percentile 1-butene concentrations in HGB from June-September during 2004-2021.

From 2004 to 2013, HRM3 has relatively high concentrations, but beginning in 2014, the concentrations decrease and flatten out. By contrast, the 1-butene concentrations at MIPK remain at about the same magnitude (with some interannual variation) from 2005 to 2021. Most of the other industrial sites (LYNF, DRPK, CLIN, HCHV, WALV) show a gradual decline from 2004–2021. The lower sites (TX34, LKJK, and DANC) show interannual variation, but the 95th percentile concentrations remain well below 1 ppbv.

The concentrations of t-2-butene are much lower than the other HRVOCs. Given that all but a few 95th percentile concentrations do not exceed 1 ppbv, they will not be presented here.

3.5.3.2.5 Isoprene

Isoprene is clearly a highly-reactive VOC, but has not been included in TCEQ's control strategy because its primary source is natural: trees emit isoprene, especially oaks, poplars, willows, sycamores, and sweetgums. If it were emitted by anthropogenic sources, it would qualify as a highly-reactive VOC, which not only serves as an ozone precursor, but also as a particulate matter precursor. Therefore, this analysis examines isoprene concentrations in depth to determine whether there is evidence indicating an anthropogenic source in the industrial area of HGB.

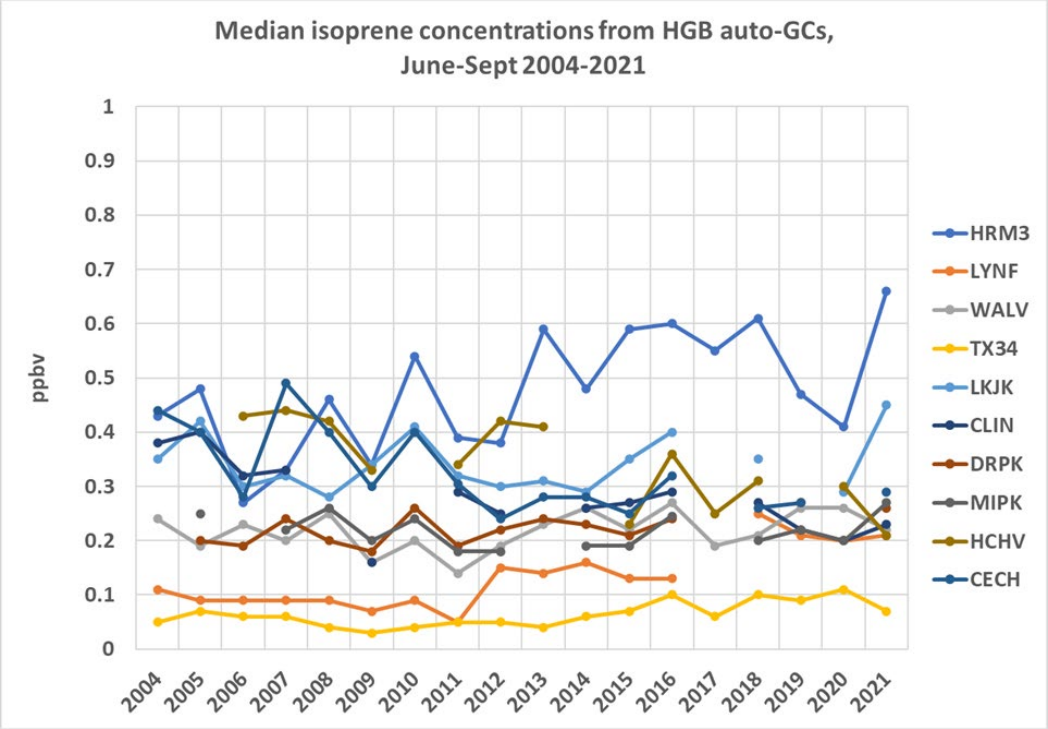

Figure 3.5.18: *Median isoprene concentrations in HGB from June-September during 2004-2021.*

The highest median isoprene concentrations observed in HGB are at HRM3 (**Figure 3.5.18**). Although this is considered an industrial site, it is also located near a small forested area. Isoprene appears to increase at HRM3 from 2004–2021. The second highest site is LKJK (Lake Jackson) in rural Brazoria County. There is not an obvious trend in most of these time series. The 95th percentile data shows HRM3 and LKJK as the highest sites again, but most of the other sites have concentrations below 1 ppbv.

Additional analyses are needed to determine whether the isoprene sources are anthropogenic or biogenic. **Figure 3.5.19** shows the average diurnal variation of isoprene concentrations at each site during June–September 2021.

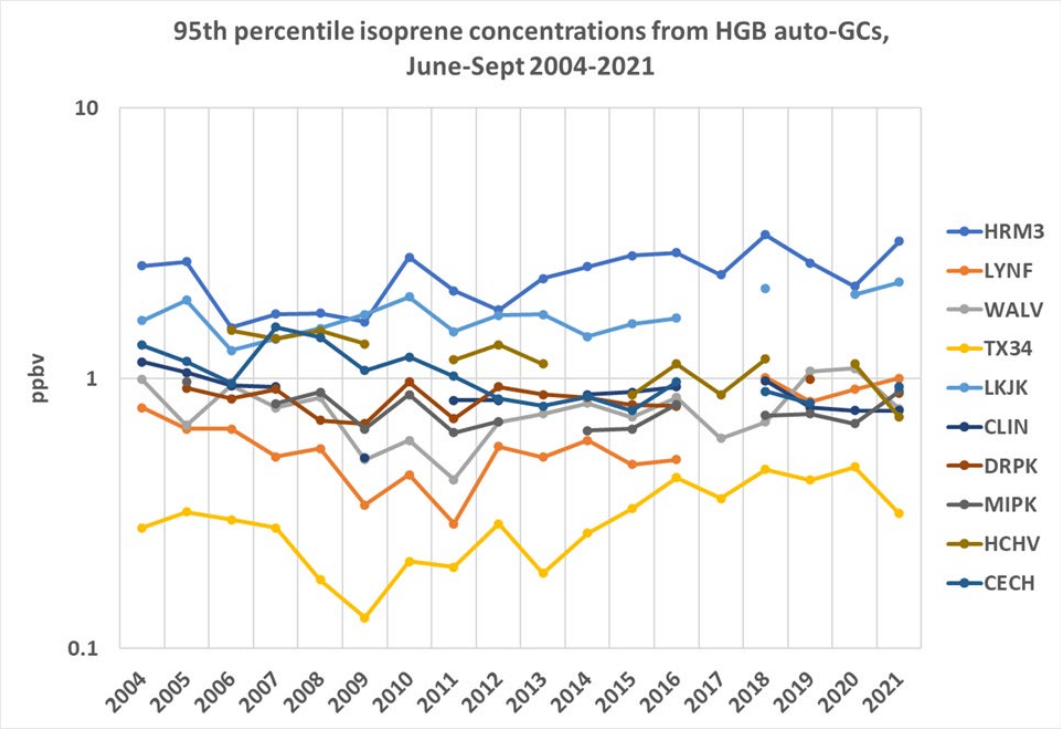

Figure 3.5.19: *95th percentile isoprene concentrations in HGB from June-September during 2004-2021.*

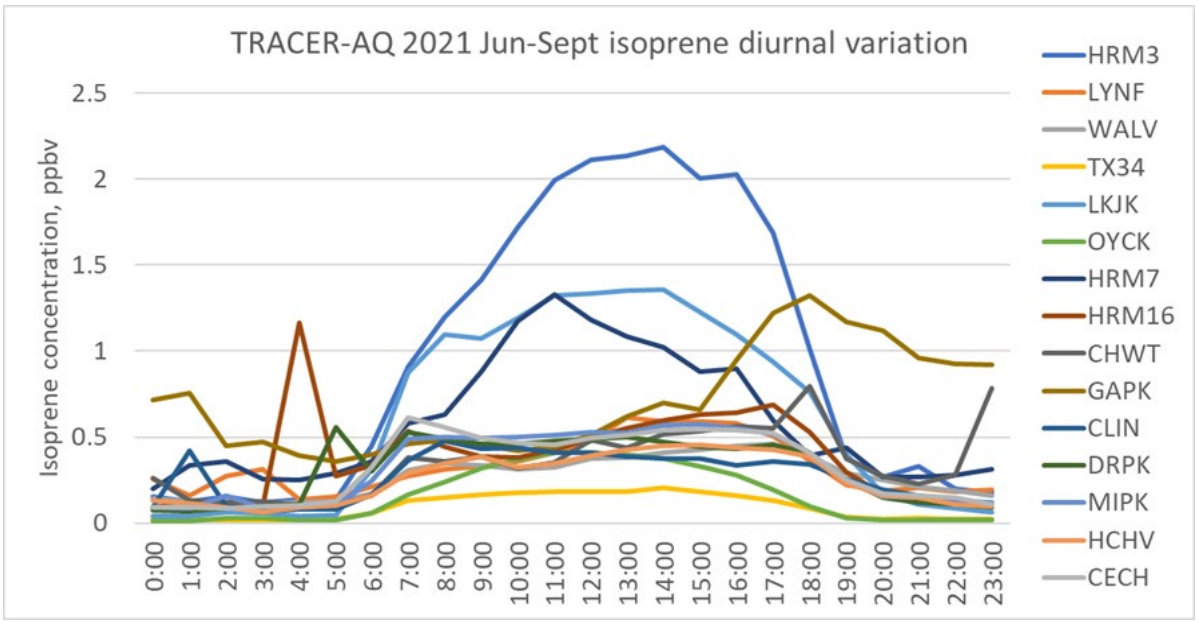

Figure 3.5.20: *Diurnal variation of average isoprene concentrations, June-September 2021.*

Figure 3.5.20 shows that HRM3 isoprene is near zero during nighttime hours, with a rapid increase beginning at sunrise and a peak just after 12:00, when both sunlight and temperatures are high. The concentrations drop beginning at about 16:00 and decrease to near zero by about 20:00. Since it is well-established that isoprene emissions from trees are sunlight-dependent, the diurnal profile exhibited by HRM3 data clearly indicate a biogenic

source of isoprene. LKJK and HRM7 also exhibit this behavior. However, GAPK (Galena Park) does not; its concentrations peak at about 18:00, and remain high until about 2:00. HRM16, CHWT, and LYNF also have off-hour peaks in the early morning. When looking at the entire data record for isoprene measured by auto-GC back to 2004, the highest concentrations have been measured at HRM3, LYNF, HRM16, CHWT, GAPK, and DRPK. Of these sites, HRM3, LYNF, and DRPK have long data records (≥ 40,000 valid hourly measurements), but HRM16 and CHWT have only 4400 hours of valid data, and GAPK has only about 9000 hours. This pattern indicates that the monitors with short data records have seen some of the highest concentrations, but they are not observing isoprene that exhibits a biogenic emission pattern, and the nature of the high isoprene is spiky. When considering the diurnal profile data and the maximum concentration data together, there are indications that an anthropogenic source of isoprene exists in the eastern part of the Ship Channel.

3.5.3.2.6 Aromatic hydrocarbons

Although some aromatic hydrocarbons could be considered highly reactive VOCs, they have not been included in ozone control strategy regulations. Nonetheless, examination of the trends of aromatic hydrocarbons is warranted, given the changes in the chemical industry due to fracking and other developments.

One class of VOCs initially considered for the HRVOC regulations was xylenes: para-xylene, meta-xylene, and ortho-xylene. When measured by auto-GC, para- and meta-xylene co-elute, and so they are analyzed here together. **Figure 3.5.21**and **Figure 3.5.22** show the time series for these co-eluting compounds.

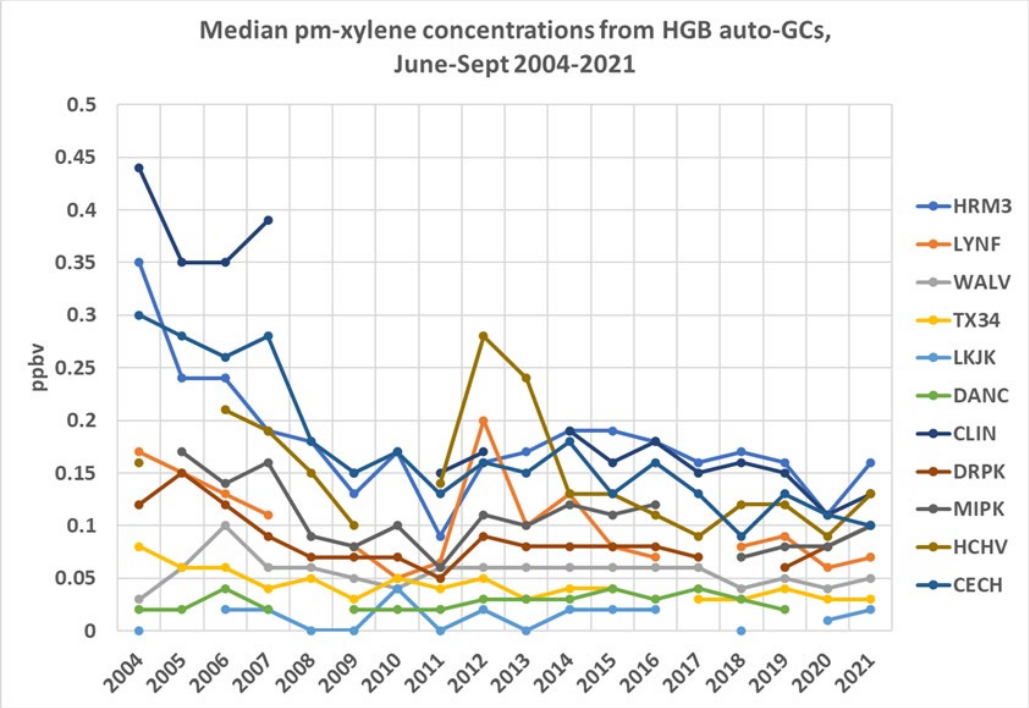

Figure 3.5.21: *Median p- and m-xylene concentrations in HGB from June-September during 2004-2021.*

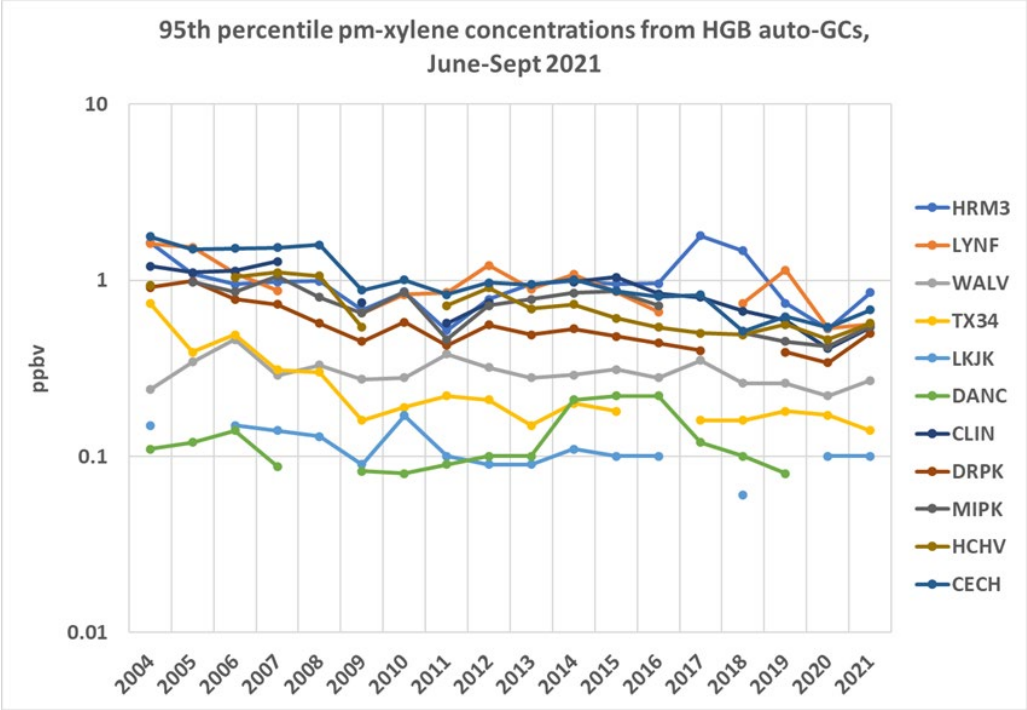

Figure 3.5.22: *95th percentile p- and m-xylene concentrations in HGB from June-September during 2004-2021.*

An interesting pattern in **Figure 3.5.21** is the downward trend in xylenes from 2004–2010. Even though xylenes were not included as official HRVOCs, there was apparently a decrease in emissions during the same period that the emissions on official HRVOCs were being controlled. Like the other HRVOCs, the concentrations since 2010 have not changed very much at any site. The only deviation from this pattern is a spike in 2012, which is apparent in the median graph but for which this analysis has no explanation. The 95th percentile concentrations (**Figure 3.5.22**) are between 0.1 and 1 ppbv for nearly every site and every year, and indicate no trend. The lack of high concentrations or upward trends suggests that p- and m-xylene are not a serious concern as ozone precursors compared to the official HRVOCs.

In examining data from other aromatic compounds (e.g., trimethylbenzenes), it is difficult to evaluate trends for these species because many of the measurements are below the detection limit, or the measurements have been invalidated. Hence, the other compounds will not be analyzed here.

3.5.3.3 Comparisons of modeling for 2006 and 2021 ozone episodes

Given the similarities in meteorology between 2006 and 2021, a comparison between modeling results between these two years seems appropriate. TRACER-AQ modeling for 2021 events has been completed (Wang et al. Task 8 TRACER-AQ Analysis). These results can be compared to 2006 modeling analyses by the TCEQ. However, care needs to be taken

so that the comparisons are commensurate, i.e., are on the same scale. TRACER-AQ modeling was performed at 1.33km resolution; the TCEQ modeling for 2006 was carried out at 1km resolution for a research project in 2012 (Estes et al., 2012). These two modeling exercises should be similar enough in model structure, domain size, grid size, and parameterizations that any differences observed should be due to factors besides modeling artifacts.

Figure 3.5.23 illustrates the observed hourly average ozone concentrations for the three episodes of interest: June 4–9, 2006; September 6–11, 2021; and September 23–26, 2021. These are averages of all operational monitors in the HGB area during the episode. The 2006 episode had notably higher ozone than the 2021 episodes. **Table 3.8** shows the maximum daily 8-hour ozone value measured at regulatory monitors in HGB during each episode day.

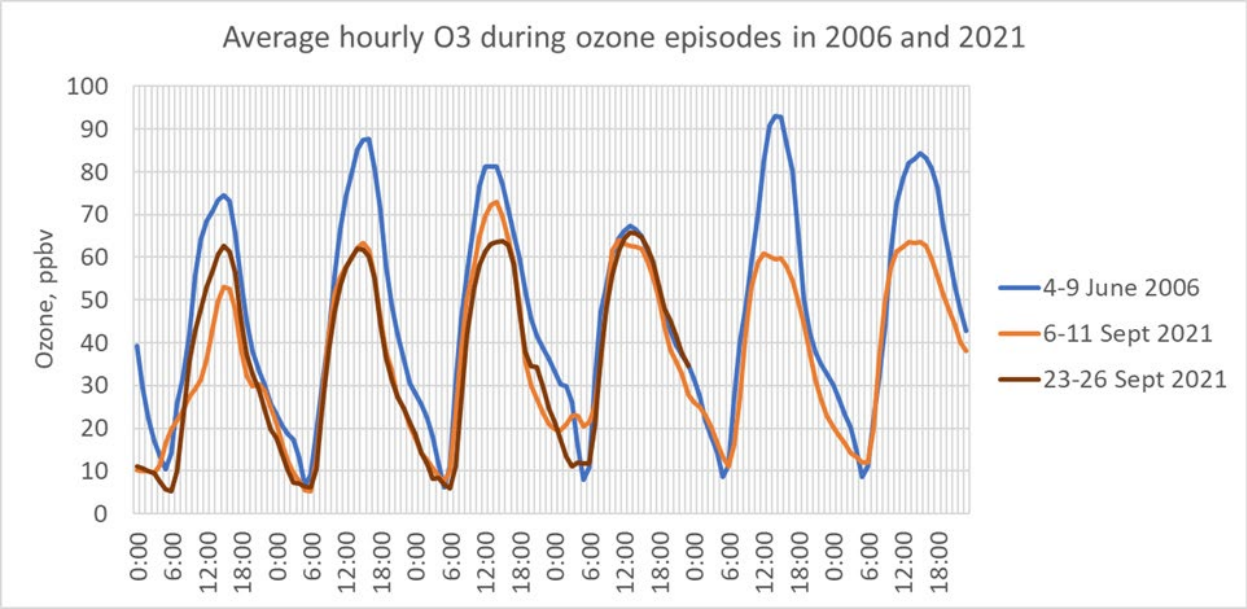

Figure 3.5.23: *Observed hourly average ozone concentrations for one episode in June 2006 and two episodes during September 2021.*

Table 3.8: *Maximum 8-hour daily average ozone for each episode day.*

Episode	Day 1	Day 2	Day 3	Day 4	Day 5	Day 6
June 4-9, 2006	102	103	110	73	111	101
Sept 6-11, 2021	60	75	89	79	71	74
Sept 23-26, 2021	73	73	76	75		

Although the intensity of the 2006 episode appears to be much greater than the 2021 episodes, it should be recalled that the design value in 2006 for HGB was 103 ppbv, whereas

in 2021 it was 77 ppbv. Therefore, all three of these events are close to the design value for their respective years.

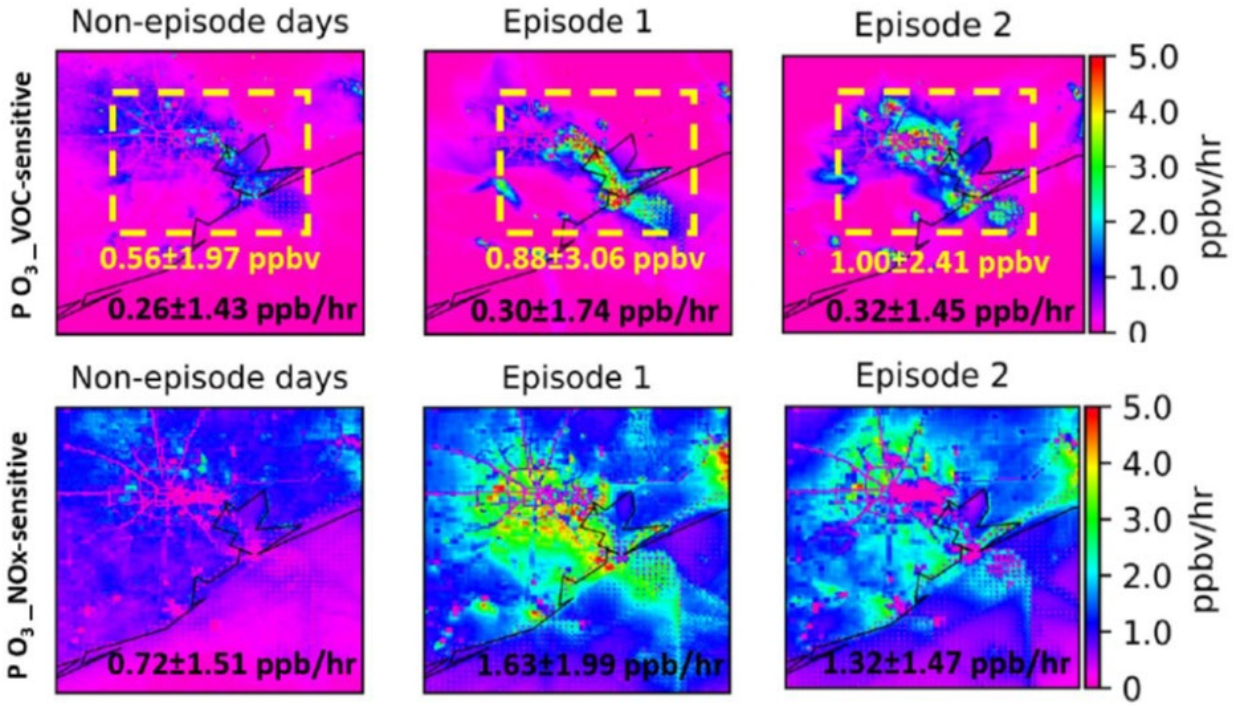

Figure 3.5.24: *Maps of VOC-sensitive and NOx-sensitive ozone production within the HGB area during daytime hours for September 6–11 (Episode 1) and September 23–26 (Episode 2). These figures illustrate the results of 1.33km photochemical grid modeling with process analysis algorithms invoked.*

Photochemical grid modeling of the two TRACER-AQ episodes in 2021 has been described in the documentation for Task 8 of the TRACER-AQ Data Analysis report, (Wang et al., 2022). The maps shown in **Figure 3.5.24** show the average hourly ozone formation rate for each grid cell in the 1.33km domain. The top row shows the ozone production rate (PO_3) for ozone formed in VOC-sensitive conditions (i.e., where NO_X is abundant), and the bottom row shows PO_3 in NO_X-sensitive conditions (where NO_X is scarce). Within the whole domain, NO_X -sensitive PO_3 is larger on average than VOC-sensitive PO_3, but it is noted that the intensity of VOC-sensitive PO_3 is large in very small subregions of the domain. In the Ship Channel and other industrial areas, near the Parish power plant, and within the shipping lanes in Galveston Bay, VOC-sensitive PO_3 is enhanced, and sometimes reaching the top of the color scale. The NO_X -sensitive PO_3 is more broadly distributed at lower intensity throughout the HGB area, including suburban, exurban, and offshore shipping areas.

Figure 3.5.25–**Figure 3.5.28**show the daily total ozone production for each grid cell in VOC-sensitive and NO_X -sensitive conditions for the two highest days of the 2006 episode. Overall, the patterns of high and low values in 2006 are similar to the patterns observed in the 2021 modeling shown in **Figure 3.5.24**.

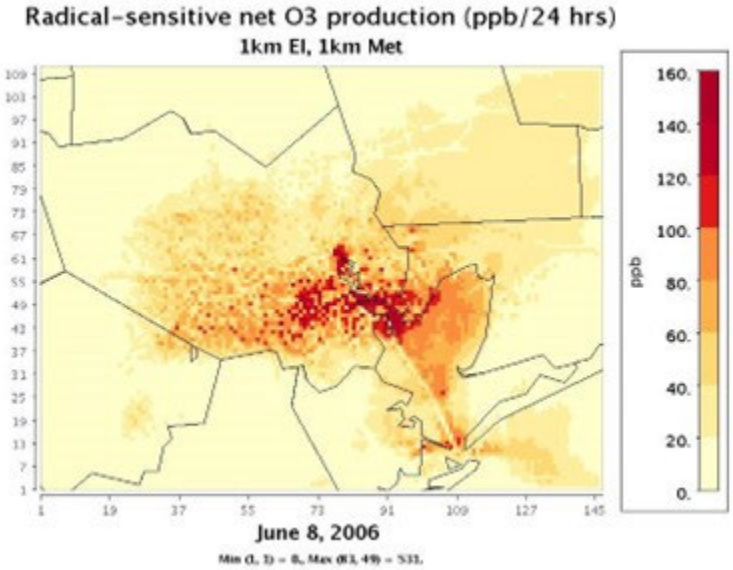

Figure 3.5.25: *VOC-sensitive PO3 for June 8, 2006, 24-hour total.*

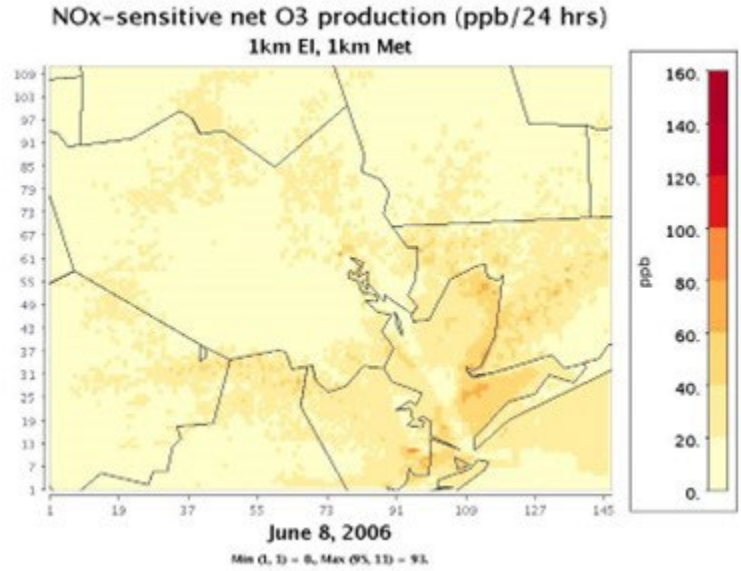

Figure 3.5.26: *NOx-sensitive PO3 for June 8, 2008, 24-hour total.*

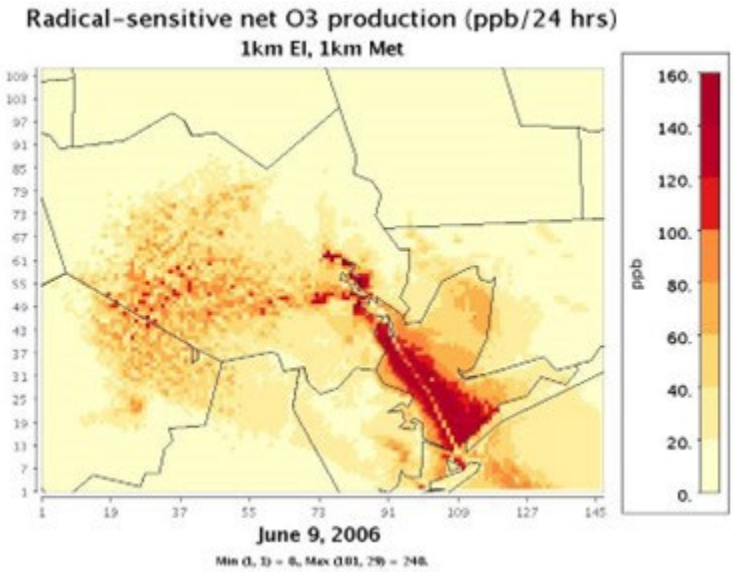

Figure 3.5.27: *VOC-sensitive PO3 for June 9, 2006, 24-hour total.*

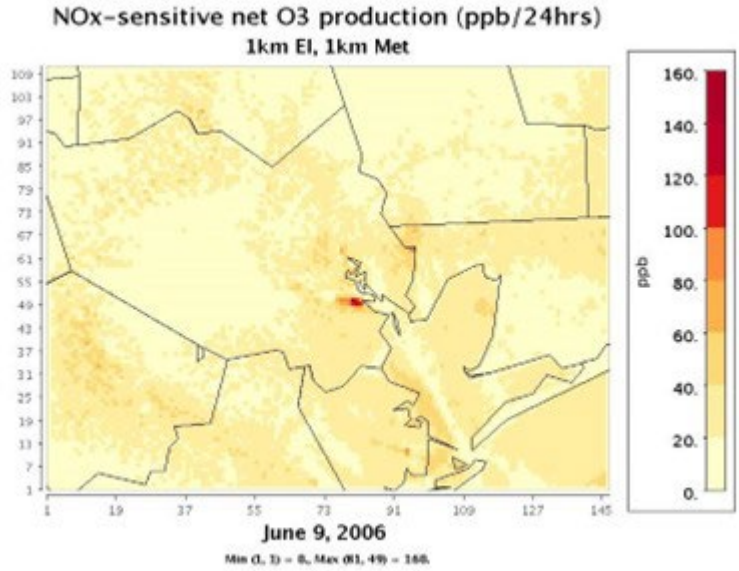

Figure 3.5.28: *NOx-sensitive PO3 for June 9, 2006, 24-hour total.*

The 2006 domain roughly matches the 2021 domain shown by the dashed yellow line in **Figure 3.5.24**. **Table 3.9** presents a comparison of the mean ozone production rate for VOC- and NO_X -sensitive conditions for the two highest MDA8 O_3 days of the 2006 episode and both 2021 episodes. The 2006 episode has a higher mean ozone production rate than the two later episodes, though the mean differences are not very large.

Table 3.9: *Comparison of the mean zone production rate for VOC and NO_X*

Episode	PO3 VOC-sensitive, ppb/hr	PO3 NOx-sensitive, ppb/hr
	Mean	**Mean**
8 June 2006	1.05	0.74
9 June 2006	1.11	0.84
8 Sept 2021	0.92	0.51
9 Sept 2021	0.81	0.74
25 Sept 2021	0.58	0.59
26 Sept 2021	0.52	0.52

Figure 3.5.29 and **Figure 3.5.30** show the quantity LN/Q, as calculated for daytime hours for the DISCOVER-AQ 2013 field campaign and the TRACER-AQ 2021 campaign. LN/Q (Kleinman et al. 2005) is a quantity that tracks the loss of NO_X compared to the loss of radicals during the ozone production process. Hence, it is an indicator of either instantaneous VOC-sensitive or NO_X -sensitive ozone production. The values in the two figures, however, are not quantitatively comparable, because the DISCOVER-AQ values are the median of binned hourly values, and the TRACER-AQ values are mean hourly values for the entire month of September 2021. The patterns observed, however, are similar, with the highest values observed in the early morning, indicating VOC-sensitive ozone formation dominates during these hours. By about 10:00 a.m., however, the LN/Q values drop, suggesting a shift to NO_X -sensitive conditions.

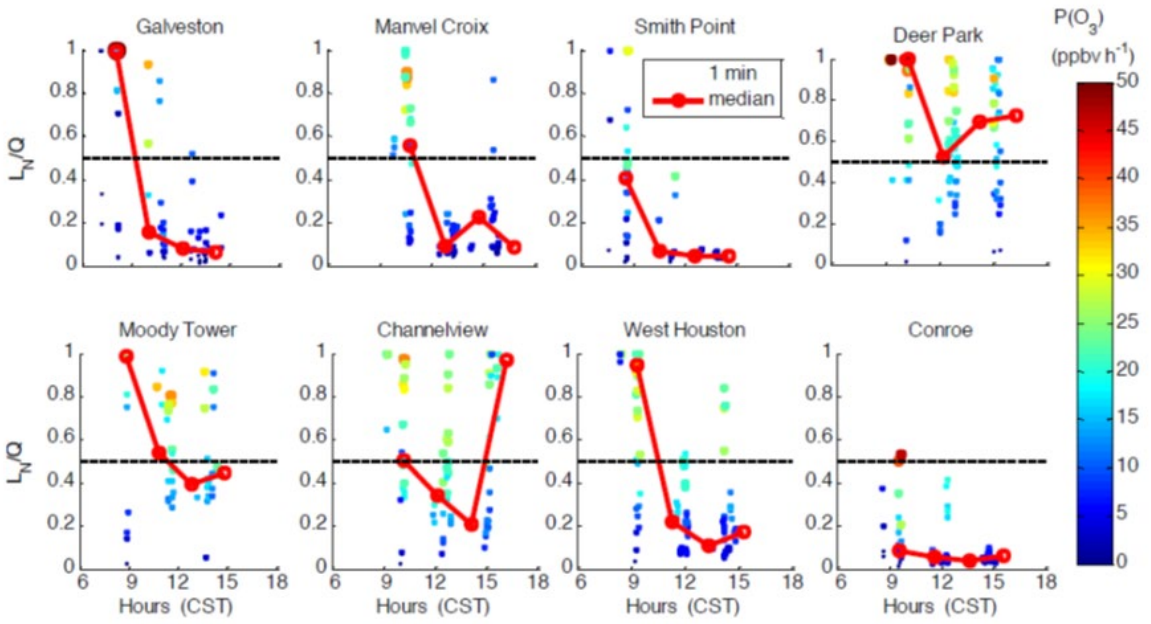

Figure 3.5.29: *LN/Q calculations for DISCOVER-AQ 2013 in Houston, excerpted from Mazzuca et al. (2016). The lines represent the median of binned hourly values.*

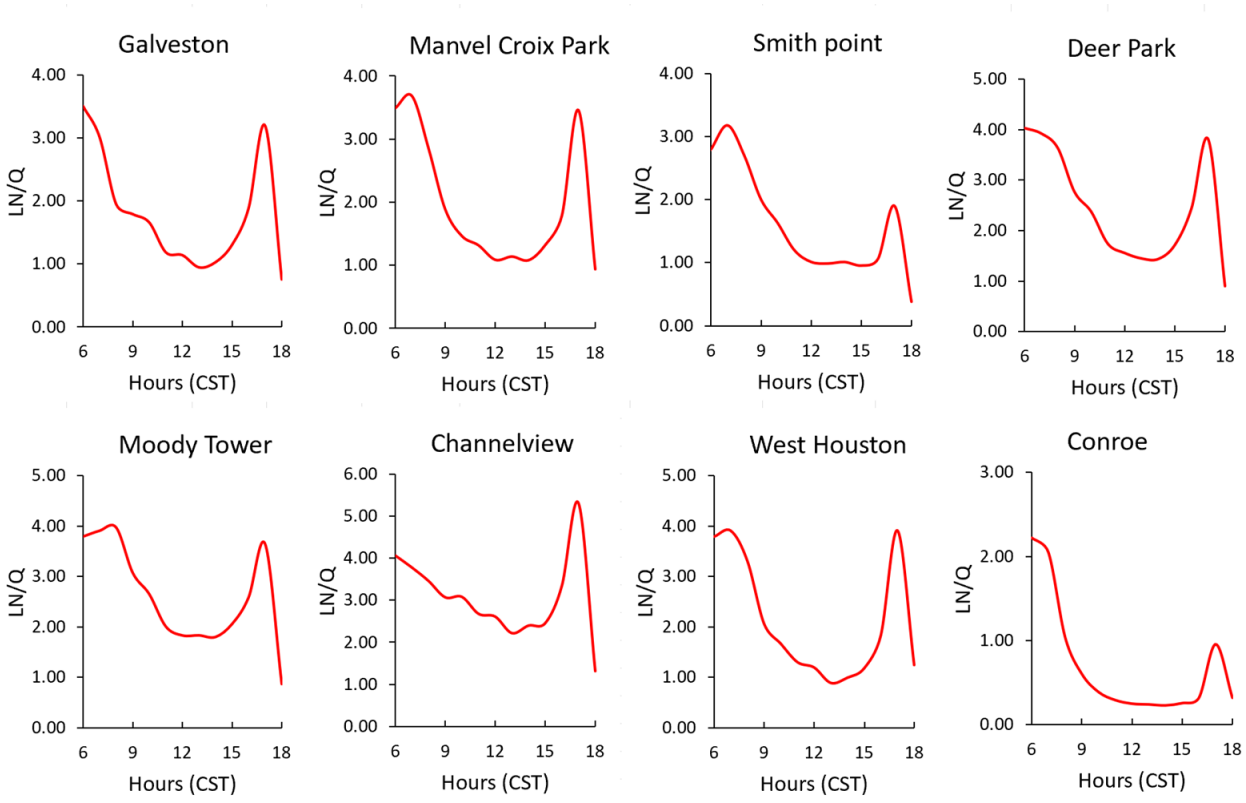

Figure 3.5.30: *LN/Q values from photochemical grid modeling of 2021 episodes. These are only qualitatively comparable to the DISCOVER-AQ values shown in Figure 30.*

3.6 Point source impacts on isoprene and select other VOC near the Ship Channel

3.6.1 Summary and Key Findings (Preliminary)

- Isoprene emission events were observed at Battleground occurring almost exclusively at night. CPF plots indicate a south-southwest source direction.
- Benzene emission events were observed as well from a southerly direction, while toluene emission events were primarily westerly. The maximum hourly concentration for benzene was 37.9 ppbv at 5:00 a.m. on 9/2 and again at ~midnight on 9/25. The peak hourly toluene concentration was 12. 2 ppbv at ~4:00 a.m. on 9/8.
- Nighttime events and nighttime overlapping events dominated for VOCs.

3.6.2 Methodology

VOC measurements were completed in the MAQL2 platform located at the Battleground site during September 2021 using a PTRMS (PTRMS Q300; Ionicon Analytik, Austria) modified with a cold trap inlet. A "cold trap" sample drying was implemented to reduce any effects of water vapor that can occur with operating the PTRMS at a lower E/N (100 Td). This sample drying stabilizes the water concentration in the same line. An intercomparison of VOC instruments has been included in Section 3.9 of this report. Based on those results, we can confidently compare the MAQL2 and MAQL1 VOC results.

3.6.3 Results

For this section the focus will be on VOC events for a select group of compounds: benzene, toluene, 1,3 butadiene and isoprene. Benzene and isoprene in particular, had frequent high event periods. These are plotted below.

Table 3.10: *VOCs Monthly averages.*

VOCs	Average	SD	Average+1SD
Benzene	2.66	5.50	8.17
Toluene	0.64	0.91	1.55
1,3-Butadiene	0.45	0.36	0.81
Isoprene	1.40	3.58	4.98

Isoprene had one extreme event and multiple additional event periods which almost exclusively occurred in the nighttime and early morning hours. The timing of these events precludes an obvious biogenic emission source. Biogenic emissions of isoprene are regulated by exposure to the sun's radiation and therefore do not peak in the middle of the night.

Similarly, frequent previous studies of isoprene in wooded areas surrounding Houston have not reported peaks in isoprene as high as recorded here in the nighttime. Additionally, it would be necessary to put these extreme events into historical context.

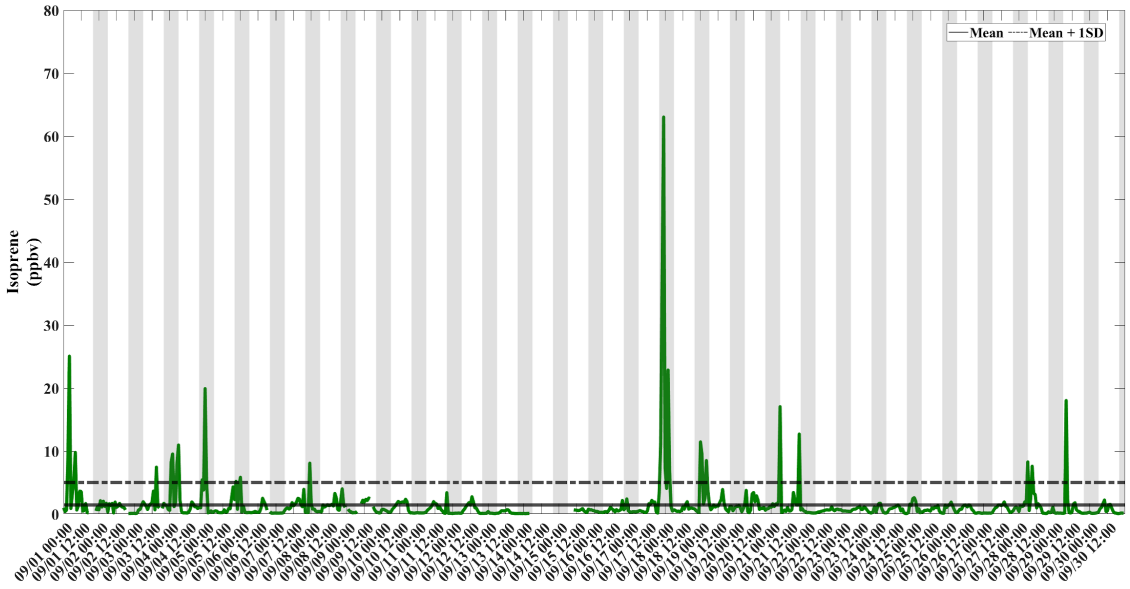

Figure 3.6.1: *Campaign time series for isoprene as measured by PTRMS at Battleground.*

The peak hourly isoprene concentration was 63.02 ppbv at ~11p.m. on 9/17. Isoprene can be oxidized in the atmosphere to form methyl vinyl ketone and methacrolein (MVK, MACR, respectively) as well as methyl ethyl ketone (MEK). These oxidation products are also plotted with isoprene for select event periods. However, it is clear that in the Shipping Channel area measured by the MAQL2 at Battleground that oxidation from isoprene cannot account for the MEK concentrations measured during the September campaign. This is evident because the MEK peaks are neither coincident nor subsequent to the peak isoprene but occur under a different pattern. More investigation is needed to understand potential sources of this MEK which peak at nearly 300 ppbv. In contrast, the MVK+MACR was coincident with the isoprene nighttime peaks in most cases. Additional modeling is needed to understand the chemistry of these events.

Table 3.11: *Concentration and timing of Isoprene events at Battleground, with the maximum concentration in red text, blue background indicating nighttime and green background indicating daytime.*

Start	Stop	Average	Threshold	Max ppbv
9/1/2021 2:00	9/1/2021 5:00	16.98	4.98	25.06
9/1/2021 6:00	9/1/2021 9:00	7.56	4.98	9.78
9/3/2021 14:00	9/3/2021 16:00	7.44	4.98	7.44
9/4/2021 0:00	9/4/2021 3:00	8.86	4.98	9.52
9/4/2021 4:00	9/4/2021 7:00	9.57	4.98	10.96
9/4/2021 21:00	9/5/2021 1:00	9.71	4.98	19.90
9/5/2021 20:00	9/5/2021 22:00	5.19	4.98	5.19
9/5/2021 23:00	9/6/2021 1:00	5.83	4.98	5.83
9/8/2021 22:00	9/9/2021 0:00	1.09	4.98	1.09
9/17/2021 20:00	9/18/2021 4:00	21.84	4.98	63.02
9/18/2021 23:00	9/19/2021 2:00	10.45	4.98	11.45
9/19/2021 3:00	9/19/2021 5:00	8.49	4.98	8.49
9/21/2021 5:00	9/21/2021 7:00	17.05	4.98	17.05
9/21/2021 18:00	9/21/2021 20:00	12.69	4.98	12.69
9/28/2021 5:00	9/28/2021 7:00	8.28	4.98	8.28
9/28/2021 8:00	9/28/2021 10:00	7.60	4.98	7.60
9/29/2021 7:00	9/29/2021 9:00	18.02	4.98	18.02

17 total events: Nighttime events (blue) = 9, Daytime events (white) = 5, Events during both day and night (green) = 3. Max concentration is shown in red.

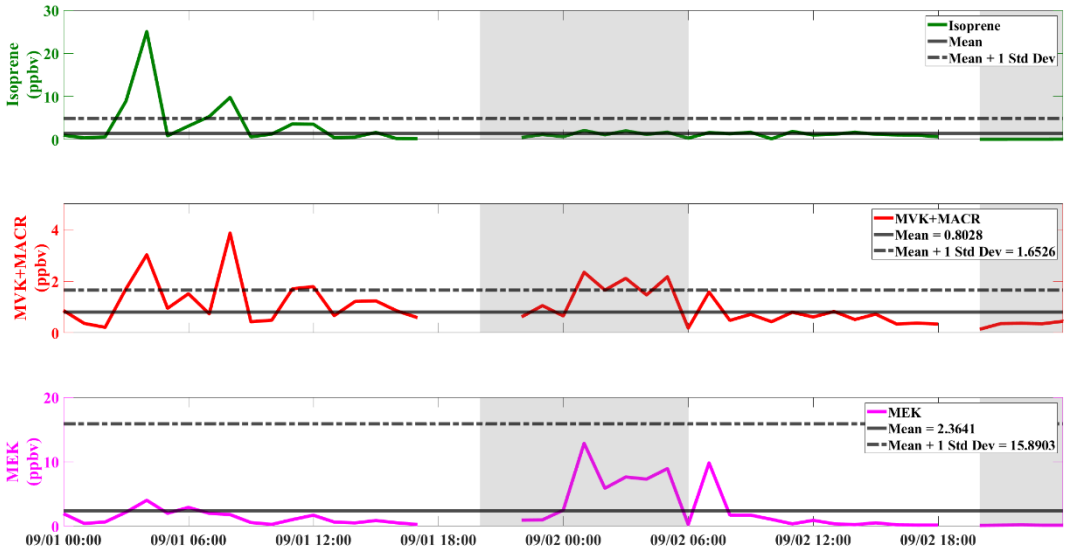

Figure 3.6.2: *Time series for isoprene, MVK + MACR and MEK measured by PTRMS at Battleground on 9/1/21–9/2/21.*

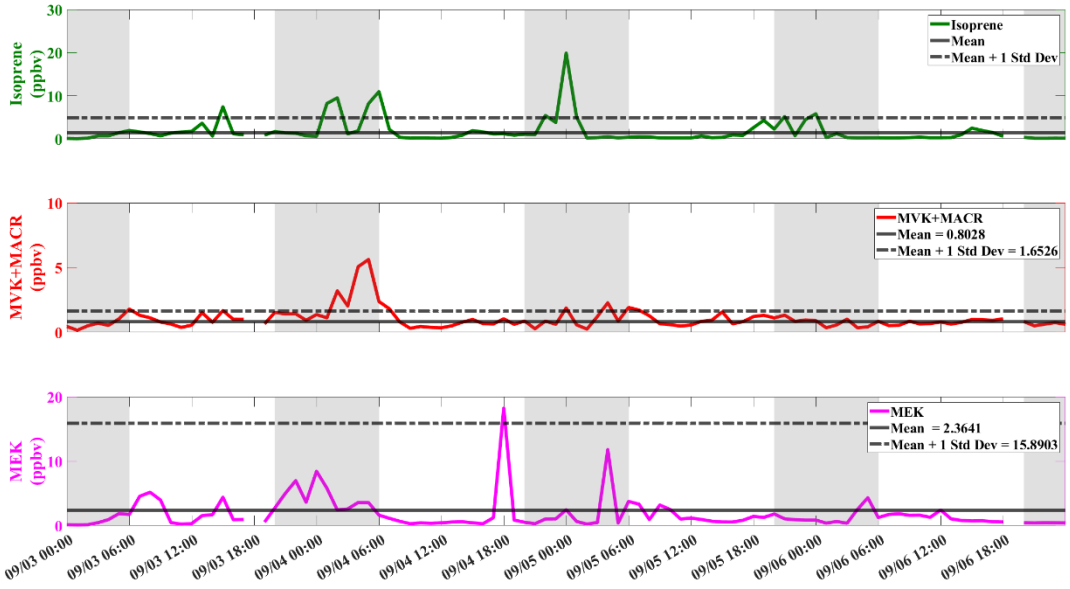

Figure 3.6.3: *Time series for isoprene, MVK + MACR and MEK measured by PTRMS at Battleground on 9/3/21–9/6/21.*

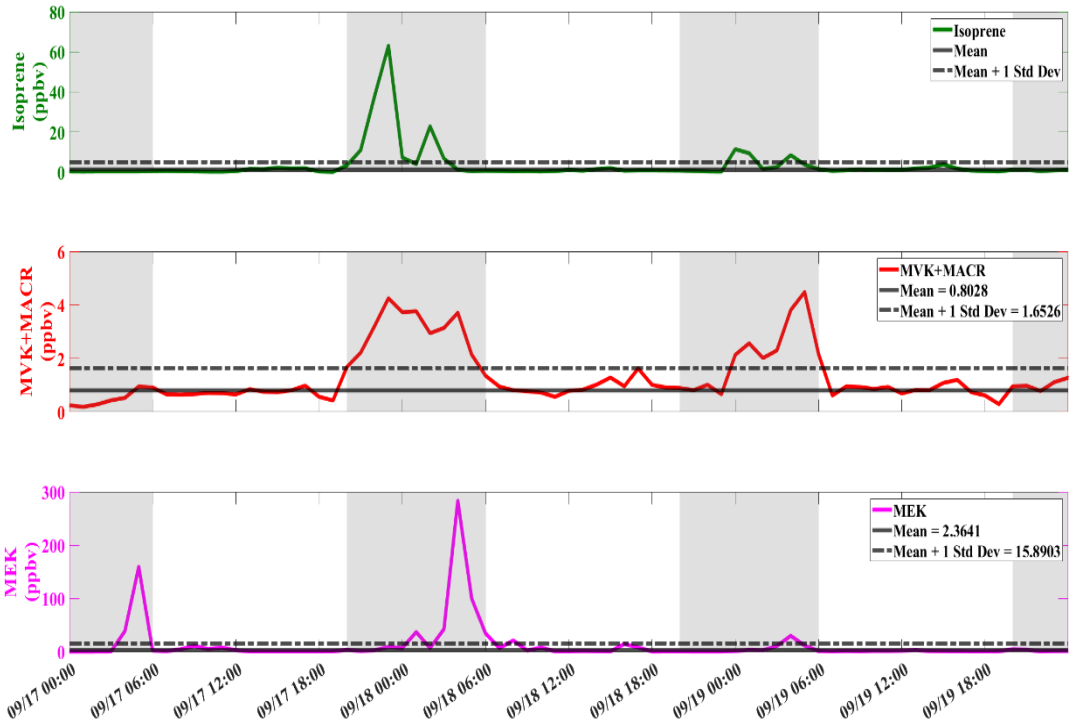

Figure 3.6.4: *Time series for isoprene, MVK + MACR and MEK measured by PTRMS at Battleground on 9/17/21–9/19/21.*

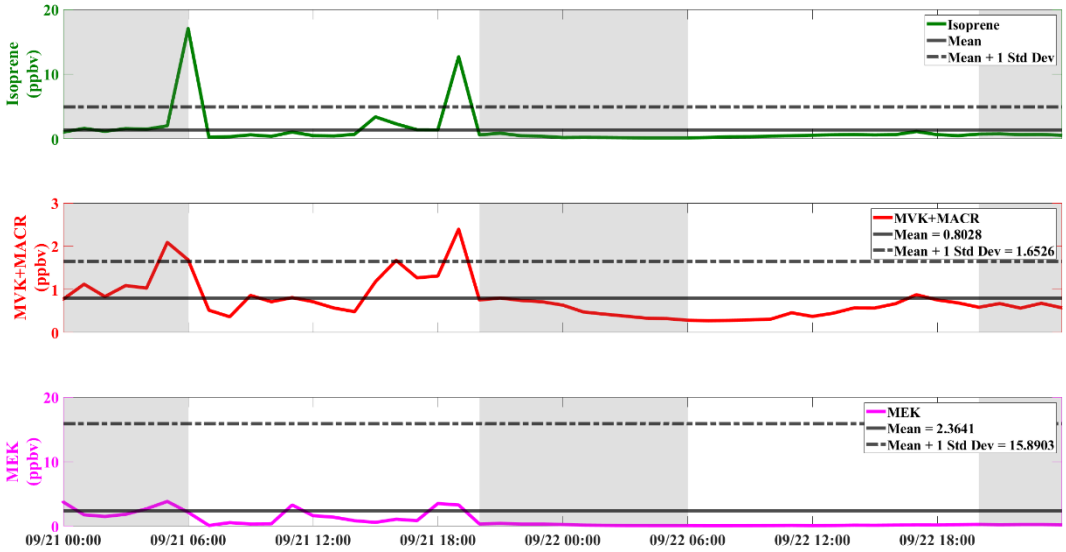

Figure 3.6.5: *Time series for isoprene, MVK + MACR and MEK measured by PTRMS at Battleground on 9/21/21–9/22/21.*

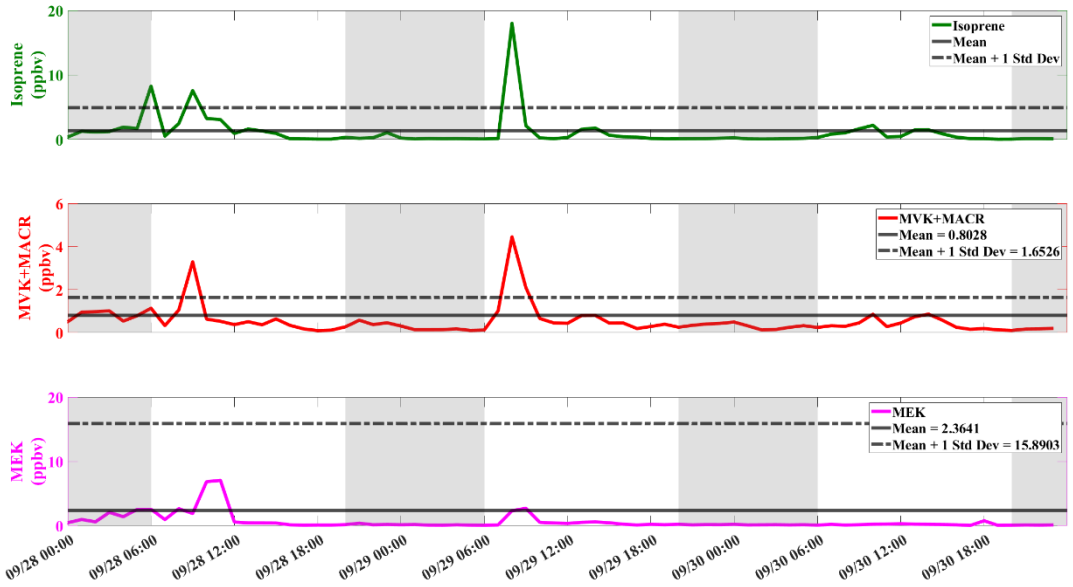

Figure 3.6.6: *Time series for isoprene, MVK + MACR and MEK measured by PTRMS at Battleground on 9/28/21–9/30/21.*

We completed conditional bivariate probability function (CPF) analysis on these select VOCs. The CPF approach is a receptor modelling method used to identify and characterize emission sources. CPF is a widely used tool to identify the physical location of emission sources. It uses surface wind speed and direction and a time series of the ambient data. The CPF for isoprene, MVK + MACR and MEK reveal the same source region for isoprene and MVK+MACR, which is south-southwest of the site, while MEK has a source due west of the site.

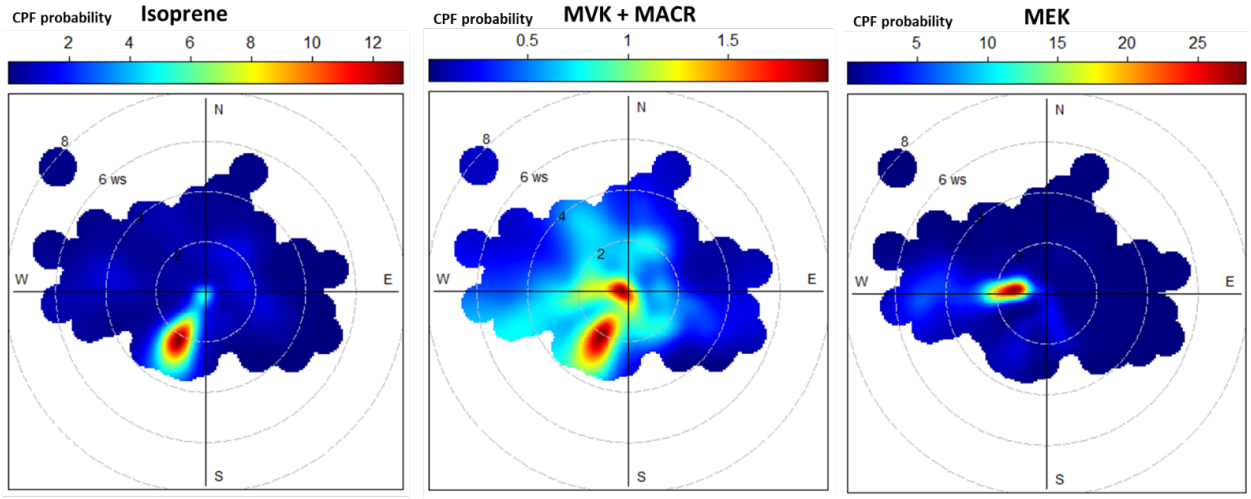

Figure 3.6.7: *CPF plots of isoprene, MVK+MACR and MEK concentrations at Battleground site during TRACER-AQ1.*

To understand potential sources for the high isoprene, we looked into the isoprene emissions inventory and identified several local sources which are plotted in the map below.

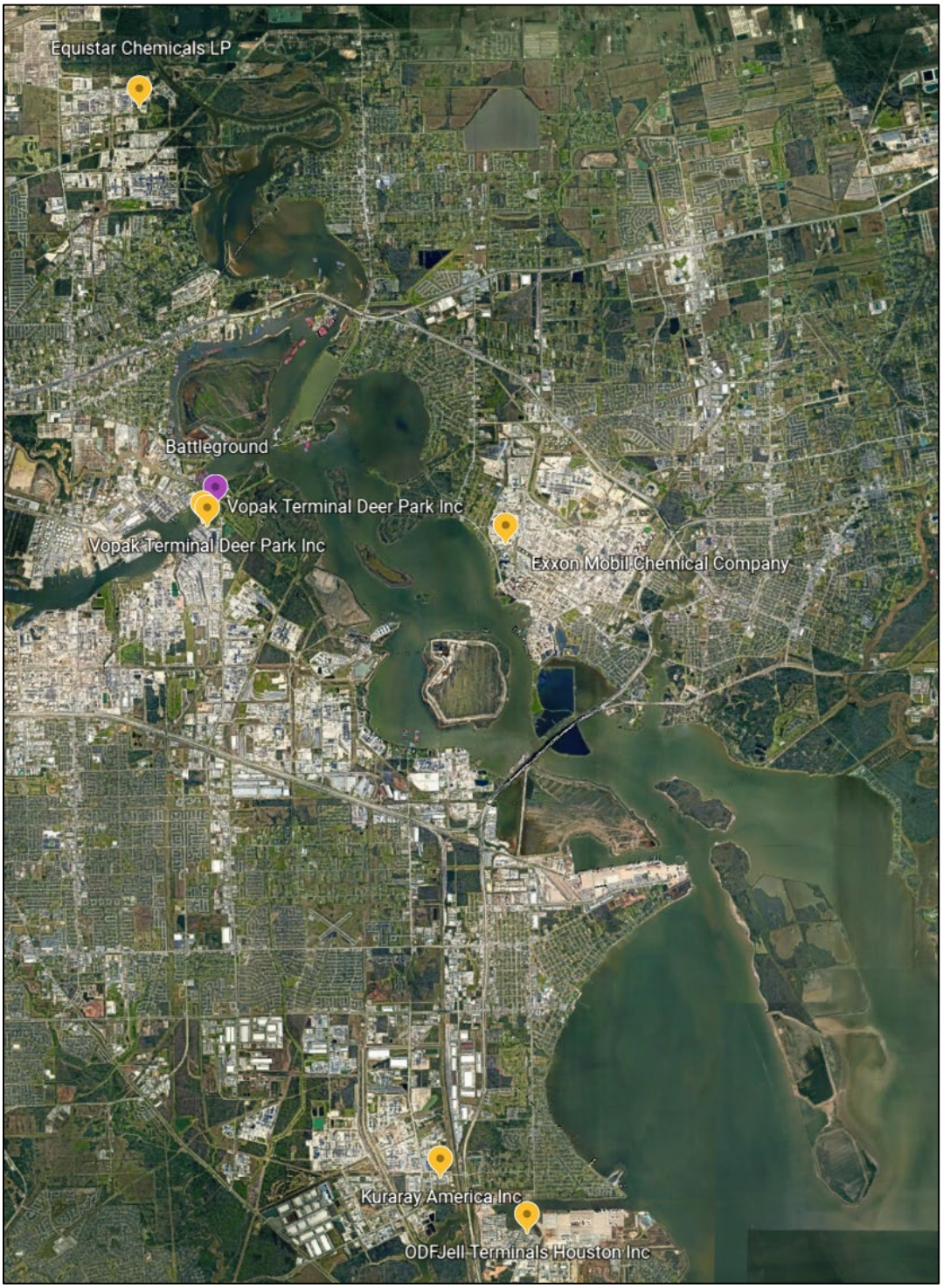

Figure 3.6.8: *Map of isoprene emitters in the immediate area to Battleground.*

Based on the CPF plots, we investigated the sources located to the south-southwest of the Battleground site. Additional investigation is needed to understand potential transport and chemistry between these potential source locations and the Battleground site.

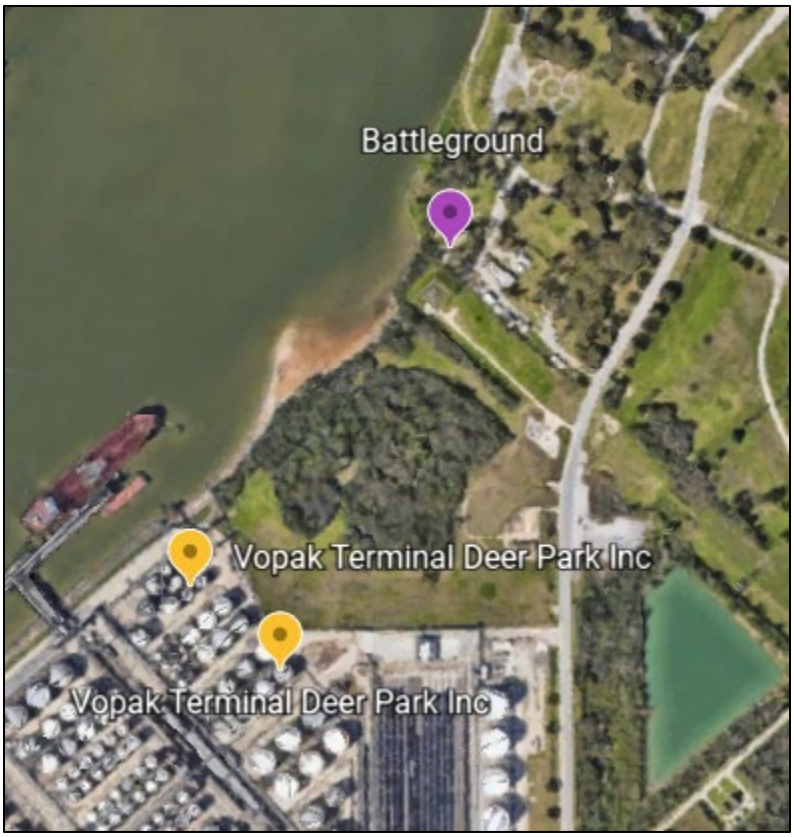

Figure 3.6.9: Emission *sources to the south-southwest of Battleground.*

Most of the benzene events included in the table below were overnight, or had overlapping nighttime periods. The maximum hourly concentration was 37.9 ppbv at 5:00 a.m. on 9/2 and again at ~midnight on 9/25. The campaign time series and select event periods are plotted below. We will add wind direction and emission source analysis to this discussion for the final report.

Table 3.12: *Concentration and timing of benzene events at Battleground, with the maximum concentration in red text, blue background indicating nighttime and green background indicating daytime.*

Start	Stop	Average	Threshold	Max ppbv
9/1/2021 3:00	9/1/2021 8:00	11.33	8.17	19.86
9/1/2021 22:00	9/2/2021 6:00	25.02	8.17	37.87
9/2/2021 7:00	9/2/2021 8:00	21.62	8.17	21.62
9/3/2021 5:00	9/3/2021 11:00	7.80	8.17	14.20
9/3/2021 19:00	9/4/2021 3:00	15.99	8.17	22.99
9/7/2021 22:00	9/8/2021 0:00	20.54	8.17	20.54
9/8/2021 19:00	9/8/2021 22:00	22.46	8.17	25.53
9/17/2021 19:00	9/18/2021 2:00	14.76	8.17	32.86
9/18/2021 5:00	9/18/2021 8:00	15.84	8.17	20.59
9/19/2021 14:00	9/19/2021 17:00	6.29	8.17	12.08
9/19/2021 19:00	9/20/2021 6:00	15.14	8.17	23.08
9/20/2021 23:00	9/21/2021 7:00	16.12	8.17	21.88
9/21/2021 17:00	9/21/2021 20:00	9.43	8.17	12.61
9/23/2021 23:00	9/24/2021 4:00	13.85	8.17	26.45
9/24/2021 21:00	9/25/2021 2:00	25.61	8.17	37.93
9/26/2021 0:00	9/26/2021 4:00	10.68	8.17	12.76
9/27/2021 20:00	9/28/2021 6:00	10.74	8.17	16.77

17 total events: Nighttime events (blue) = 6, Daytime events (white) = 3, Events during both day and night (green) = 8. Maximum concentration shown in red.

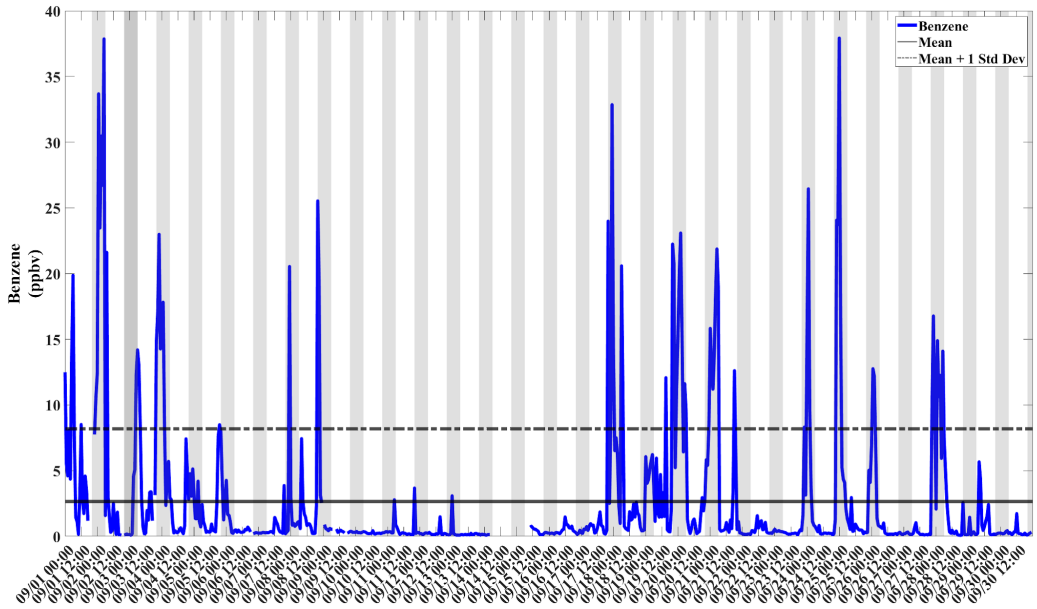

Figure 3.6.10: *Campaign time series for benzene measured by PTRMS at Battleground.*

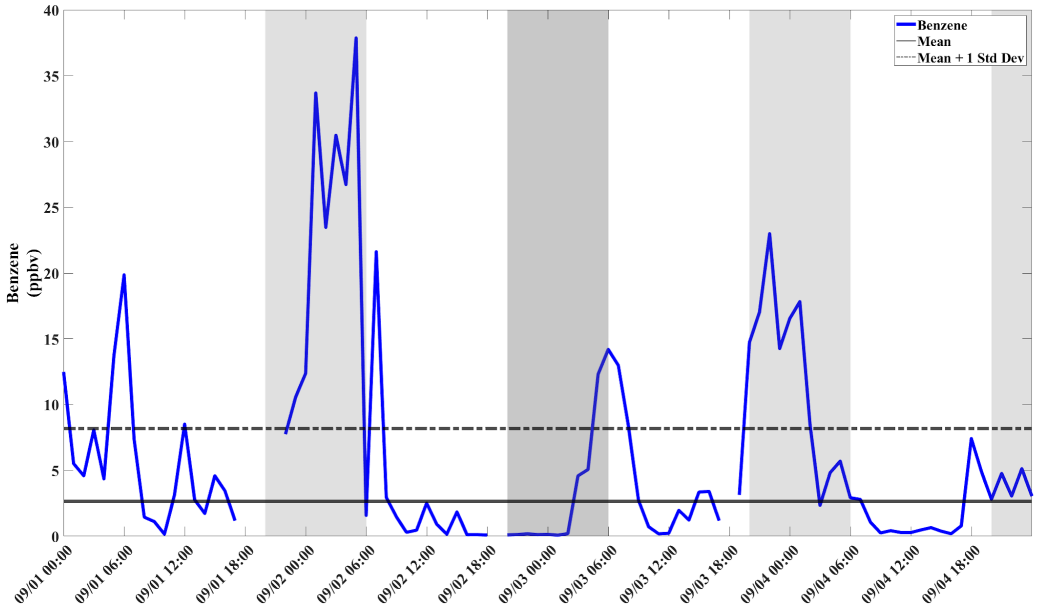

Figure 3.6.11: Event time series for benzene at Battleground 9/1/21–9/4/21.

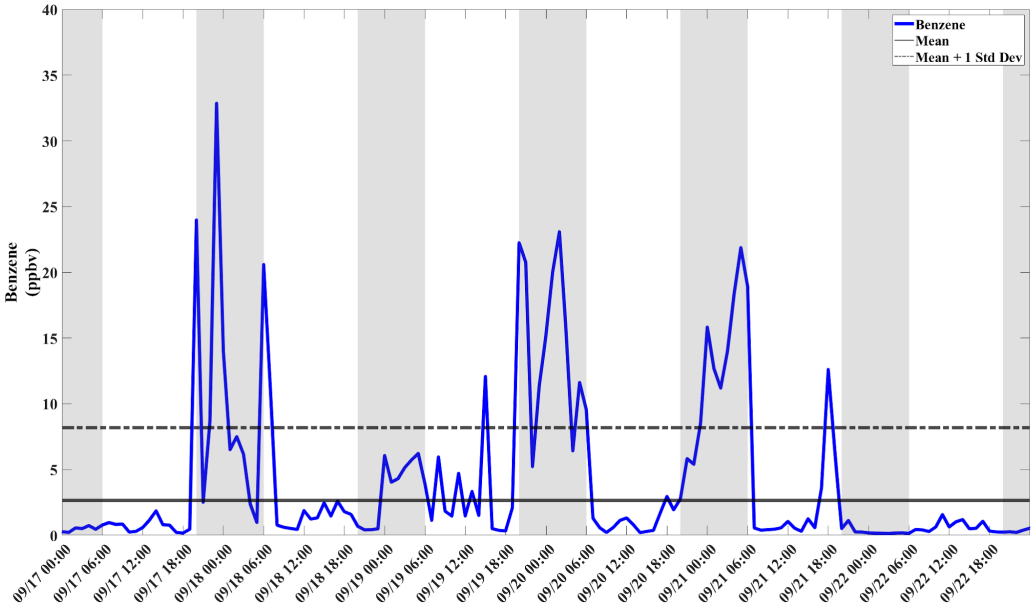

Figure 3.6.12: Event time series for benzene at Battleground 9/17/21–9/22/21.

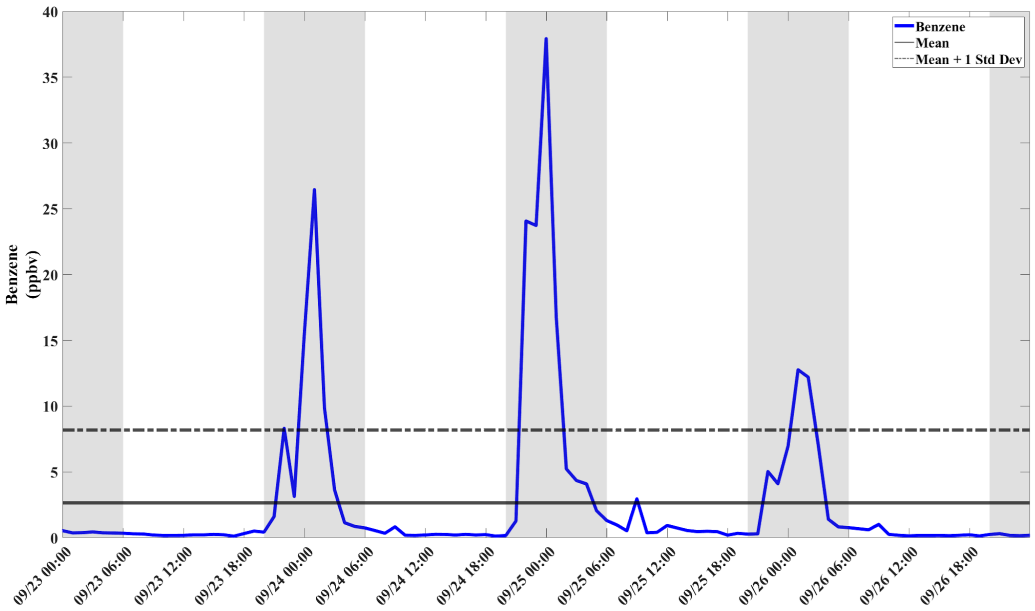

Figure 3.6.13: *Event time series for benzene at Battleground 9/23/21–9/26/21.*

Toluene had primarily nighttime event periods, although the maximum concentration did not reach the same extremes as benzene. The peak hourly toluene concentration was 12. 2 ppbv at ~4:00 a.m. on 9/8.

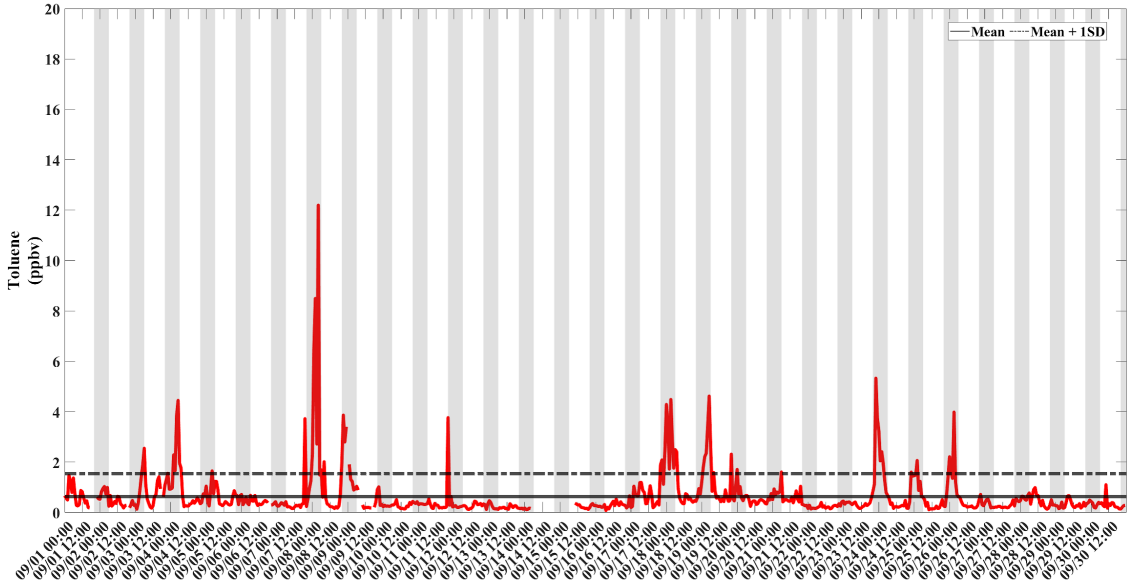

Figure 3.6.14: *Campaign time series for toluene measured by PTRMS at Battleground*

Table 3.13: *Concentration and timing of Toluene events at Battleground, with the maximum concentration in red text, blue background indicating nighttime and green background indicating daytime.*

Start	Stop	Average	Threshold	Max ppbv
9/3/2021 4:00	9/3/2021 6:00	1.89	1.55	1.89
9/4/2021 1:00	9/4/2021 8:00	2.66	1.55	4.45
9/5/2021 3:00	9/5/2021 5:00	1.65	1.55	1.65
9/7/2021 18:00	9/7/2021 20:00	3.73	1.55	3.73
9/7/2021 23:00	9/8/2021 5:00	6.44	1.55	12.20
9/8/2021 19:00	9/9/2021 3:00	2.54	1.55	3.87
9/11/2021 19:00	9/11/2021 21:00	3.77	1.55	3.78
9/17/2021 19:00	9/18/2021 8:00	2.58	1.55	4.48
9/19/2021 0:00	9/19/2021 7:00	2.83	1.55	4.62
9/19/2021 19:00	9/19/2021 22:00	1.44	1.55	2.32
9/23/2021 20:00	9/24/2021 5:00	2.64	1.55	5.33
9/26/2021 0:00	9/26/2021 4:00	2.32	1.55	3.99

12 total events: Nighttime events (blue) = 4, Day time events (white) = 1, Events during both day and night (green) = 7. Max concentration shown in red.

In the figures below it is clear that toluene events only occur over the nighttime, with a small overlap into daylight hours. Additional wind direction and source investigation will be completed for the final report.

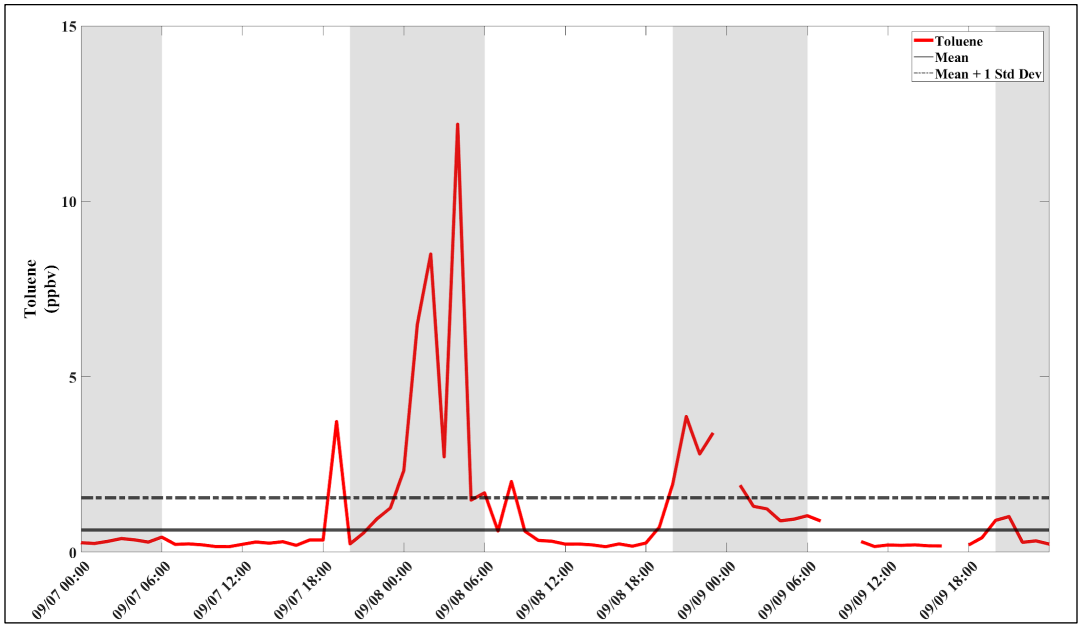

Figure 3.6.15: *Time series of select toluene events at Battleground.*

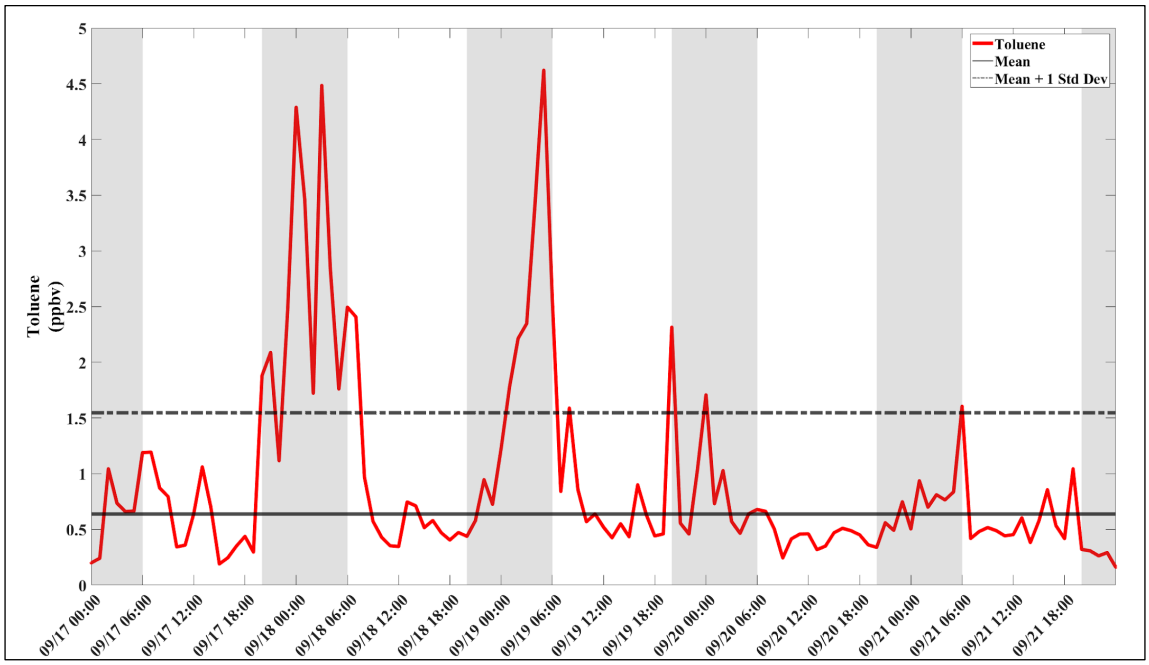

Figure 3.6.16: *Time series of select toluene events at Battleground.*

To understand whether the benzene and toluene had the same source area, CPF was also completed for these compounds along with xylene, another aromatic compound. It appears that toluene and m-xylene were co-emitted by similar sources at the west of the sampling site.

Benzene concentration was mostly contributed from the nearby sources on the south of the sampling site.

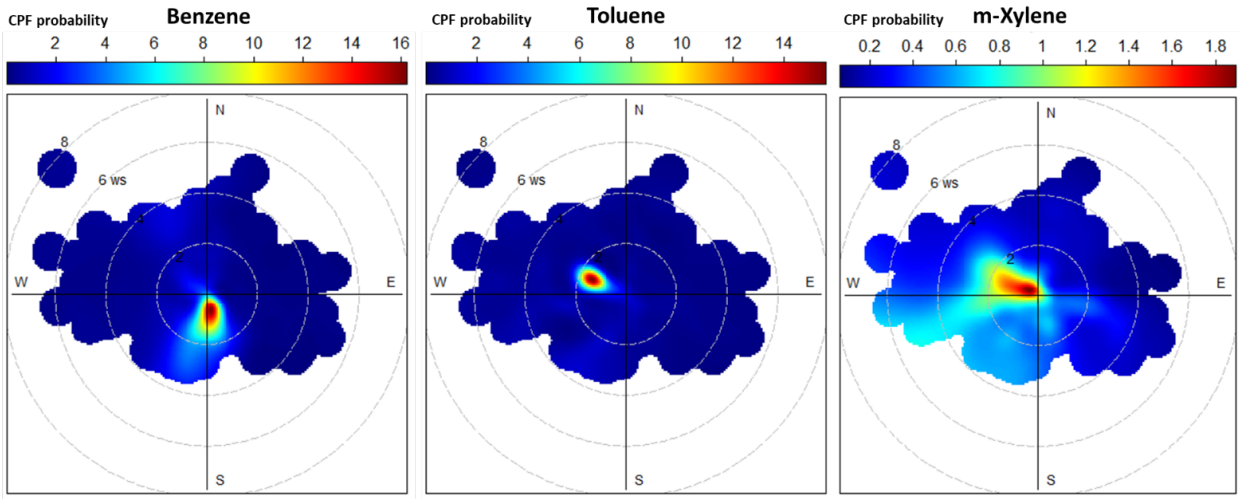

Figure 3.6.17: *CPF plots of benzene, toluene and m-xylene concentrations at Battleground site during TRACER-AQ1.*

The last VOC that was investigated was 1,3 butadiene, which did not have the extremes seen with isoprene and benzene. The nighttime average was 0.55 ppbv while the daytime average was 0.44 ppbv.

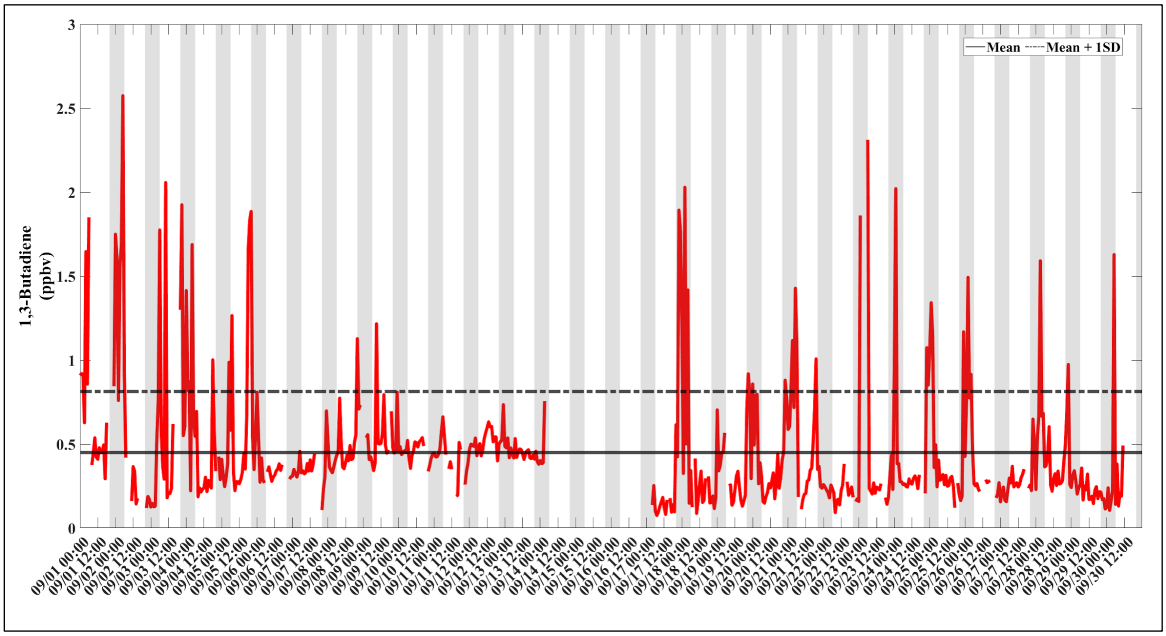

Figure 3.6.18: *Campaign time series of 1,3 butadiene measured by SRI-PTRMS at Battleground.*

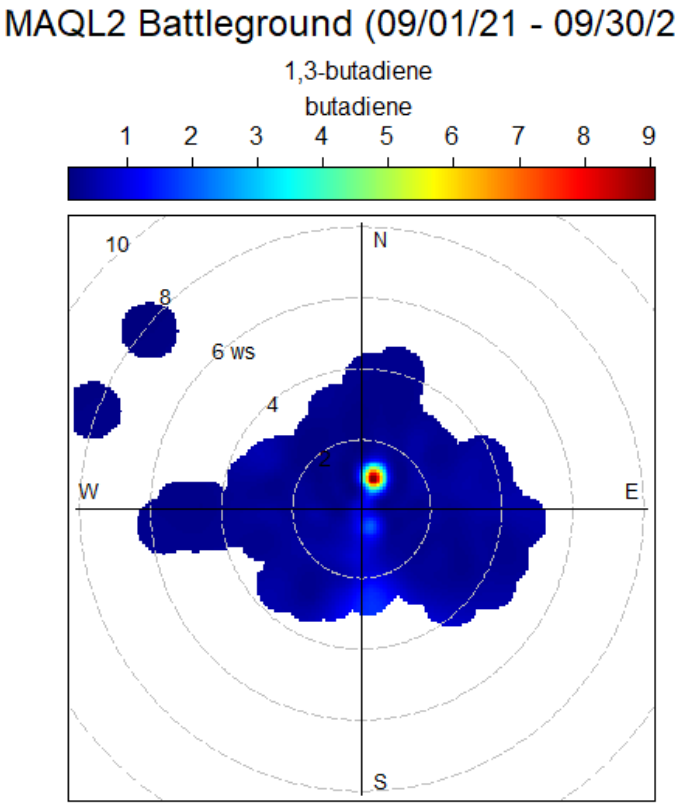

Figure 3.6.19: *CPF plot of 1,3 butadiene at Battleground site during TRACER-AQ1. The plot highlights a key wind direction component to this VOC max concentrations with a potential source in the northeast sector.*

3.7 Ethylene Emission Event Near La Porte (Sergio and Subin w/ support from Baylor)

3.7.1 Summary and Key Findings

- On September 27, 2021, a high concentration ethene event was sampled over a four-hour period by MAQL1 at the La Porte TCEQ site. Four main peaks were observed, each measuring several ppmv or more.
- Four TCEQ sites with GCs also measured high ethylene concentrations during this same period, Cesar Chavez, Deer Park HRM 16, Deer Park 2 and Milby Park. The Baylor PTR-MS did not see the main event but did see ethene in the low hundreds of ppbv prior to the start of the main event, however it has yet to be determined if this was a precursor or unrelated plume.
- There was very strong correlation between the reactive alkenes and HCHO in the four peaks. While the first three plumes maintained a relatively consistent ratio, the fourth plume detected had a different relative ratio between the two signals. It is worth noting that the first two plumes occurred in darkness, the third shortly after sunrise, but the fourth was while the sun was well above the horizon.
- It appears that this event was primarily a VOC plume as there was no correlation found with NO_X, CO and SO_2.
- Wind data from these sites indicates that the source was east of the Deer Park monitors and southeast of the La Porte airport.

3.7.2 Methodology

On the morning of September 27, 2021, a high alkene event was detected by the MAQL1 between 3:45 a.m. and 7:46 a.m. CST. High concentrations of alkenes were measured during that time interval with three distinct elevated peaks that correlated with formaldehyde. A fourth peak was measured towards the end of the event, but not as high as the previous peaks and the correlation with HCHO was different. Although the Reactive Alkene Detector (RAD) responds to ethene, propene, 1,3-butadiene, and isoprene TCEQ Auto-GCs also detected the plume and identified it as primarily being composed of ethene. Because the RAD has a different sensitivity to each of the VOCs it detects it is difficult to disentangle the specific composition and magnitude of the VOCs. The data is therefore reported as propene or propene equivalents as the instrument is regularly calibrated with propene and that calibration factor is applied to the data. In the future, discrete events such as this where we have external corroboration that the plume is primarily a compound other than propene it would be possible to apply a more specific sensitivity to the data, however there would still be various caveats to the use and interpretation of the data. The data is plotted as propene,

however it is understood that the likely compound measured by the RAD in the MAQL1 was ethene.

During this event there were two wind direction shifts. At 6:12 a.m. the wind direction shifted from the southeast to an easterly wind. Then, at 6:49 a.m. the wind direction shifted from the east to south and southwest direction. The wind speed for the event was in the range of one to two miles per hour which makes it difficult to define a broader wind field flow, and at the relative scales involved, back trajectories are challenging to interpret as well because of the coarse nature of the grid cells used.

3.7.3 Results

Figure 3.7.1 shows the time series data from the MAQL1 at the La Porte site during stationary measurements for key species. The most prominent features are the large peaks in HCHO (30–40 ppbv) and in the RAD, reported here as propene equivalents, which approached 6,000 ppbv. The fourth and final major plume detected shows a sharp drop and was associated with the lowering of the MAQL1 sampling mast from six to two meters in preparation for a mobile sampling day. Shortly after the mast was lowered the MAQL1 relocated from the TCEQ site at the La Porte airport over to the DOE ARM site for the TRACER campaign which was also located at the same airport, only 500 m east of the TCEQ site. The data gap in the RAD and HCHO signals from shortly before 7:00 to 9:00 CST are due to baseline and calibration checks on the instrument to rule out potential instrument malfunction as a cause for such high values. It is worth noting that the CO, NO_Y, and SO_2 measurements do not show consistent correlations with the VOC or HCHO data. Other measurements onboard of aromatic VOCs (not shown) were low, mostly at or below detection limit and did not exhibit any correlation with the main plumes. Of note is the shift in relative abundance of HCHO in the final plume which may be related to the increasing solar intensity (i.e. photochemistry) as seen in the j_{NO2} signal.

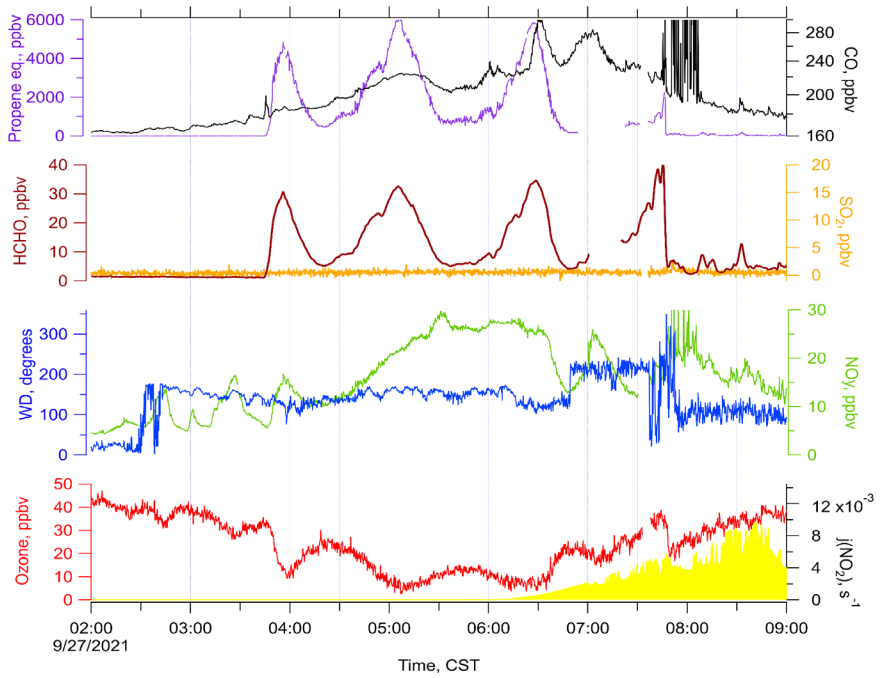

Figure 3.7.1: *Time series of propene equivalent and CO (first row), HCHO and SO_2 (2^{nd} row), wind direction (WD) and NO_Y (third row), and ozone and j_{NO2} (bottom row) observed during stationary periods at the La Porte site on September 27, 2021. Four distinct peaks during the ethene event are most prevalent in propene and HCHO.*

In addition to the observations at MAQL1, several other TCEQ Auto-GC sites also detected this event. A time series of ethene from Cesar Chavez, Deer Park (HRM16), Deer Park 2, and Milby Park are shown below (**Figure 3.7.2**). Both Deer Park monitors exceeded 1,000 ppbv for at least one measurement cycle. Ethene-wind roses (**Figure 3.7.3**) show that the highest concentrations for Cesar Chavez and Milby Park were associated with easterly winds and had ethene magnitudes significantly lower than the two Deer Park monitors, consistent with their relative location at the western end of the HSC. Wind data for the TCEQ Deer Park monitor was unavailable for this period, however the Deer Park HRM 16 monitor also had an easterly wind direction associated with its highest measurements. The MAQL1 shows that there were two slightly different wind directions associated with the highest alkene measurements (**Figure 3.7.4**), but both were from the southeast. Taken together, it is likely that the source was east of the Milby Park, Cesar Chavez, and Deer Park monitors and southeast of the La Porte area (**Figure 3.7.5**).

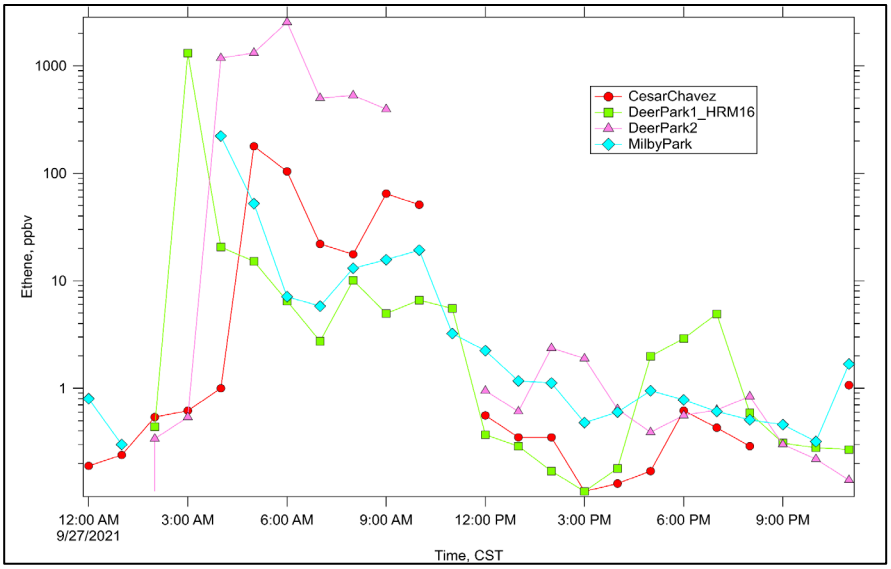

Figure 3.7.2: *Time series of ethylene mixing ratios observed at four TCEQ sites - Cesar Chavez, Deer Park 1 (HRM16), and Milby Park. All four sites concurrently measured elevated mixing ratios of ethylene.*

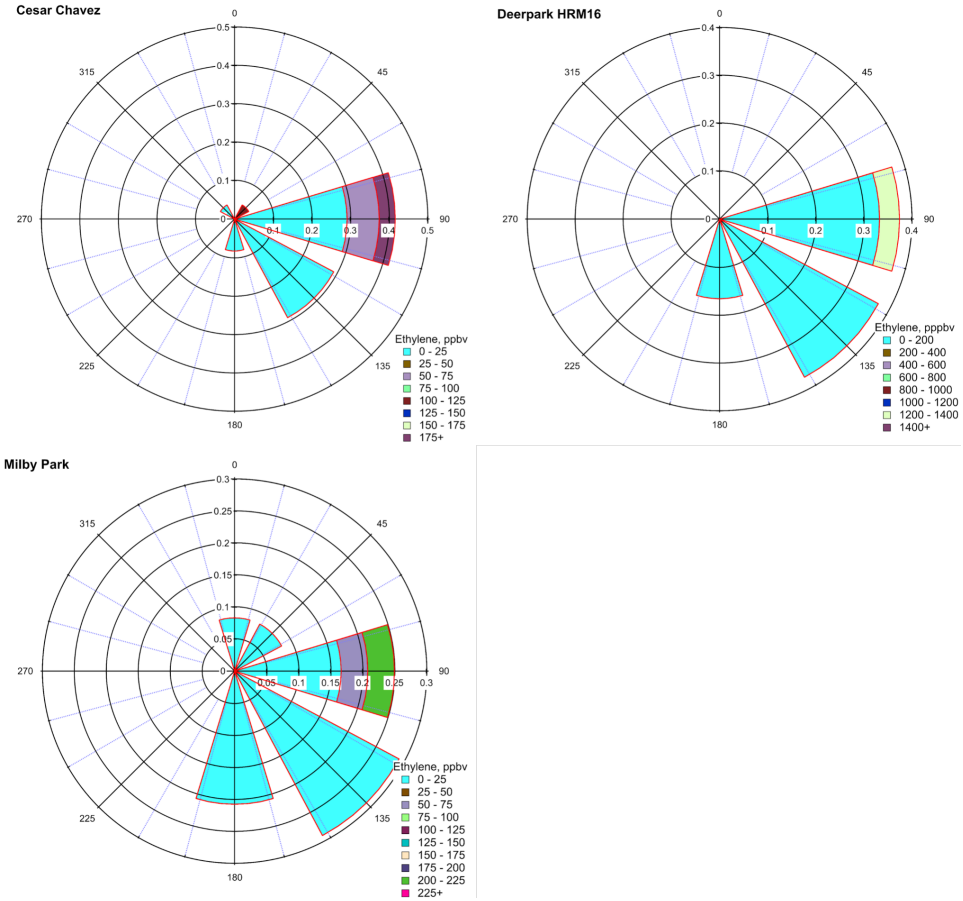

Figure 3.7.3: *Wind rose plots showing the frequency and direction of ethylene mixing ratios at Cesar Chavez, Deer Park 1 (HRM 16), and Milby Park. The mixing ratios of ethylene are color-coded, with the*

range of concentrations represented in the legend on the lower right corner. The colors correspond to different mixing ratios of ethylene, with each plot providing a visual wind pattern at each site.

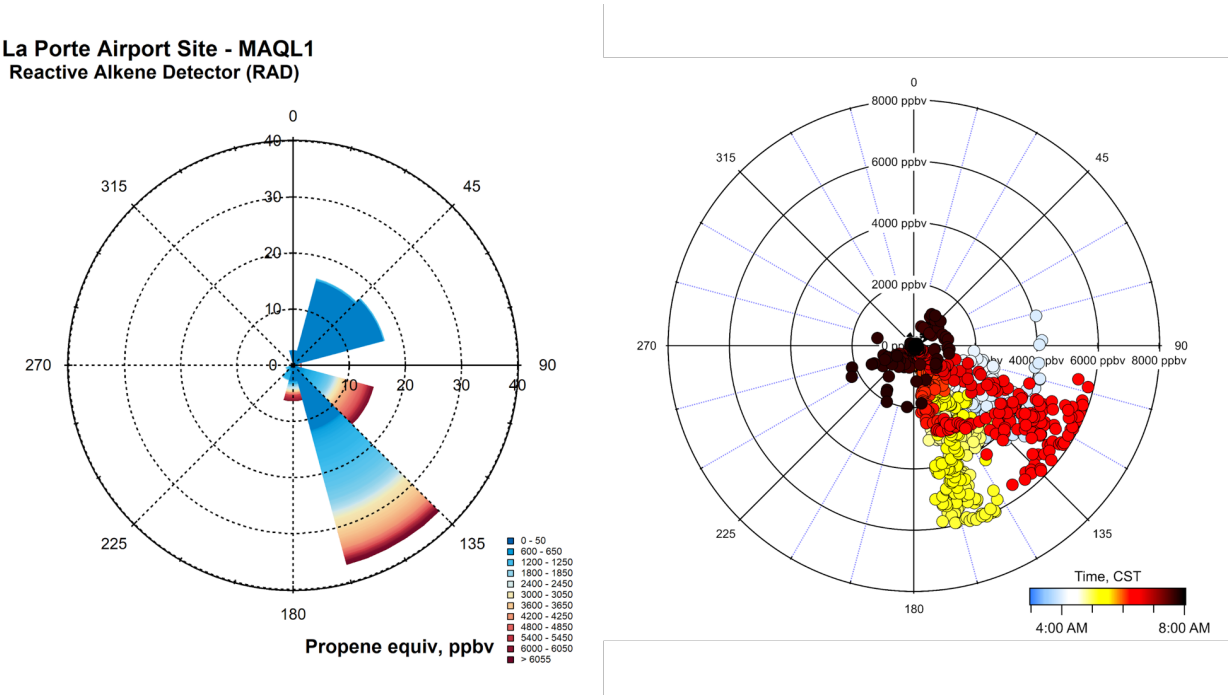

Figure 3.7.4: *The wind rose plot on the left shows the frequency and direction of propene equivalent mixing ratios as measured by the reactive alkene detector instrument at the La Porte airport, where the mobile lab was located. The plot is color-coded to represent mixing ratios of ethylene with the range of concentrations represented in the legend on the lower right corner. The wind rose plot on the right, also from La Porte airport, shows the frequency and direction of propene concentrations as measured by the reactive alkene detector. The radius represents the concentration, and the plotted data points are color-coded to represent the time of day, with colors corresponding to different times from 3 a.m. to 8 a.m. (CST).*

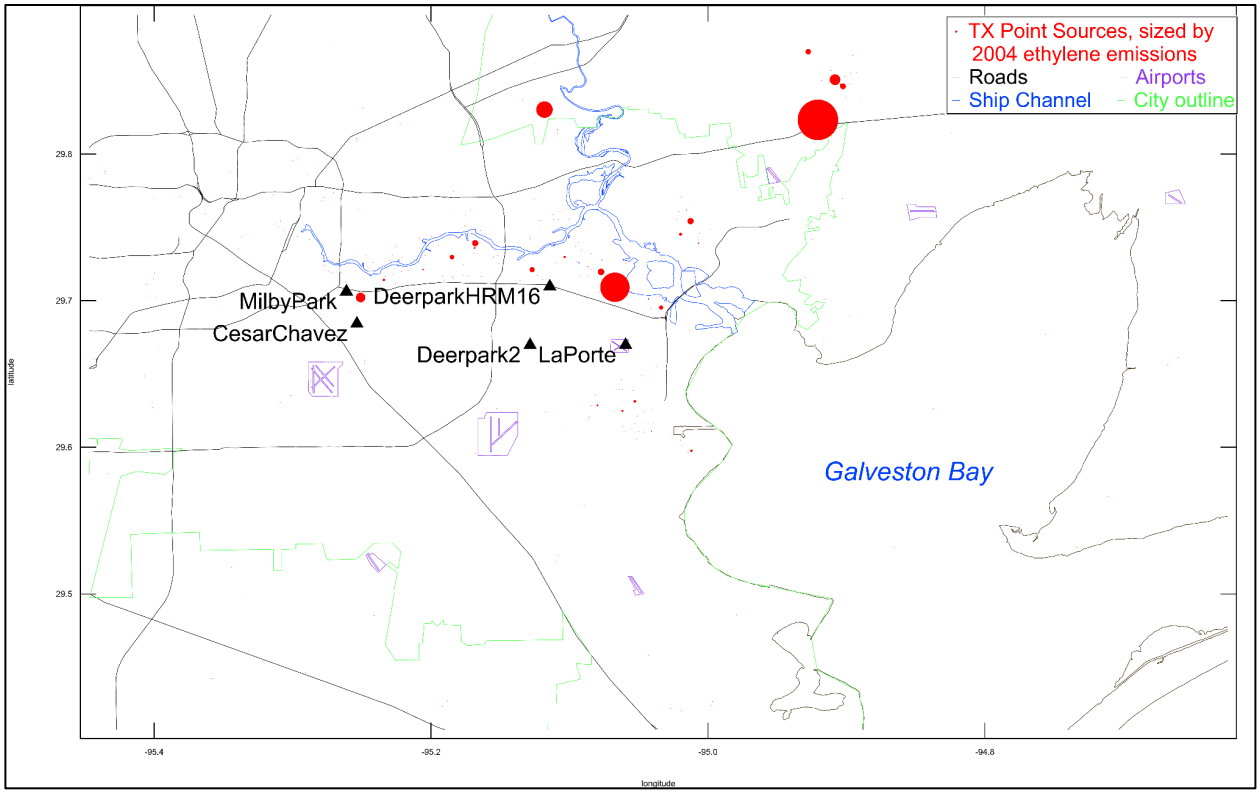

Figure 3.7.5: *Map plot showing the location of four sites in the Houston Ship Channel area where ethylene measurements were taken. The sites are Milby Park, Deer Park 1 (HRM16), Deer Park 2, and Cesar Chavez. The mobile lab was also located in La Porte airport.*

3.8 Shipping Emissions

3.8.1 Summary and Key Findings

- Evidence of shipping emissions was observed over Galveston Bay by the UH pontoon boat, including commercial and recreational watercraft.
- Crossing the Houston Shipping channels regularly accompanied ozone titration.
- Spatial Gradients of O_3 and NO_2 are less pronounced when examining the total reservoir of O_X (O_3 + NO_2)

3.8.2 Methodology

Periods of ozone titration while downwind of an active shipping channel were noted.

During the non-operational period, caused by Hurricane Nicholas, an O_X (O_3 + NO_2) instrument was installed in the UH pontoon boat instrument package. Combined with the O_3 measurement on board an estimate of NO_2, an indicator of possible shipping emission, was possible.

3.8.3 Results

3.8.3.1 Galveston Bay and Shipping Channel Observations

Although there are fewer mobile sources on the water than land, exhaust plumes from large ships were still encountered, mainly when operating the UH pontoon boat on Galveston Bay near the Houston Ship Channel. A clear example of one such plume is shown in (**Figure 3.8.1**). This observation was made while the UH Pontoon boat was anchored in north Galveston Bay in preparation for an ozonesonde launch. While at anchor, the UH science team on the pontoon boat smelled the distinctive smell of a ship exhaust from a passing ship, seen in (**Figure 3.8.2**). Although this was prior to the addition of the NO_2 photocell, an approximately 50 ppbv titration of O_3 is a clear indicator of the ship plume.

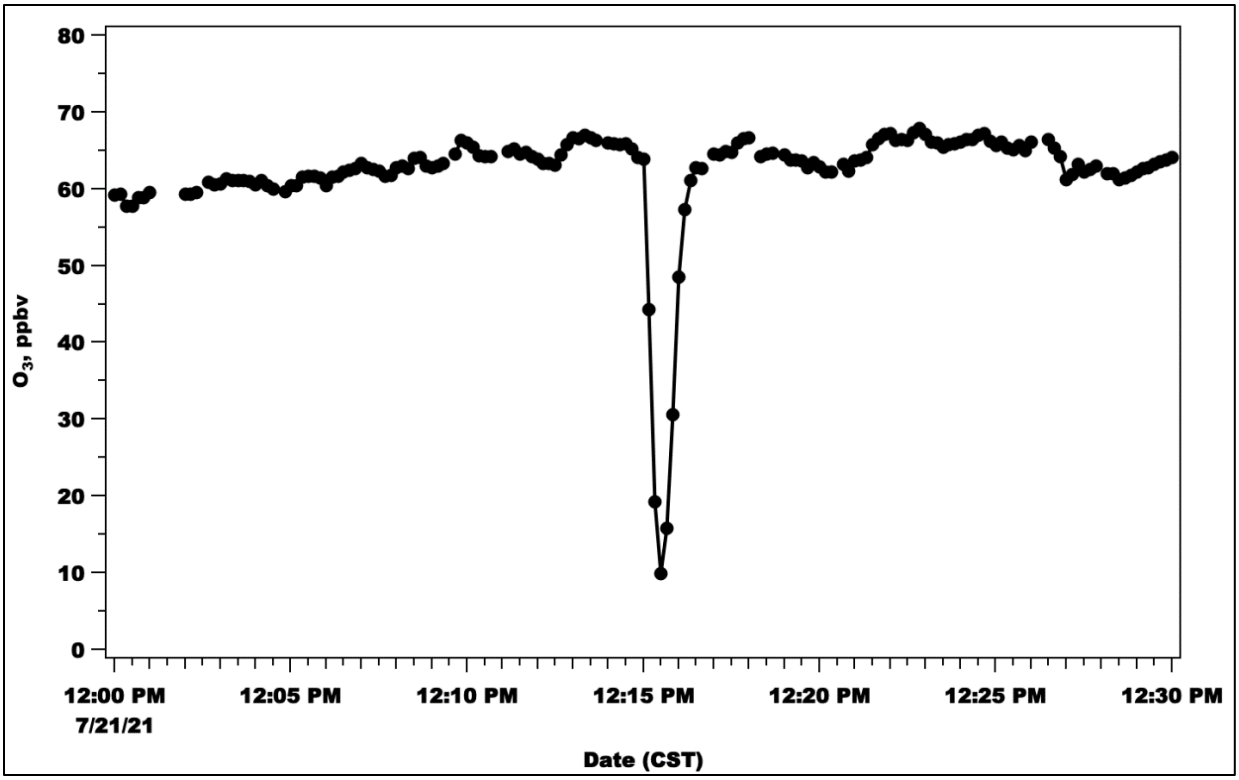

Figure 3.8.1: *Time-series of 10-second averaged O3 during encountered ship exhaust plume.*

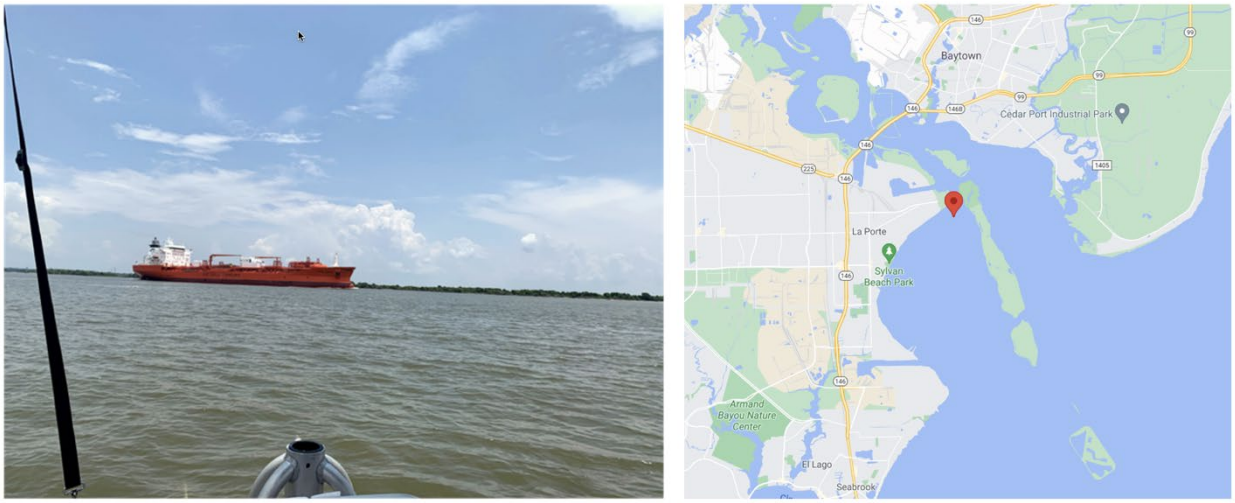

Figure 3.8.2: *Picture of a large commercial ship taken at 12:13p.m., just before the titration dip observed on the UH pontoon boat (left) and a map showing the location of the measurement as shown by the red pin in the map on the right.*

3.8.3.1.1 October 7, 2021

October 7, 2021 was designated as an 'Ozone Action Day' by TCEQ and was in a post-frontal environment with light offshore winds and abundant sunshine. The UH Pontoon Boat

recorded the highest over water ozone values (> 130 ppbv) during the campaign in the W/NW area of Galveston Bay. The approximate locations of the retrieved boundary layers from the ceilometer on the UH Pontoon Boat show the diurnal evolution of the boundary layer over and around Galveston Bay on 7 October 2021. The overnight to approximately two hours after sunrise period (~00:00–14:00 UTC) show a division with the nocturnal boundary layer measuring between 500–1000 m. and the residual layer between 1500–2000m. Just after sunrise a shallow marine boundary layer developed, measuring as low as 80m to begin the day, and appeared to trap surface emissions. This layer developed as the convective boundary layer with surface heating, growing to ~1700m. Just before sunset the convective boundary layer was cut-off from the surface with the redevelopment of the nocturnal boundary layer (**Figure 3.8.3**).

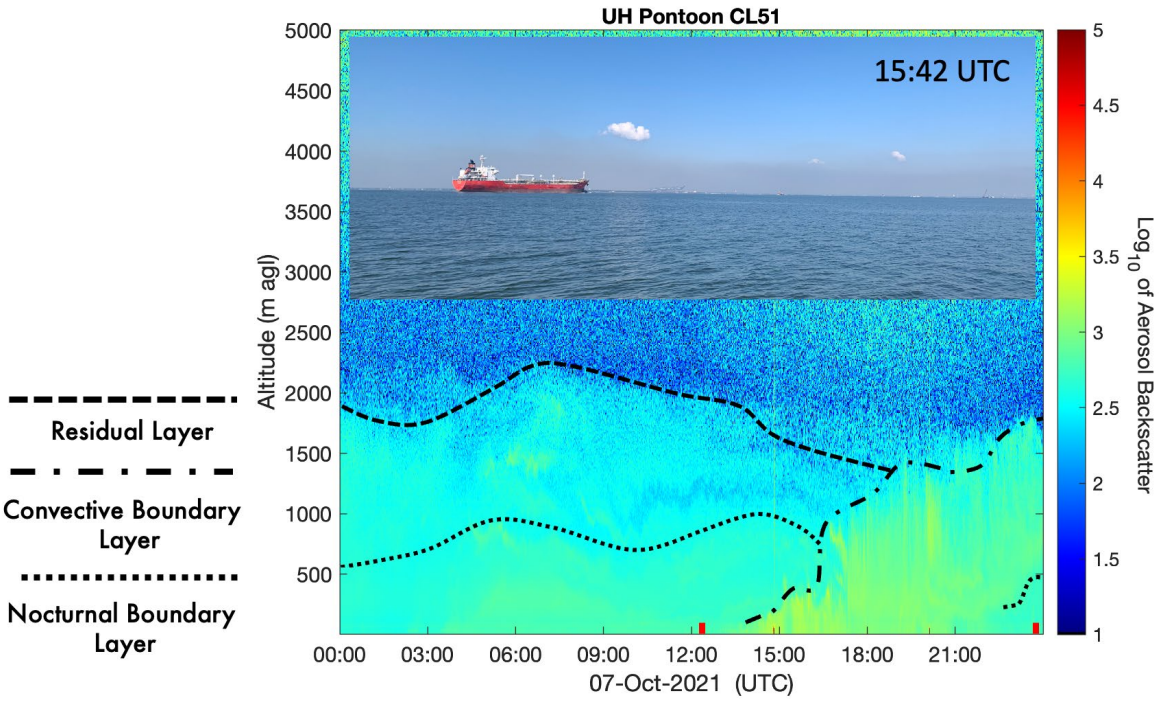

Figure 3.8.3: *Ceilometer backscatter data plotted versus altitude on 7 October 2021 showing a low mixing layer trapping emissions in the afternoon. The picture inset was taken over Galveston Bay at 15:42 UTC showing the visually identifiable low boundary layer. The black dashed lines are the approximate locations of boundary layers identified by the Vaisala CL-51 ceilometer and raw backscatter data. The red dashes on the x-axis are the timing of sunrise and sunset respectively.*

High NO_2 values observed over Galveston Bay on this day (**Figure 3.8.4**), both in broad and discrete plumes. The initial 8 km transect across the western portion of Galveston Bay, denoted with a black arrow in **Figure 3.8.4**, showed area-wide elevated levels of NO_2 that coincided with the minimum values of observed ozone and boundary layer height during the deployment.

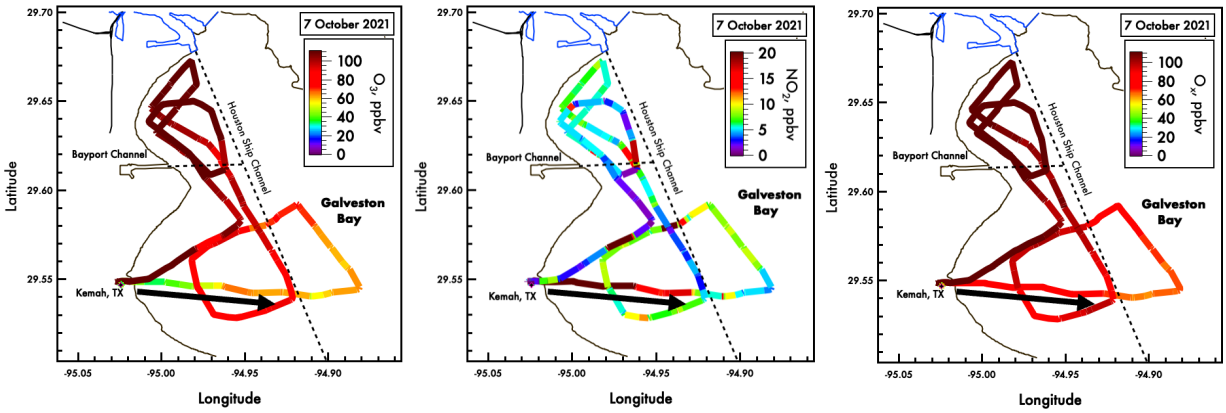

Figure 3.8.4: *Spatial plot of mobile ozone (left), NO_2 (middle) & O_x (O_3 + NO_2) (right) observations from the UH pontoon boat on Galveston Bay 7 October 2021. The black arrow on the plots highlights the initial 8 km transect across Galveston Bay with broadly elevated NO_2 over the water.*

The time series of ozone, NO_2 and Ox (O_3 + NO_2) in Figure 3 from the UH Pontoon Boat deployment on 7 October 2021 show the relationship between the trace gases. Initially, the NO_2 was elevated over a broad area of Galveston Bay, possibly resulting from morning rush-hour and ship emissions being trapped by a low marine boundary layer, while the ozone was suppressed. The O_X values during this initial transect did not show as much spatial variability as either ozone or NO_2. During the mid-morning to afternoon period, NO_2 concentrations generally decreased while photolysis rates and ozone concentrations increased.

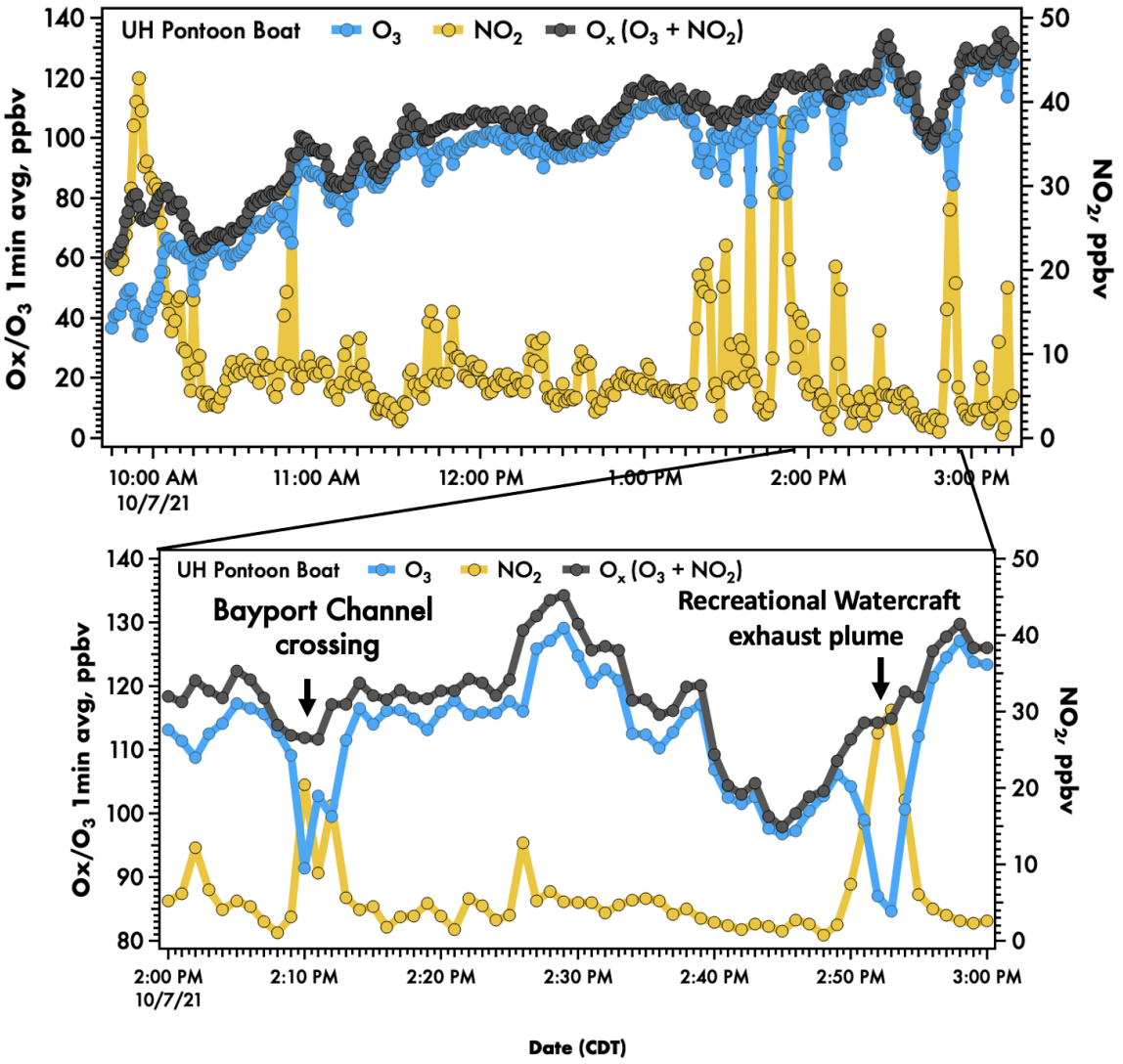

Figure 3.8.5: *Time-series of ozone and NO_2 during a sampling route on the UH Pontoon Boat from 7 October 2021.*

Occasionally, NO_2-rich exhaust plumes were encountered while nearby or crossing the ship channel, which coincided with a precipitous drop in ozone. Figure 3 shows two such instances that occurred during the 14:00–15:00 CDT hour while the UH Pontoon Boat was transiting back to dock. The first observation occurred while crossing the Houston Shipping Channel and titrated as much as 25 ppbv of ozone. A second ozone titration event occurred while traveling near a large recreational vessel and generated a similar response in ozone, titrating approximately 22 ppbv during the event. Notably, when examining the O_X concentrations during these events there is little response to the emissions. These observations illustrate the value of considering the total reservoir of O_X as titration and photolysis causes an exchange between species over the water.

3.9 Measurement intercomparisons between platforms

3.9.1 Summary and Key Findings

The trace gas species measured by the two MAQLs trended well. For ozone (O_3), nitric oxide (NO), reactive nitrogen compounds (NO_Y), and carbon monoxide (CO), all differences were within 15% and strong correlations ($r^2 > 0.80$) were observed. For nitrogen dioxide (NO_2), strong correlation was observed ($r^2 = 0.94$) with a 26% difference (slope = 1.26). For SO_2, a moderately good correlation ($r^2 = 0.66$) with a difference within 3% (slope = 0.97) was observed.

The volatile organic compound (VOC) species measured by the two MAQLs showed generally good consistency given individual measurement techniques of AeroLaser, RAD, AROMA, Peak Performer 1 and PTR-MS, when considering instrumental differences (e.g., detection limits, calibration differences and observation time periods). The PTRMS measurements on MAQL2 for benzene, toluene, formaldehyde, isoprene, ethyl benzene and xylenes, and propene, are compared to the equivalent measurement from the MAQL1-based AROMA, AeroLaser, PP1 and RAD. The AROMA vs. PTR-MS were within 5% for benzene and toluene, with a strong correlation ($r^2 > 0.80$) considering background and event periods together. Formaldehyde compared well between the AeroLaser and PTRMS with an $r^2 =$ 0.60. The average (± one standard deviation) was 4.52 ± 2.50 ppbv on the Aerolaser (MAQL1) and 4.98 ± 2.15 ppbv on the PTRMS (MAQL2) during the co-located period after removing all below DL measurements. For isoprene, which was measured by three instruments (AROMA, Peak Performer 1, and PTR-MS) on two platforms, the intercomparison results revealed confirmation of large isoprene event on 9/18 and good intercomparison for the periods of background isoprene. Styrene and the combined ethylbenzene and xylenes from AROMA had insufficient data points for more detailed intercomparison after points below DL were removed. However, available measurements trended well with PTR-MS from the time series perspective and indicated the capability of AROMA to serve as an event identifier for C8-Aromatics. An intercomparison of the RAD propene-equivalent and the PTRMS propene revealed good comparison in the time series during non-event time periods. A longer time series of VOC intercomparison would be helpful to better characterize the differences among the instruments.

The meteorological parameters and the photolysis rate of NO_2 from zenith direction measured by the two MAQLs trended well, with temperature, pressure, RH, and j_{NO2Z} all showing strong correlations ($r^2 > 0.90$). For pressure, RH and j_{NO2Z}, the differences between the measurements from two MAQLs were all within 7%. For temperature, the difference was slightly higher (27%) but mostly due to the period around 09/20 midnight.

3.9.2 Methodology

The UH Mobile Air Quality Lab 1 (MAQL1) and the Baylor Mobile Air Quality Lab 2 (MAQL2) were collocated at the Battleground site (29.75, -95.09) from 09/17/2021 11:30:00

to 09/20/2021 11:30:00 CST during the TRACER-AQ campaign. This area of the park is used as RV parking for caretakers and as such provides paved parking pads for the mobile labs as well as electrical service. These pads were adjacent to the Ship Channel water (35 m) and roughly 30–40 m away from the maintenance facilities. During the intercomparison one caretaker was parked between the two mobile labs and was actively working in the park, coming and going in his personal vehicle. As a result, the two mobile labs were roughly 15 m apart. Additionally, the MAQL1 inlets were raised to approximately 6 m elevation while the MAQL2 tower was able to raise its inlet to 10 m above ground.

Species that we intercompared included meteorological (MET) measurements (T, P, RH), the photolysis rate of NO_2 from zenith direction (j_{NO2Z}) measured by radiometers, trace gases (O_3, NO, NO_2, NO_Y, CO, SO_2), and speciated VOCs including formaldehyde, propene, benzene, toluene, combined ethylbenzene and xylenes, styrene, and isoprene from both MAQL1 and MAQL2. Instruments, detection limits (DL), and below DL percent of each species on both mobile labs were summarized in **Table 3.14**–**Table 3.17**.

The UH MAQL 1 and UH Pontoon boat conducted an intercomparison between platforms on 21 September 2021 from 09:39–11:27 CST near the end of the Texas City Dike. The UH pontoon boat, anchored in Galveston Bay, and the UH MAQL1 was parked at the end of the Texas City Dike. The intercomparison period consisted of a stationary and mobile phase. The species evaluated between the platforms consisted of: O_3, O_X, Boundary Layers (Ceilometer retrieved), Wind Speed and Wind Direction.

Table 3.14: *Detection limits and below DL percent of trace gas measurements from MAQL1 (original time resolution in black, averaged 5-min data for intercomparison in red).*

TGs	Instruments	DL (10s, ppbv)	Below DL %	DL (5min, ppbv)	Below DL %
CO	Los Gatos	0.51	0	0.27	0
NO	Air Quality Design (AQD)	0.06	4.02	0.01	0.09
NO_2	AQD	0.07	0.02	0.02	0
NO_y	Thermo Sci.	0.43	0.06	0.21	0
O_3	2B Tech	4.73	6.25	3.04	3.6
SO_2	Thermo Sci.	0.97	51.53	0.47	8.76

Table 3.15: *Detection limits and below DL percent of VOC measurements from MAQL1 (original time resolution in black, averaged 5-min data for intercomparison in red).*

VOCs	Instruments	DL (10s, ppbv)	Below DL %	DL (5min, ppbv)	Below DL %
HCHO	AeroLaser	0.21	1.55	0.11	0.78
Propene (eq)	RAD Hills Sci.	3.12	21.47	0.95	0.21
Isoprene	Peak Performer 1			0.2	40.16
		DL (10min, ppbv)	**Below DL %**		
Benzene	AROMA	0.0375	9.42		
Toluene	AROMA	0.1875	51.8		
Ethylbenzene	AROMA	0.375	87.58		
Xylene	AROMA	0.375	63.96		
Styrene	AROMA	1.875	99.91		
Isoprene	AROMA	0.375	79.24		

Table 3.16: *Detection limits and below DL percent of trace gas measurements from MAQL2.*

TGs	Instruments	DL (5min, ppbv)	Below DL %
CO	Thermo Sci.	16.4	0.06
NO	Thermo Sci.	0.13	31.00
NO_2	Thermo Sci.	0.38	0.16
NO_Y	Thermo Sci.	0.66	0.15
O_3	Thermo Sci.	1.06	5.01
SO_2	Thermo Sci.	0.17	36.79
CO_2	LiCor Li-7000	1.15	0

Table 3.17: *Detection limits and below DL percent of VOC species measured by PTR-MS from MAQL2 that are relevant for intercomparison. A finalized 5-min DL and below DL % for all PTR-MS species will be provided in the final report.*

VOCs	Instrument	DL (30s, ppbv)	Below DL %
Ethene	PTR-MS	2.71	29.42
HCHO	PTR-MS	2.26	25.83
Propene	PTR-MS	0.41	1.3
1,3-Butadine	PTR-MS	0.18	13.92
Isoprene	PTR-MS	0.26	26.53
Benzene	PTR-MS	0.26	33.13
Toluene	PTR-MS	0.29	39.12
Styrene	PTR-MS	0.43	85.68
C8-Aromatics (Ethylbenzene and Xylenes)	PTR-MS	0.47	56.9

3.9.3 Results

3.9.3.1 MAQL1 and MAQL2

Ozone (O_3) measurements from the two MAQLs trended well (**Figure 3.9.1**; $r^2 = 0.97$, slope = 1.05). The average (± one standard deviation) was 30.19±17.33 ppbv on MAQL1 and 31.01 ± 18.82 ppbv on MAQL2 during the collocated period after removing all below DL measurements.

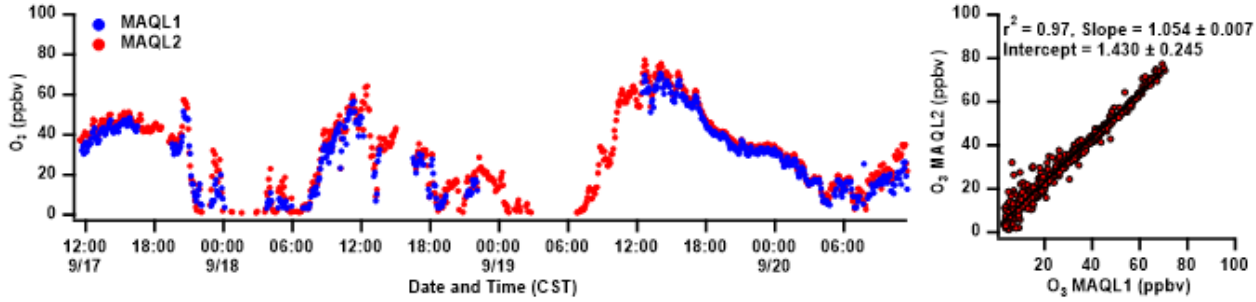

Figure 3.9.1: *Time series (left) and scatter plot (right) of O_3 measured by MAQL1 and MAQL2 during the collocated time period.*

Nitric oxide (NO) measurements from the two MAQLs trended well (**Figure 3.9.2**; $r^2 = 0.82$, slope = 0.99). The average (± one standard deviation) was 7.31 ± 14.50 ppbv on MAQL1 and 11.50 ± 15.96 ppbv on MAQL2 during the collocated period after removing all below DL

measurements. The higher average from MAQL2 was due to its higher DL, which eliminated measurements below 0.13 ppbv during the calculations.

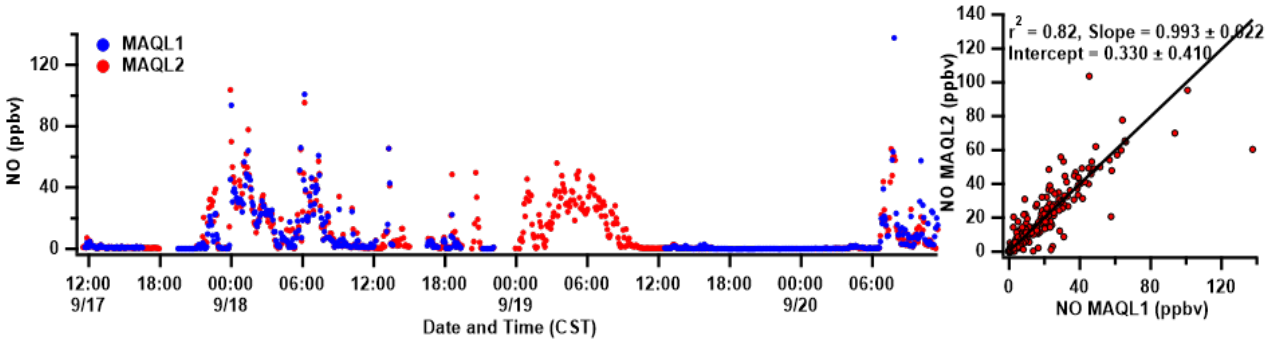

Figure 3.9.2: *Time series (left) and scatter plot (right) of NO measured by MAQL1 and MAQL2 during the collocated time period.*

Nitrogen dioxide (NO_2) measurements from the two MAQLs trended well (**Figure 3.9.3**; r^2 = 0.94, slope = 1.26). The average (± one standard deviation) was 15.35 ± 12.51 ppbv on MAQL1 and 18.61 ± 15.17 ppbv on MAQL2 during the collocated period after removing all below DL measurements.

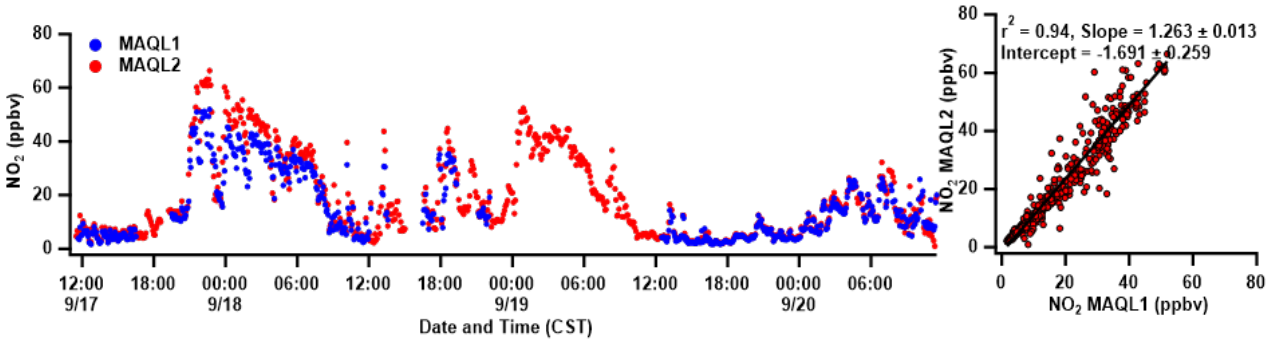

Figure 3.9.3: *Time series (left) and scatter plot (right) of NO_2 measured by MAQL1 and MAQL2 during the collocated time period.*

Reactive nitrogen compounds (NO_Y) measurements from the two MAQLs trended well (**Figure 3.9.4**; r^2 = 0.91, slope = 1.13). The average (± one standard deviation) was 23.72 ± 23.78 ppbv on MAQL1 and 28.22 ± 26.43 ppbv on MAQL2 during the collocated period after removing all below DL measurements.

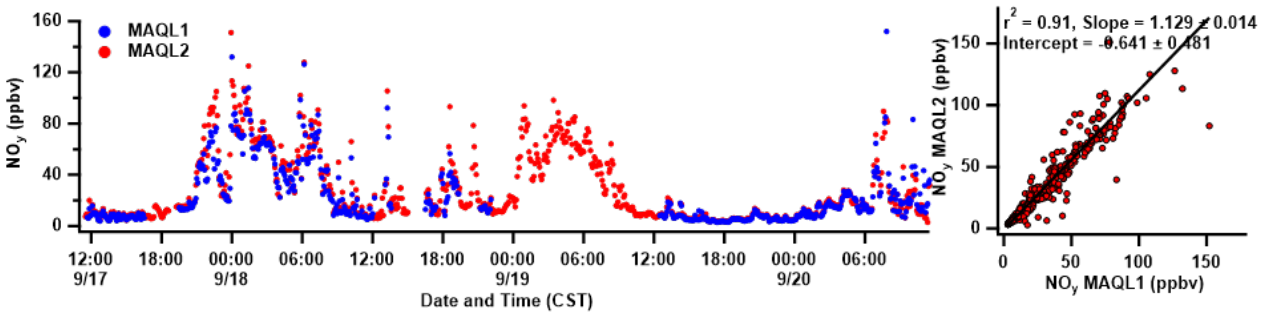

Figure 3.9.4: *Time series (left) and scatter plot (right) of NO_y measured by MAQL1 and MAQL2 during the collocated time period.*

Carbon monoxide (CO) measurements from the two MAQLs trended well (**Figure 3.9.5**; r^2 = 0.99, slope = 0.94). The average (± one standard deviation) was 209.95 ± 78.25 ppbv on MAQL1 and 199.83 ± 87.56 ppbv on MAQL2 during the collocated period after removing all below DL measurements.

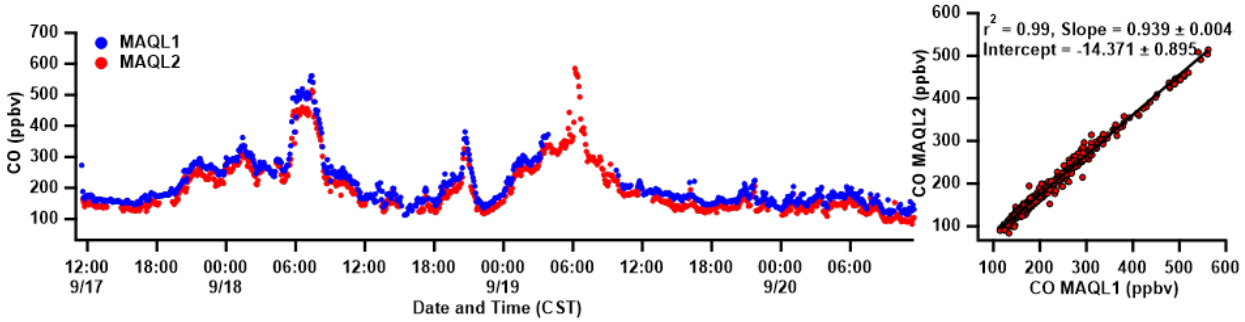

Figure 3.9.5: *Time series (left) and scatter plot (right) of CO measured by MAQL1 and MAQL2 during the collocated time period.*

Sulfur dioxide (SO_2) measurements from the two MAQLs trended well (**Figure 3.9.6**; r^2 = 0.66, slope = 0.97). The average (± one standard deviation) was 1.49 ± 1.46 ppbv on MAQL1 and 0.90 ± 1.38 ppbv on MAQL2 during the collocated period after removing all below DL measurements. Since 80% of the SO_2 from measured by MAQLs during the collocated period were less than 2 ppbv (80th percentile above DL SO_2 was 1.15 ppbv for MAQL1 and 1.98 ppbv for MAQL2), the insufficient spread of ambient SO_2 limited the robustness of linear fitting.

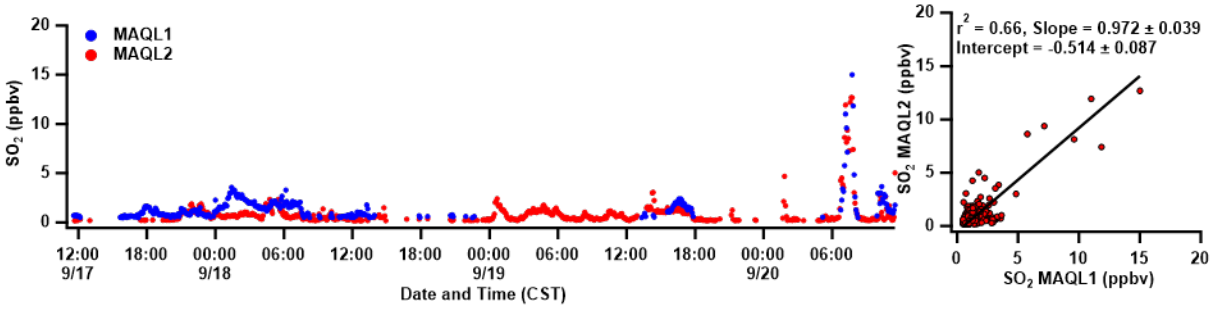

Figure 3.9.6: *Time series (left) and scatter plot (right) of SO_2 measured by MAQL1 and MAQL2 during the collocated time period.*

The time series of the benzene measured by the two instruments trended well (**Figure 3.9.7**). We saw a tight correlation between the two instruments (r^2 = 0.80, slope = 1.04). The high benzene loading periods were observed around 09/18 00:00 CST by both instruments and 09/20 00:00 CST by the PTR-MS while the speciated AROMA measurement was not available. Benzene level increased between the midnight and morning of 09/19, the magnitude of this increase above the intercomparison was similar to other VOCs (e.g. toluene, combined ethylbenzene and xylenes). The average (± one standard deviation) was 5.02 ± 7.74 ppbv for AROMA on MAQL1 and 6.11 ± 8.98 ppbv for PTR-MS on MAQL2.

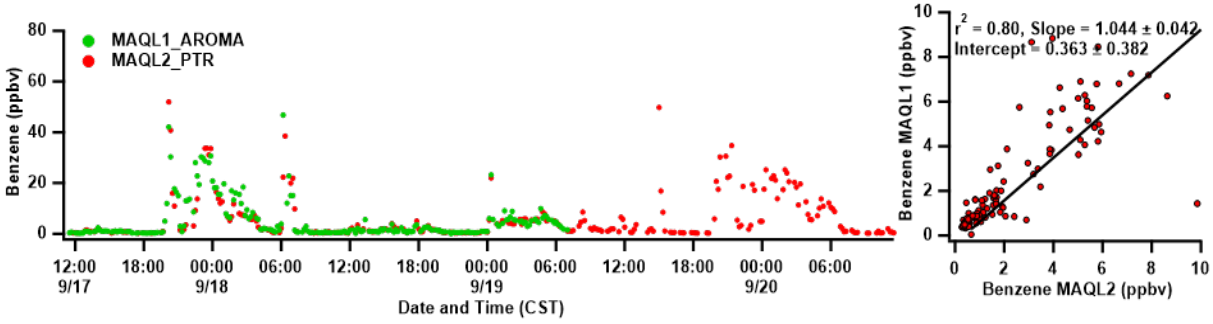

Figure 3.9.7: *Time series (left) and scatter plot (right) of benzene measured by MAQL1 and MAQL2 during the collocated time period.*

The time series of the toluene measured by the two instruments trended well (**Figure 3.9.8**). Excluding 2 outliers from the comparison, we saw an even better fit (r^2 = 0.83, slope = 1.00). Two high toluene loading periods were observed around 09/18 00:00 to 06:00 and 09/19 00:00 to 06:00 CST. A third peak in the evening till late night of 09/19 was observed by the PTR-MS while the speciated AROMA measurement was not available. The average (± one standard deviation) was 1.31 ± 1.19 ppbv for AROMA on MAQL1 and 1.28 ± 1.17 ppbv for PTR-MS on MAQL2.

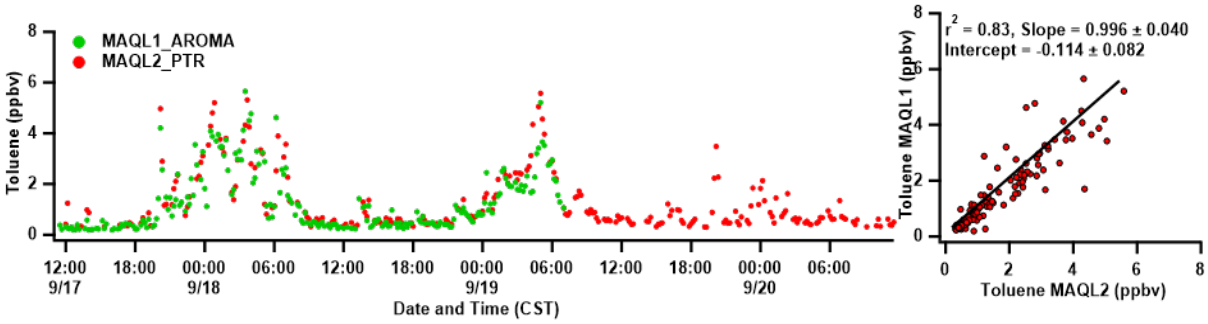

Figure 3.9.8: *Time series (left) and scatter plot (right) of toluene measured by MAQL1 AROMA and MAQL2 PTR-MS during the collocated time periods.*

Formaldehyde (HCHO) measurements from the PTRMS and AeroLaser (MAQL2 and MAQL1, respectively) trended well (**Figure 3.9.9**; $r^2 = 0.60$, slope = 1.30). The average (± one standard deviation) was 4.52 ± 2.50 ppbv on the AeroLaser (MAQL1) and 4.98 ± 2.15 ppbv on the PTRMS (MAQL2) during the collocated period after removing all below DL measurements.

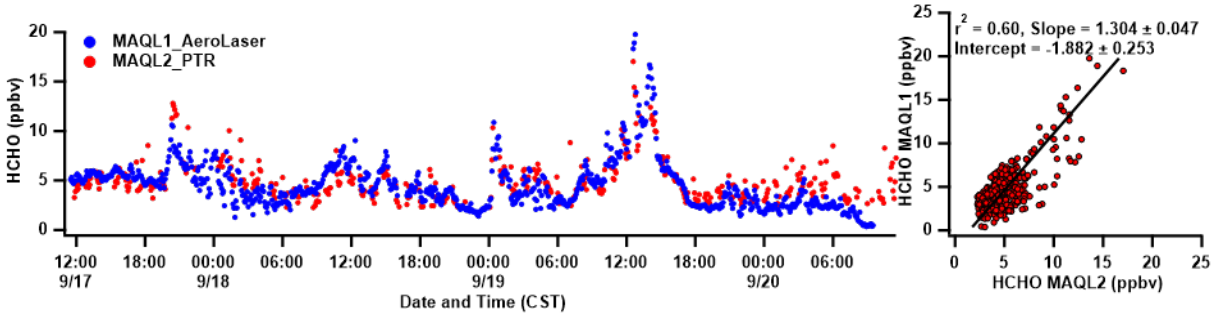

Figure 3.9.9: *Time series (left) and scatter plot (right) of HCHO measured by MAQL1 and MAQL2 during the collocated time period.*

Isoprene measured by AROMA on MAQL1 was in speciated mode and reported data in 10-minute time interval based on 2 minute sampling and 8 min analysis, while that measured by Peak Performer 1 on MAQL1 and PTR-MS on MAQL2 were reported in 5-minute time resolution. To enable intercomparison, we remapped all isoprene data to 10-min time resolution. All three instruments saw high peaks of isoprene at Battleground and these high isoprene episodes occurred multiple times (e.g. 09/17/2021 20:30 to 09/18/2021 03:00, and 09/19 00:00 to 09/16 06:00). By doing the intercomparison, we found that isoprene measured by AROMA had an upper detection limit of 30 ppbv. However, VOCs measured during the TRACER-AQ field campaign were rarely above 30 ppbv. Mapping the time series of propene (equivalent) measured by RAD on MAQL1 (**Figure 3.9.10**) confirmed the elevated propene-equivalent in **Figure 3.9.13** was influenced by isoprene and potentially other reactive alkenes, and all instruments successfully identified the event.

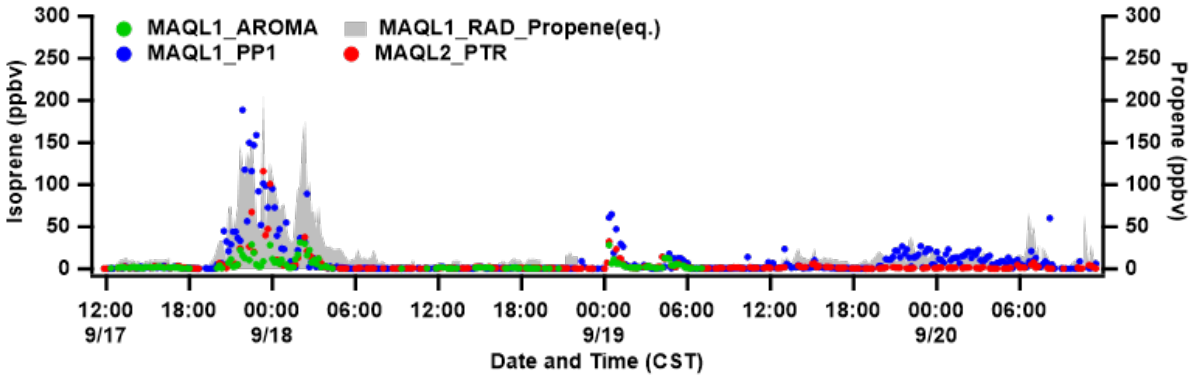

Figure 3.9.10: *Top: Isoprene measured by three instruments – MAQL1 AROMA, Peak Performer 1, and MAQL2 PTR-MS on the left axis, and propene (equivalent) measured by MAQL1 RAD on the right axis during the collocated time period.*

When excluding the high isoprene periods (> 3 ppbv), we saw improved trends among the three instruments (PTRMS, PP1 and AROMA, **Figure 3.9.11**). In specific, for the two instruments with sufficient above DL data points, a moderately good correlation (r^2 = 0.41, slope = 0.98 for PTR-MS vs. Peak Performer 1) was observed. The average (± one standard deviation) was 1.03 ± 0.68 ppbv for PTR-MS on MAQL2, 1.00 ± 0.71 ppbv for Peak Performer 1 on MAQL1 during the collocated period. Linear fit was not performed between AROMA and other instruments because 79% of its data were below DL. A longer intercomparison study is needed between the AROMA and PTRMS to understand this relationship.

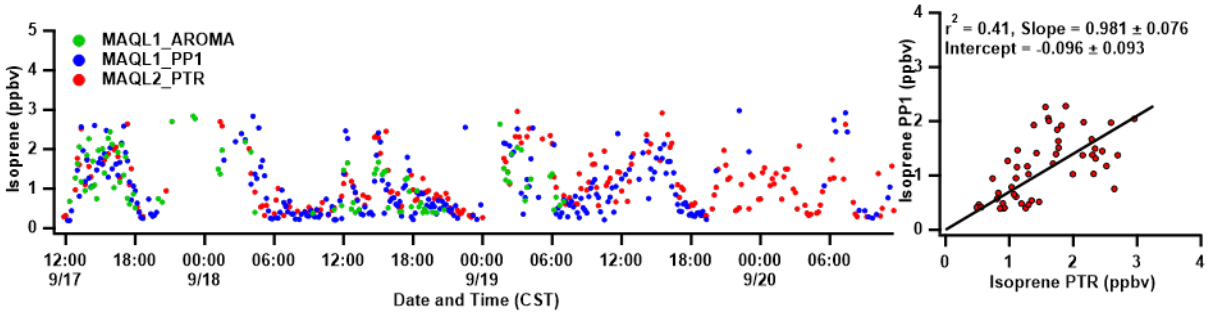

Figure 3.9.11: *Intercomparison of isoprene measured by three instruments – MAQL1 AROMA, Peak Performer 1, and MAQL2 PTR-MS – during the collocated time period excluding the periods when isoprene concentration was greater than 3 ppbv (left) and the scatter plot between Peak Performer 1 and PTR-MS (right). The AROMA was not in speciation mode starting at ~7:00 a.m. on 9/19.*

The time series of combined ethylbenzene and xylenes (denoted by C8-Aromatics in **Table 3.17**) measured by the two platforms trended well (**Figure 3.9.12**). But 87.58% of the ethylbenzene and 63.96% of xylene measured by the AROMA were below the DL (**Table 3.15**). For C8-aromatics, 56.90% of the PTR-MS measurement were below the DL. The insufficient above DL points hindered more detailed intercomparison. Even though, two high loading periods were still detected by both instruments around 09/18 00:00 to 06:00 and 09/19 00:00 to 06:00 CST. The difference between the instruments (consistently higher

mixing ratios reported by the AROMA) needs to be investigated more thoroughly as these two instruments have different methods for compound detection, in addition to differences between the platforms for VOCs (e.g. inlets). The capability of AROMA to serve as the event identifier was revealed for C8-Aromatics, while the PTR-MS with higher precision and time resolution supplied more above DL data points that would be useful for future ozone modeling.

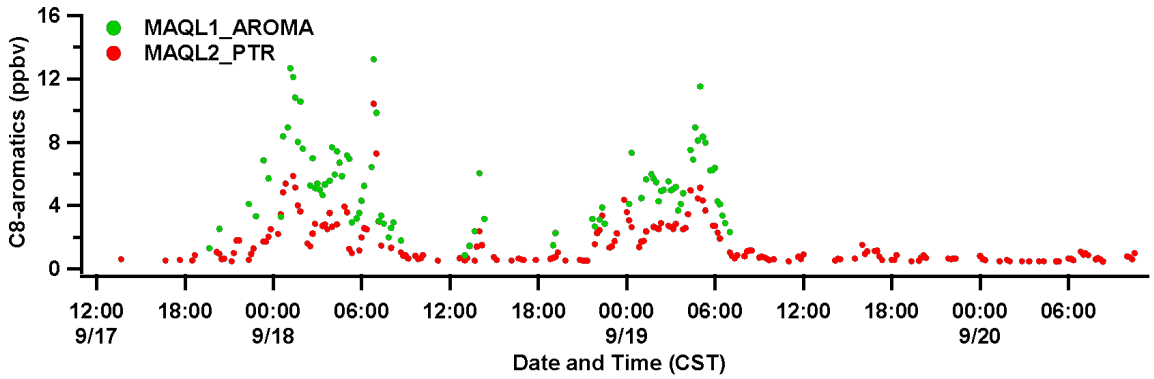

Figure 3.9.12: Time series of combined ethylbenzene and xylene measured by MAQL1 and MAQL2 during the collocated time period.

Styrene was measured by the AROMA on MAQL1 and PTR-MS on MAQL2. However, due to its low ambient level, 99.91% of the AROMA styrene and 85.68% of the PTR-MS styrene were below their corresponding DL. Detailed intercomparison on the insufficient paired dataset was not possible to perform.

Propene measurements from the two instruments (PTRMS and RAD) generally trended together, except for the high loading plume around 09/18 00:00 (**Figure 3.9.13**). RAD on MAQL1 reported a propene (equivalent) level greater than 150 ppbv yet the PTR-MS on MAQL2 remained below 40 ppbv of propene. However, since the RAD measured a combination of propene, ethene, 1,3-butadiene and isoprene, it was likely that the plume was driven by VOCs other than propene. This was also implied in the isoprene comparison that at the same time, an elevated isoprene plume was observed, and PTR-MS response (**Figure 3.9.10** in red) peaked at around 100 ppbv. Excluding this high loading plume from the comparison, the average (± one standard deviation) was 11.07 ± 6.00 ppbv on MAQL1 and 12.52 ± 9.87 ppbv on MAQL2 during the collocated period. Given the different mechanisms of detecting VOCs between the two instruments, further quantitative comparisons are not warranted at this time. Meanwhile, the collaborators will find every possible opportunity to improve the quality of intercomparison in the final report.

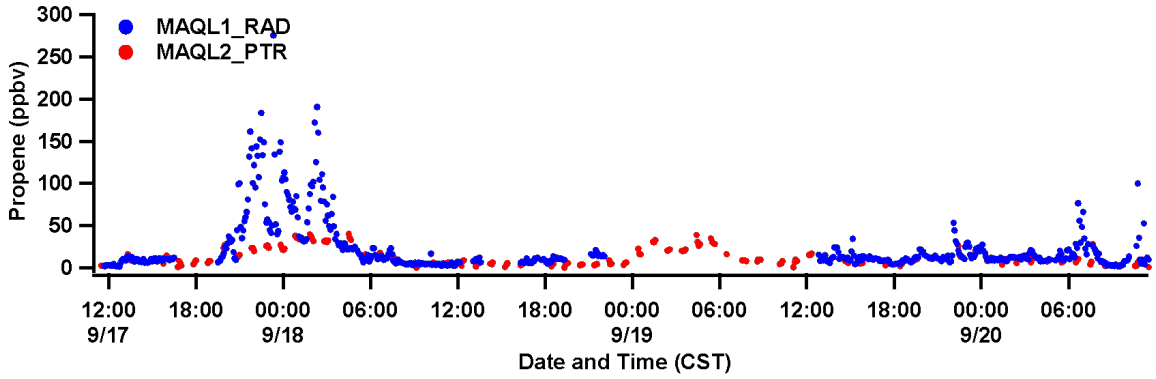

Figure 3.9.13: *Time series of propene (equivalent) measured by MAQL1 and propene measured by MAQL2 during the collocated time periods.*

Temperature (T) measurements from the two MAQLs trended well (**Figure 3.9.14**; r^2 = 0.90, slope = 1.27). The average (± one standard deviation) was 27.24 ± 2.80℃ on MAQL2 and 27.90 ± 2.23℃ on MAQL1. Some discrepancies were seen around the midnight of 09/20.

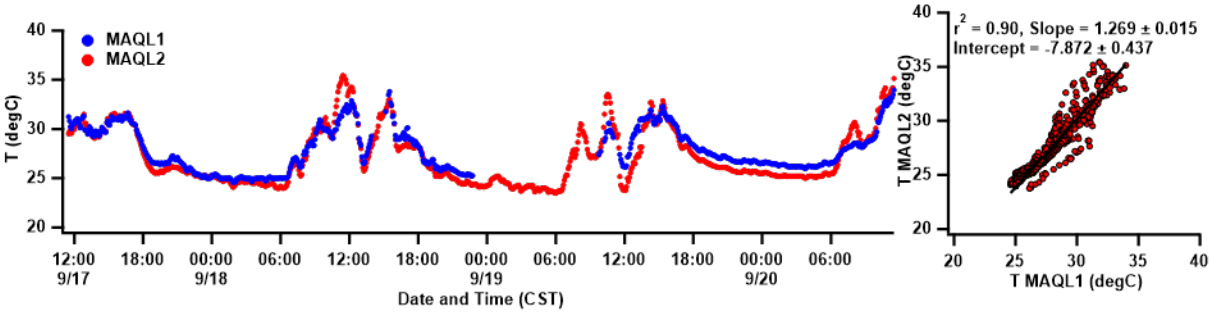

Figure 3.9.14: *Time series (left) and scatter plot (right) of temperature (T) measured by MAQL1 and MAQL2 during the collocated time period.*

Pressure (P) measurements from the two MAQLs trended well (**Figure 3.9.15**; r^2 = 0.95, slope = 1.06). The average (± one standard deviation) was 1013.02±1.70 mbar on MAQL2 and 1010.55±1.75 mbar on MAQL1. The average difference was less than 2.5 mbar.

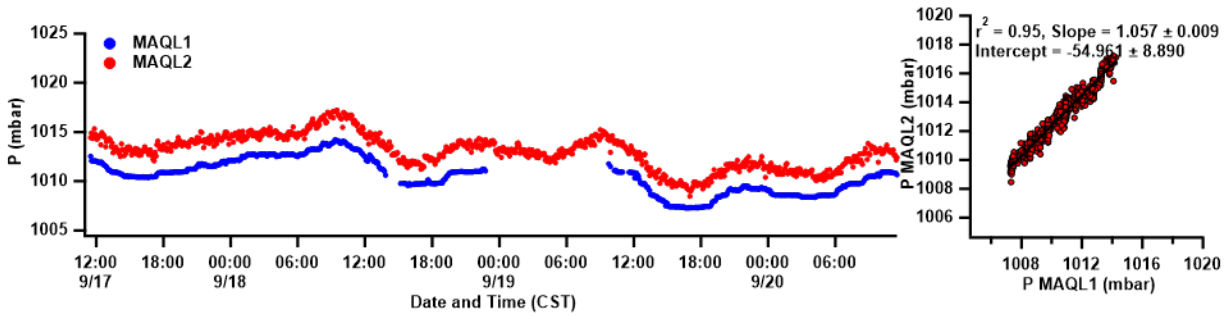

Figure 3.9.15: Time series (left) and scatter plot (right) of pressure (P) measured by MAQL1 and MAQL2 during the collocated time period.

Relative humidity (RH) measurements from the two MAQLs trended well (**Figure 3.9.16**; r^2 = 0.92, slope = 1.03). The average (± one standard deviation) was 72.48 ± 11.07 on MAQL2 and 72.82 ± 11.00 on MAQL1.

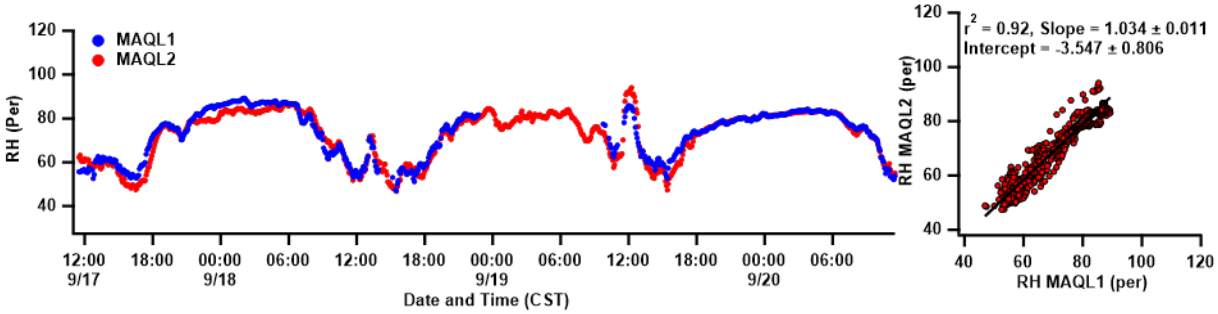

Figure 3.9.16: *Time series (left) and scatter plot (right) of relative humidity (RH) measured by MAQL1 and MAQL2 during the collocated time period.*

The photolysis rate of NO_2 from the zenith direction (j_{NO2Z}) measurements from the two MAQLs trended well **Figure 3.9.17**; r^2 = 0.95, slope = 1.06). The average (± one standard deviation) was 0.00232 ± 0.00311 s^{-1} on MAQL2 and 0.00207 ± 0.00297 s^{-1} on MAQL.

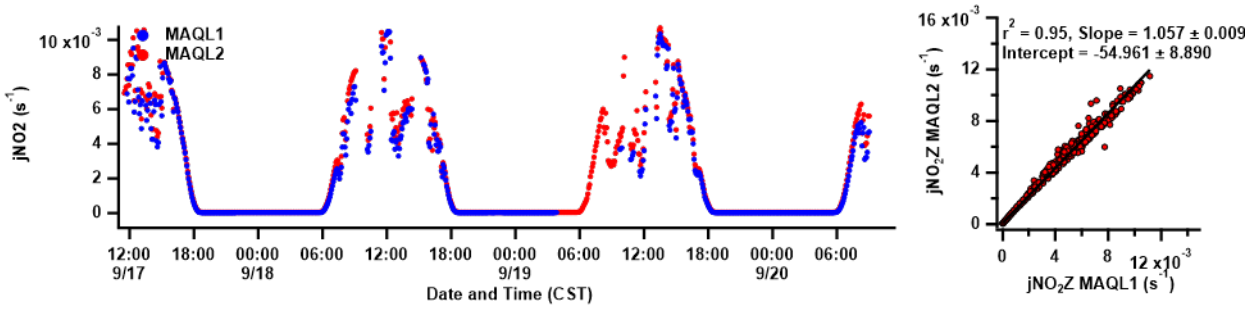

Figure 3.9.17: *Time series (left) and scatter plot (right) of j_{NO2Z} measured by MAQL1 and MAQL2 during the collocated time period.*

3.9.3.2 MAQL1 and the UH Pontoon Boat

To assess the accuracy of measurements between platforms as well as small spatial scale gradients at the land-water interface a sampling period between the UH pontoon boat, anchored in Galveston Bay, and the UH MAQL1, parked at the end of the Texas City Dike, was completed on 21 September 2021. The following plots are the results from that intercomparison which consisted of a 1-hour stationary period from 09:39–10:41 CST followed by two mobile passes along the Texas City Dike and the adjacent water of Galveston Bay, while the labs matched speeds from 10:42–11:17 CST. The Texas City Dike is a popular fishing destination and while parked at the end little traffic is encountered, while traversing the length of the Dike, which is approximately 4 miles long, vehicular traffic is encountered. The parameters that were compared during the sampling period are in **Table 3.18** below.

Limitations of this comparison were the relatively short lived-nature of the period during which sampling occurred and the time-period in which it did occur was a day with regionally low O_3 and NO_2 as well as light, southerly winds. Furthermore, the NO_2 measurement comparison was limited by the short sampling period and low dynamic range (a clean air quality day) of observed values, with 96% of the data falling below detection limit for the UH Pontoon system. However, the O_X (O_3 + NO_2) measurement was a better evaluation of the two platforms. Additionally, the UH pontoon boat and UH MAQL1 mobile labs were not able to be directly collocated due to the different nature of the labs which operated over water and land respectively.

Table 3.18: *Trace gas and meteorological variables, detection limits and percent of data within the detection limit for the instruments used to make the observations on the UH pontoon boat.*

Variable Compared	Instrument	DL (1min, ppbv)	Below DL%
O_3	Thermo 49c	2.30	0.0
O_X	Thermo 49i	2.01	0.0
Wind Speed	Airmar 220wx	0.1 m/s	0.0
Wind Direction	Airmar 220wx	0.1	0.0

Table 3.19: *Trace gas and meteorological variable statistical summary for the overall comparison period.*

Variable Compared	MAQL1	UH Pontoon Boat
O_3 (ppbv)	15.9 ± 3.6	21.5 ± 3.5
O_x (ppbv)	16.8 ± 3.8	20.5 ± 3.7
Wind Speed (mph)	5.9 ± 2.6	9.2 ± 1.9
Wind Direction (°)	213 ± 80	230 ± 12
Boundary Layer – 1 (meters)	425 ± 109	590 ± 236
Boundary Layer – 2 (meters)	942 ± 101	888 ± 118

The inter-comparison between the UH pontoon boat and the MAQL1 labs showed reasonable agreement of the O_3 trend with the UH pontoon boat consistently recording higher ozone during the sampling period (**Figure 3.9.18**). The mobile and stationary periods did show significant differences with an increasing O_3 trend seen at both platforms throughout.

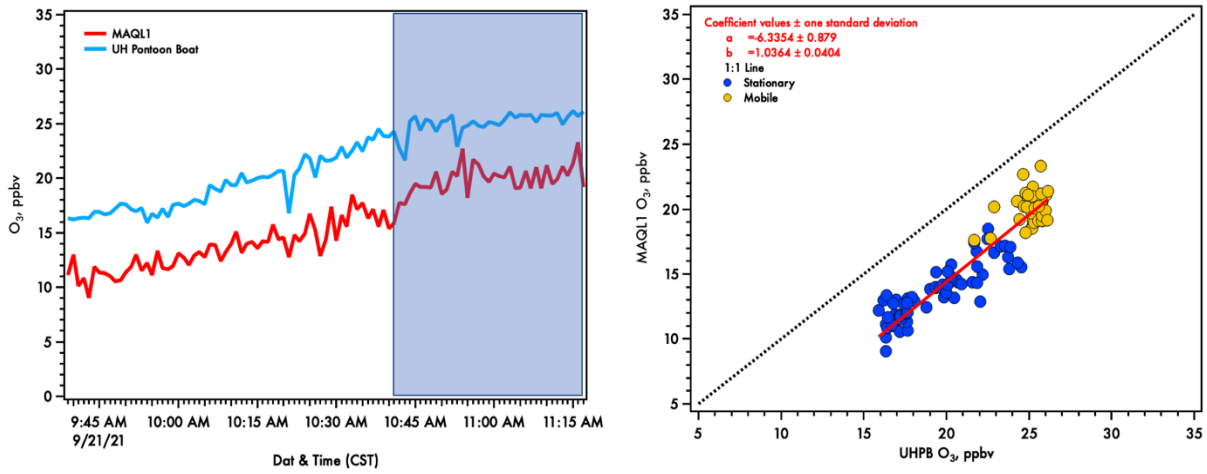

Figure 3.9.18: *Time Series (left) and scatter plot (right) of O_3 values during the intercomparison. Periods of mobile sampling are highlighted on the time-series and marked with different colors on the scatter plot.*

The comparison of O_X between the platforms in **Figure 3.9.19** show the UH pontoon boat measured higher O_X throughout the sampling period. These results are very similar to the O_3 comparison as the comparison period was a clean period with little NO_2.

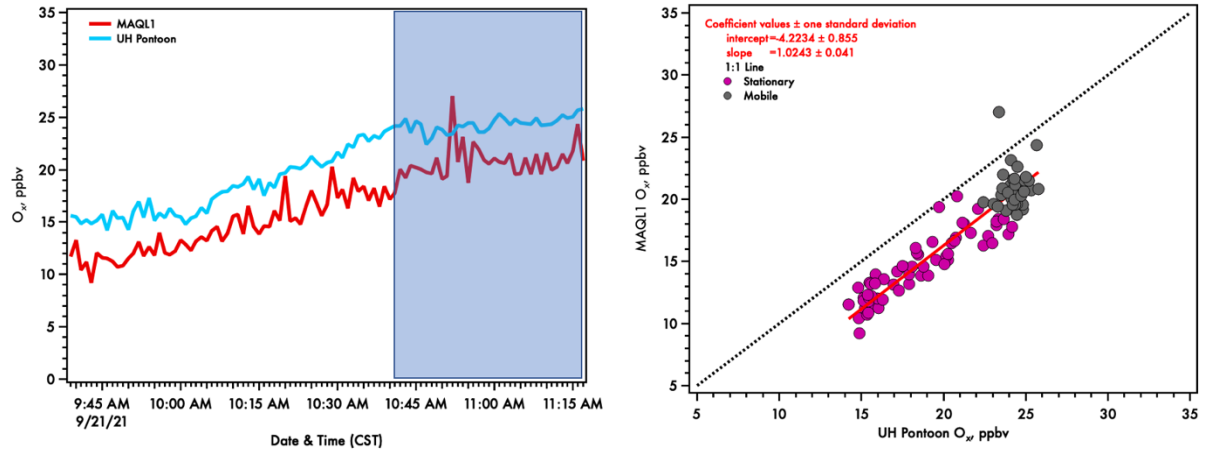

Figure 3.9.19: *Time Series (left) and scatter plot (right) of O_X values during the intercomparison. Periods of mobile sampling are highlighted on the time-series and marked with different colors on the scatter plot.*

The spatial plots of O_3 and O_X from the two mobile labs in **Figure 3.9.20** does show the consistent difference in measured values over a roughly 400 m distance at the land-water interface. Comparison of the O_X measurements is restricted because of the low NO_2 during the sampling period which was below the threshold of the UH pontoon system for the majority of the sampling period.

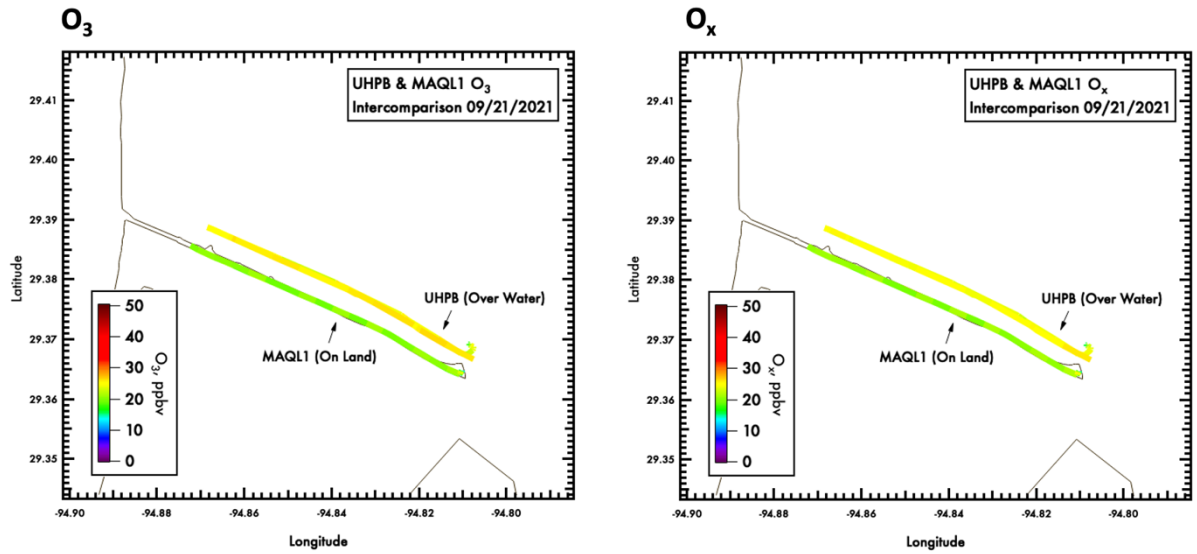

Figure 3.9.20: *Spatial plot of O_3 & O_x mixing ratio from the MAQL1 and UH Pontoon boat while sampling approximately 400m apart over land on the Texas City Dike and over water in Galveston Bay.*

Wind speed and direction also showed a general agreement between the platforms (**Figure 3.9.21**) with the UH pontoon boat recording a higher wind speed for the majority of the time. The wind direction trends were also in broad agreement between the two mobile labs with the largest divergence coming during the beginning of the mobile period when the UH MAQL1 lab showed a wind shift from the SW to the E. These differences may be accounted for by differences in the surface topography, distance separated, an incomplete correction for movement from the mobile platforms in the wind data or a combination of these factors.

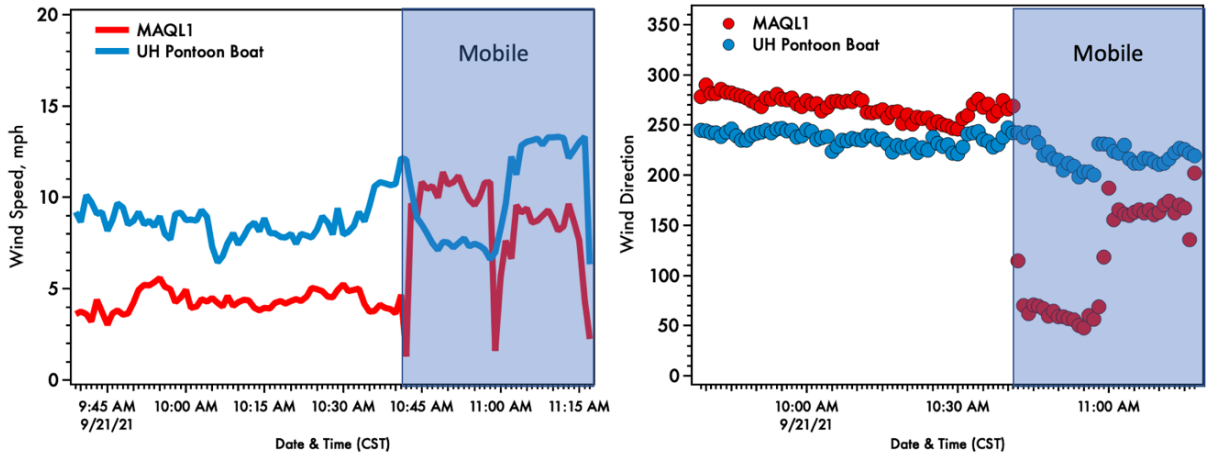

Figure 3.9.21: *Time Series (left) and scatter plot (right) of wind speed values during the intercomparison. Periods of mobile sampling are highlighted on the time-series and marked with different colors on the scatter plot.*

Vaisala ceilometers output up to three retrieved boundary layers during operation. The first retrieved layer is often considered the mixing layer; however, retrieval algorithms are not always able to resolve the true mixing layer depending on environmental conditions (i.e clouds or additional aerosol gradients). In the marine environment sea salt layers especially complicate interpretation. The comparison between ceilometers retrieved first boundary layer (**Figure 3.9.22**) shows initially good agreement with the UH pontoon, however after 40 minutes of sampling the UH pontoon begins diverging with an increase in the lowest retrieved layer beginning approximately at 10:30. This time-period of the morning is a time of known transition from a nocturnal to convective driven boundary layer regime, so it is difficult to discern between instrument variability and observational variability given the short sampling time and small spatial variability.

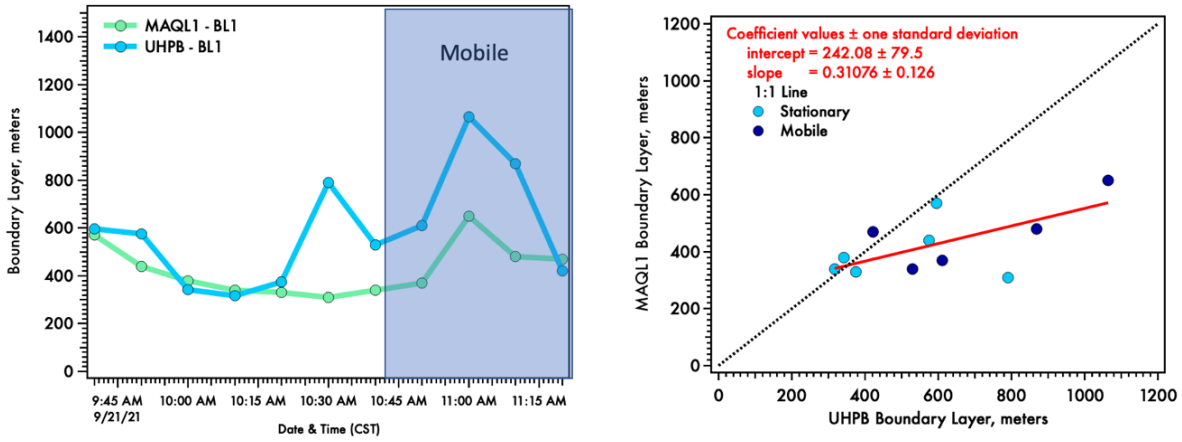

Figure 3.9.22: *Time Series (left) and scatter plot (right) of the first retrieved boundary layer during the intercomparison. Periods of mobile sampling are highlighted on the time-series and marked with different colors on the scatter plot.*

The comparison of the second retrieved layer between ceilometers shows a good agreement and a better agreement than the first retrieved layer. This layer is assumed to be less impacted by changes at the surface which drive boundary layer evolution

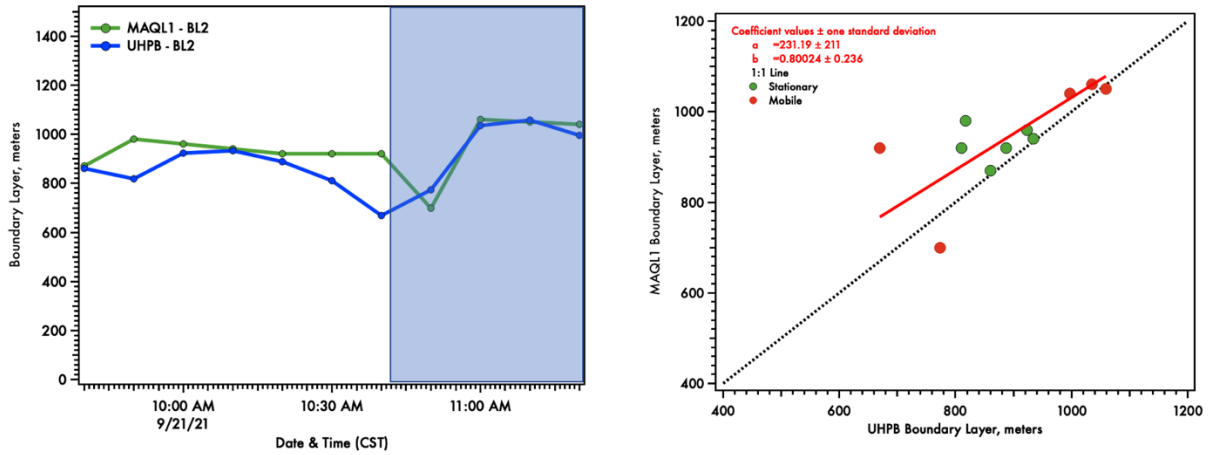

Figure 3.9.23: *Time Series (left) and scatter plot (right) of the first retrieved boundary layer during the intercomparison. Periods of mobile sampling are highlighted on the time-series and marked with different colors on the scatter plot.*

When the layers did not agree well with each other the difference was often in the first retrieved level, which may be a difference in internal processing of the data from the different ceilometers, Vaisala CL-31 vs CL51 or a factor of steep gradients of meteorological variables at the land-water interface that would impact the surface layer the greatest.

3.9.3.3 The mobile boat platforms and the TCEQ continuous air monitoring stations

A comparison of the three mobile boat platforms while measuring stationary, at the dock, with the nearest TCEQ continuous air monitoring station (CAMS) is shown in the following figures. Comparison between stationary ozone and docked boat platforms shows good agreement. The best agreement between platforms was between the shrimp boat and Smith Point C1606 monitor (**Figure 3.9.24**). These platforms were also located closest together, at a distance of 200m when the shrimp boat was docked.

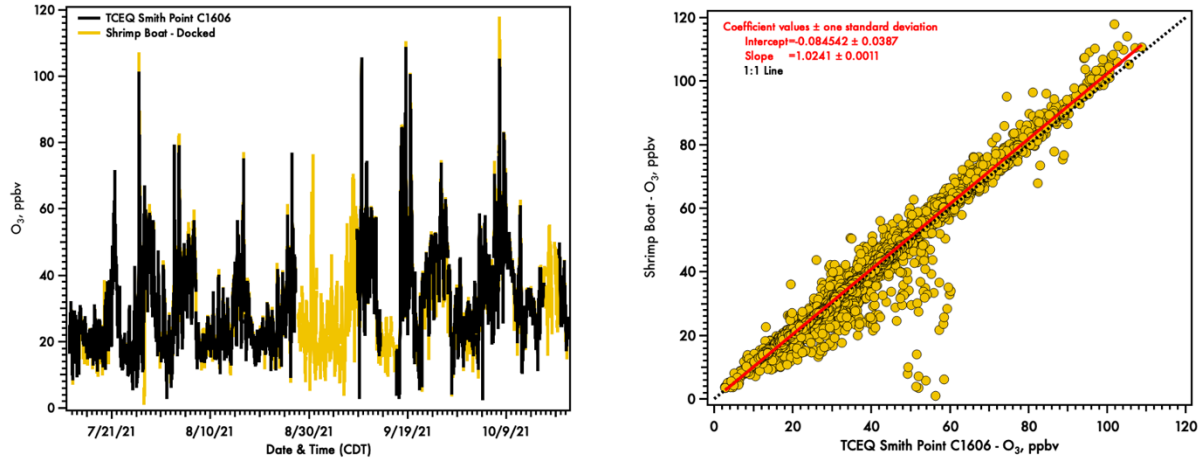

Figure 3.9.24: *Time-series (left) and scatter plot (right) of 5-minute averaged O_3 values from the shrimp boat platform, while docked, and the nearest TCEQ monitor, Smith Point (C1606). Measurements from July–October 2021.*

The Red Eagle platform showed the widest spread between platforms (**Figure 3.9.25**), but still showed reasonable agreement under most conditions. The Red Eagle was the most active mobile platform and did often observe different levels of ozone compared with on land. The location of the TCEQ monitoring site near to the Gulf coast shoreline was also reasonably different to the pier that the Red Eagle docked at near to the urban center and cruise line terminal in Galveston, TX. The distance between the Red Eagle and TCEQ Galveston C1034 was the furthest between platforms, at a distance of 10.25 km.

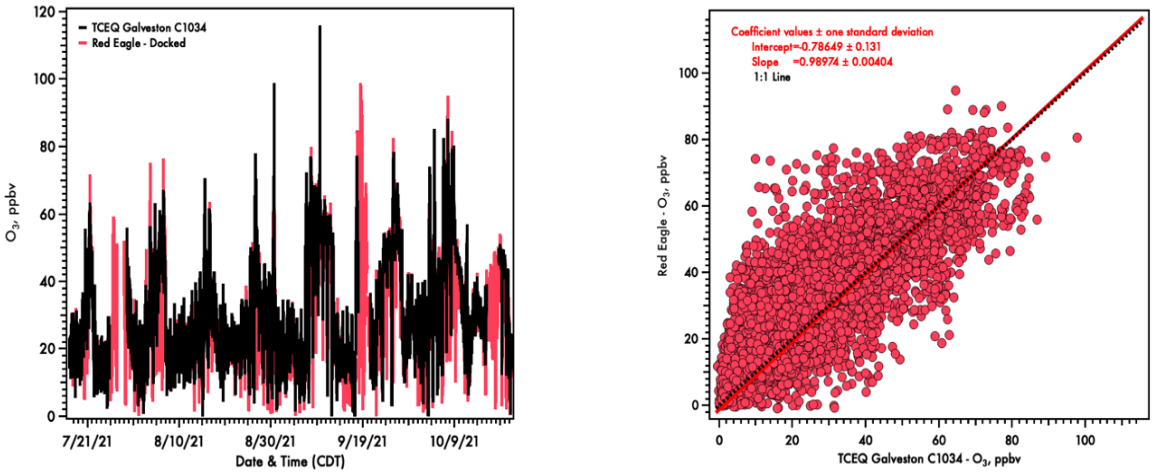

Figure 3.9.25: *Time-series (left) and scatter plot (right) of 5-minute averaged O_3 values from the Red Eagle boat platform, while docked, and the nearest TCEQ monitor, Galveston (C1034). Measurements from July–October 2021.*

The comparison between the docked UH pontoon boat data and Seabrook C45 monitor (**Figure 3.9.26**) showed a low bias at the Seabrook C45 monitor under most conditions, with a near 5 ppbv offset. The measured trends of ozone between sites was satisfactory. The locations of the two monitors were approximately 4 km apart with a major highway between them as well as the Seabrook monitor is located approximately 0.5 miles further inland. Given the persistent nature of the high bias it is possible the baseline on the instrument at Seabrook is incorrect.

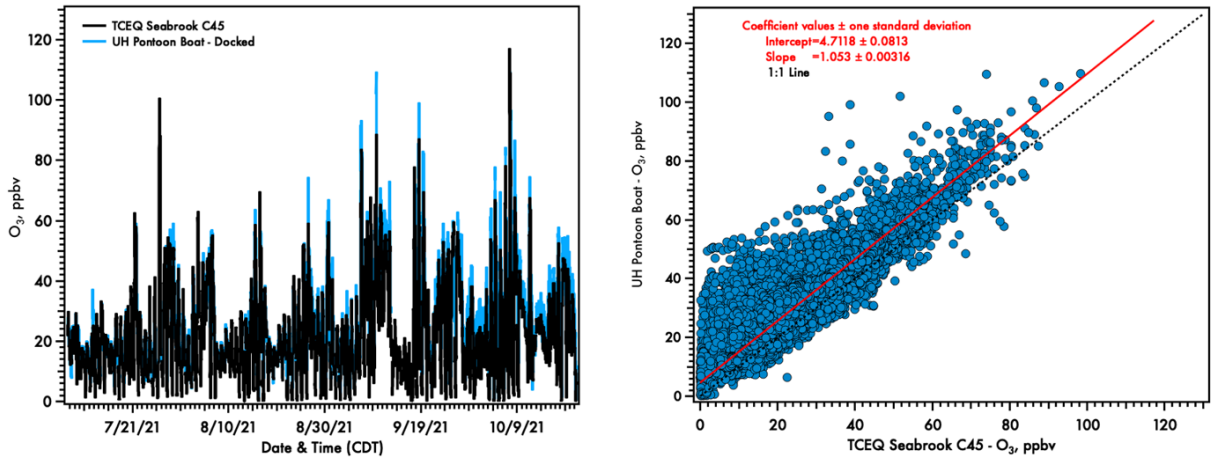

Figure 3.9.26: *Time-series (left) and scatter plot (right) of 5-minute averaged O_3 values from the UH Pontoon boat platform, while docked, and the nearest TCEQ monitor, Seabrook (C45). Measurements from July–October 2021.*

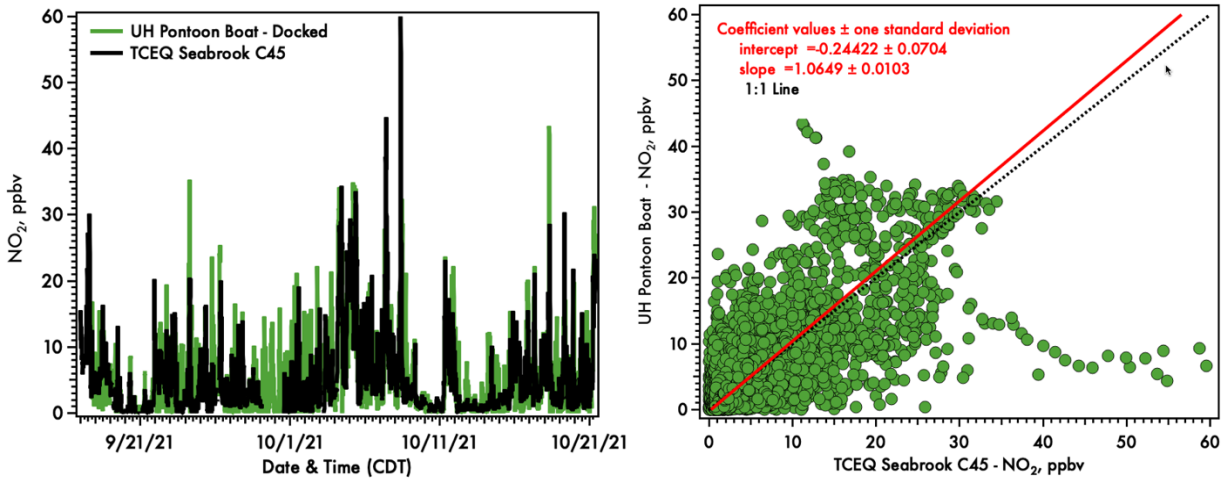

Figure 3.9.27: *Time-series (left) and scatter plot (right) of 5-minute averaged NO_2 values from the UH pontoon boat platform, while docked, and the nearest TCEQ monitor, Seabrook (C45). Measurements from 17 September –21 October 2021.*

Comparison of NO_2 values at the UH pontoon boat, which were derived from the O_X measurement, and TCEQ Seabrook C45 monitoring site shows a good overall agreement (**Figure 3.9.27**). There are a few high outlier points at both sites, which does go to show the localized impacts of nearby emissions and short lifespan of NO_2.

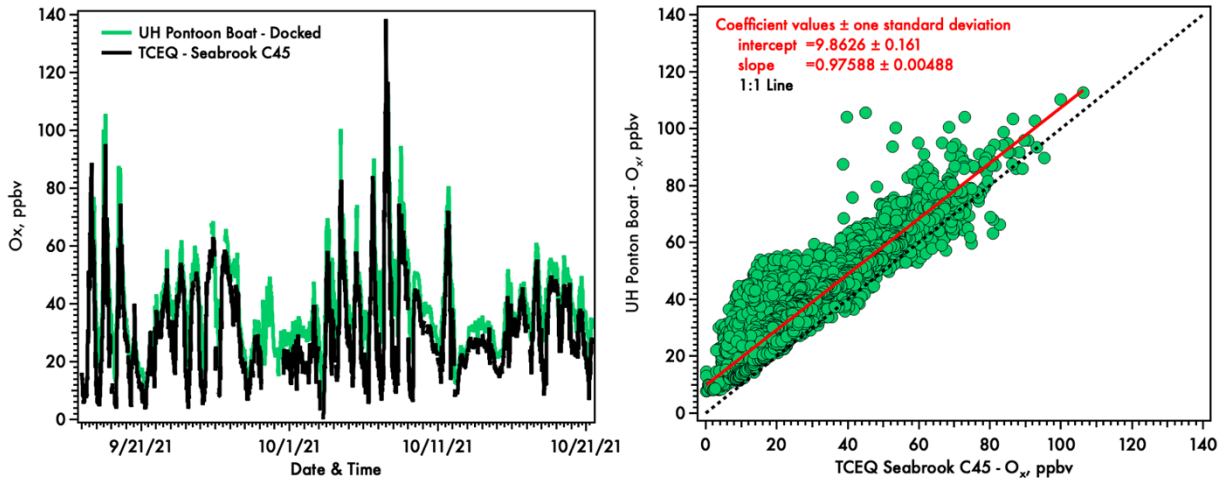

Figure 3.9.28: *Time-series (left) and scatter plot (right) of 5-minute averaged NO2 values from the UH pontoon boat platform, while docked, and the nearest TCEQ monitor, Seabrook (C45). Measurements from 17 September–21 October 2021.*

A comparison of O_X measurements between the UH pontoon boat and Seabrook monitoring sites was performed and shown in **Figure 3.9.28**. Due to the apparent negative offset and low bias of the ozone observations at the Seabrook C45 site compared with the UH pontoon boat, the O_X comparison showed a strong positive bias towards the UH pontoon boat, although good correlation.

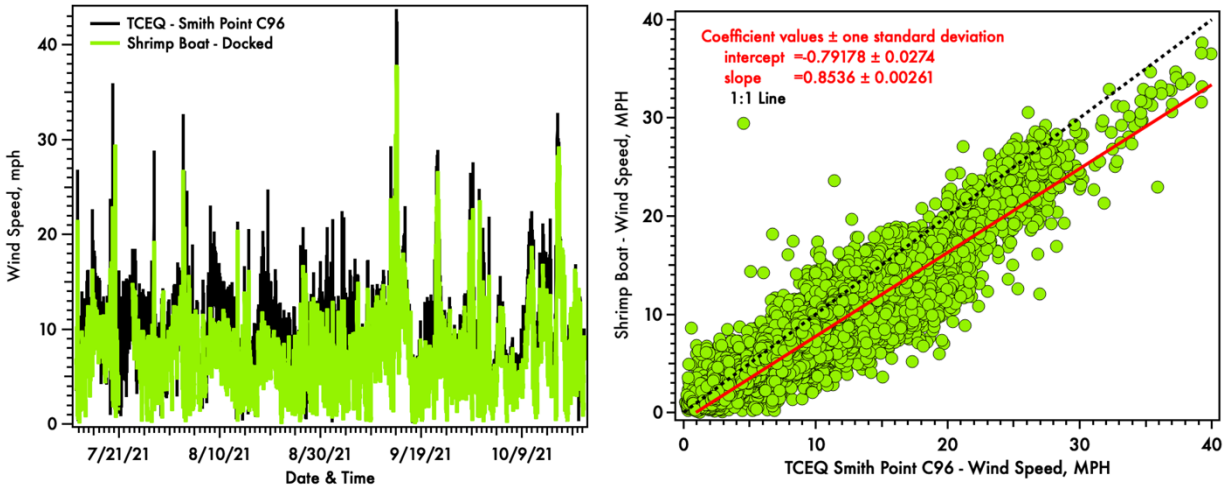

Figure 3.9.29: *Time-series (left) and scatter plot (right) of 5-minute averaged wind speed values from the shrimp boat platform, while docked, and the nearest TCEQ monitor, Smith Point (C1606). Measurements from July–October 2021.*

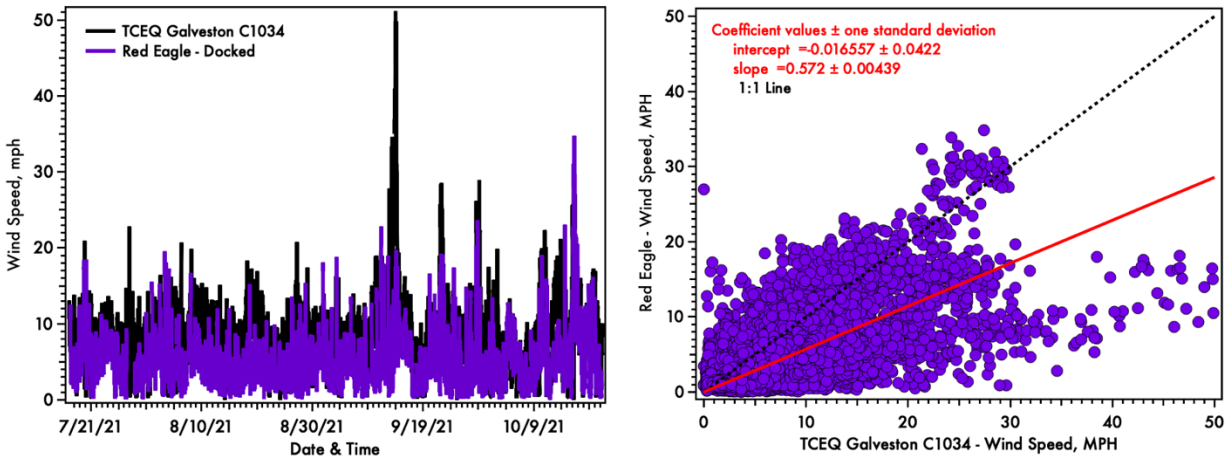

Figure 3.9.30: *Time-series (left) and scatter plot (right) of 5-minute averaged wind speed values from the Red Eagle boat platform, while docked, and the nearest TCEQ monitor, Galveston (C1034). Measurements from July–October 2021.*

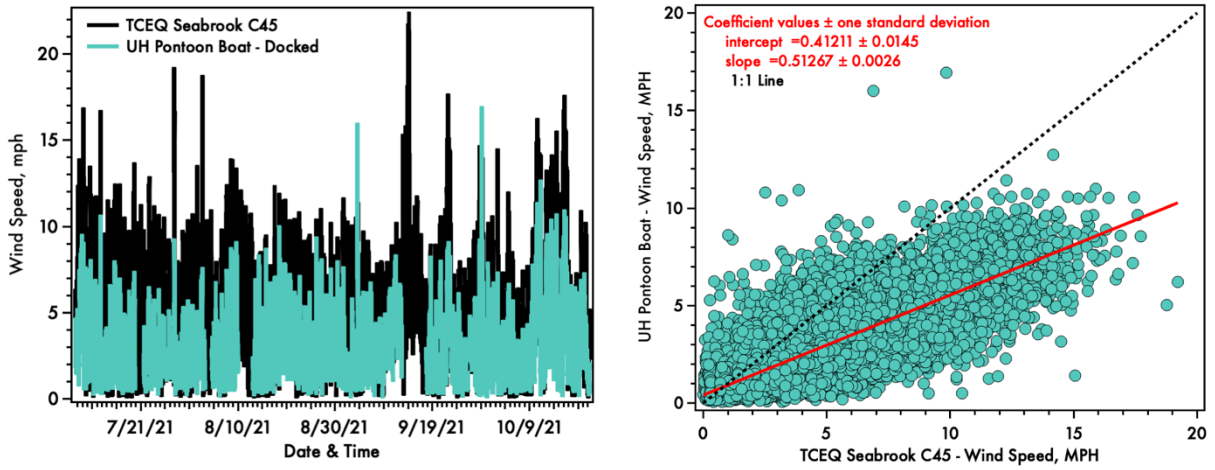

Figure 3.9.31: *Time-series (left) and scatter plot (right) of 5-minute averaged wind speed values from the UH Pontoon boat platform, while docked, and the nearest TCEQ monitor, Seabrook (C45). Measurements from July–October 2021.*

Comparison of the wind speeds at the three boat platforms, while they were stationary at dock, with the nearest TCEQ monitor is presented in **Figure 3.9.29**–**Figure 3.9.31**. The best agreement between measurements is between the shrimp boat and TCEQ Smith Point sites, which were closest together. The UH pontoon boat and Seabrook C45 monitor had the worst agreement between measurements despite being closer than the Red Eagle and Galveston C1034 monitor. All three boat platforms tended to measure low relative the nearest TCEQ monitor. While surface topography in complex environments can alter winds even at nearby locations, this result seems to indicate an instrumental bias or data correction difference between platforms.

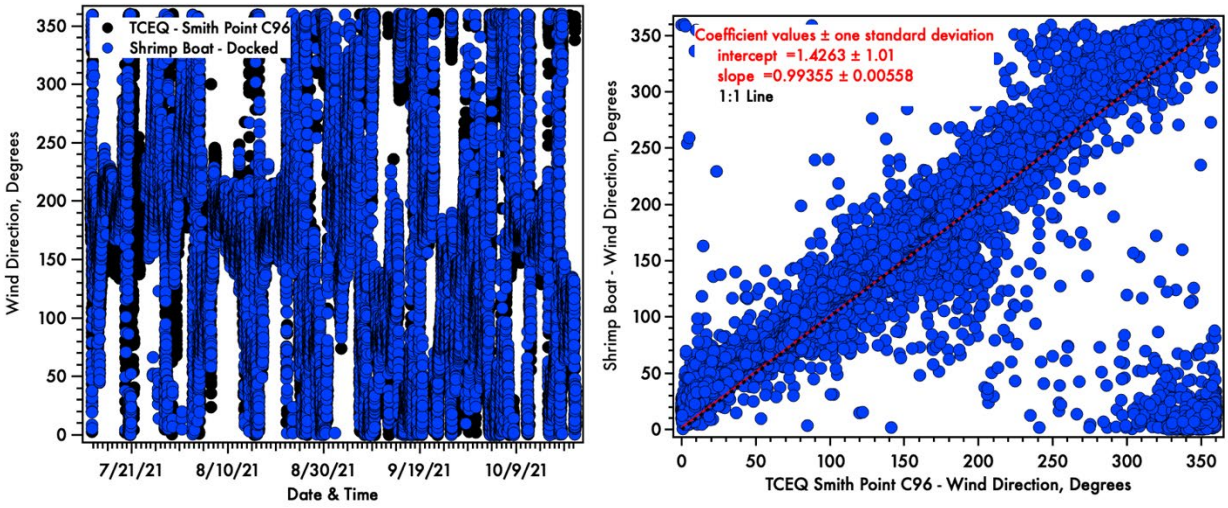

Figure 3.9.32: *Time-series (left) and scatter plot (right) of 5-minute averaged wind direction values from the shrimp boat platform, while docked, and the nearest TCEQ monitor, Smith Point (C1606). Measurements from July–October 2021.*

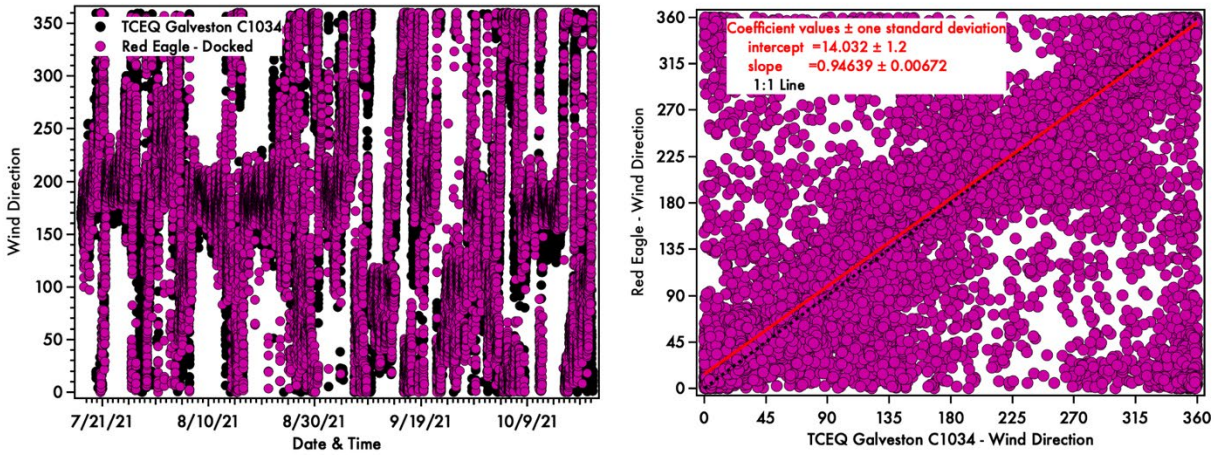

Figure 3.9.33: *Time-series (left) and scatter plot (right) of 5-minute averaged wind direction values from the Red Eagle boat platform, while docked, and the nearest TCEQ monitor, Galveston (C1034). Measurements from July–October 2021.*

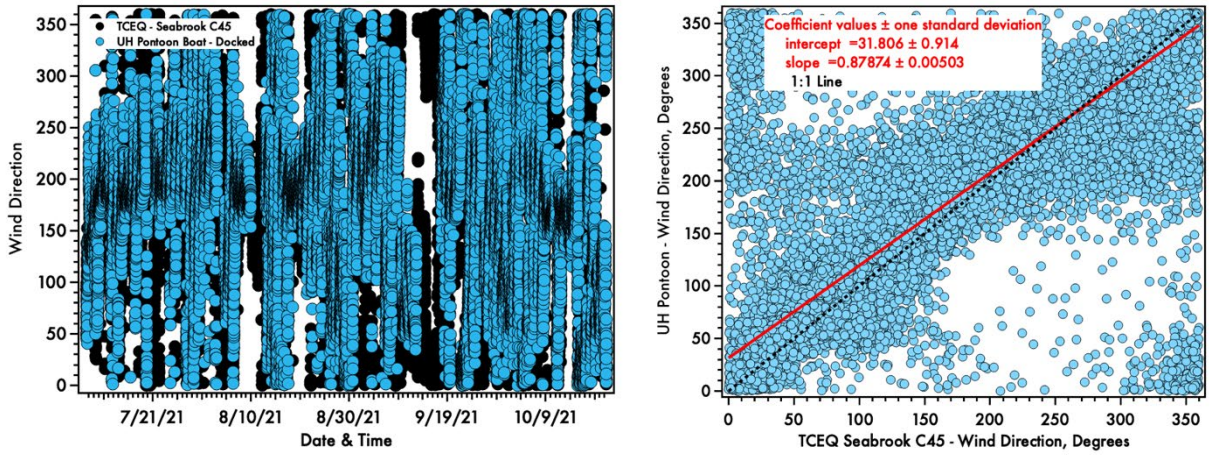

Figure 3.9.34: *Time-series (left) and scatter plot (right) of 5-minute averaged wind direction values from the UH Pontoon boat platform, while docked, and the nearest TCEQ monitor, Seabrook (C45). Measurements from July–October 2021.*

Comparison of 5-minute averaged wind direction values at the three boat platforms with the nearest TCEQ monitor is presented in **Figure 3.9.32**–**Figure 3.9.34**. The pattern of best to worst agreement followed the pattern of shortest to longest distance between compared monitoring locations. Given changes in surface features and natural errors in measurements between sites these differences fall within an acceptable range.

3.9.3.4 Ozonesonde and other platforms

3.9.3.4.1 Ceilometer-ozonesonde intercomparison from Galveston Bay

During the 2021 TRACER-AQ campaign, 30 ozonesondes were released from the UH Pontoon Boat operating in Galveston Bay. As an example, two ozonesondes were released from the UH Pontoon Boat on September 9, 2021. The first ozonesonde profile (launched near the Texas City Dike at 10:55 a.m. CST; **Figure 3.9.35 a**) from Galveston Bay shows a marine layer at 0.2 km. Ceilometer data from the pontoon boat (**Figure 3.9.36**) shows general agreement with an aerosol layer at 0.25 km at the same time. The ceilometer data shows a second layer at 1.8 km, just above an ozone enhancement observed in the ozonesonde profile.

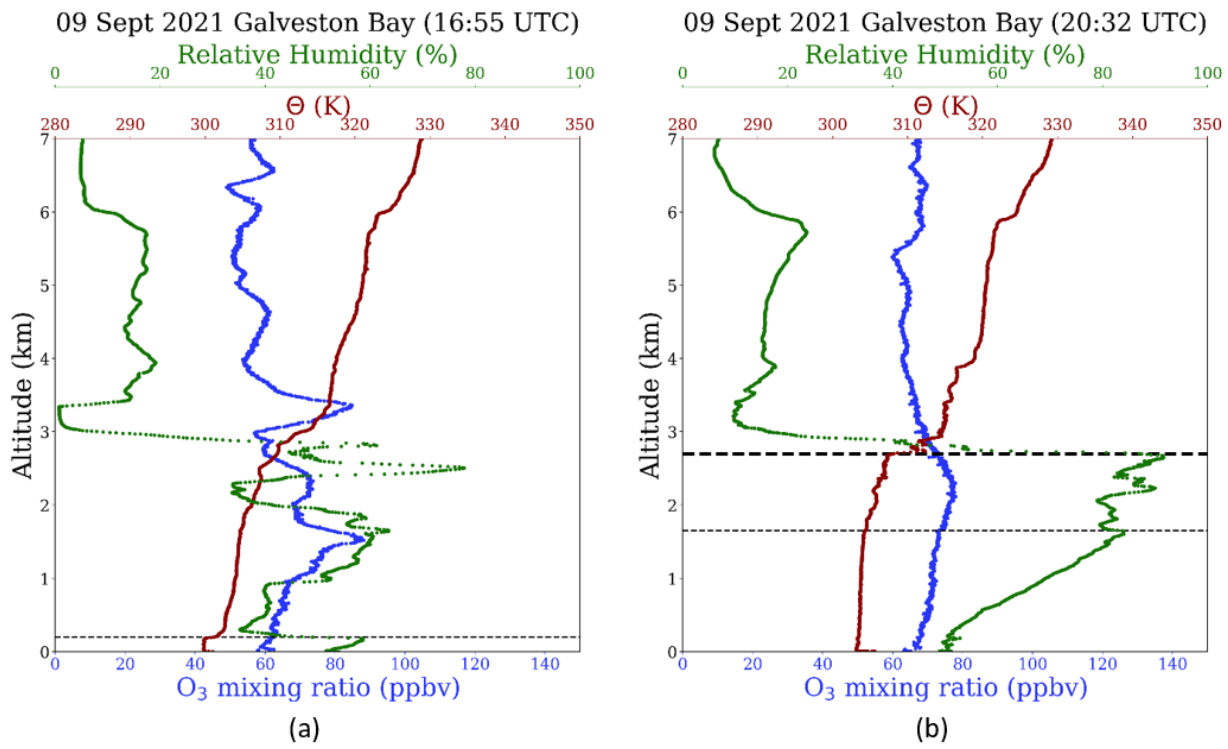

Figure 3.9.35: *Profiles from two ozonesondes released on 9 September 2021 from the UH Pontoon boat operating in Galveston Bay. Profiles of the ozone mixing ratio (blue), potential temperature (dark red), and relative humidity (green) are shown. In panel (a) the horizontal dashed line is the top of the marine layer. In panel (b) the thin dashed line marks what would be the top of the boundary layer if it were not for convection reaching up to the top of the thicker dashed line.*

The second ozonesonde profile from the pontoon boat in Galveston Bay (launched in the NW quadrant of Galveston Bay at 2:32 p.m. CST; **Figure 3.9.35 b**) shows features between 1.7 km and 2.7 km AMSL that are also observed in the UH Pontoon Boat ceilometer data (**Figure 3.9.36**). That potential temperature and relative humidity profiles may suggest convection was occurring in that region.

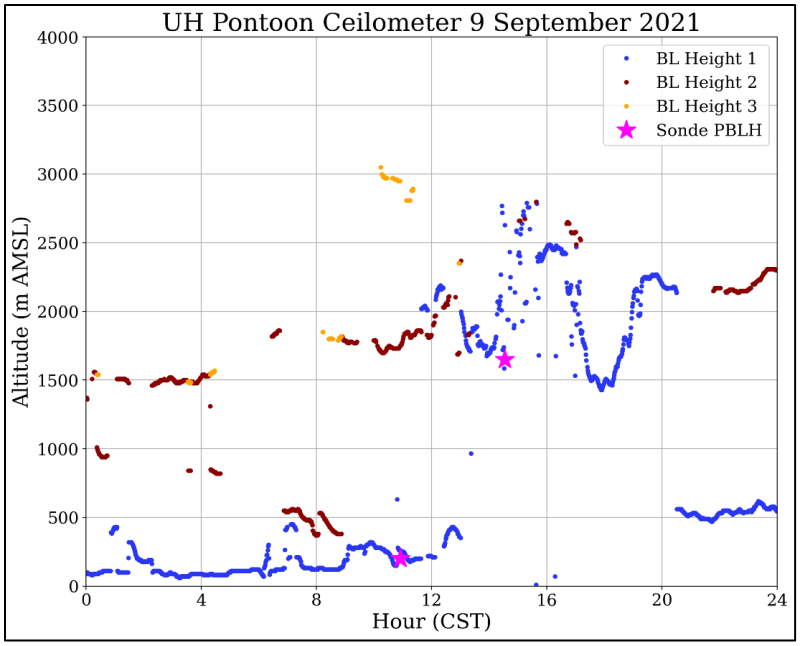

Figure 3.9.36: *Ceilometer data from the pontoon boat on 9 September 2021. The magenta stars show the altitudes of first layers in the ozonesonde profiles.*

For ozonesonde launches that occurred from the UH Pontoon Boat, a comparison of the boundary layer heights from the ozonesonde profiles versus the Vaisala CL-51 ceilometer first identified boundary layer height is shown in **Figure 3.9.37**. The trend line has a slope of 0.58 ± 0.12 and a y-intercept of 223 ± 129 with an r^2 value of 0.45.

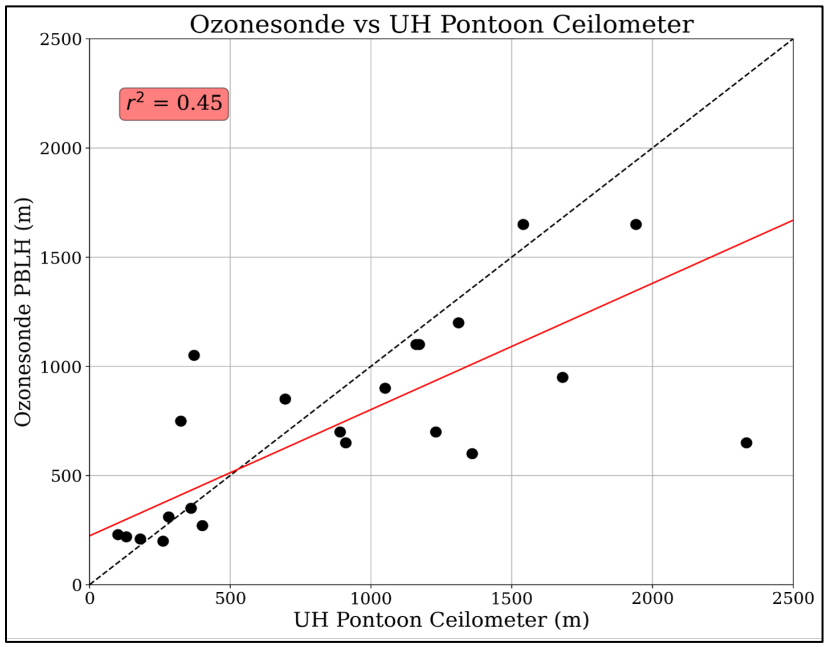

Figure 3.9.37: *Comparison of boundary layer heights determined from profiles of collated ozonesonde launches versus the UH Pontoon Boat Vaisala CL-51 ceilometer first identified boundary layer height. The red line shows a linear best fit with a slope of 0.58 ± .12 and a y-intercept of 223 ± 129. The dashed black line shows a 1-to-1 trendline.*

3.9.3.4.2 Lidar-ozonesonde intercomparisons

Figure 3.9.38 shows the TROPOZ ozone measurements on 9 September 2021 at La Porte, a day in which ozone in the residual layer was transported downward and mixed into the afternoon boundary layer and contributed to the high ozone observed at the surface. Overlaid on the plot are ozone profiles from two ozonesondes released from La Porte collocated with the TROPOZ lidar. There were 25 ozonesondes from La Porte collocated with TROPOZ during the campaign.

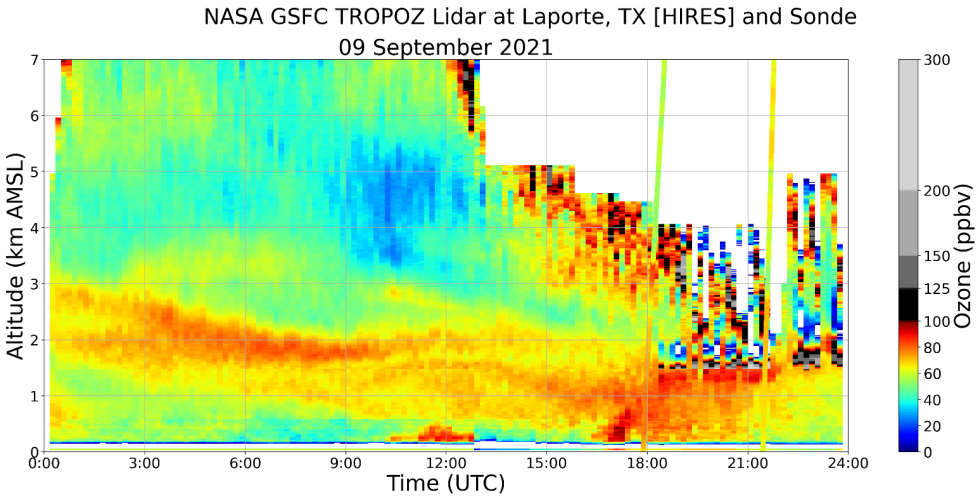

Figure 3.9.38: *NASA Goddard Space Flight Center (GSFC) Tropospheric Ozone (TROPOZ) Lidar measurements from La Porte, TX, on 9 September 2021. Ozone profiles of two ozonesondes released from La Porte are overlaid.*

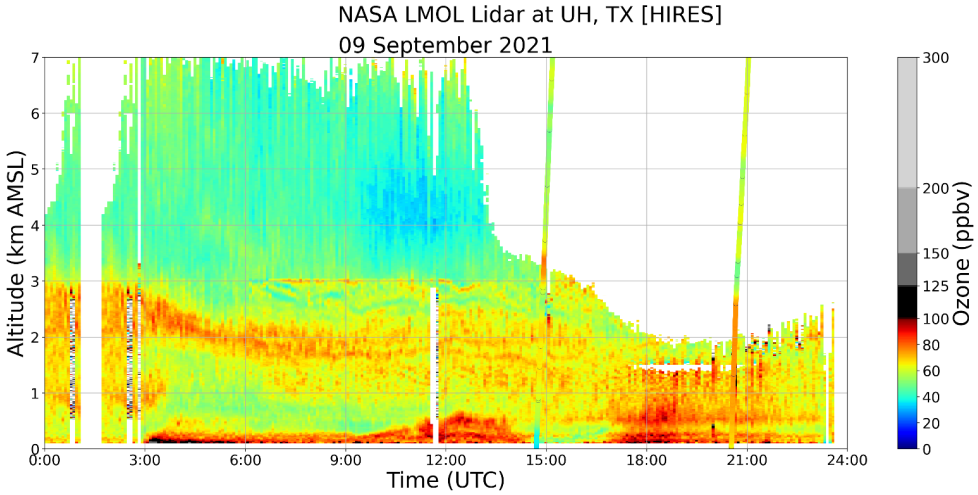

Figure 3.9.39: NASA Langley Research Center Mobile Ozone Lidar (LMOL) measurements from the University of Houston on 9 September 2021. Ozone profiles of two ozonesondes released from La Porte are overlaid.

Figure 3.9.40 shows HSRL-2 ozone measurements from aboard the G-V aircraft on the same day. The elevated residual layer ozone was present over much of the HGB region. The

ozone profiles of the two ozonesondes that were released from La Porte are overlaid and qualitatively show agreement between the two measurements.

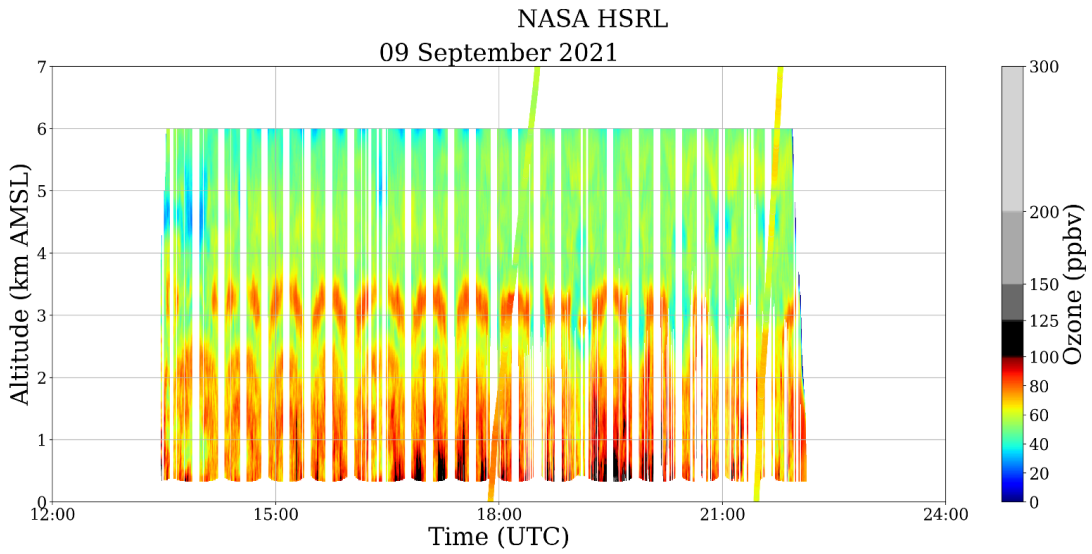

Figure 3.9.40: *NASA High Spectral Resolution Lidar-2 (HSRL-2) measurements from the NASA G-V aircraft, which completed three raster patterns over the Houston-Galveston-Brazoria region on 9 September 2021. Ozone profiles of two ozonesondes from La Porte are overlaid.*

Figure 3.9.41 shows an example of the analysis by Taylor Shingler (NASA) comparing ozone profiles of the ozonesondes to the HSRL-2. In the first three panels, the ozonesonde ozone profile is shown by the small blue points and the HSRL-2 data points are larger. In the left panel, the HSRL-2 data are colored by the average horizontal distance the G-V aircraft is from the ozonesonde. In the second panel from the left, the HSRL data are colored by the average time elapsed of the G-V aircraft from the ozonesondes location. In the third profile from the left, the HSRL-2 data are colored by the number of unique independent HSRL-2 data points that were used at that altitude.

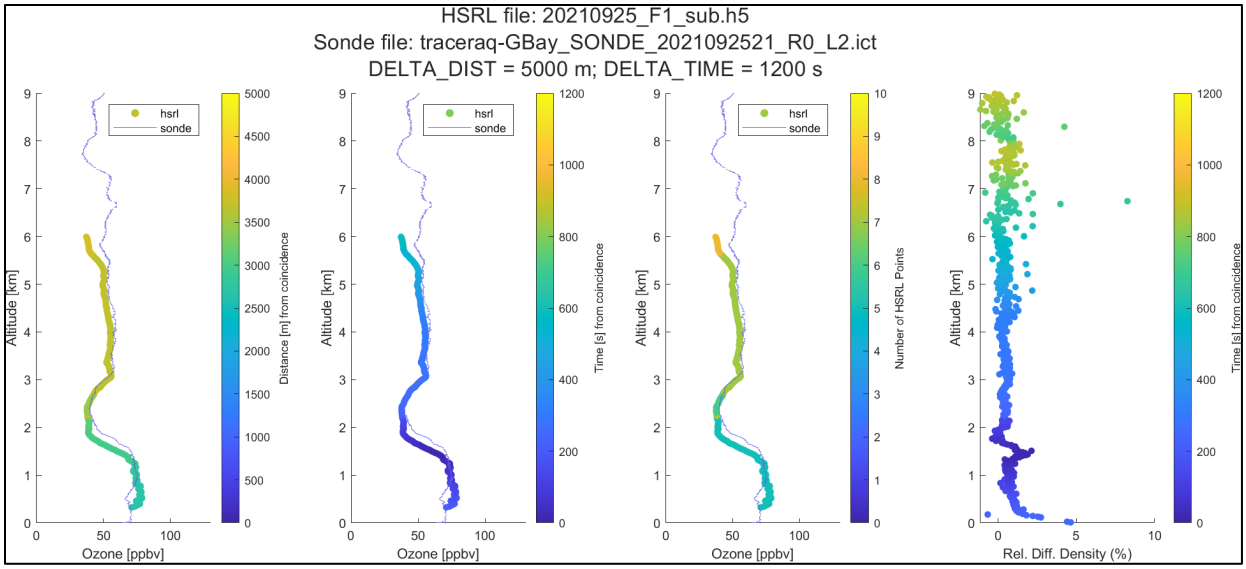

Figure 3.9.41: *Comparison of an ozone profile from an ozonesonde released from the UH Pontoon boat in Galveston Bay on 25 September 2021 at ~21 UTC with HSRL-2 measurements from that time. Image courtesy of Taylor Shingler (NASA).*

There were 45 ozonesondes where the G-V aircraft was close enough that there was sufficient HSRL-2 data for an intercomparison, of which four ozonesonde profiles had an offset in the ozone mixing ratio. That offset was determined to be from post-processing of the ozonesonde data where a pressure offset (Stauffer et al., 2014) that was applied was an unrealistic value. Those pressure offsets were removed and those profiles showed much better agreement than they had previously. **Figure 3.9.42** is an example of a corrected ozonesonde profile that now shows agreement with the HSRL-2 data.

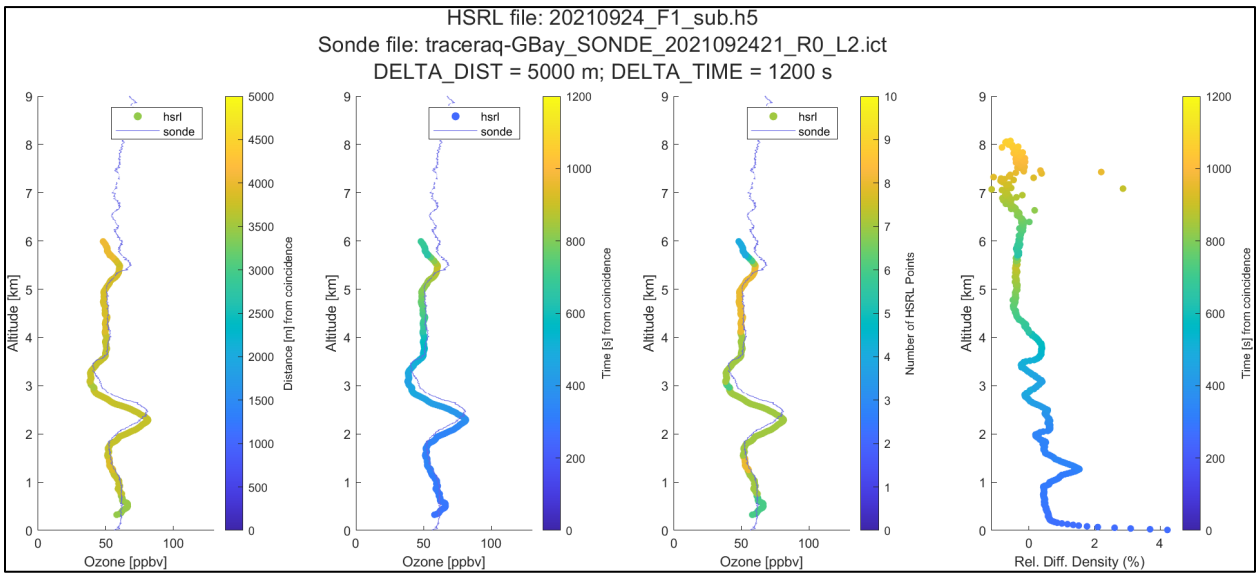

Figure 3.9.42: *Comparison of an ozone profile from an ozonesonde released from the UH Pontoon boat in Galveston Bay on 24 September 2021 at ~21 UTC with HSRL measurements from that time. Image courtesy of Taylor Shingler (NASA).*

Figure 3.9.43 shows an intercomparison for an ozonesonde released from near the N Anchoring location offshore of Galveston in the Gulf of Mexico, and is an example of when there is less agreement between the two instruments than for most profiles.

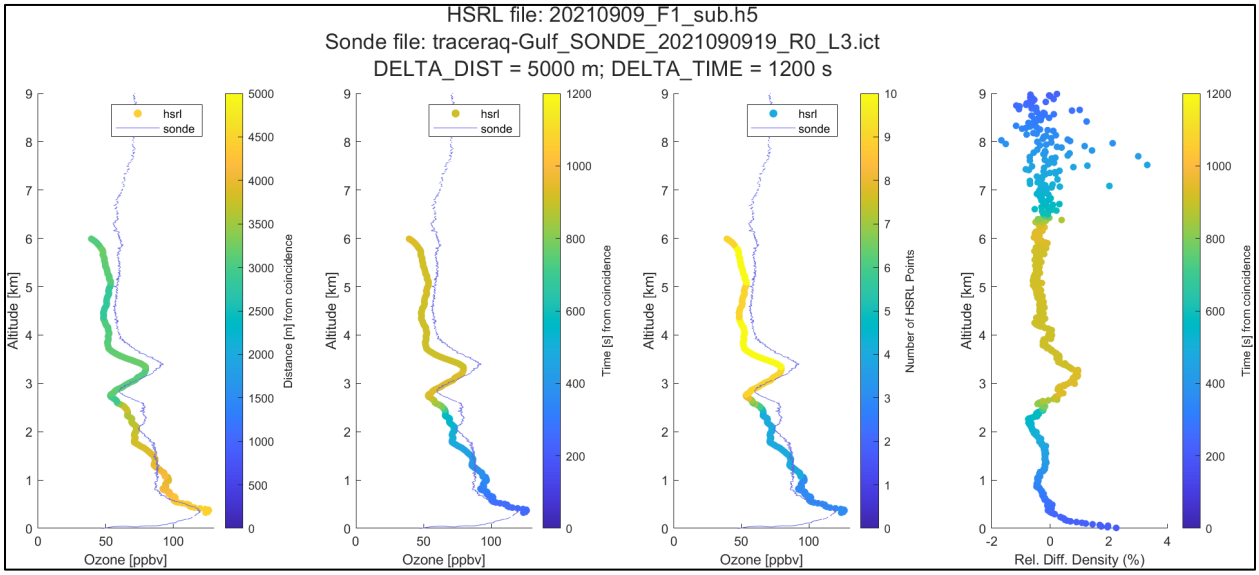

Figure 3.9.43: *Comparison of an ozone profile from an ozonesonde released from the Red Eagle operating off the coast of Galveston in the Gulf Mexico near the North Anchoring area on 9 September 2021 at ~19 UTC with HSRL measurements from that time. Image courtesy of Taylor Shingler (NASA).*

There is general agreement between the ozonesonde and lidar observations, which can be more fully quantified. One item of future work is to reprocess the ozonesonde data to account for the response time of the ECC solutions as is described in Vömel et al. (2020), which may lead to improved agreement between the ozonesonde and lidar ozone profiles.

3.10 Other findings of interest

3.10.1 Power plant emissions of SO2

3.10.1.1 Summary

Periods of enhanced SO_2 levels with peak concentrations up to 30 ppbv (30 s averaged data) were measured during multiple mobile days in southwest and west of Houston. These enhancements were not due to local motor vehicle emissions. The location of these enhancements were in close proximity to the WA Parish Generating Station in Fort Bend County. Modeled CAMx SO_2 levels observed enhanced concentrations southwest of the Houston city and generally agree with in situ SO_2 measurements. The September 25th case was previously hypothesized that the plume structure may show the power plant plume overlaid on a broader plume, however the model results from this study indicate that it is likely different parts of the same plume related to the power plant. Two days where the Parrish Power Plant plume was likely encountered were analyzed. The additional two days observations along with CAMx modeled results will be included in the final report.

3.10.1.2 Methods

The mobile in situ SO_2 measurements were made on the MAQL1 platform using a pulsed fluorescence Thermo Scientific (Waltham, MA) SO_2 analyzer. The trace gas and GPS measurement were averaged to 30s. All MAQL1 mobile measurement days were scanned for enhanced SO_2 levels excluding when these enhancements are due to apparent motor vehicle emissions. There are several MAQL1 mobile days (September 9, 11, 25, and 26) where high levels of SO_2 were measured southwest and west of Houston. The location of the enhanced SO_2 levels were in close proximity to the WA Parish Generation Station, which is referred to as the Parish Power Plant. For this interim report, two of the four days, September 9 and 25, were analyzed.

In addition to the in situ measurements, SO_2 levels were modeled for September 9 and 25 using the Comprehensive Air quality Model with extensions (CAMx). CAMx is an open-access photochemical model that can simulate emissions, chemical reactions, dispersion, and removal of pollutants in the atmosphere from urban to continental scales. This tool solves the 3-dimensional Eulerian continuity equation based on a “one atmosphere” framework for different chemical species to model their distribution over a defined domain. CAMx is the regulatory model suggested by TCEQ to simulate pollutants concentrations and their sensitivities to various state control policies. In this study, we applied CAMx version 7.10 over the contiguous United States, Southeast Texas, and the Houston-Galveston region (as shown in **Figure 3.10.1**) during September 2021. The model requires grided input of meteorology and emissions to simulate the chemical fields. We ran CAMx on the three-nested domain similar to WRF (**Figure 3.10.1**) that share the same Lambert Conformal Conic projection. The WRF meteorological outputs were translated into a CAMx-friendly format using WRF-CAMx pre-processor tool. To alleviate the CAMx computational costs,

WRF vertical layers were collapsed into 30 unevenly distributed levels with higher resolution near the surface that extend up to ~11 km AGL (100 hPa).

Emission data from the 2019 State Implementation Plan (SIP) modeling platform provided by TCEQ was used after cropping the gridded data to match the boundaries of the CAMx simulations. The on-road emissions were re-distributed from 4 km to 1.33 km over the Houston area. The 4 km emission fluxes were disaggregated to 1.33 km grids and then, collected onto major roads using a 1 km rasterized road shapefile to produce temporary on-major-road 1.33 km emissions. To deal with the missing values in the generated emission file, a smoothing method was applied to fill the missing values by averaging the eight nearby grids and the temporary off-major-road 1.33 km emissions were obtained. The scaling factors for on- and off-major-road emissions were kept in order to keep the on-road emission budget consistent before and after the spatial redistribution. Finally, total emissions were calculated by summing up the 1.33 km on- and off-major-road emission data. The emissions for other sectors were also similarly interpolated to 1.33 km without separating into no- or off-major-road temporary emissions.

The CAMx simulation was operated with a spin-up period of 10 days to minimize the effects of initial and boundary conditions. The initial and boundary conditions for the 12-km domain were obtained from GEOS-Chem (version 12.2.1) global simulation with emissions from National Emission Inventory (NEI) released in 2011, whereas those for 4 km and 1.33 km domains were subsequently extracted from the hourly coarser simulation outputs. The chemical process analysis (CPA) probing tool was also enabled to provide detailed information on the chemical processes during model simulations.

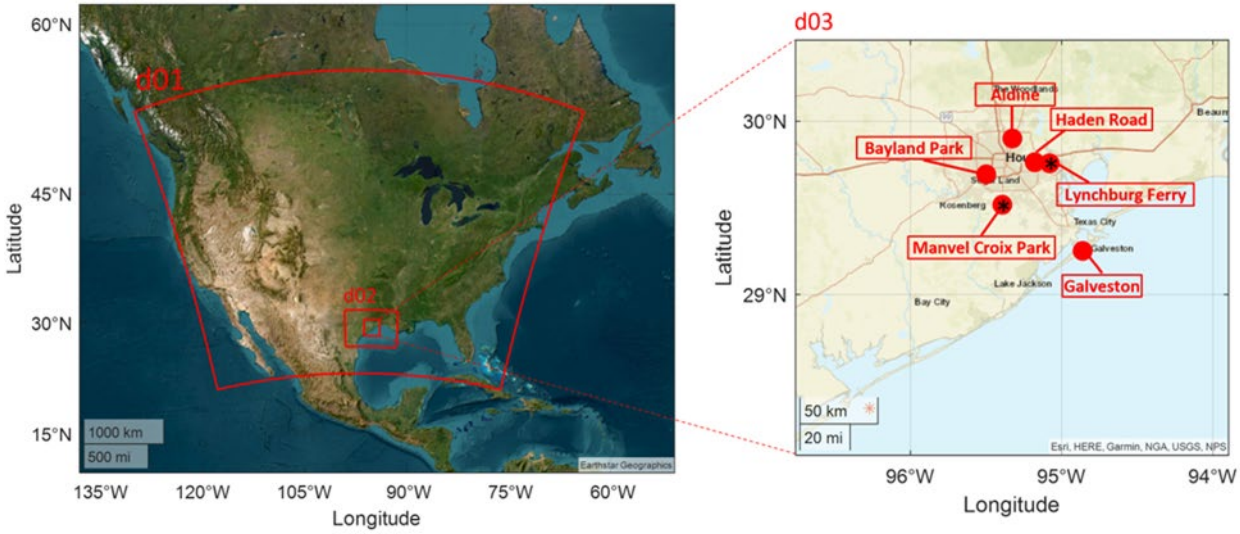

Figure 3.10.1: *WRF-CAMx nested modeling domains and horizontal resolutions.*

3.10.1.3 Results

Several episodes of elevated SO_2 were observed during MAQL1 mobile measurements during the campaign. **Table 3.20** listed all the SO_2 plumes attributable to non-motor vehicle emission sources on September 9 and 21.

Table 3.20: *Information for each SO_2 plume (non motor vehicle emission source) observed during MAQL1 mobile measurements on September 9 and 25, 2021. Information includes start time of the peak, plume time duration and drive duration, location of SO_2 peak, drive direction of MAQL1, peak SO_2 concentration (30 s), and hourly resultant wind direction provided by local CAMS sites.*

Date	Start Time (CST)	Plume Duration (min/km)	Latitude (dd)*	Longitude (dd)*	Drive Direction	SO_2 Peak (ppbv)
9/9	10:54	7 min/ 9 km	29.342	-95.6858	west	29.5
	12:21	6 min/ 8 km	29.4311	-95.6903	southwest	20.1
	12:32	9 min/ 9 km	29.3358	-95.7614	southeast then northeast	15.5
9/25	10:34	10 min/ stationary	29.3961	-95.8339	stationary	34.6
	13:36	7 min/ 9 km	29.4671	-95.8171	south	16.2
	14:08	4 min/ 6 km	29.4115	-95.8351	north	13.9

*latitude and longitude at peak SO_2 concentration
**wind direction from CAMS C84 (Manvel Croix) or C409 (Houston Croquet)

On September 9, the MAQL1 encountered multiple plumes of SO_2 during its traverses southwest of Houston. The likely plume from the Parrish Power Plant was observed southwest of the facility on the first pass from the east to west with a peak of 30 ppbv (**Figure 3.10.2**). The following traverse through the area encountered the plume twice, one sharper and narrower peak near 20 ppbv southwest of the facility and then again south of the initial plume intercept where a broader plume with a 16 ppbv peak value was measured (**Figure 3.10.3**). Although visually the plumes do not appear to line up with the same source, plumes can have bends in them depending on the wind direction at the time of emission if there is a shift or rotation in the winds.

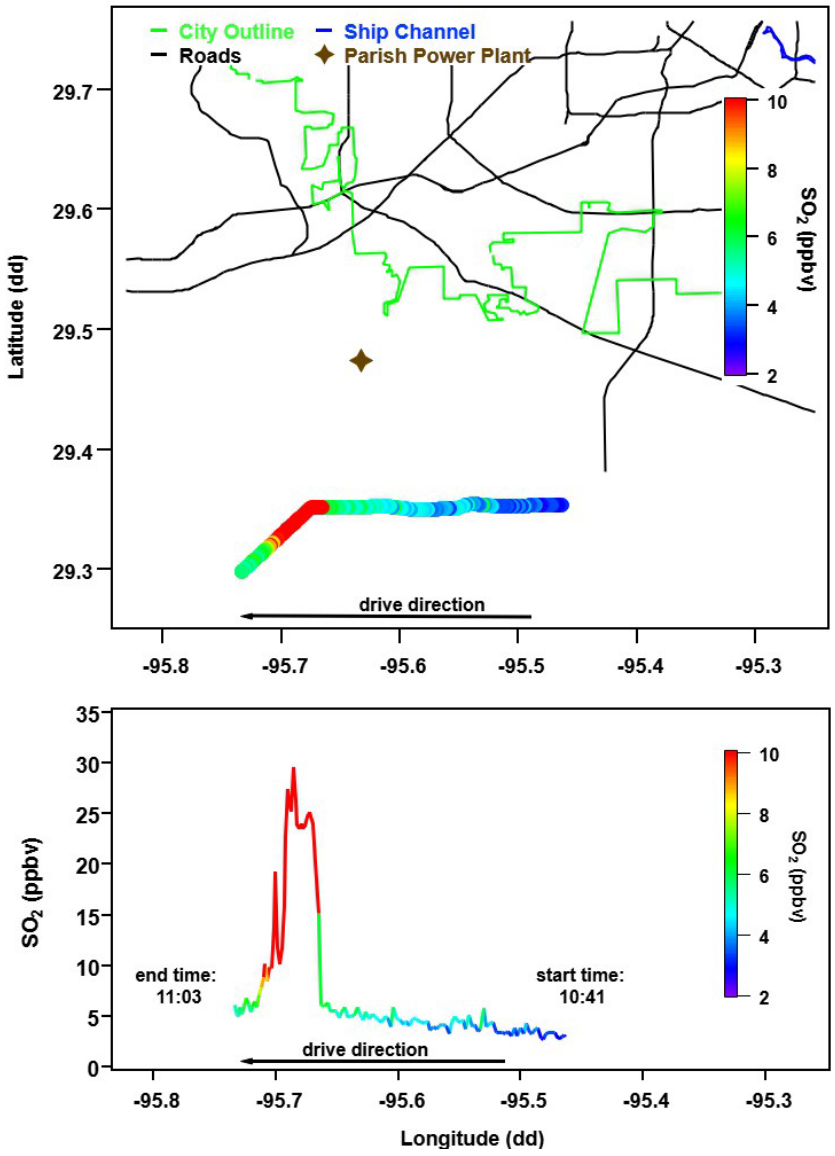

Figure 3.10.2: *An SO_2 plume measured on the MAQL1 during mobile measurements (30s averaged) on September 9, 2021. Top figure is a spatial plot of an east to west transect starting from 10:41 to 11:03 CST with measured SO_2. Bottom figure is the SO_2 plume concentration relative to longitude with a peak concentration of 29.5 ppbv.*

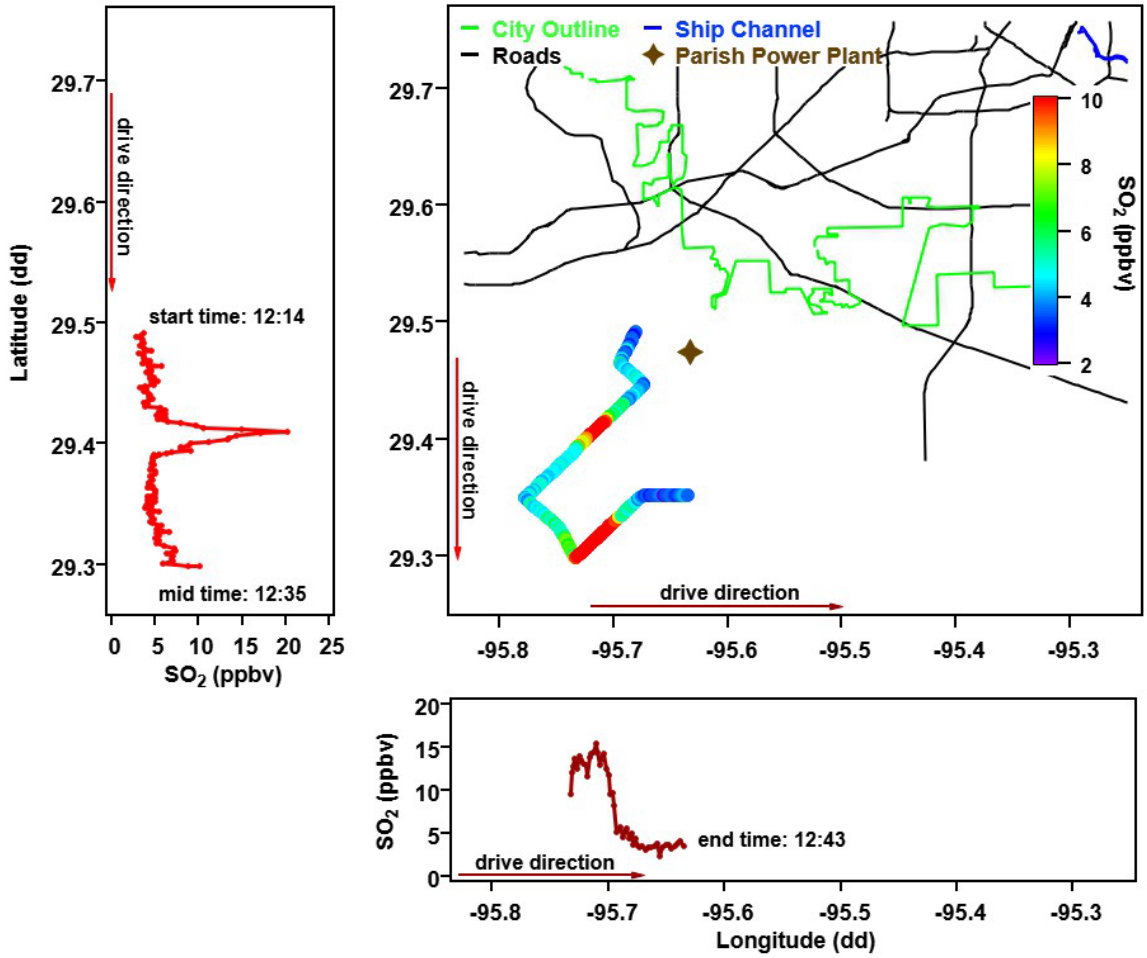

Figure 3.10.3: *Two SO_2 plumes measured on the MAQL1 during mobile measurements (30s averaged) on September 9, 2021. Top right figure is a spatial plot of a driving segment starting from 12:14 to 12:43 CST with the measured SO_2. Top left and bottom figure are the SO_2 plume concentration relative to latitude and longitude for the north to south and west to east transects, respectively. Peak SO_2 concentration for the north to south and west to east transect was 29.4 and 15.5 ppbv, respectively.*

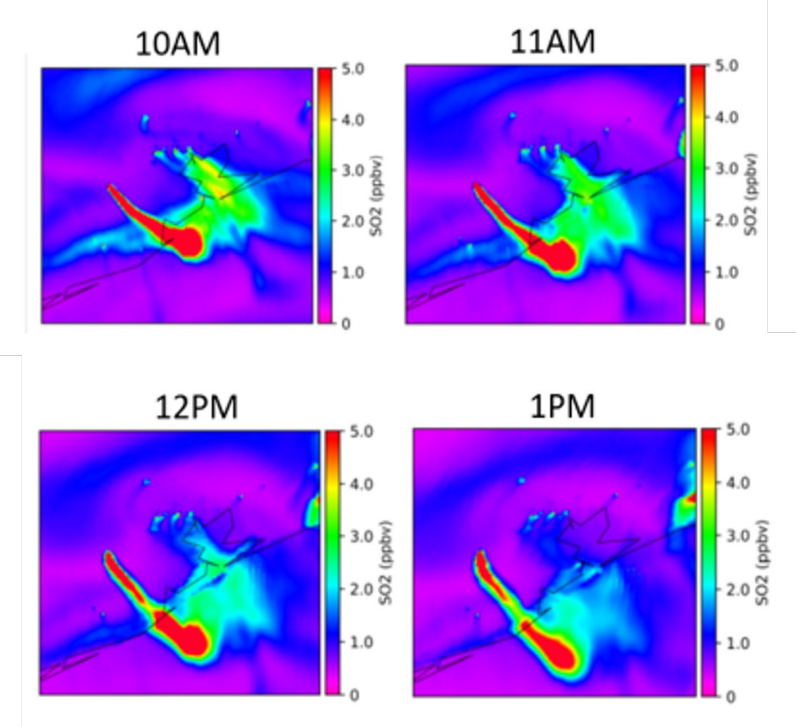

Figure 3.10.4: *CAMx-modeled SO_2 levels on September 9, 2021 near MAQL1 location at 10:00, 11:00, 12:00, and 13:00 CST.*

The CAMx model results clearly show a significant plume emanating from the power plant, and moving consistently to the southeast of the plant (**Figure 3.10.4**). While the precise location of the source can be determined from these figures, the measurement location is harder to discern at this scale and resolution. The 13:00 (1 p.m.) figure does show a bend in the plume that is qualitatively consistent with the second two plume intercept locations on this date. This will be investigated further for the final report.

The September 25th SO_2 plume encounter shown in **Figure 3.10.5** has been presented previously and speculated that the shape of the plume may be from different sources, such as the narrow sharp peak being related to the power plant and the relatively broad lower concentration plume north of the narrow peak could be from a more distant broad source such as the urban core or HSC. The south to north transect (**Figure 3.10.6**) also observes similar SO_2 plume characteristics and SO_2 peak location as the north to south (**Figure 3.10.5**) transect.

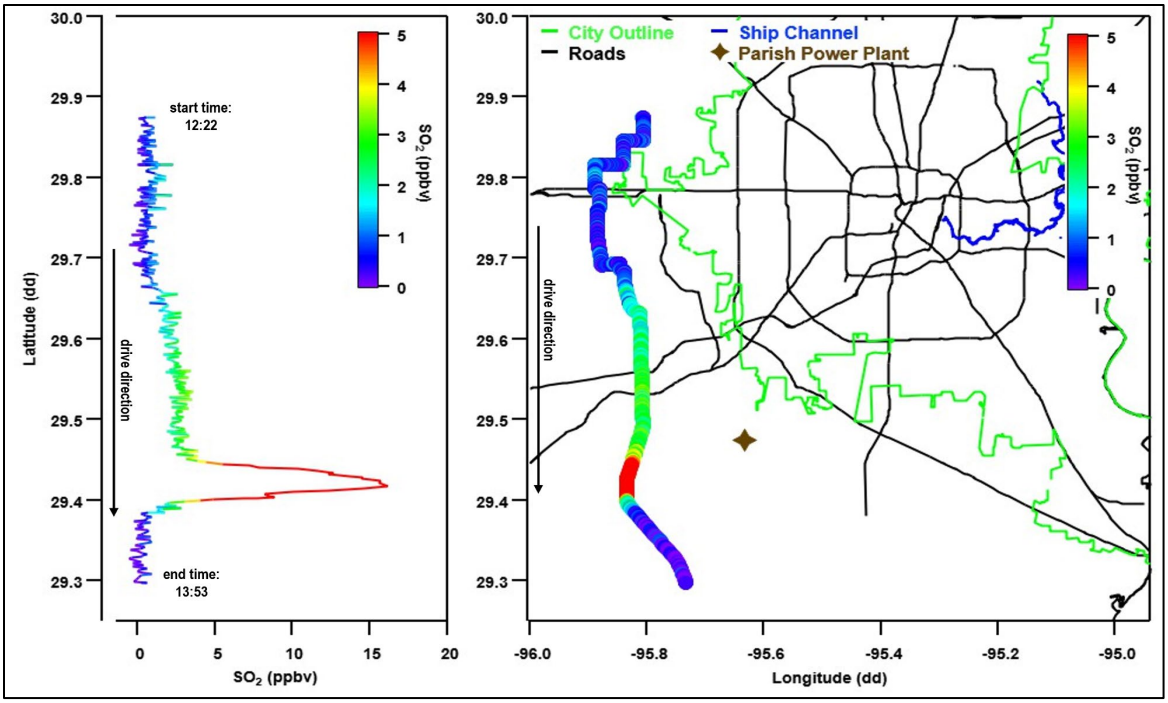

Figure 3.10.5: *An SO_2 plume measured on the MAQL1 during mobile measurements (30s averaged) on September 25, 2021. Right figure is a spatial plot of a north to south transect starting from 12:22 to 13:53 CST with measured SO_2. Left figure is the SO_2 plume concentration relative to latitude with a peak concentration of 16.2 ppbv.*

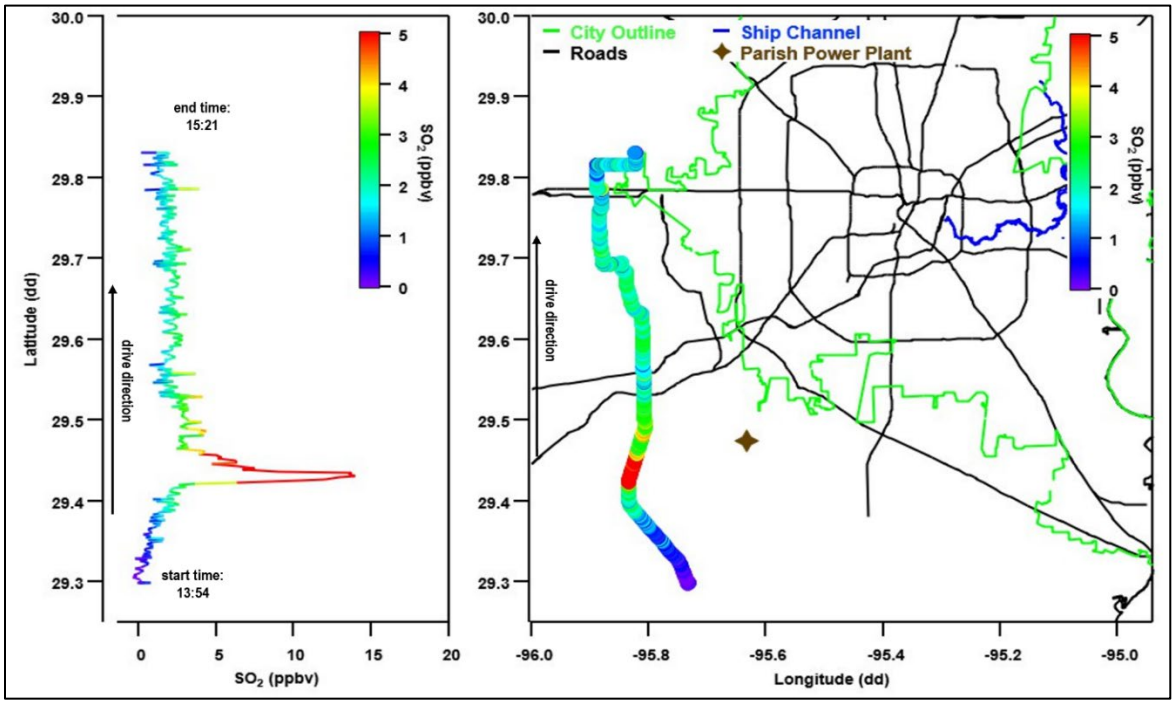

Figure 3.10.6: *An SO_2 plume measured on the MAQL1 during mobile measurements (30s averaged) on September 25, 2021. Right figure is a spatial plot of a south to north transect starting from 13:54 to 15:21 CST with measured SO_2. Left figure is the SO_2 plume concentration relative to latitude with a peak concentration of 13.9 ppbv.*

Model results indicate that the observed SO_2 plume all related to the Parrish Power Plant (**Figure 3.10.7**). **Figure 3.10.7** shows that in the 11:00 hour the plume initially moves to the west before becoming stretched along a northeast-southwest axis. Subsequent model steps show the portion of the plume located along this axis becoming more dispersed and by the time the MAQL1 encountered the plume near the 13:00 (1 P.M.) time step a cross section of the model may look remarkably similar to the observations. The open star in the CAMx figure shows the location of the MAQL1 when encountering the main plume, and a slight east-west shift in the model could easily result in the broad low concentration plume to the north of the main plume. As a result, the current interpretation of this and subsequent passes on this date are that the plume here and in **Figure 3.10.5** are most likely related to power plant emissions.

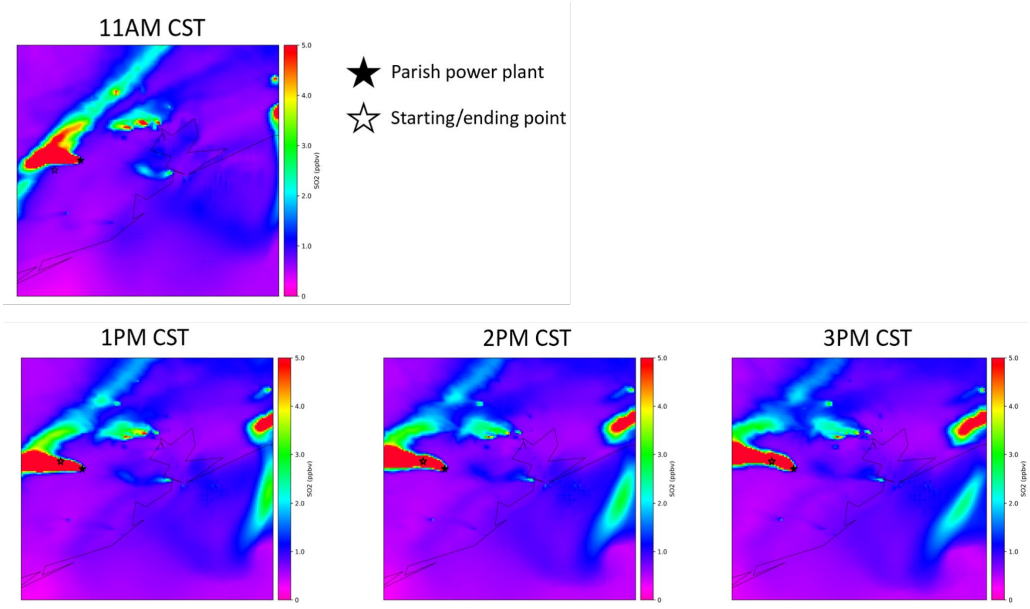

Figure 3.10.7: *CAMx-modeled SO_2 levels on September 25, 2021 near MAQL1 location at 11:00, 13:00, 14:00, and 15:00 CST. Solid star-shaped marker is the location of the Parish Power Plant. The hollow star-shaped marker is the location of the MAQL1 at approximate time. The 11:00 model is prior to measuring SO_2 plumes while 13:00, 14:00, and 15:00 is when MAQL1was driving within the SO_2 plume (Figure 3.10.4 and Figure 3.10.6).*

3.10.2 Formaldehyde plume in Houston Ship Channel-Tidal Road, September 5, 2021

On September 5, 2021 the MAQL1 conducted a number of traverses through the Independence Parkway and Tidal Road area. Each of the traverses are shown in **Figure 3.10.8** with the MAQL1 in situ HCHO in the first column, Pandora column abundance of HCHO in the center column, and time series plots of the HCHO, boundary layer height, and NO_2 photolysis rate (j_{NO2}) are shown on the right column. The j_{NO2} data are included here as an indication of cloud cover as evidenced by transient dips in j_{NO2} during partly cloudy conditions or relatively stable but suppressed values during overcast conditions. As the day

progressed the HCHO measurements tended to decrease relative to the previous pass through the area for the first three traverses. The third and fourth traverses were similar to each other.

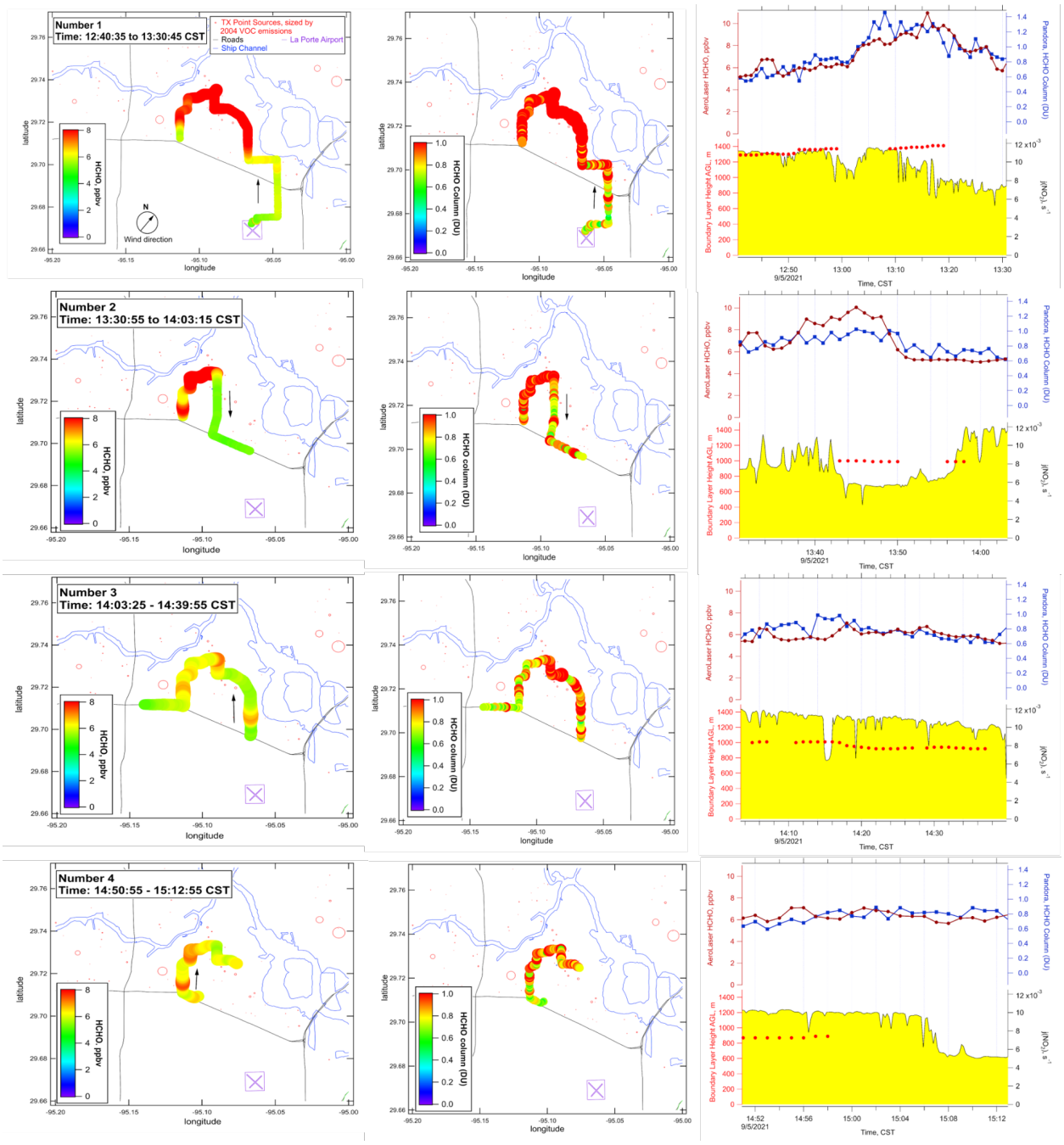

Figure 3.10.8: *Four passes of Tidal Road in the Houston Ship Channel on September 5th, 2021. Panel rows one through four are different passes. The first columns show spatial plots of the mobile lab track color-coded with in-situ HCHO mixing ratios measured by the AeroLaser and the second column show spatial plots of the remote sensing Pandora instrument color-coded by Dobson units. The third column shows time-series plots of the AeroLaser measurements (red dotted lines), the Pandora measurements (blue dotted lines), boundary layer height (red dots) and j_{NO2} (yellow shade).*

Although this is the first time a Pandora has been installed on the MAQL1 and deployed in a mobile fashion in the Houston area, it has been deployed previously in Hawaii for a volcano SO_2 study during the major eruption of Kilauea in 2018. During that pilot study there were periods where the in situ SO_2 and Pandora column were highly correlated and tracked each other well and has been interpreted that the SO_2 was reasonably well mixed within the boundary layer (other supporting SO_2 sonde vertical profile data showed that the plumes were almost entirely contained within the boundary layer). At other times the Pandora columns were quite high while surface concentrations remained low and suggested a lofted SO_2 plume. Similarly high surface concentrations with low column measurements were interpreted as an indication of a strong but shallow layer of SO_2 at the surface.

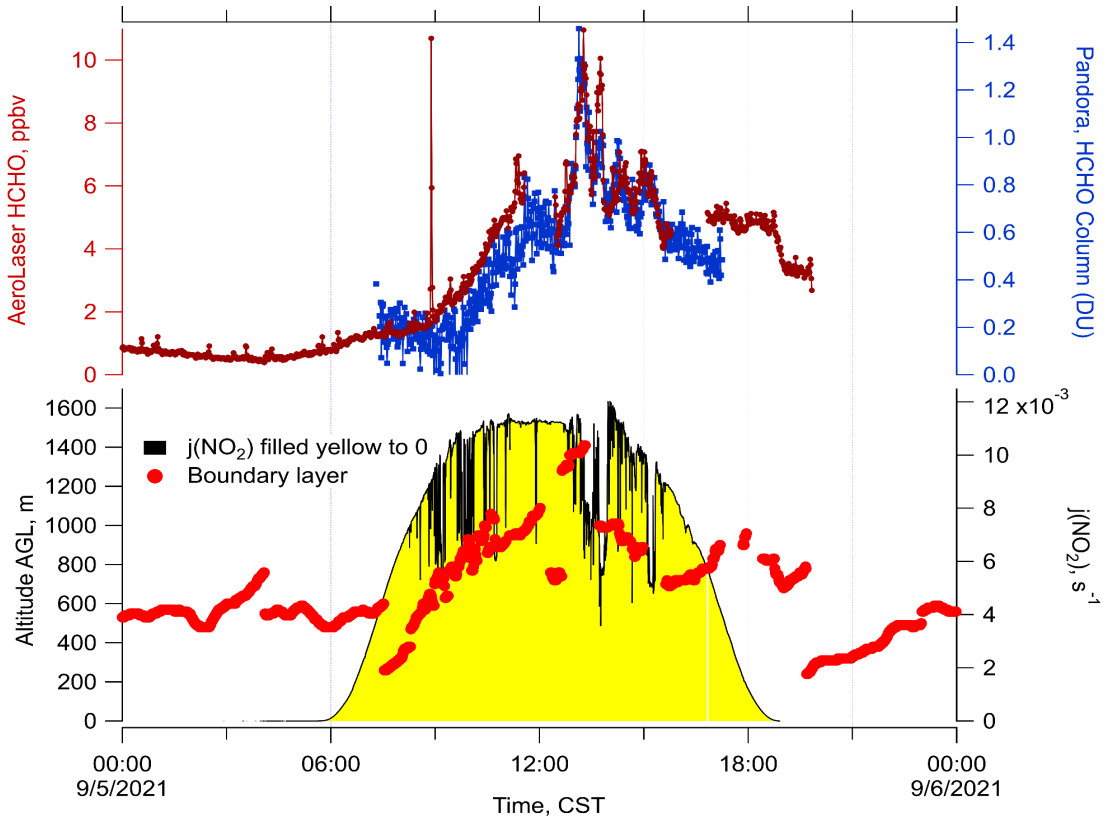

Figure 3.10.9: *Time-series plot for September 5, 2021 of Pandora and AeroLaser measurements on the top graph. The bottom graph shows the boundary layer height and* j_{NO2}.

The scatter plot below (**Figure 3.10.10**) shows that the Pandora and in situ HCHO measurements are well correlated outside of a narrow transient HCHO plume visible around 09:00 in **Figure 3.10.9** Applying the logic derived from the Kilauea observations described above these plumes seem to be relatively well mixed to a height sufficient that the column abundances are proportional to the surface data. Although no high resolution HCHO profiles

exist for these data sets it is reasonable to assume that the plumes are effectively constrained to the boundary layer.

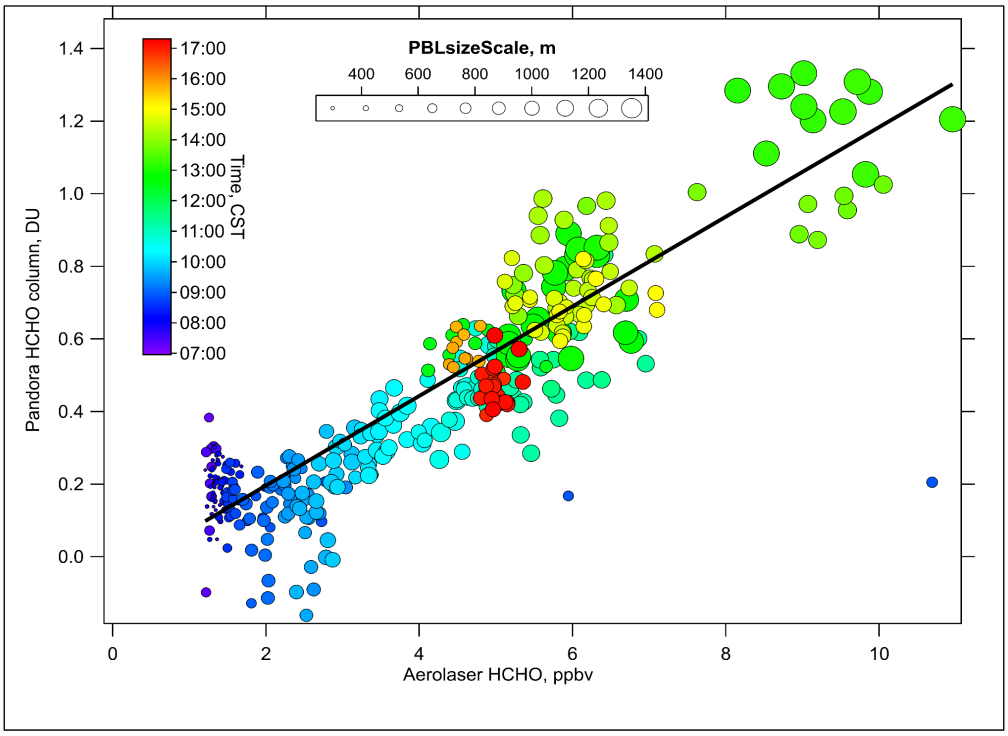

Figure 3.10.10: *Scatter plot of the four passes through the Tidal Road area on 5 September 2021 of the remote sensing Pandora and the in-situ AeroLaser instruments measuring HCHO. The solid circles are color-coded as time in central standard time and sized to the height of the boundary layer measured by the CL31 ceilometer. The in situ and remote sensing measurements were well correlated on this day.*

3.10.3 Formaldehyde in Houston urban plume, 11 September 2021

Formaldehyde was also observed in conjunction with the Houston urban plume and is likely a result of secondary photochemistry. An example of this is shown in the figures below (**Figure 3.10.11**). The MAQL1 transited to the west side of Houston on I-10 where it began a series of north-south traverses on relatively low traffic roads to reduce interference from mobile emission sources as compared to more populated areas. During these traverses it was noted that the HCHO was well correlated and tended to peak at approximately the same location as the O_3 plume peak. During this day the synoptic winds began out of the northeast, moving the plume to the southwest. As the day progressed the winds rotated to the east, and eventually southeast resulting in the plume shifting progressively northward during subsequent traverses.

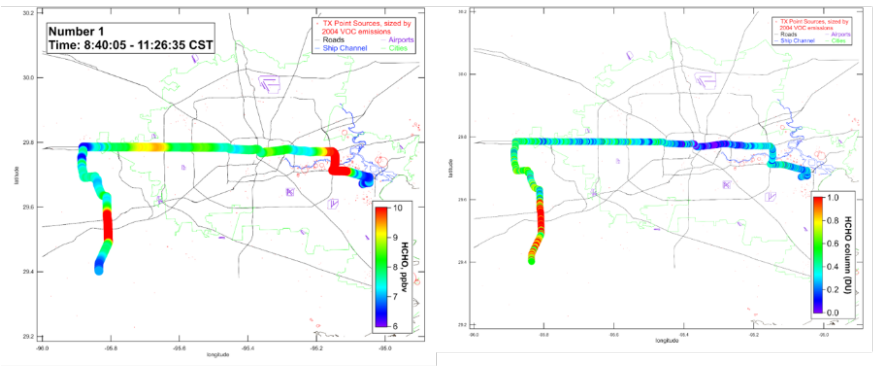
Number 1
Time: 8:40:05 - 11:26:35 CST
TX Point Sources, sized by 2004 VOC emissions
Roads
Airports
Ship Channel
Cities
HCHO, ppbv
HCHO column (DU)
latitude
longitude

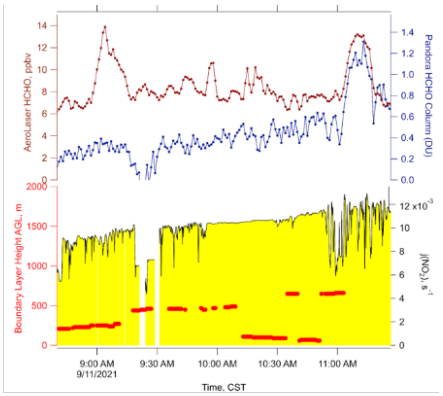
AeroLaser HCHO, ppbv
Pandora HCHO Column (DU)
Boundary Layer Height AGL, m
j(NO2), s-1
9:00 AM
9/11/2021
9:30 AM
10:00 AM
10:30 AM
11:00 AM
Time, CST

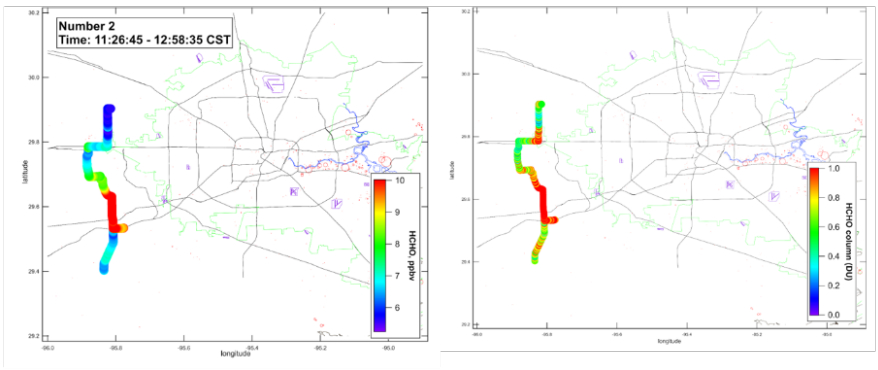
Number 2
Time: 11:26:45 - 12:58:35 CST
HCHO, ppbv
HCHO column (DU)
latitude
longitude

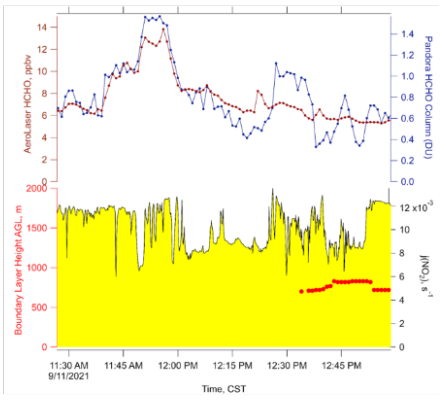
AeroLaser HCHO, ppbv
Pandora HCHO Column (DU)
Boundary Layer Height AGL, m
j(NO2), s-1
11:30 AM
9/11/2021
11:45 AM
12:00 PM
12:15 PM
12:30 PM
12:45 PM
Time, CST

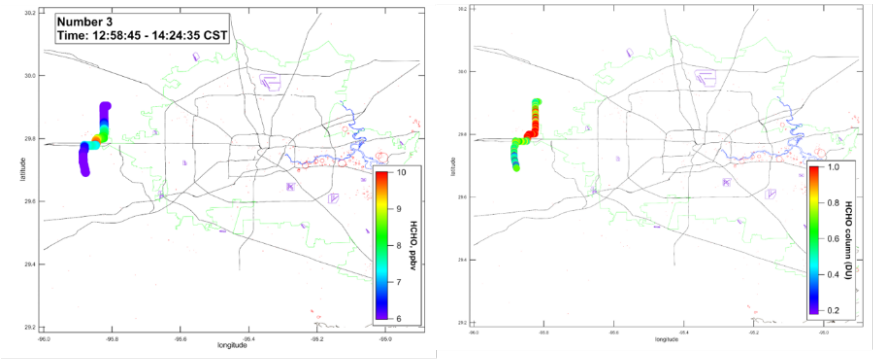
Number 3
Time: 12:58:45 - 14:24:35 CST
HCHO, ppbv
HCHO column (DU)
latitude
longitude

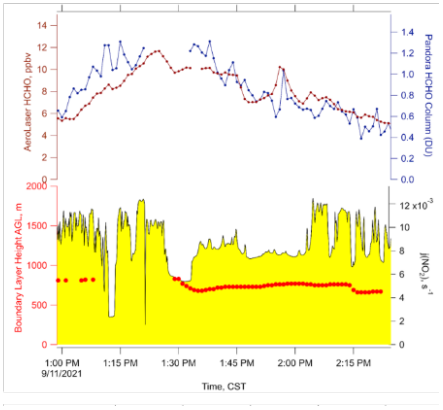
AeroLaser HCHO, ppbv
Pandora HCHO Column (DU)
Boundary Layer Height AGL, m
j(NO2), s-1
1:00 PM
9/11/2021
1:15 PM
1:30 PM
1:45 PM
2:00 PM
2:15 PM
Time, CST

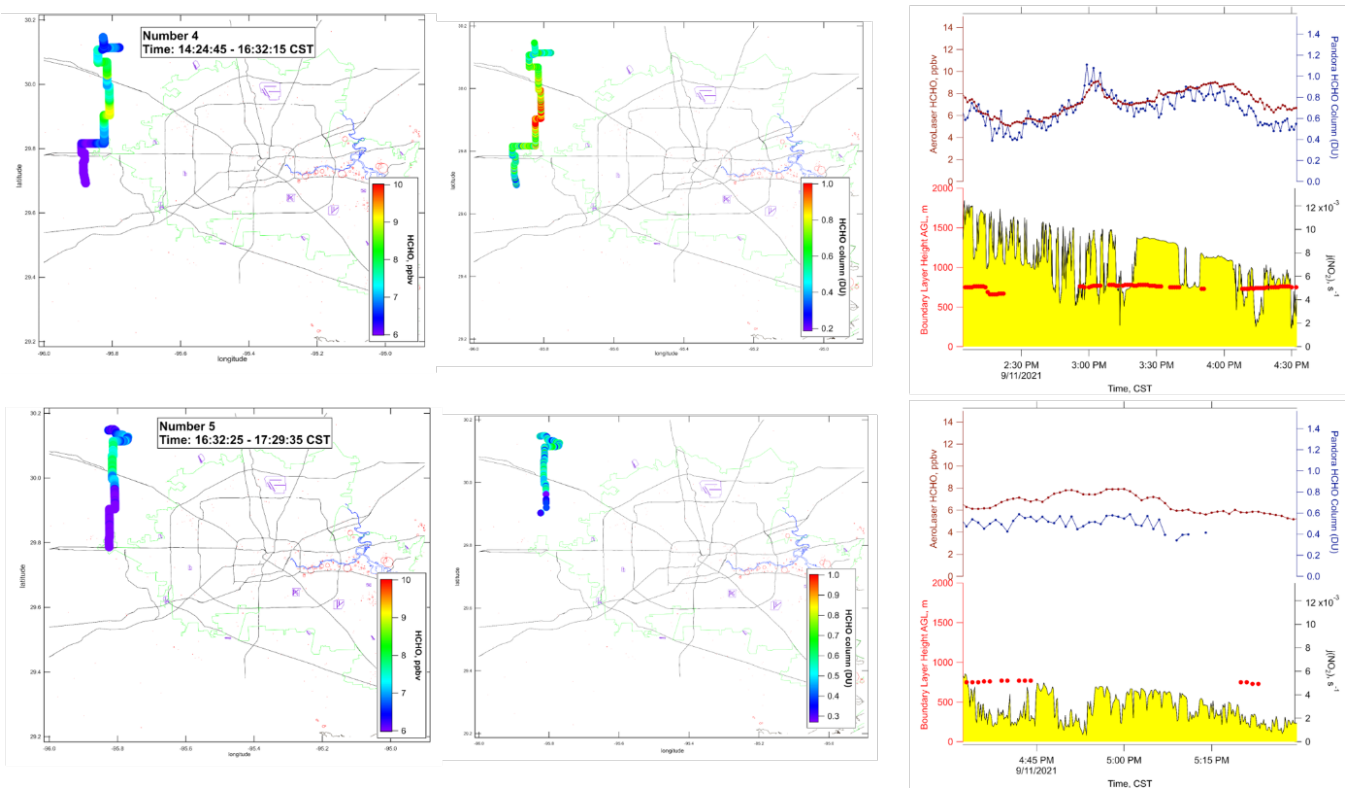

Figure 3.10.11: *Panel rows one through five are different segments of MAQL1 traverses downwind of the Houston urban core. The first columns show spatial plots of the mobile lab track color-coded with in-situ HCHO mixing ratios measured by the AeroLaser and the second column show spatial plots of the remote sensing Pandora instrument color-coded by Dobson units. The third column shows time-series plots of the AeroLaser measurements (red dotted lines), the Pandora measurements (blue dotted lines), boundary layer height (red dots) and j_{NO2} (yellow shade).*

Figure 3.10.12 below shows that during the first part of the morning, roughly through 11:00 a.m., the Pandora measurements did not track the same patterns as the later periods or the previous case study described above. This timing marks the approximate location that the mobile lab first encountered the core of the urban plume, likely fairly well mixed through the boundary layer due to transport time and convective mixing. Prior to this the MAQL1 was primarily transiting to the sampling area via major highways and interstates where the observed in situ HCHO may be more related to mobile emission sources which would be more likely to reside closer to the emission point at the surface, consistent with the interpretation of the Kilauea data.

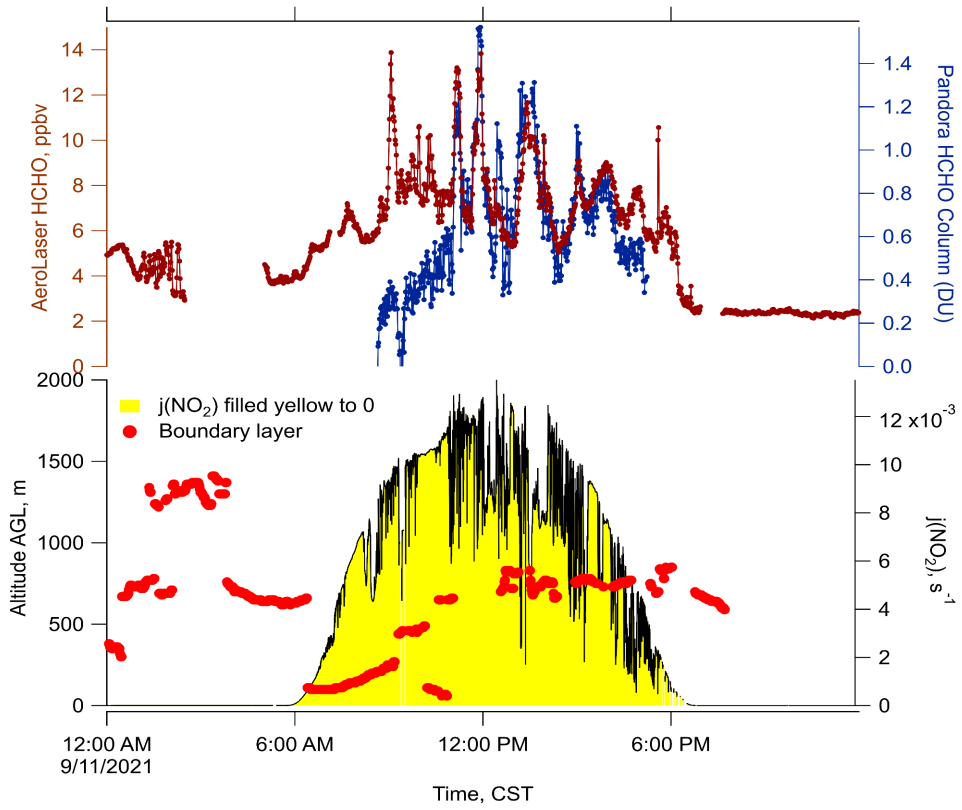

Figure 3.10.12: *Time-series plot for 11 September 2021 of Pandora and AeroLaser measurements on the top graph. The bottom graph shows the boundary layer height and* j_{NO2}.

Similar to the time series figure above (**Figure 3.10.12**), the correlation plot of the Pandora and in situ HCHO measurements clearly shows a strong relationship after 11:00 a.m. CST when the first of the urban plume "core" was encountered. Points prior to 11:00 a.m. have been excluded from the fit line but can be seen as the smaller blue dots, indicating a lower boundary layer and earlier time of day.

Taken together, it appears that the Pandora may not have detected a significant increase in the column abundance of HCHO while on major roads but did identify HCHO during the remainder of the day that appears to be more related to the urban plume.

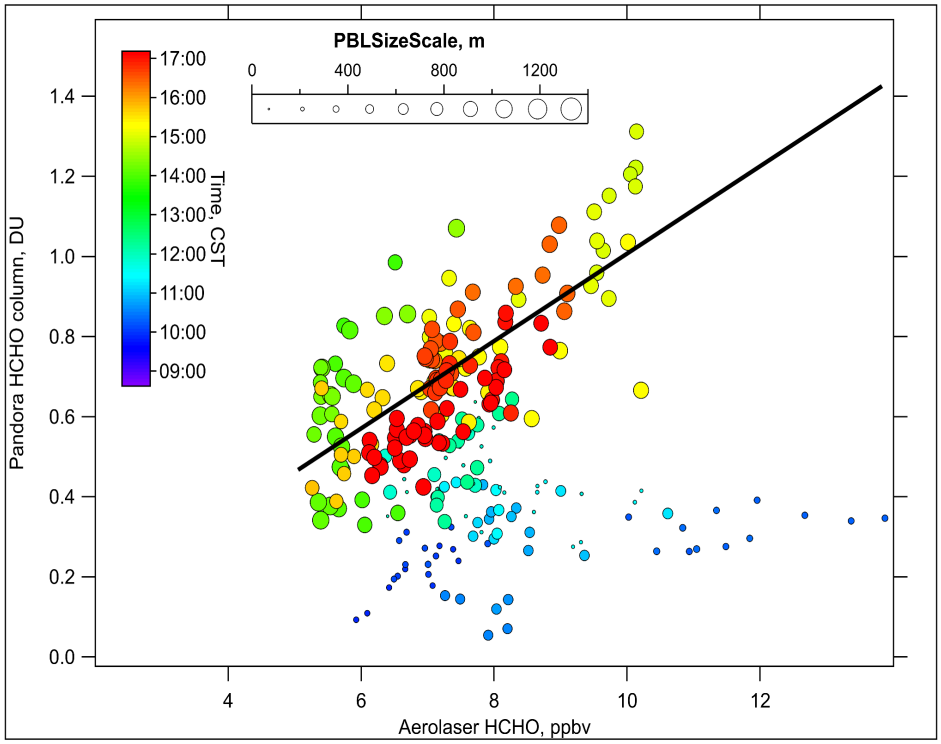

Figure 3.10.13: *Scatter plot between the remote sensing Pandora and the in-situ AeroLaser instruments measuring HCHO. The solid circles are color-coded as time in Central Standard Time and sized to the height of the boundary layer measured by the CL31 ceilometer. The correlation line plotted excludes the blue points where the in situ and remote sensing measurements are not well correlated. These points occurred with low boundary layer heights and in the morning hours while the daytime boundary layer was still developing.*

3.10.4 Formaldehyde at Battleground Site, September 2021

For Battleground, we calculated a campaign average of 3.8 ± 2.2 ppbv (average ± standard deviation). The campaign time series for HCHO at Battleground reveals distinct events over the entire month. To better discern periods of enhanced HCHO at Battleground, we are labeling periods that exceed the campaign mean plus one standard deviation as an "event".

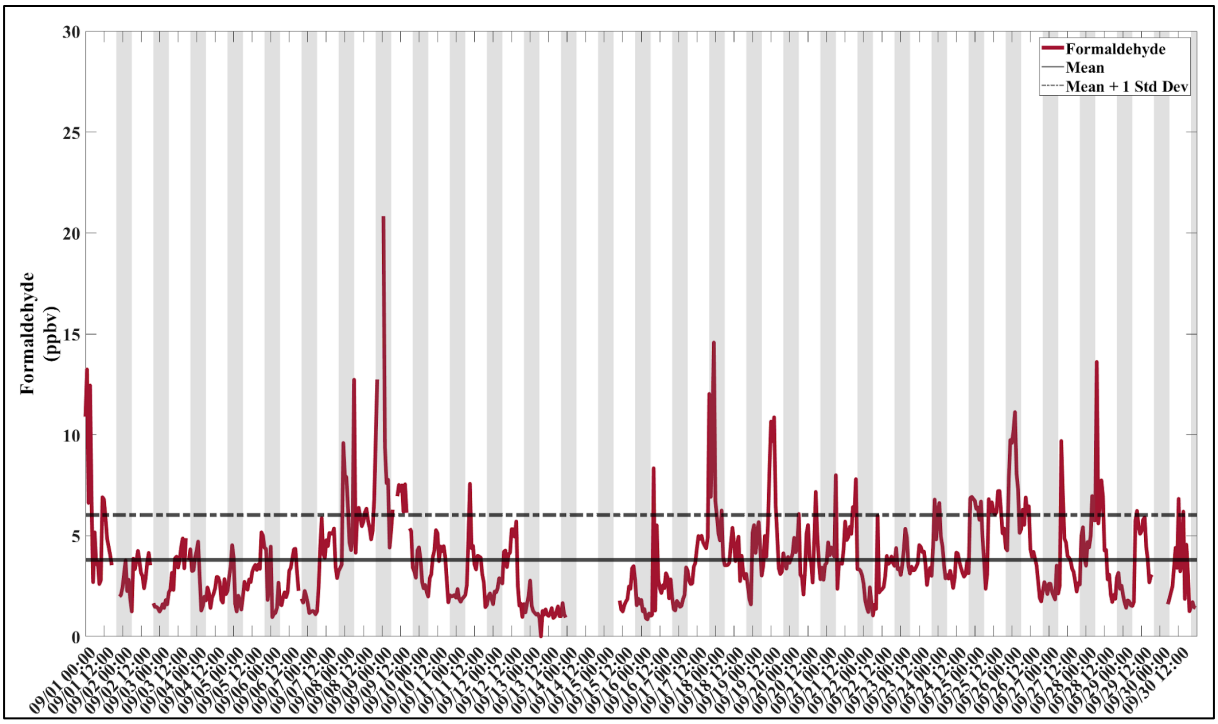

Figure 3.10.14: *Ambient concentration of HCHO at Battleground measured with the PTRMS modified with a cold trap inlet. Grey shading indicates nighttime periods (8 p.m.–6a.m). The campaign mean is marked with a solid line, while the mean plus one standard deviation is marked with a dashed line.*

To characterize HCHO events at Battleground we have prepared a table which includes the duration, event average mixing ratio and maximum ppbv for each event. There were 19 separate events in the September campaign. Peak events occurred the morning of 9/8, overnight 9/8–9/9 (**Figure 3.10.15**) and overnight 9/17–9/18 (**Figure 3.10.16**).

Table 3.21: *Formaldehyde events measured at Battleground during Sept 2021. Max concentration shown in red. Nighttime events shown in blue, Night and daytime events shown in green.*

Start	Stop	Average	Threshold	Max ppbv
9/1/2021 0:00	9/1/2021 5:00	9.72	6.02	13.24
9/1/2021 10:00	9/1/2021 13:00	6.85	6.02	6.91
9/7/2021 21:00	9/8/2021 2:00	7.26	6.02	9.60
9/8/2021 5:00	9/8/2021 7:00	12.73	6.02	12.73
9/8/2021 18:00	9/9/2021 5:00	10.71	6.02	20.83
9/9/2021 7:00	9/9/2021 18:00	7.01	6.02	7.55
9/11/2021 8:00	9/11/2021 10:00	7.57	6.02	7.57
9/15/2021 7:00	9/15/2021 9:00	8.34	6.02	8.34
9/17/2021 19:00	9/18/2021 1:00	10.03	6.02	14.57
9/19/2021 3:00	9/19/2021 16:00	6.41	6.02	10.87
9/23/2021 21:00	9/24/2021 2:00	6.09	6.02	6.79
9/24/2021 20:00	9/25/2021 7:00	6.12	6.02	6.92
9/25/2021 2:00	9/25/2021 17:00	5.64	6.02	7.22
9/25/2021 21:00	9/26/2021 5:00	9.12	6.02	11.12
9/26/2021 6:00	9/26/2021 12:00	6.25	6.02	6.90
9/27/2021 7:00	9/27/2021 9:00	9.70	6.02	9.70
9/28/2021 3:00	9/28/2021 14:00	6.77	6.02	13.61
9/30/2021 11:00	9/30/2021 13:00	6.83	6.02	6.83
9/30/2021 14:00	9/30/2021 16:00	6.20	6.02	6.20

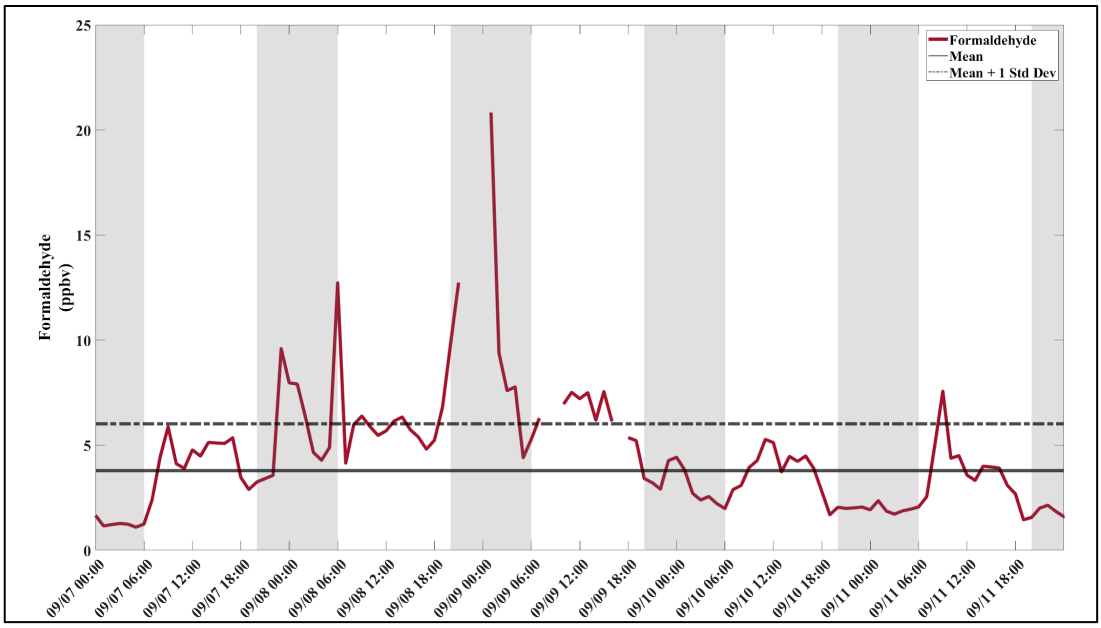

Figure 3.10.15: *Event periods in early September at Battleground.*

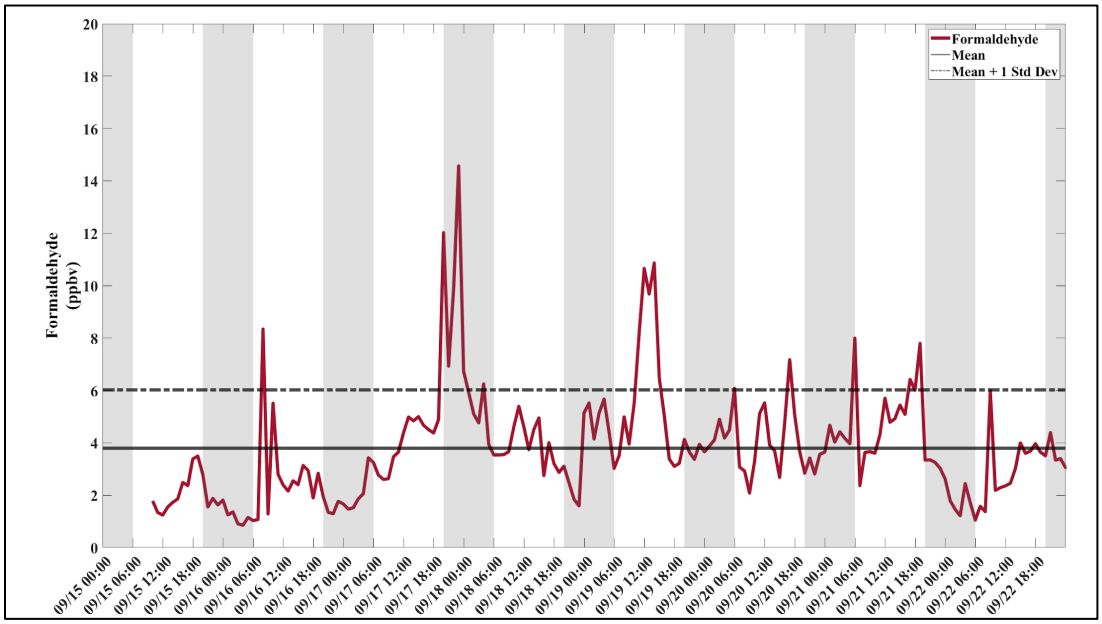

Figure 3.10.16: *Event periods in mid- September at Battleground.*

3.10.5 Boundary Layer Profiles Across Galveston Bay

Boundary layer processes around the land-water interface involve a complicated mix of meteorological factors with steeper gradients than in other areas (Simpson 1994). The lowest ceilometer retrieved layers were compared at sites on the east and west sides of Galveston Bay during July and August of 2021 using a monthly averaged diurnal profile (**Figure 3.10.17**). The lowest layer retrieved in both months showed significant differences throughout the day. In the early morning, before sunrise, the profiles are separated by 200–

500m. In the afternoon another difference in the lowest layer develops, when the profile at the shrimp boat in Smith Point, TX collapses early in the afternoon while the UH Pontoon on the west side of Galveston Bay continues to maintain development through sunset. During the afternoon hours a 500–800m difference was recorded between the two boat platforms. These differences may be a result of the diurnal sea/bay breeze development during July and August, where the shrimp boat profile shows a marine influence and the pontoon a profile more typical of land-based measurements. The second retrieved layer at both locations show much better agreement throughout the observation period and is likely more representative of a regional feature.

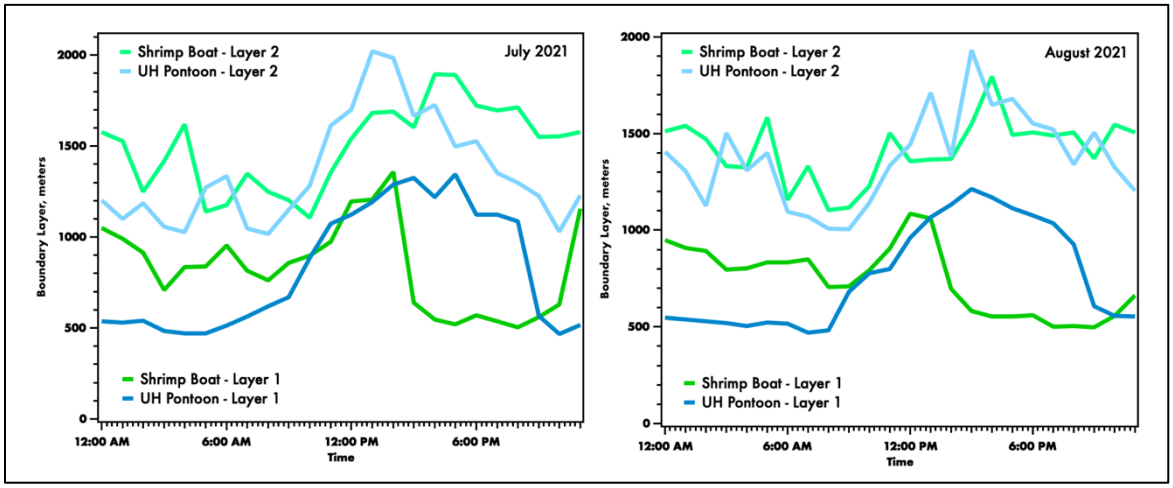

Figure 3.10.17: *Diurnal profiles of boundary layers 1 and 2 retrieved by ceilometers mounted on the UH pontoon and shrimp boat docked in Kemah, TX (west side of bay) and Smith Point, TX (east side of bay) respectively.*

3.10.6 Low Ozone Day-18 July 2021

A day with low ozone was targeted for an ozonesonde launch to assess the vertical depth of low ozone for comparison of previous work done (Tuite et al., 2018) on the Texas coast near Galveston, TX. In 2016 a TCEQ study with UH, UCLA, and Environ (now Ramboll) to determine whether proposed halogen chemistry resulting from interactions with the ocean surface could be responsible for the observations of low O_3 reaching the Texas Gulf Coast during periods of onshore flow. Tuite et al., 2018 found that air masses that spent a longer time over the water tended to have lower ozone when observed along the Texas Gulf Coast, with air masses originating from the central Atlantic showing the lowest ozone. A question that remained from the project was to what extent the low ozone at the surface extended vertically and was it constrained by the boundary layer dynamics.

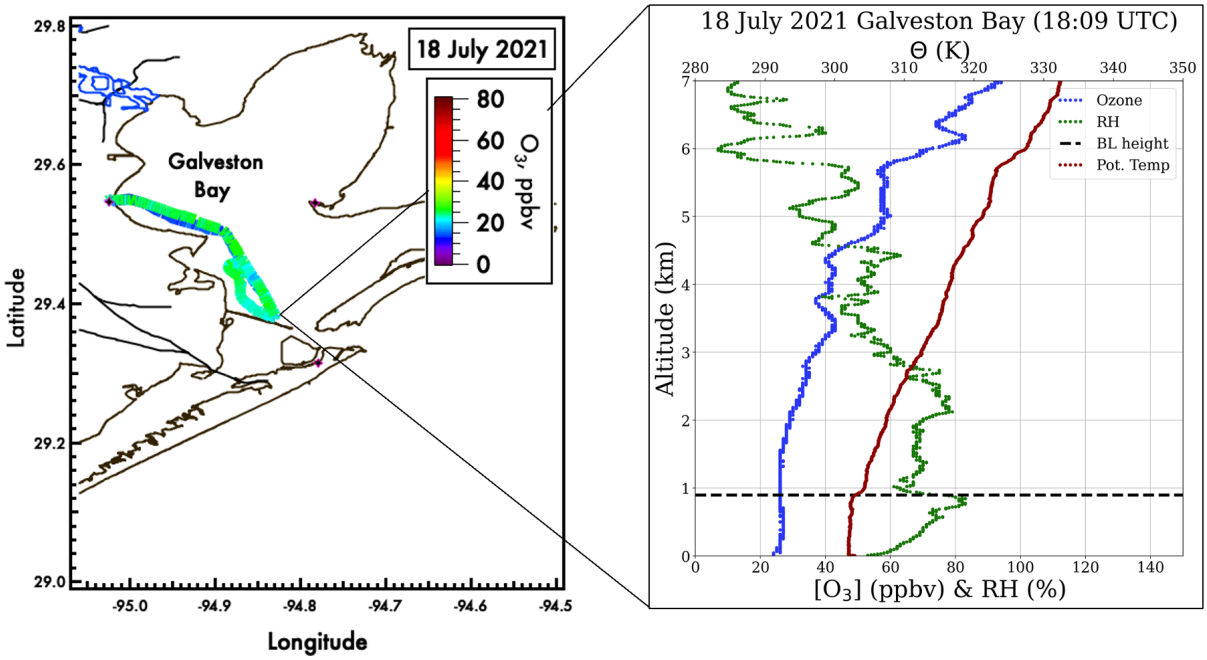

Figure 3.10.18: *(Left) Spatial plot of the UH pontoon boat tracks with associated ozone concentrations from 18 July. (Right) Ozonesonde profile released near the Texas City Dike during a period of low ozone.*

The vertical profile of ozone (**Figure 3.10.18**) from the launch on 18 July, a day where low O_3 was forecast along with persistent onshore flow, shows that O_3 was between 20–30 ppbv from the surface to approximately 2,000 m (2 km), nearly 1000 m above the boundary layer height as determined by the height of the inversion in the potential temperature profile.

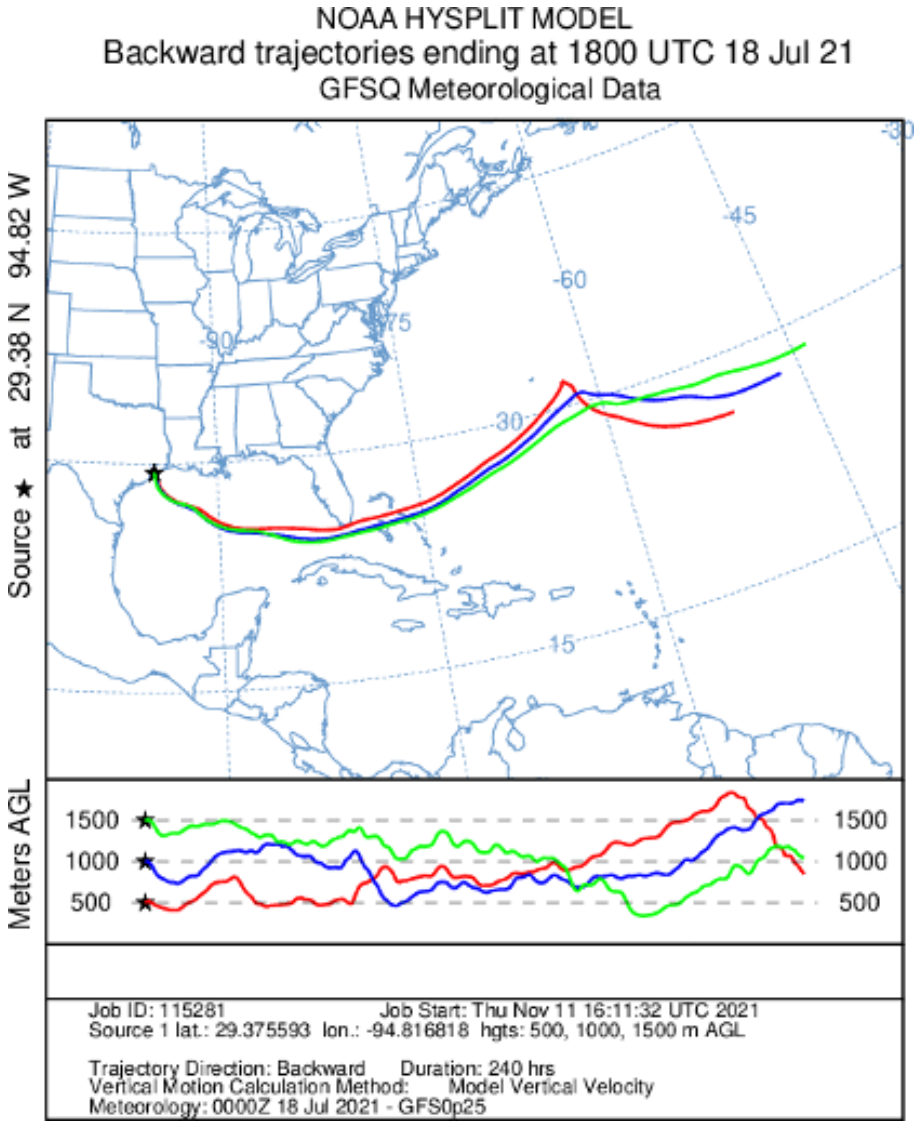

Figure 3.10.19: *HYSPLIT 10-day backward trajectory for 18 July 2021 showing the origin of the observed air mass that accompanied the targeted low ozone launch.*

Figure 3.10.19 shows the ten-day back trajectory for the ozonesonde launch on 18 July, from three heights over the Bay, 500 m (red), 1,000 m (blue), and 1,500 m (green). These trajectories all originate in the central Atlantic and are comparable to the findings from Tuite et al., 2018. All three heights mixed between 500–1,500 m showing the likely interactions with the ocean surface layer.

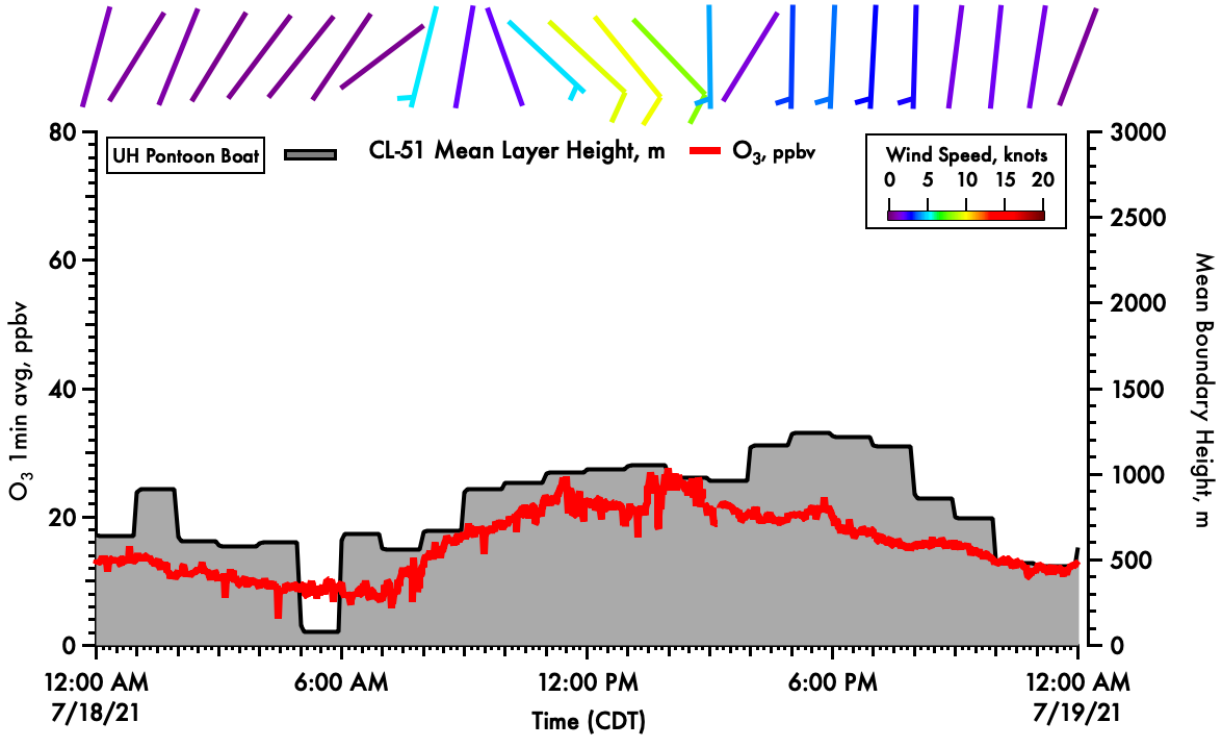

Figure 3.10.20: *Time-series of ozone, winds and mean boundary height (ceilometer retrieved) on the UH pontoon boat from 18 July 2021.*

Conditions on the surface of Galveston Bay were consistent with forecast and previous work showing low ozone (< 30 ppbv) and persistent onshore flow (**Figure 3.10.20**). The height of the ceilometer retrieved boundary layer was lower than the vertical depth of low ozone observed from the 18 July ozonesonde launch. Additionally, more info can be found in the final report for the Galveston Offshore Ozone Observations (GO3) project #20-004.

4 TASK UPDATES

TASK 1 - GAD

This task was completed on February 4, 2022.

TASK 2 - PROGRESS REPORTS

This task was completed each month, a total of 14 monthly activity reports were submitted.

TASK 3 - ANALYSIS OF TRACE GASES AND METEOROLOGICAL MEASUREMENTS FROM VARIOUS MOBILE PLATFORMS

This task was completed, and the final data set was submitted to the TCEQ on April 30, 2023. We evaluated the trace gas measurements, spatially and temporally, from the ground, mobile, ozonesonde, and boat platforms during TRACER-AQ1 and, where applicable, compare to the NASA Gulfstream-V aircraft data and ozone Light Detecting and Ranging (LIDAR) instruments. We assessed the potential influence of emissions from power plant, vehicles, shipping, and/or other sources on trace gas measurements, using meteorological measurements and trajectory models. We used traditional statistical methods (e.g., correlations, diurnal profiles, wind/pollution roses, multivariate analysis) to evaluate strength, characterization, and/or contribution. We examined and characterized observed air quality events, such as the high ethene observed on September 27, 2021. The trace gases used in the analyses included oxides of nitrogen (NOx), sulfur dioxide (SO2), ozone, carbon monoxide, formaldehyde, and volatile organic compounds (VOCs), including HRVOC using data collected from the UH Mobile Air Quality Lab (MAQL1), the Baylor University Mobile Air Quality Lab (MAQL2), the three instrumented boats, ozonesondes, and the surface monitoring network. We also incorporated external datasets within the overall data analysis.

TASK 4 - COMPARE TRACER-AQ MEASUREMENTS TO RELEVANT TEXAS-BASED AIR QUALITY DATASETS

This task was completed, and the final data set submitted to the TCEQ on March 15, 2023. We compared measurements collected during the TRACER-AQ field campaign with measurements performed during other field campaigns (Texas Air Quality Study (TexAQS) 2000, TexAQS 2006, SHARP 2009, DISCOVER-AQ 2013) and reported TCEQ monitoring data. We reviewed measurements from DISCOVER-AQ 2013 and 2006, with a specific focus on the high ozone event associated with the last days of the campaign. We compared the observations between 2021 TRACER-AQ1 and 2006, specifically the VOC/NOx sensitivity and ozone production efficiency.

TASK 5 – CHEMISTRY AND DYNAMICS OF HIGH OZONE EPISODES

This task was completed, and the final data set submitted to the TCEQ on April 15, 2023.

We examined how the distinct meteorological regimes during the TRACER-AQ campaign impacted the chemistry and the horizontal and vertical transport of gases. Specifically, we examine how the horizontal and vertical transport of ozone and ozone precursors impacted background levels in Houston during high ozone events and determine if ozone aloft had sources outside the Houston region. We reviewed how changes in the wind field impact the chemical environment and subsequently affect the timing and distribution of high ozone. We used the MAQL2 aerosol optical data to identify periods of smoke plume influence from biomass burning during high ozone episodes.

TASK 6 – CHEMISTRY AND DYNAMICS OF OVERWATER OBSERVATIONS

This task was completed, and the final data set submitted to the TCEQ on 30 April 2023. We analyzed how high ozone over the Gulf of Mexico and/or Galveston Bay relate to measurements over land. We examined under what synoptic and mesoscale meteorological conditions was high ozone observed over the water. We examined the spatial distribution of high ozone concentrations in Galveston Bay and the Gulf of Mexico with meteorological measurements to determine potential precursor sources and/or source regions.

TASK 7 – MEASUREMENT INTERCOMPARISONS BETWEEN PLATFORMS

This task was completed, and the final data set submitted to the TCEQ on 30 April 2023. We conducted a quality assurance intercomparison of the collected data during the 2021 field campaign in Houston from the MAQL1, MAQL2, boat, and ozonesonde platforms. We included in the intercomparison: Nitric Oxide (NO), Oxides of Nitrogen (NO_X), Reactive Oxides of Nitrogen (NO_Y), Nitrogen Dioxide (NO_2), Carbon Monoxide (CO), Sulfur Dioxide (SO_2), Ozone (O_3), Formaldehyde (HCHO), VOCs, Planetary Boundary Layer (PBL) height, and winds. We also performed comparisons of in situ methods with the best available ground based and airborne remote sensing measurements. The analysis and performance of specific platforms, new instrumentation and instrumentation upgrades were conducted, including the Peak Performer 1 Reducing Compound Photometer isoprene monitor, Proton Transfer Mass Spectrometer with the Selective Reagent Ionization (SRI) module, and the AROMA-VOC Mobile Trace Chemical Analyzer.

TASK 8 – MODELING ANALYSIS TO AID THE OBSERVATIONAL ANALYSIS

This task was completed, and the final data set submitted to the TCEQ on 31 March 2023. We conducted modeling analysis to complement, corroborate, and/or validate the observational analyses in Tasks 3 through 7. We designed model sensitivity simulations to investigate the separate and combined roles of local emissions, dynamics, chemistry, and background airmass on high pollution events from the 2021 observations. We reviewed different modeling tools and selected the best suited for the analysis of interest in consultation with the TCEQ Project Manager. Specifically, we identified the significance of transport (e.g., regional, continental) on high ozone days and if the summer 2021 overwater

measurements during low ozone days were consistent with the role of halogen chemistry on marine air observed in 2016 (UCLA, 2016).

5 RECOMMENDATIONS FOR FUTURE WORK

The results from this project highlight several important findings as well as areas for additional research. Some recommendations for future work include:

- Based on the 2021 observations at Battleground, an examination of black carbon in the ship channel with an emphasis on association with varying wind directions to help identify potential sources. Mobile/portable measurements on land and by boats may also be helpful in identifying black carbon source locations.
- With the addition of a larger research boat, more complete payloads of monitoring equipment can be deployed. The navigation equipment aboard the boat which receives the maritime Automatic Information System identifiers of boats and ships in the area it may be possible to characterize emissions from individual ships in the Houston/Galveston area. Although opportunistic and anecdotal, during this project the team determined it was possible to link some observations of plumes with individual ships via AIS and publicly available information. The deployment of more robust measurements could be coupled with AIS information and help validate other emission inventory efforts which link AIS information such as vessel speed and draft with estimated emission factors to improve the shipping emissions inventory.
- By continuing measurements over the water, changes in shipping emissions over time may be discernable. This will be important to determine both the frequency of occurrence of ships which may be running inefficiently, or which do not switch to cleaner fuels as well as possible impacts on shipping due to offshore terminals, such as the Sea Port Oil Terminal, one of several terminals which will be constructed off the Texas coast. Baseline measurements prior to construction could be compared to measurements during construction and once the terminals become operational.
- For 2023 the small automated O_3/Ox sampling systems have been deployed as part of the TCEQ funded HNET project (PGA 582-23-43322-029). Additional $PM_{2.5}$ measurements could be added to the payload using similar techniques to the $(BC)^2$ project (PGA 582-18-81339) to identify potential smoke and/or dust in the marine boundary layer prior to entering Texas. It would be useful to collocate a second set of instruments at a $(BC)^2$ sampling site, such as the one in Galveston to provide a more direct comparison of the two instrument suites and allow for a normalization of the data such that the offshore measurements could more directly be compared to the inland BC^2 measurements in the Houston, DFW, and El Paso areas. The offshore measurements, particularly when coupled with the ceilometer measurements on the O#/Ox package in the Gulf may help determine whether these long-range and international transport events are occurring within the marine layer or aloft, and if the plume is lofted, how the smoke and dust mix down to the surface once reaching land.

- With the proposed lowering of the NAAQS for $PM_{2.5}$, additional measurements of PM composition may help to better characterize sources of PM as well as precursor species. This information could be useful in developing additional control strategies should a $PM_{2.5}$ SIP be needed.
- Together, the UH, Baylor, and St. Edward's groups have significant capabilities for making measurements of primary and secondary pollutants as well as a wide variety of research platforms ranging from stationary sites to multiple scales of mobile laboratories on land and the water, as well as drone-based sampling. Recent additions of new faculty and VOC and aerosol instrumentation at Texas A&M has led to conversations regarding an expanded collaboration. It is hoped that their complimentary measurements would further strengthen Texas' ability to collect and analyze advanced datasets to help improve air quality in Texas. The PIs are always looking for opportunities such as this to work towards sustainable collaborations.

6 REFERENCES

Actkinson, B., Ensor, K., and Griffin, R. J.: SIBaR: a new method for background quantification and removal from mobile air pollution measurements, Atmos. Meas. Tech., 14, 5809–5821, https://doi.org/10.5194/amt-14-5809-2021, 2021.

Actkinson, B. 2022. SIBaR_Background_Removal_and_Quantification. San Francisco (CA): GitHub; [accessed 2021 December 15]. https://github.com/bactkinson/SIBaR_Background_Removal_and_Quantification.

Al-Fadhli, Fahad M., Yosuke Kimura, Elena C. McDonald-Buller, and David T. Allen (2012), Impact of Flare Destruction Efficiency and Products of Incomplete Combustion on Ozone Formation in Houston, Texas, *Industrial and Engineering Chemistry Research*, DOI: 10.1021/ie201400z. [TexAQS 2006;]

Alvarado, L., Richter, A., Vrekoussis, M., Hilboll, A., Kalisz Hedegaard, A.B., Schneising, O., Burrows, J.P., 2020. Unexpected long-range transport of glyoxal and formaldehyde observed from the Copernicus Sentinel-5 Precursor satellite during the 2018 Canadian wildfires. Atmos. Chem. Phys. 20, 2057–2072.

Banta, R. M., C. J. Senff, J. Nielsen-Gammon, L. S. Darby, T. B. Ryerson, R. J. Alvarez, S. P. Sandberg, E. J. Williams, and M. Trainer. "A Bad Air Day in Houston." Bulletin of the American Meteorological Society 86, no. 5 (May 2005): 657–70.

Berlin, S.R., A.O. Langford, M. Estes, M. Dong, D.D. Parrish (2013), Magnitude, decadal changes, and impact of regional background ozone transported into the greater Houston, Texas area, *Environ. Sci. Technol*., 47(24): 13985-13992, doi: 10.1021/es4037644.

Brioude, J., Arnold, D., Stohl, A., Cassiani, M., Morton, D., Seibert, P., Angevine, W., Evan, S., Dingwell, A., Fast, J.D., 2013. The Lagrangian particle dispersion model FLEXPART-WRF version 3.1. Geosci. Model Dev. 6, 1889–1904.

Chen, F., Dudhia, J., 2001. Coupling an advanced land surface–hydrology model with the Penn State–NCAR MM5 modeling system. Part I: Model implementation and sensitivity. Mon. Weather Rev. 129, 569–585.

Chen, S., Ren, X., Mao J., Chen, Z., Brune, W. H., Lefer, B., Rappengluck, B., Flynn J., Olson, J., and Crawford, J. H. (2010). A comparison of chemical mechanisms based on TRAMP-2006 field data. Atmospheric Environment, 44(33), 4116-4125. https://doi.org/10.1016/j.atmosenv.2009.05.027

Caicedo, V., B. Rappenglueck, G. Cuchiara, J. Flynn, R. Ferrare, A. J. Scarino, T. Berkoff, C. Senff, A. Langford, and B. Lefer. "Bay Breeze and Sea Breeze Circulation Impacts on the Planetary Boundary Layer and Air Quality from an Observed and Modeled DISCOVER-AQ Texas Case Study." Journal of Geophysical Research: Atmospheres 124, no. 13 (2019): 7359–78.

Cooper, O. et al., 2007. Evidence for a recurring eastern North America upper tropospheric ozone maximum during summer, *J. Geophys. Res*., 112(D23304), doi: 10.1029/2007JD008710EPA

Crawford, J., Davis, D., Olson, J., Chen, G., Liu, S., Gregory, G., Barrick, J., Sachse, G., Sandholm, S., Heikes, B., Singh, H., and Blake, D. (1999). Assessment of upper tropospheric HOx sources over the tropical Pacific based on NASA GTE/PEM data: Net effect on HOx and other photochemical parameters. Journal of Geophysical Research: Atmospheres, 104(D13), 16255-16273. https://doi.org/10.1029/1999JD900106

Draxler, R.R., Rolph, G.D., 2010. HYSPLIT (HYbrid Single-Particle Lagrangian Integrated Trajectory) model access via NOAA ARL READY website (http://ready. arl. noaa. gov/HYSPLIT. php), NOAA Air Resources Laboratory. Silver Spring, MD 25.

Goldberg, Daniel L., Christopher P. Loughner, Maria Tzortziou, Jeffrey W. Stehr, Kenneth E. Pickering, Lackson T. Marufu, and Russell R. Dickerson. "Higher Surface Ozone Concentrations over the Chesapeake Bay than over the Adjacent Land: Observations and Models from the DISCOVER-AQ and CBODAQ Campaigns." Atmospheric Environment 84 (February 2014): 9–19.

Goldberg, D.L., Anenberg, S.C., Griffin, D., McLinden, C.A., Lu, Z., Streets, D.G., 2020. Disentangling the impact of the COVID-19 lockdowns on urban NO2 from natural variability. Geophys. Res. Lett. 47, e2020GL089269.

Grosjean, D., Grosjean, E., Williams, E.L., 1994. Thermal decomposition of PAN, PPN and vinyl-PAN. Air Waste 44, 391–396.

Guo, F., Bui, A. A. T., Schulze, B. C., Yoon, S., Shrestha, S., Wallace, H. W., Sakai, Y., Actkinson, B. W., Erickson, M. H., Alvarez, S., Sheesley, R., Usenko, S., Flynn, J., and Griffin, R. J. (2021). Urban core-downwind differences and relationships related to ozone production in a major urban area in Texas. Atmospheric Environment, 262, 118624. https://doi.org/10.1016/j.atmosenv.2021.118624

Haman, C. L., Lefer, B., & Morris, G. A. (2012). Seasonal variability in the diurnal evolution of the boundary layer in a near-coastal urban environment. Journal of Atmospheric and Oceanic Technology, 29(5), 697–710.

Iacono, M.J., Delamere, J.S., Mlawer, E.J., Shephard, M.W., Clough, S.A., Collins, W.D., 2008. Radiative forcing by long-lived greenhouse gases: Calculations with the AER radiative transfer models. J. Geophys. Res. Atmos. 113.

Kleinman, L. I. (1994). Low and high NOx tropospheric photochemistry. Journal of Geophysical Research: Atmospheres, 99(D8), 16831-16838. https://doi.org/10.1029/94JD01028

Kleinman, L. I. (2005). The dependence of tropospheric ozone production rate on ozone precursors. Atmospheric Environment, 39(3), 575–586, https://doi.org/10.1016/j.atmosenv.2004.08.047.

Kleinman et al. (2005). A comparative study of ozone production in five US metropolitan areas, J. Geophys. Res., 110, D02301, doi:10.1029/2004JD005096.

Komhyr, W. D. (1972). U.S. Patent No. 3,681,228. Washington, DC: U.S. Patent and Trademark Office.

Komhyr, W. D. (1986). Operations handbook-ozone measurements to 40-km altitude with Model 4A Electrochemical Concentration Cell (ECC) ozonesondes (used with 1680-MHz radiosondes). Tech. Memo. ERL ARL-149, 49Air Resour. Lab., Boulder, Colo.

Langford, A. O., C. J. Senff, R. M. Banta, R. M. Hardesty, R. J. Alvarez II, Scott P. Sandberg, and Lisa S. Darby. "Regional and Local Background Ozone in Houston during Texas Air Quality Study 2006." Journal of Geophysical Research: Atmospheres 114, no. D7 (2009).

Lefer, B., Rappenglück, B., Flynn, J., Haman, C. (2010), Photochemical and meteorological relationships during the Texas-II Radical and Aerosol Measurement Project (TRAMP), *Atmospheric Environment*, doi: 10.1016/j.atmosenv.2010.03.011.

Lei, R.; Talbot, R.; Wang, Y.; Wang, S.-C.; Estes, M. (2018), Influence of Cold Fronts on Variability of Daily Surface O_3 over the Houston-Galveston-Brazoria Area in Texas USA during 2003–2016. *Atmosphere 9:* 159, doi:10.3390/atmos9050159.

Li, L., Chen, C. H., Huang, C., Huang, H. Y., Zhang, G. F., Wang, Y. J., ... & Jang, C. J. (2012). Process analysis of regional ozone formation over the Yangtze River Delta, China using the Community Multi-scale Air Quality modeling system. Atmospheric Chemistry and Physics, 12(22), 10971-10987.

Li, L., Xie, S., Zeng, L., Wu, R., Li, J., 2015. Characteristics of volatile organic compounds and their role in ground-level ozone formation in the Beijing-Tianjin-Hebei region, China. Atmos. Environ. 113, 247–254.

Mazzuca et al. (2016). Ozone production and its sensitivity to NOx and VOCs: results from the DISCOVER-AQ field experiment, Houston 2013, Atmos. Chem. Phys., doi: 10.5194/acp-16-14463-2016.

Morrison, H., Thompson, G., Tatarskii, V., 2009. Impact of cloud microphysics on the development of trailing stratiform precipitation in a simulated squall line: Comparison of one-and two-moment schemes. Mon. Weather Rev. 137, 991–1007.

Nakanishi, M., Niino, H., 2009. Development of an improved turbulence closure model for the atmospheric boundary layer. J. Meteorol. Soc. Japan. Ser. II 87, 895–912.

NOAA. What percentage of the American population lives near the coast? National Ocean Service website, https:// https://oceanservice.noaa.gov/facts/population.html, 02/26/21.

NORTH AMERICAN REGIONAL REANALYSIS: A long-term, consistent, high-resolution climate dataset for the North American domain, as a major improvement upon the earlier

global reanalysis datasets in both resolution and accuracy, Fedor Mesinger et. al, submitted to BAMS 2004.

Olson, J. R., Crawford, J. H., Chen, G., Brune, W. H., Faloona, I. C., Tan, D., Harder, H., and Martinez, M. (2006). A reevaluation of airborne HOx observations from NASA field campaigns. Journal of Geophysical Research: Atmospheres, 111(D10). https://doi.org/10.1029/2005JD006617

Pavlovic, Radovan T., Fahad M. Al-Fadhli, Yosuke Kimura, David T. Allen, and Elena C. McDonald-Buller, Impacts of Emission Variability and Flare Combustion Efficiency on Ozone Formation in the Houston–Galveston–Brazoria Area, *Industrial and Engineering Chemistry Research,* Publication Date (Web): April 5, 2012 (Article), DOI: 10.1021/ie203052w.

Pisso, I., Sollum, E., Grythe, H., Kristiansen, N.I., Cassiani, M., Eckhardt, S., Arnold, D., Morton, D., Thompson, R.L., Groot Zwaaftink, C.D., 2019. The Lagrangian particle dispersion model FLEXPART version 10.4. Geosci. Model Dev. 12, 4955–4997.

Schroeder, J. R., Crawford, J. H., Fried, A., Walega, J., Weinheimer, A., Wisthaler, A., Wisthaler, A., Muller, M., Mikoviny, T., Chen, G., Shook, M., Blake, D., and Tonesen, G. S. (2017). New insights into the column CH2O/NO2 ratio as an indicator of near-surface ozone sensitivity. Journal of Geophysical Research: Atmospheres, 122(16), 8885-8907. https://doi.org/10.1002/2017JD026781, 2017.

Sillman, S. (1995). The use of NO y, H2O2, and HNO3 as indicators for ozone-NOx-hydrocarbon sensitivity in urban locations. Journal of Geophysical Research: Atmospheres, 100(D7), 14175–14188. https://doi.org/ 10.1029/94JD02953

Simpson, John E. Sea Breeze and Local Winds. Cambridge University Press, 1994.

Smit, H. G. J., et al. (2007), Assessment of the performance of ECC-ozonesondes under quasi-flight conditions in the environmental simulation chamber: Insights from the Juelich Ozone Sonde Intercomparison Experiment (JOSIE), J. Geophys. Res., 112, D19306, doi:10.1029/2006JD007308.

Stauffer, R. M., Morris, G. A., Thompson, A. M., Joseph, E., Coetzee, G. J. R., & Nalli, N. R. (2014). Propagation of radiosonde pressure sensor errors to ozonesonde measurements. Atmospheric Measurement Techniques, 7(1), 65–79.

Sullivan, J. T., Berkoff, T., Gronoff, G., Knepp, T., Pippin, M., Allen, D., ... & McGee, T. J. (2019). The ozone water–land environmental transition study: An innovative strategy for understanding Chesapeake Bay pollution events. Bulletin of the American Meteorological Society, 100(2), 291-306.

Thompson, A. M., Smit, H. G. J., Witte, J. C., Stauffer, R. M., Johnson, B. J., Morris, G., von der Gathen, P., Van Malderen, R., Davies, J., Piters, A., Allaart, M., Posny, F., Kivi, R., Cullis, P., Hoang Anh, N. T., Corrales, E., Machinini, T., da Silva, F. R., Paiman, G., Thiong'o, K., Zainal, Z., Brothers, G. B., Wolff, K. R., Nakano, T., Stübi, R., Romanens,

G., Coetzee, G. J. R., Diaz, J. A., Mitro, S., Mohamad, M., & Ogino, S. (2019). Ozonesonde quality assurance: The JOSIE–SHADOZ (2017) experience. Bulletin of the American Meteorological Society, 100(1), 155–171.

Tuite, K., Brockway, N., Colosimo, S. F., Grossmann, K., Tsai, C., Flynn, J., ... & Stutz, J. (2018). Iodine catalyzed ozone destruction at the Texas Coast and Gulf of Mexico. Geophysical Research Letters, 45(15), 7800-7807.

Vömel, H., Smit, H. G., Tarasick, D., Johnson, B., Oltmans, S. J., Selkirk, H., ... & Stübi, R. (2020). A new method to correct the electrochemical concentration cell (ECC) ozonesonde time response and its implications for "background current" and pump efficiency. *Atmospheric Measurement Techniques*, *13*(10), 5667-5680.

Wang, Yuxuan, Beixi Jia, Sing-Chun Wang, Mark Estes, Lu Shen, Yuanyu Xie (2016), Influence of the Bermuda High on interannual variability of summertime ozone in the Houston-Galveston-Brazoria region, *Atmos. Chem. Phys.,* 16: 15265-15276, doi: 10.5194/acp-16-15265-2016.

Webster, Mort, Junsang Nam, Yosuke Kimura, Harvey Jeffries, William Vizuete, David T. Allen (2007), The effect of variability in industrial emissions on ozone formation in Houston, Texas, *Atmospheric Environment* 41 (2007) 9580–9593.

Zhang, G., Jing, S., Xu, W., Gao, Y., Yan, C., Liang, L., Huang, C., Wang, H., 2021. Simultaneous observation of atmospheric peroxyacetyl nitrate and ozone in the megacity of Shanghai, China: Regional transport and thermal decomposition. Environ. Pollut. 274, 116570.

Zhang, R., Lei, W., Tie, X., Hess, P., 2004. Industrial emissions cause extreme urban ozone diurnal variability. Proc. Natl. Acad. Sci. 101, 6346–6350.